POWER FACTOR CORRECTION TOPOLOGIES AND SMALL-SIGNAL MODELING

I: Single-Phase and Three-Phase Power Factor Correction

II: Small-Signal Analysis of Converters in Discontinuous Conduction Mode

Thesis by
Kurt Schenk

In Partial Fulfillment of the Requirements
for the degree of Doctor of Philosophy

California Institute of Technology
Pasadena, California

1999
(Submitted August 7, 1998)

meinen Eltern Albrecht und Frieda Schenk

Acknowledgements

I whish to thank my advisor, Professor Slobodan Ćuk, for accepting me into the Power Electronics Group, for the freedom to choose research topics, for his support, and most of all for the teacher-student relationship we have shared. Special thanks must go to Dr. Andrzej Pietkiewicz for encouraging me to pursue graduate studies at Caltech and for many fruitful discussions.

I gratefully acknowledge the financial support of Caltech, in the form of Graduate Teaching Assistantships, the Powell Fellowship, the Killgore Followship, and the following corporations who supported the Power Electronics Group during my stay: ELGAR Corporation, Lucent Technologies, General Electric Co., Ascom Energy Systems AG, Hughes Aircraft Co., Boeing Company, Olivetti, Dong-Ah Electric Co., Ltd. and GEC Marconi.

I greatly appreciate the valuable help of Mr. Dennis Danielson, Mr. Colin Wood, Mrs. Angela Wood, Dr. James Lazar and Professor R. D. Middlebrook in editing this thesis.

Every graduate of the Power Electronics Group is indebted to his predecessors, who have left behind helpful tools, useful computer programs, and a large body of knowledge representative of the Power Electronics Group.

Finally and most importantly, I would like to thank my wife Christine for her love, support and infinite patience during my stay at Caltech.

Abstract

Part I:

This thesis is motivated by the increasing demand for power quality improvement. Power factor correction topologies for both single- and the three-phase utility lines are investigated and new modes of operation are introduced. The discussed topologies are so-called automatic power factor correctors. The current shaping function is a natural property of these circuits, and no extra current control loop is necessary.

In both the single- and three-phase cases, a control method is introduced which provides full output regulation and simultaneously reduces the distortion of the input current at no extra cost.

Whereas in the single-phase topology, galvanic isolation is easily obtained, in the three-phase topology, some obstacles have to be overcome. The isolated three-phase converter has an inherent output voltage ripple. This problem is analyzed and a solution is presented.

Results obtained on experimental circuits agree well with the prediction and therefore confirm the validity of the analysis.

Part II:

The small-signal behavior of converters in discontinuous conduction mode (DCM) is investigated using an alternative approach. Transfer functions obtained by state-space averaging in DCM do not provide accurate results at higher frequencies. A correction term is introduced that can be added to the transfer function. This greatly enhances the accuracy.

For converters operating in DCM, the state-space averaging method as originally introduced is relatively complicated if more than one element operates in discontinuous conduction mode. In this thesis, a standardized procedure is introduced to perform state-space averaging. Also, the complexity of this procedure does not increase as the number of discontinuous states increases.

Contents

Part I

Single-Phase and Three-Phase Power Factor Correction

Chapter 1

Introduction

In today's world the need for electrical power is ever present. Electrical power appears in two different forms, namely as dc-power or ac-power. The discipline of power electronics is concerned with the conversion of power from one form to another. Power converters can be classified into four basic categories. The four types are dc-to-dc converters, ac-to-dc rectifiers, dc-to-ac inverters and ac-to-ac cycloconverters. This part of the thesis is concerned with ac-to-dc rectification.

Electrical power is predominantly distributed in the form of ac-power. In recent decades the demand for dc-power has increased exponentially. This is due to electronic equipment such as computers, consumer electronics and communication systems to name a few. All these loads require dc-power in order to operate. Therefore, there is a rapidly growing need for ac-to-dc rectification circuits. These circuits constitute the interface between the ac-power line and the dc-load.

Ideally, the input voltage and input current to an ac-to-dc rectifier are both in-phase sine waves, and the output voltage is constant, independent of the current drawn from the rectifier. Thus, the input impedance is purely resistive, and the output impedance is zero. The subject of power quality is concerned with how closely the ideal situation is obtained at the input to the rectifier. In Chapter 2, the basic definitions quantifying power quality are defined and their mutual relation is derived. The two most important indicators of power quality are total harmonic distortion (*THD*) and power factor (*PF*). The *THD* is a measure of the distortion of a signal. A pure sine wave has a *THD* equal to zero. The power factor indicates what fraction of the apparent power (VA-product) present in a system is actually delivered to the load. Ideally, the power factor is unity.

Ac-power systems can be divided in two groups, namely single-phase systems and three-phase systems. The simplest, and historically most frequently employed, method of the ac-to-dc rectification is the use of a full-wave rectifier bridge followed by a large energy storage capacitor. This type of rectifier, discussed in Chapter 3, generates a large amount of distortion in the input current. Since the utility line is a non-ideal voltage source with a finite impedance, the current distortion also causes a voltage distortion. Although a single rectifier circuit has little effect on the voltage waveform, the immense number of these rectifiers causes severe problems. Chapter 3 also deals with conventional three-phase ac-to-dc rectification. In this case, the distortion is naturally less severe but still substantial.

Because the distortion problem has increased so dramatically, international standards have been imposed with the objective to limit the current distortion. In order to meet these limits, new and more sophisticated ac-to-dc rectifier circuits are necessary. In the past decade, power electronics engineers have invested a considerable amount of effort in search of suitable topologies which avoid the current distortion, or reduce it to an acceptable level. These circuits are called power factor correctors (PFC) or current shapers.

A vast number of topologies have been proposed. The most straightforward approach is a two-stage solution. The first stage removes the distortion from the input current, and the second stage regulates the output voltage. Both stages are decoupled by means of a large energy storage capacitor between them.

There are two distinct types of power factor correctors, controlled PFC circuits and automatic PFC circuits. In the topologies of the first group, the input current is monitored and compared with an ideal reference. The difference is used in a fast feedback loop which controls the input current so that it closely follows the reference.

Automatic PFC circuits do not require current sensing as current shaping is a natural property of these circuits. When the basic automatic power factor correction topologies, such as the Boost and the Buck-Boost, were first introduced, they were operated with constant duty ratio over one line cycle. However, in many practical cases, the output voltage of the converter must be tightly controlled by some means. The most obvious

method is the implementation of a feedback loop. The bandwidth of this loop, however, must be well below the line frequency in order to ensure the required constant duty ratio over one line cycle. This does not allow tight load regulation, and is therefore contradictory. These ac-to-dc rectifiers also exhibit an undesirable output voltage ripple at twice the line frequency, requiring in most cases a post regulator.

These two-stage solutions are however, bulky, complex and expensive. It is therefore natural to search for single-stage solutions which can simultaneously provide low distortion of the input current, and well-regulated output voltage. This search has lead to single-stage solutions which incorporate a high bandwidth output voltage control loop, and inherently possess a high quality input current waveform.

All topologies presented in this thesis are automatic power factor correctors. A fast feedback loop is not only possible but is in fact essential for optimum performance with regard to the input current distortion. Such a topology for a three-phase ac-to-dc rectifier is introduced and analyzed in Chapter 4. This circuit is not able to completely avoid the input current distortion, but can drastically reduced it. If a fast output feedback loop is employed, the current waveform can be further improved. Thus, with a fast control loop, two goals are achieved simultaneously, an improved input current waveform and a well-regulated output voltage. Therefore, in this topology the fast output regulation is not merely an option; it is required to achieve optimum performance at the input of the rectifier. In addition, because the topology is based on a Boost converter high efficiency is achieved.

The disadvantages of this converter are the high output voltage and also the fact that galvanic isolation is not easily implemented. In Chapter 5, two extensions of the converter are discussed. These extensions, derived from the Cuk and the Sepic converters, are able to solve both problems. Galvanic isolation is easily included, and the output voltage can be chosen arbitrarily. The principal problem associated with these topologies is that they tend to have an output voltage ripple at six times the line frequency. The nature of this problem is investigated, and a solution is presented.

In Chapter 6, a single-phase ac-to-dc rectifier is investigated. It can be realized as both, an isolated or non-isolated version. The topology exhibits similar characteristics

to the three-phase ac-to-dc rectifier discussed in Chapter 4. Optimum performance is achieved when a fast output feedback is employed. If the converter is designed appropriately, the input current distortion nearly vanishes. Once again, a fast control loop performs two tasks simultaneously, both improving the input current waveform and providing full output regulation.

Chapter 2

Definitions

In this chapter the definitions of the most important quantities characterizing the power quality of ac systems are briefly reviewed. Most power electronics and power processing engineers are familiar with the concepts introduced here. Nevertheless, it is important to clearly state all the definitions since some quantities may be defined slightly differently by various sources.

2.1 Periodic Signals

All the definitions introduced in this chapter apply to periodic functions. A function $f_t(t)$ is periodic with a period length T if it satisfies

$$f_t(t) = f_t(t+T) \tag{2.1.1}$$

It is common practice to normalize $f_t(t)$ with respect to t such that the period of the function becomes 2π. The normalized function $f(\theta)$ must satisfy

$$f(\theta) = f_t\left(\theta\frac{T}{2\pi}\right) \tag{2.1.2}$$

The periodicity of $f(\theta)$ stated in (2.1.1) can be expressed as

$$f(\theta) = f(\theta + 2\pi) \tag{2.1.3}$$

The normalized expressions tend to be simpler. Therefore, in this thesis, this form is always used.

2.2 Fourier Series Representation of a Periodic Signal

Each function satisfying (2.1.3) has a Fourier series expansion of the form

$$f(\theta) = a_o + \sqrt{2}\sum_{k=1}^{\infty}(a_k \cos(k\theta) + b_k \sin(k\theta)) \tag{2.2.1}$$

where

$$a_o = \frac{1}{2\pi}\int_0^{2\pi} f(\theta)\,d\theta \tag{2.2.2}$$

$$a_k = \frac{1}{\sqrt{2}\pi}\int_0^{2\pi} f(\theta)\cos(k\theta)\,d\theta \tag{2.2.3}$$

$$b_k = \frac{1}{\sqrt{2}\pi}\int_0^{2\pi} f(\theta)\sin(k\theta)\,d\theta \tag{2.2.4}$$

This definition was chosen because a_k $(k = 0,1,2,...)$ and b_k $(k = 1,2,3,...)$ are the rms-values of each individual component of the expansion in (2.2.1). The definition of the rms-value is stated in the next section. Sometimes an alternative form of the Fourier series expansion is more useful because it consists of a single term for each frequency.

$$f(\theta) = c_o + \sqrt{2}\sum_{k=1}^{\infty} c_k \sin(k\theta + \varphi_k) \tag{2.2.5}$$

where

$$c_o = \frac{1}{2\pi}\int_0^{2\pi} f(\theta)\,d\theta \tag{2.2.6}$$

$$c_k = |k_k| \tag{2.2.7}$$

$$\varphi_k = \arg(k_k) \tag{2.2.8}$$

$$k_k = \frac{\mathrm{j}}{\sqrt{2\pi}} \int_0^{2\pi} f(\theta) e^{-\mathrm{j}k\theta}\, d\theta \tag{2.2.9}$$

The relation between the coefficients of the two forms of the Fourier series is as follows:

$$c_o = a_o \tag{2.2.10}$$

$$k_k = \mathrm{j}a_k + b_k \quad \text{for } k = 1,2,3,... \tag{2.2.11}$$

In this thesis both versions, i.e., (2.2.1) and (2.2.5) respectively, are used depending on the particular case. The components of the Fourier series expansion (2.2.5) are also called *harmonic components* or simply *harmonics*. The component of order 1 (i.e., for $k = 1$) is called the *fundamental component*.

2.3 Root-Mean-Square Value

The root-mean-square value (rms-value) is defined for periodic functions, i.e., functions satisfying (2.1.3). The rms-value F_{rms} of a function $f(\theta)$ is given by

$$F_{rms} \equiv \sqrt{\frac{1}{2\pi} \int_0^{2\pi} f^2(\theta)\, d\theta} \tag{2.3.1}$$

The result is of course unique for any choice of the integration interval. Substituting the Fourier series expansion of the $f(\theta)$ according to (2.2.5) into the formula for the rms-value leads to the following expression:

$$F_{rms} = \sqrt{\frac{1}{2\pi} \int_0^{2\pi} \left(c_o + \sqrt{2} \sum_{k=1}^{\infty} c_k \sin(k\theta + \varphi_k) \right)^2 d\theta} \tag{2.3.2}$$

In order to simplify this relation, the following two equalities are useful:

$$\int_0^{2\pi} \sin(m\theta + \varphi)\, d\theta = 0 \quad ; \qquad \text{for } m = \text{integer} \tag{2.3.3}$$

$$\int_0^{2\pi} \sin(m\theta+\varphi)\sin(n\theta+\varphi)\,d\theta = \begin{cases} 0 & \text{if } m \neq n \\ \pi & \text{if } m = n \end{cases} ; \quad \text{for } m,n = \text{integer} \qquad (2.3.4)$$

The rms-value can then simply be expressed as

$$F_{rms} = \sqrt{\sum_{k=0}^{\infty} c_k^{\,2}} \qquad (2.3.5)$$

This relation is known as Parseval's theorem.

If the function in question is a voltage $v(\theta)$ or a current $i(\theta)$ respectively, then the corresponding rms-values are given by

$$V_{rms} = \sqrt{\sum_{k=0}^{\infty} V_k^{\,2}} \qquad (2.3.6)$$

$$I_{rms} = \sqrt{\sum_{k=0}^{\infty} I_k^{\,2}} \qquad (2.3.7)$$

2.4 Total Harmonic Distortion

The Total Harmonic Distortion (*THD*) is defined for periodic functions, i.e., functions satisfying (2.1.3), with no dc-component. It is a measure of the amount of higher order harmonics of a signal normalized with respect to the fundamental component. In this thesis the following, widely accepted definition for the *THD* of a function $f(\theta)$ will be used:

$$THD \equiv \frac{\sqrt{\sum_{k=2}^{\infty} c_k^{\,2}}}{c_1} \qquad (2.4.1)$$

where c_k is defined according to (2.2.7) and (2.2.9). By assumption c_0 is zero. Using (2.3.5) and the fact that $c_o = 0$, the *THD* can be rewritten as

$$THD = \sqrt{\frac{F_{rms}^{\ 2}}{c_1^{\ 2}} - 1} \tag{2.4.2}$$

It is evident that the *THD* is zero if the function $f(\theta)$ is a pure sine wave since under this condition c_1 is identical to F_{rms}.

2.5 Power Factor

The power factor is defined if both the voltage and the current have periodic waveforms with the same frequency. That means the voltage waveform $v(\theta)$ and current waveform $i(\theta)$ satisfy (2.1.3) simultaneously. (Note that the dc quantities are also allowed.) The power factor *PF* is then defined as

$$PF = \frac{P}{S} \tag{2.5.1}$$

where P is the averaged power over one period (P is also called the active power) and S is the apparent power. P and S are defined by

$$P = \frac{1}{2\pi}\int_0^{2\pi} v(\theta) i(\theta)\, d\theta \tag{2.5.2}$$

$$S = V_{rms} I_{rms} \tag{2.5.3}$$

Equation (2.5.2) can be rewritten using the Fourier series expansion of $v(\theta)$ and $i(\theta)$ according to (2.2.5).

$$P = \frac{1}{2\pi}\int_0^{2\pi} \left(V_o + \sqrt{2}\sum_{k=1}^{\infty} V_k \sin\left(k\theta + \varphi_{v_k}\right) \right)\left(I_o + \sqrt{2}\sum_{k=1}^{\infty} I_k \sin\left(k\theta + \varphi_{i_k}\right) \right) d\theta \tag{2.5.4}$$

Also this expression can be simplified using (2.3.3) and the following equality.

$$\int_0^{2\pi} \sin(m\theta+\varphi_1)\sin(n\theta+\varphi_2)\,d\theta = \begin{cases} 0 & \text{if } m \neq n \\ \pi\cos(\varphi_1-\varphi_2) & \text{if } m = n \end{cases} ; \quad \text{for } m,n = \text{integer} \tag{2.5.5}$$

With this the power given in (2.5.4) can be expressed as

$$P = V_o I_o + \sum_{k=1}^{\infty} V_k I_k \cos(\varphi_{v_k} - \varphi_{i_k}) \tag{2.5.6}$$

From (2.2.7) it can easily be concluded that V_k and I_k are both real non-negative numbers. Therefore, the following inequalities hold:

$$P = V_o I_o + \sum_{k=1}^{\infty} V_k I_k \cos(\varphi_{v_k} - \varphi_{i_k}) \leq \sum_{k=0}^{\infty} V_k I_k \leq \underbrace{\sqrt{\sum_{k=0}^{\infty} V_k^2}}_{=V_{rms}} \cdot \underbrace{\sqrt{\sum_{k=0}^{\infty} I_k^2}}_{=I_{rms}} = S \tag{2.5.7}$$

The left inequality is obvious since the cosine of real arguments is always equal or smaller than unity. This inequality becomes an equality if and only if

$$\varphi_{v_k} = \varphi_{i_k} \quad \text{for all } k \tag{2.5.8}$$

Therefore, the voltage and current of any given harmonic component must have the same phase displacement. The right inequality in (2.5.7) is the well-known Schwarz inequality with equality if and only if

$$V_k = \alpha \cdot I_k \quad \text{for all } k \tag{2.5.9}$$

Note that α must be real and non-negative since I_k and V_k are real and non-negative. If the conditions (2.5.8) and (2.5.9) are satisfied then the following holds:

$$v(\theta) = \alpha \cdot i(\theta) \tag{2.5.10}$$

This can be concluded due to the linearity of the Fourier series expansion given in (2.2.5), or equivalently, since the value of a resistor is a real non-negative number,

$$v(\theta) = R \cdot i(\theta) \tag{2.5.11}$$

Thus, to achieve the special case where $P = S$, the current waveform must be proportional to the voltage waveform. Conversely, if $v(\theta)$ and $i(\theta)$ are related according to (2.5.11), then a substitution into (2.2.9) must lead to the conditions (2.5.8) and (2.5.9). Therefore, it can be concluded that

$$PF \leq 1 \tag{2.5.12}$$

with equality if and only if the voltage and current exhibit resistive behavior on the observed terminals; or equivalently if and only if (2.5.11) is satisfied.

2.6 Power Factor Under Ideal Voltage Condition

The voltage waveform in most ac power systems such as the utility line is ideally a clean sine wave. Even though in many cases some distortion in the voltage waveform is present, unless otherwise mentioned in this thesis an ideal sine wave is assumed. Without loss of generality it is further assumed that this sine wave has no phase shift, i.e., $\varphi_{v_1} = 0$. Thus, the line voltage is represented by

$$v(\theta) = V_1 \sqrt{2} \sin(\theta) \tag{2.6.1}$$

With this choice:

$$V_1 = V_{rms} \tag{2.6.2}$$

Substituting this voltage into the general expression for the power (2.5.6) and into (2.5.3) leads to

$$P = V_1 I_1 \cos(\varphi_{i_1}) \tag{2.6.3}$$

$$S = V_1 I_{rms} \tag{2.6.4}$$

The power factor can now be found by substituting these two equations into (2.5.1)

$$PF = \frac{I_1}{I_{rms}} \cos(\varphi_{i_1}) \tag{2.6.5}$$

or equivalently

$$PF = DF \cdot \cos(\varphi) \tag{2.6.6}$$

where

$$DF = \frac{I_1}{I_{rms}} \tag{2.6.7}$$

and φ is the phase displacement between the voltage and fundamental current component I_1. The subscript of φ has been dropped because it is the only relevant phase shift. DF is commonly referred to as the distortion factor whereas the $\cos(\varphi)$ is called the displacement factor. Clearly, each of these two components of the power factor is either equal to or smaller than unity.

If the voltage is an ideal sine wave, then the power factor, the distortion factor and the total harmonic distortion can be related. Equations (2.4.2) and (2.6.5) can be combined to result in

$$THD = \sqrt{\frac{\cos^2(\varphi)}{PF^2} - 1} \tag{2.6.8}$$

which can be rearranged as

$$PF = \frac{\cos(\varphi)}{\sqrt{THD^2 + 1}} \tag{2.6.9}$$

2.7 Symmetrical Current and Ideal Voltage Waveform

Very often special current waveforms are encountered which even further simplify the expressions. The input currents of the circuits discussed in this thesis satisfy the following two relations:

$$i(\theta) = i(\pi - \theta) \tag{2.7.1}$$

$$i(\theta) = -i(\pi + \theta) \tag{2.7.2}$$

Thus, each half wave is symmetrical with respect to the vertical line through its center and the negative half wave is equivalent to the positive one (except for the sign). Applying the Fourier series expansion according to (2.2.1) through (2.2.4) to these currents yields zero for all a_k and for all even order b_k. These results are derived in the Appendix of [1]. The above conditions combine the definitions for the odd periodic expansion and the alternating periodic expansion as defined in [1]. Therefore, currents satisfying the above conditions can be decomposed using only sine terms of odd order. Thus,

$$i(\theta) = \sqrt{2}\sum_{k=1}^{\infty} I_{2k-1}\sin((2k-1)\theta) \tag{2.7.3}$$

The fundamental component of such a current is in phase with the voltage. Under this condition the power factor given in (2.6.5) reduces to

$$PF = \frac{I_1}{I_{rms}} \tag{2.7.4}$$

And (2.6.8) and (2.6.9) simply become

$$THD = \sqrt{\frac{1}{PF^2} - 1} \tag{2.7.5}$$

$$PF = \frac{1}{\sqrt{THD^2 + 1}} \tag{2.7.6}$$

Thus, there is a one to one correspondence between the power factor and the *THD*. More properties concerning the special waveform are stated in Appendix A.2.

2.8 Unity Power Factor Versus Zero Total Harmonic Distortion

In energy processing systems a unity power factor is very desirable. One reason is that at unity power factor the rms-values of the voltage and current are minimized for a

given power level. The current ratings of the components of energy generation and transmission systems can be minimized under this condition. This topic is treated in greater detail in Chapter 3.

In Section 2.5 it has been shown that the current must be proportional to the voltage to achieve unity power factor. If the voltage waveform is not an ideal sine wave, then its *THD* is not zero and, thus, the current *THD* is also not zero. In fact, both the voltage and the current *THD* are equal. If the voltage is an ideal sine wave, then unity power factor implies that the displacement factor is 1. Therefore, the conditions under which (2.7.5) is valid are satisfied and it can be easily concluded that the *THD* is equal to zero.

Thus, a unity power factor is equivalent to a zero *THD* of the current if the voltage is an ideal sine wave. In the more general case of a distorted voltage, unity power factor is usually preferred over zero *THD*. This is because a current proportional to the voltage tends to reduce the voltage distortion. However, this effect is only weak. More important is the fact that a proportional current is much easier to generate than an ideal sine wave if the voltage is distorted.

The question might be posed why then the *THD* is used to describe the quality of power systems. The *THD* was originally introduced to specify the quality of audio amplifiers. One reason is that the power factor can be very low even with a *THD* equal to zero. This is the case when the displacement factor is low. Another reason is that the *THD* provides a better measure for the distortion of the current waveform even under ideal voltage conditions. The power factor can still be very high even with a quite severe current distortion. The uncorrected three-phase ac-to-dc converter is an example for this behavior. It will be treated in Section 3.2. In order to illustrate the dependence between the power factor and the total harmonic distortion, the following approximate relations are introduced. Using (2.7.6) it can be shown that for reasonably low *THDs* ($\approx\leq 30\%$), the following relations hold:

$$PF^2 + THD^2 \approx 1 \tag{2.8.1}$$

or

$$PF \approx 1 - \tfrac{1}{2} THD^2 \qquad (2.8.2)$$

These two approximations permit a much better understanding of the relation between power factor and current *THD*. For example, a *THD* of 10% still allows a power factor of 99.5%. These approximations have proven to be very helpful in making estimations. However, they are only valid if the voltage is approximately an ideal sine wave and if the fundamental component of the current is in phase with the voltage.

Chapter 3

Power Quality of Uncorrected Systems

In this chapter two different aspects that influence the power quality are briefly introduced on different examples. The distinction is made between the power factor reduction due to a phase-shift between the voltage and the current at the input terminals of a load and due to the harmonic distortion of the current. The goal is to establish the motivation for power factor correction, that means, the introduction of switching converter circuits, which avoid or at least reduce both of the above. Another aspect of power quality, which is not the subject of this thesis, is the high frequency noise commonly referred to as EMI (Electro Magnetic Interference).

3.1 Single-Phase Systems

3.1.1 Phase Displacement

Until recently the only concern in power distribution systems was the phase-shift between the voltage and current. This phase-shift is caused by loads that have a linear impedance with a reactive part. Examples of such loads are motors and fluorescent lamps with inductive ballasts. The simplified circuit shown in Fig. 3.1a represents this type of load.

Only the resistance R consumes power from the line. The necessary current I_R to deliver a given power level P to the load is given by

$$I_R = \frac{P}{V} \tag{3.1.1}$$

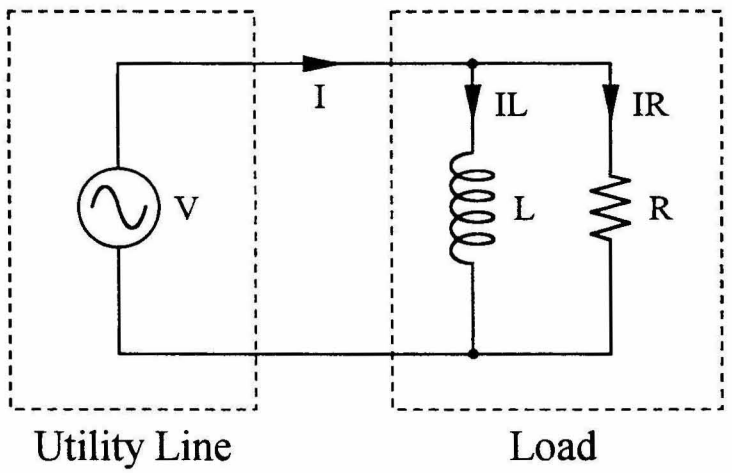

(a)

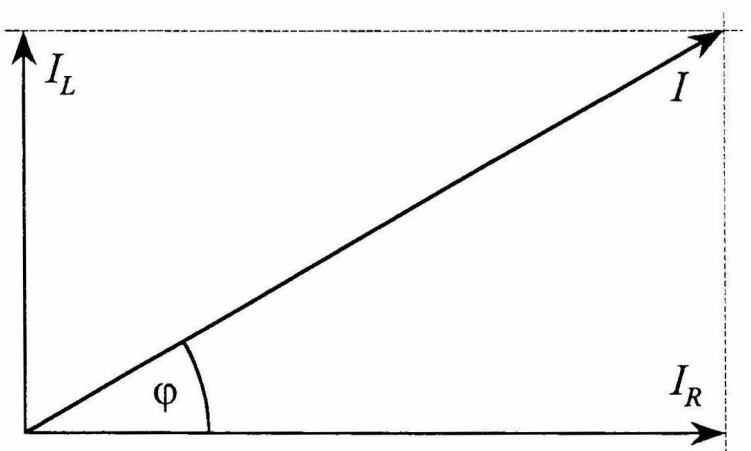

(b)

Figure 3.1: Example of a system with phase displacement. (a) A load with a reactive component connected to the utility line and (b) the corresponding current phasor diagram.

The line current I contains a second component I_L which is 90° out of phase with respect to I_R. Its magnitude is given by

$$I_L = \frac{V}{\omega L} \tag{3.1.2}$$

where ω is the angular frequency of the ac source.

The magnitude of the current that has to be provided by the utility line is the sum of the two currents above. Considering the 90° phase-shift, this sum is described by

$$I = \sqrt{I_R{}^2 + I_L{}^2} \tag{3.1.3}$$

This relation is illustrated in the phasor diagram belonging to this circuit shown in Fig. 3.1b. The distortion factor DF of such a circuit is unity since this linear circuit does not generate any harmonics of the current drawn from the source. Thus, according to (2.6.6) the power factor coincides with the displacement factor $\cos(\varphi)$, which is given by

$$PF = \cos(\varphi) = \frac{I_R}{I} \tag{3.1.4}$$

Obviously, $I \geq I_R$ with equality only if $I_L = 0$, or equivalently $\cos(\varphi) = 1$. Therefore, the power companies are interested in a unity power factor because this minimizes the line current they need to provide for a given power delivered to the load. As the power factor decreases, the magnitude of the line current I and its rms-value increases (Fig. 3.1b). This causes extra loss in the power generation and transmission system. Moreover, all components such as generators, transformers and transmission lines must be able to handle the increased current, and consequently, must be rated for higher power (higher VA rating). In a given design the maximum current is limited due to the saturation of the magnetic components, to name one reason. A reduced power factor, therefore, reduces the maximum power processing capability of this system.

These, efficiency, size and economical considerations are reasons why the power companies are interested in systems with a high power factor. In the case of a simple phase-shift, unity power factor can be achieved by connecting a capacitor in parallel with the load. This method is often used if the power is reasonably low. For high power levels other methods are available. However, this is not subject of this thesis.

3.1.2 Harmonic Distortion

In modern days the power factor problem has developed a new dimension which is discussed in this section. In the previous case an entirely linear network was considered. In recent years a growing number of non-linear loads have been connected to the utility line. A major source of the harmonic distortion is due to the use of simple ac-to-dc rectification circuits, such as diode bridges, which form a non-linear load. Such circuits constitute the interface between the ac power line and dc loads like computers, home electronics and motor drives to name a few. A similar problem exists in ac-to-ac cycloconverters, which are also in motor drives and similar applications.

A typical realization of an ac-to-dc converter is shown in Fig. 3.2. It consists of a dc-to-dc converter preceded by a full wave rectifier bridge and an energy storage capacitor C. This circuit acts as a peak detector. C is charged to the peak line voltage each half of the line cycle. This causes a high and relatively narrow peak in the line current I. The exact shape depends on the line impedance Z_L and on the size of the capacitor C. During

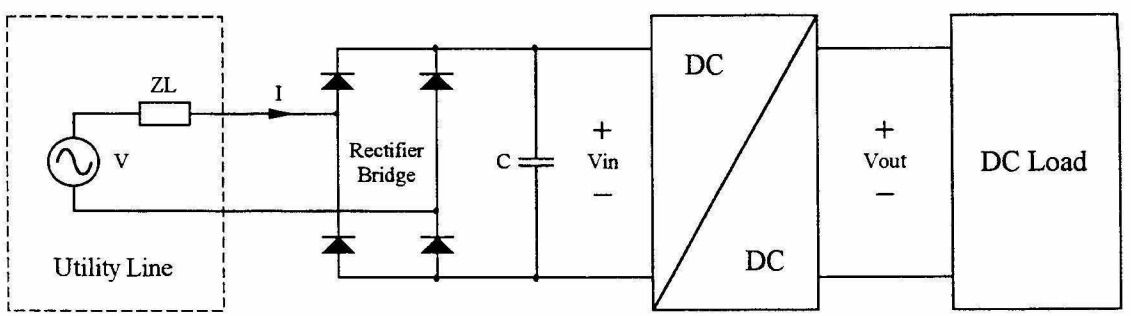

Figure 3.2: Conventional ac-to-dc rectifier circuit with "peak detector" input stage.

most of the line cycle the current I is zero and the dc-to-dc converter is fed with the energy stored in the capacitor C which is slowly discharging.

The resulting current shape is shown in Fig. 3.3a. This is a measurement on a real circuit. The consequence of such a current shape is a distorted line voltage waveform since the line impedance Z_L is not zero. The voltage waveform is also shown in Fig. 3.3a. The third trace in this figure is the ac-component of the capacitor voltage V_{in}.

The phase-shift between the voltage and the current is in this case not severe. However, the *THD* was measured to be 106% and the power factor was 67%. Equation (2.6.9) is valid if the voltage is an ideal sine wave. Given the shape in Fig. 3.3a, it can still be applied to obtain reasonably accurate results. Thus, the displacement $\cos(\varphi)$ can be determined using (2.6.9), which leads to

$$\cos(\varphi) = PF \cdot \sqrt{THD^2 + 1} \tag{3.1.5}$$

For the current waveform shown in Fig. 3.3, the displacement factor is found to be 97.6%.

Similarly, as with a phase displacement, in the case of a distorted line current, the rms-value of the line current I is also increased for a given active power delivered to the load. This leads again to increased losses. Magnetic components can saturate at a lower power level. It is easy to conclude that both the phase displacement and current distortion reduce the efficiency and the maximum power capability of power systems. Moreover, the distorted line voltage can cause other equipment connected to the line to malfunction.

Therefore, international standards have been set forth which limit the maximum allowed distortion in load currents. This topic is treated in greater detail Section 3.3. One way to alleviate the problem is to connect a low pass filter between the utility line and the ac-to-dc converter. However, for this to be effective, the bandwidth of that filter must be very low, well below 60Hz. An extensive discussion of this topic is presented in [1]. These types of filters tend to be the bulkiest and by far the heaviest part of the whole converter since they are designed for the 60Hz operation. In addition, they may

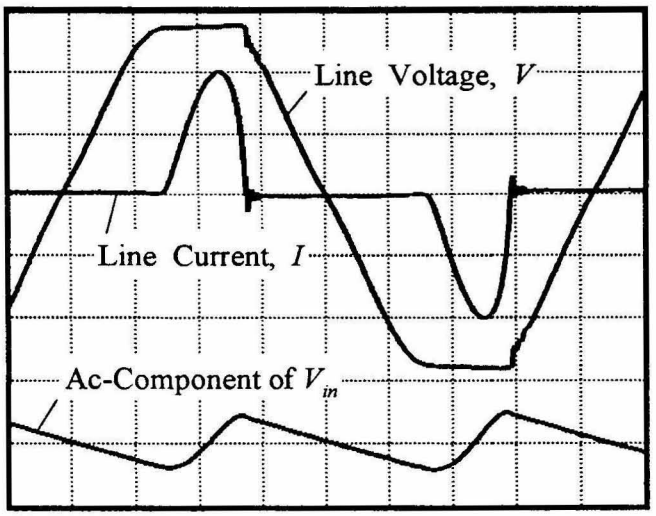

(a)

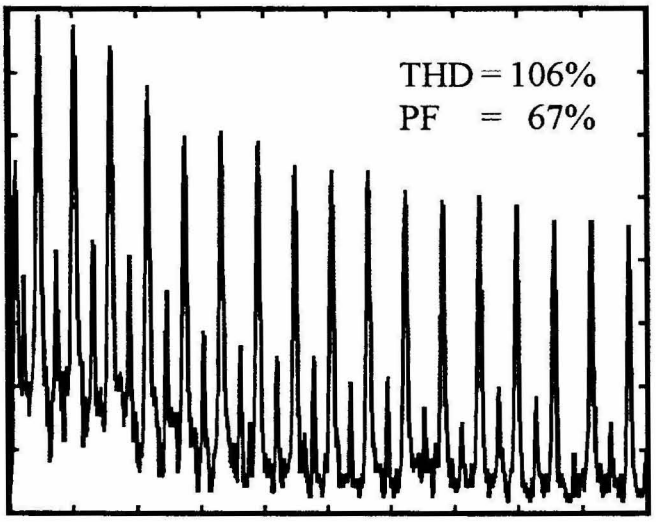

(b)

Figure 3.3: Harmonic distortion of a "peak detector" input stage. (a) Current and voltage waveforms and (b) frequency spectrum of the current. (Scales: 200Hz/Div and 10dB/DIV.)

solve the distortion problem, but not necessarily the displacement problem, particularly if the converter operates over a wide power range. In many cases different solutions are preferred. Two of the basic alternative concepts are briefly introduced in the next section. They can not only handle both the distortion problem and the displacement problem, but they can achieve that with a much smaller size and weight. Oddly enough the solution is found in the use of switching converters as power factor corrector (PFC) circuits, which can even achieve unity power factor in some cases.

3.1.3 Controlled Power Factor Correctors

In the last decade a great deal of research in the power electronics discipline has been devoted to finding more sophisticated ways of improving the input current waveform while simultaneously avoiding phase displacement. The designation *power factor corrector* is widely accepted to describe converters suitable for this purpose. These topologies are also called *current shapers*, because in many cases it is primarily the harmonic distortion present in the current waveform that has to be reduced.

One can distinguish between the two different types of power factor correction configurations, the controlled power factor correctors and the automatic power factor correctors. Into the first category belong the converters working in continuous conduction mode (CCM). In these topologies the input current is measured and shaped using a high bandwidth control loop. A very popular example is the boost converter shown in Fig. 3.4. The inner loop with fast controller C_1 controls the rectified input current such that it is proportional to the rectified input voltage. The purpose of the input filter is to remove the switching ripple. In these circuits, the switching frequency is typically more than three orders of magnitude higher than the line frequency. Thus, the bandwidth of the filter is very high and it can be realized with small components. Due to this high bandwidth, the filter does not affect the current and voltage waveforms at the line frequency. Therefore, this control method forces the input current I to be proportional to the voltage V. The second loop with slow controller C_2 has its

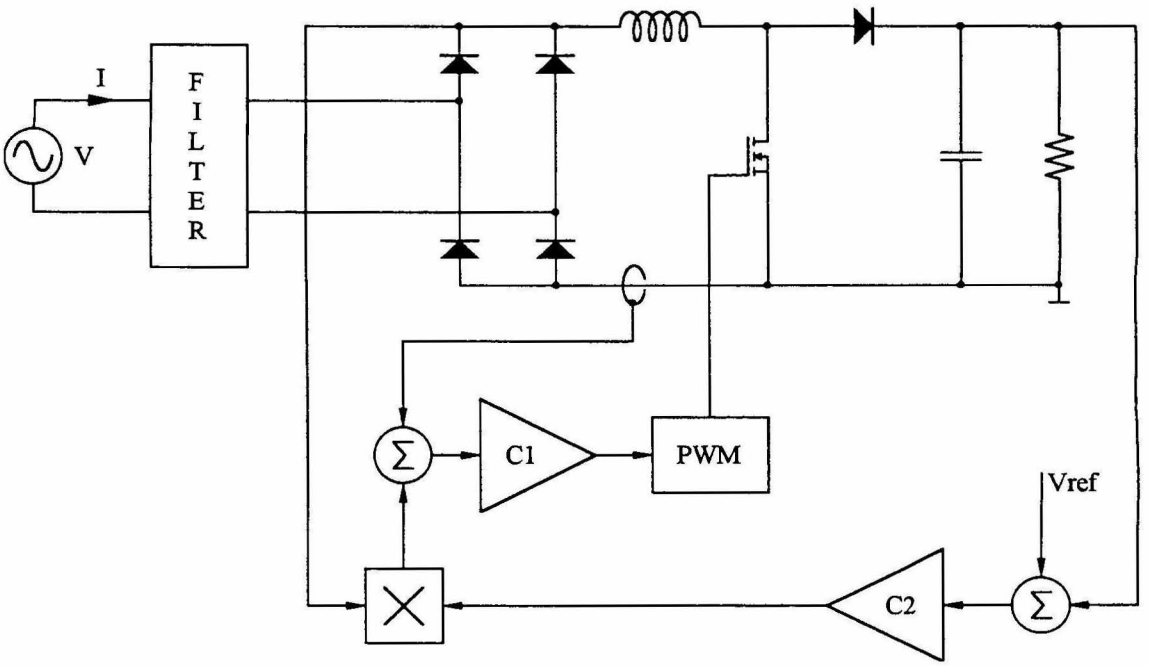

Figure 3.4: A typical Boost converter configuration in power factor corrector applications using a two-loop control structure.

bandwidth below twice the line frequency. It stabilizes the output voltage by providing the proper scale factor for the current reference in the inner loop.

It should also be pointed out that this method of current shaping is not restricted to converters in CCM. The same idea can be applied to converters in discontinuous conduction mode (DCM).

3.1.4 Automatic Power Factor Correctors

Automatic power factor correctors do not possess a current control loop. In general, no current measurement is necessary. This is advantageous since measurement of the current as shown in Fig. 3.4 can be both lossy and expensive. All converters in this group operate in DCM. The simplest example is the Buck-Boost topology as shown in Fig. 3.5a. It can be easily illustrated on this circuit how automatic current shapers operate.

The input filter is again designed with a high corner frequency, since its purpose is solely to remove the switching ripple. It does not affect the line frequency related variations of the waveforms. Thus, the switching frequency must be much higher than the line frequency. The output voltage feedback loop has to have a low bandwidth; consequently, over one line period the duty ratio is considered to be constant. If the active switch turns on, the current I_L in the inductor and I_1 at the input start to increase. The initial value is zero due to the DCM. Since the line frequency is much smaller than the switching frequency, the line voltage is approximately constant during one switching cycle. With this, the current during the on time of S can be described by the following equation:

$$i_1 = i_L = \frac{v}{L}t \tag{3.1.6}$$

Since the duty ratio is constant, the peak value at the end of the on time of the switch S is given by

$$i_{1p} = \frac{v}{L}DT_s \tag{3.1.7}$$

where D is the duty ratio and T_s is the switching period. The input filter averages the triangles out such that a continuous current is observed at the input of the filter. Using simple geometry on the triangles leads to a formula for the averaged current.

$$\bar{i}_1 = \frac{i_{1p}}{2}D = \frac{v}{2L}D^2T_s \tag{3.1.8}$$

Since all quantities except v are constant in (3.1.8), it can be concluded that the average current $\bar{i}_1$ is proportional to the instantaneous value of the input voltage. Therefore, unity power factor is achieved without any extra effort, that is automatically, hence the name automatic current shaper.

All the automatic power factor correctors work in a similar manner. Some do not provide unity power factor but instead a significantly improved current waveform as

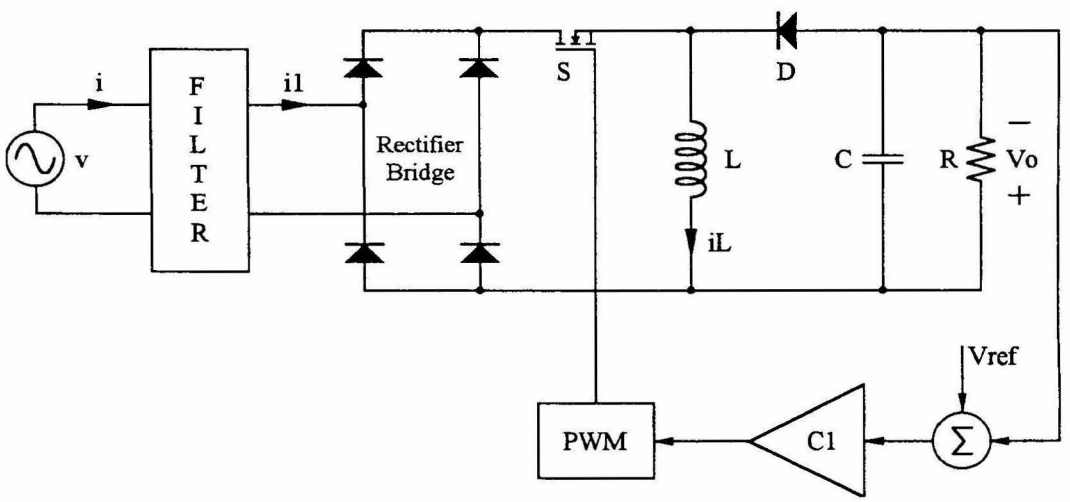

(a)

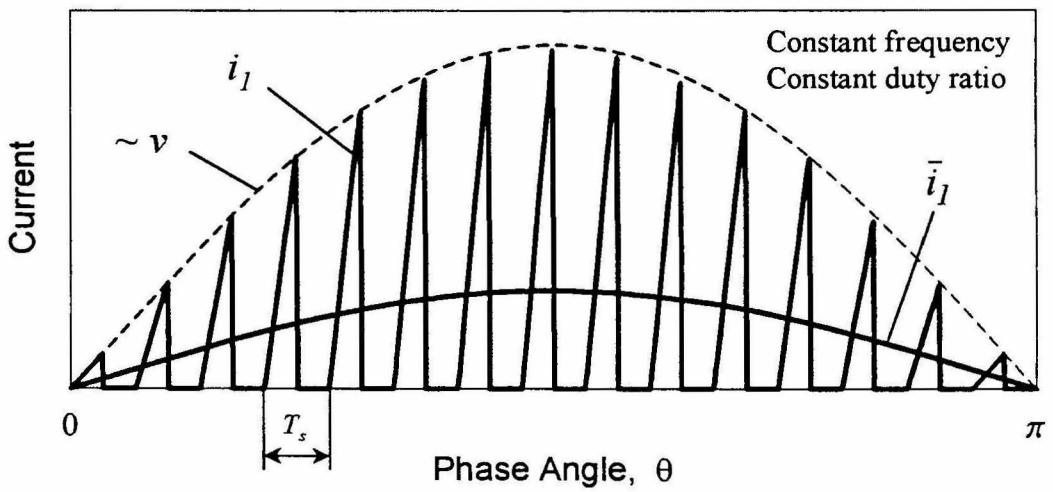

(b)

Figure 3.5: (a) Automatic current shaper using a Buck-Boost converter operating in DCM. Only a single low bandwidth control loop is present. (b) Salient current waveforms.

compared to the one in Fig. 3.3. This is the case, for example, for the Boost converter in DCM, operated with constant duty ratio over one line cycle.

The question might arise, why search for different topologies if a simple Buck-Boost converter solves the problem? A few reasons are discussed in the next section.

3.1.5 Motivation for the Search for New Topologies Suitable as Power Factor Correctors

The problem with the Buck-Boost topology is that its efficiency is lower than in many other circuits. For this reason it is limited to application in the low power range (about 300W and lower). The main reason for that is that all the processed energy is temporarily stored in the inductor L. The inductive energy storage is far less efficient than the capacitive energy storage.

Furthermore, the input power is pulsating with twice the line frequency and the output power is constant. That requires at least one energy storage element in the circuit to provide the required energy while the power delivered to the input of the converter is smaller than the output power. The only reasonable way to store energy on a line frequency scale is a capacitor. The energy density of a capacitor is much higher than the one for an inductor. The energy storage function produces a ripple voltage across the capacitor at twice the line frequency. This topic has been explored in Chapter 4 of [1]. The capacitor in the Buck-Boost topology is at the output of the converter. Therefore, this ripple is directly visible at the output. In many cases this can not be tolerated.

The feedback loop is required to have a low bandwidth in order to achieve a good power factor. On the other hand this limits the dynamic response of the converter. A fast load step response is not possible with this type of converter. This, and the presence of the output ripple, require the addition of a post regulator in most cases. Thus, the ac-to-dc conversion is in many cases realized as a two-stage solution.

In order to reduce cost, size and complexity, single stage ac-to-dc converters are preferred. Such a switching converter, which provides a very good power factor and allows a fast output regulation, is proposed and investigated in Chapter 6.

3.2 Three-Phase Systems

3.2.1 Field of Application

At higher power levels it is very often beneficial to use three-phase powered systems. Some properties of three-phase systems, which will be used in this thesis, are derived in Appendix A. One advantage of these systems is that the instantaneous power is constant if the voltage and current have no harmonic distortion. For the case of unity power factor this result is derived in Appendix A.1. This property makes three-phase sources well suited for ac-to-dc applications since an energy storage capacitor is not required, while, as pointed out earlier, capacitive storage is essential in single-phase systems due to the pulsation nature of the instantaneous power.

Three-phase sources are not commonly used in low power applications. The range of application is limited to power levels of 2kW and higher. The extra effort to bring the three-phase line to smaller loads is not usually justified. When discussing three-phase systems it should be kept in mind that higher power applications are assumed.

3.2.2 Three-Phase-to-DC Rectification

Some aspects in a Three-phase system are different than in the single-phase case. For now it is sufficient to consider the voltage sources v_1, v_2 and v_3 in Fig. 3.6a as three separate sources. They are equal in magnitude and have 120° mutual phase displacement. This can be written as

$$v_1(\theta) = V_p \sin(\theta) \tag{3.2.1}$$

$$v_2(\theta) = V_p \sin\left(\theta - \frac{2\pi}{3}\right) \tag{3.2.2}$$

$$v_3(\theta) = V_p \sin\left(\theta - \frac{4\pi}{3}\right) \tag{3.2.3}$$

where V_p is the peak value of these voltages. The resulting instantaneous voltage diagram over one line cycle is shown in Fig. 3.6b.

The input voltage v_{in} of the dc-to-dc converter is always the difference between the input voltage source with the highest and lowest instantaneous value.

$$v_{in}(\theta) = v_{max}(\theta) - v_{min}(\theta) \tag{3.2.4}$$

This is indicated in Fig. 3.6b. Unlike in the single-phase case, this voltage never goes to zero or even to low values. It can easily be verified the v_{in} satisfies

$$\frac{3}{2}V_p \le v_{in}(\theta) \le \sqrt{3}V_p\,; \quad \forall\ \theta \tag{3.2.5}$$

Therefore, an energy storage capacitor is not necessarily required as in the single-phase case. In fact, in most cases such a capacitor increases the harmonic distortion of the input current significantly since the input acts again as a "peak detector."

Since the output is dc, it can be assumed that the converter processes a constant power P for which the current i_{in} is given by

$$i_{in}(\theta) = \frac{P}{v_{in}(\theta)} \tag{3.2.6}$$

The input current belonging to the voltage source with the highest instantaneous voltage value is carrying i_{in}. The voltage source with the lowest value delivers minus i_{in}. The voltage source with the intermediate value is disconnected from the dc-to-dc converter. The resulting v_{in} and i_1 are shown in Fig. 3.6c. Using the definitions of Chapter 2.4 the *THD* of this current waveform can be found to be

$$THD = \sqrt{\frac{2\sqrt{3}}{\pi} - 1} = 0.32 \tag{3.2.7}$$

This current combined with the voltage v_1 results in the following power factor:

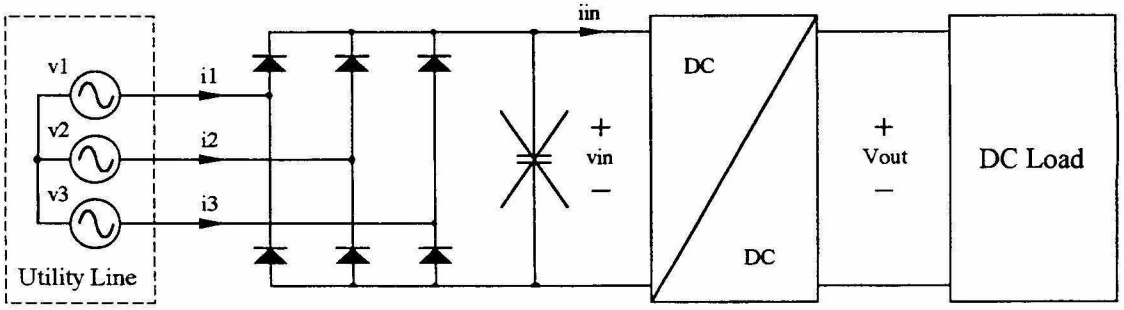

(a)

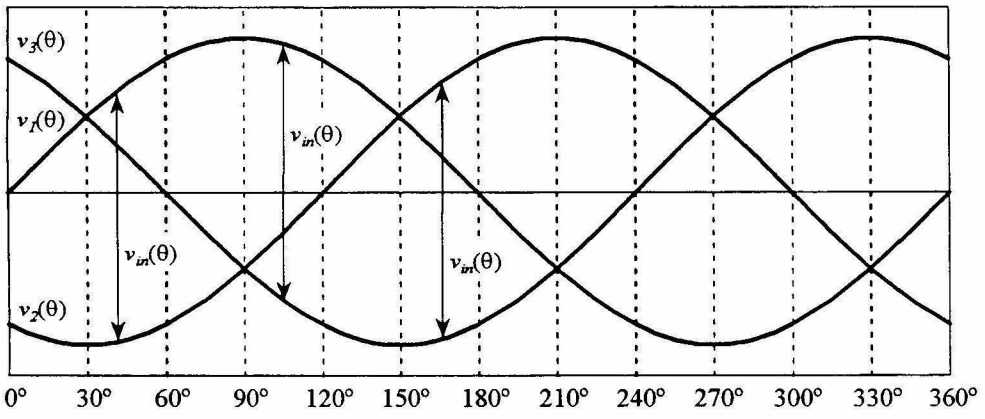

(b)

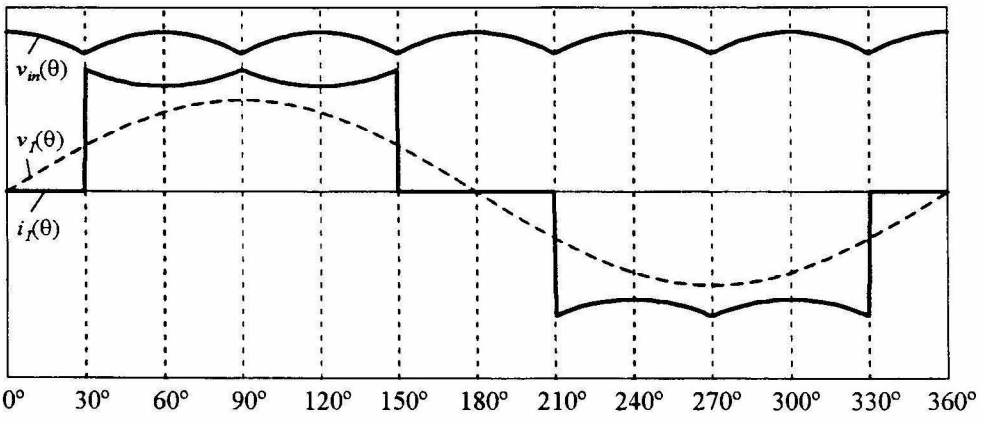

(c)

Figure 3.6: Constant power load connected to three-phase utility line. (a) Typical circuit, (b) ideal voltage waveforms in a three-phase system and (c) input current of phase one and rectified input voltage of the converter.

$$PF = \sqrt{\frac{\pi}{2\sqrt{3}}} = 0.952 \tag{3.2.8}$$

It is evident that the power factor in the three-phase ac-to-dc converter is relatively high (> 95%) even if the system has no power factor correction. This is due to the fact that this circuit does not cause a phase displacement between the voltage and the current. Thus, there may not be a need for the extra effort to improve the power factor, which is already very good. However, the harmonic distortion is still quite large (i.e., 32%). This is the more severe problem in this case and it must be corrected since the international standards limit the allowable distribution of the harmonics over the frequency spectrum. Although they do not necessarily require a minimum *THD*, they do impose a severe restriction on the magnitudes of the lowest order harmonics. (The allowed limits decrease as the frequency increases, but at a slower rate as the values of the harmonics of waveforms encountered in many practical circuits.)

According to (2.6.6) the power factor is determined by two components, namely the displacement factor and the distortion factor. It should be pointed out that the second one is more severe in its consequences. The displacement merely introduces circulating currents at the same frequency as the voltage into the system. It requires an extra effort to handle these currents. However, they do not have a negative impact on other equipment connected to the utility line. In contrast, a harmonic distortion of the line current causes a distortion of the voltage. This can affect the operation of sensitive equipment, which share the same utility line. It is therefore important to limit the harmonic distortion even if the power factor is relatively high, as in the three-phase example treated in this section.

The terms power factor correction and current shaping are used interchangeably in the power electronics community. Nevertheless, the first one is used more often, whereas the main objective is more often than not, especially in three-phase systems, the reduction of the current distortion.

3.3 International Limits

The most relevant international limit concerning the current distortion is IEC 1000-3-2 [27]. This standard is predominantly enforced in Europe. It applies to equipment with input currents smaller of equal to 16A. A good overview of the relevant aspects for this standard is provided in [28].

One distinguishes between four different classes of equipment. The limits for the majority of loads fall into class A. A balanced three-phase equipment is similarly defined as the symmetrical three-phase system in Appendix A. However, certain tolerance is

Harmonic order n	**Class A:** Balanced three-phase and equipment not covered in class B, C or D [Amps]	**Class B:** Portable tools [Amps]	**Class C:** Lighting equipment [%] of fundamental	**Class D:** Special wave shape and P≤600W [mA/W]
Odd harmonics				
3	2.30	3.45	30 *PF*	3.4
5	1.14	1.71	10	1.9
7	0.77	1.16	7	1.0
9	0.40	0.60	5	0.5
11	0.33	0.50	3	0.35
13	0.21	0.32	3	0.30
15≤n≤39	2.25/n	3.38/n	3	3.85/n
Even harmonics				
2	1.08	1.62	2	-
4	0.43	0.65	-	-
6	0.30	0.45	-	-
8≤n≤40	1.84/n	2.76/n	-	-

Table 3.1: Limits for current harmonics according to IEC 1000-3-2.

allowed between the voltages. In the terminology of IEC 1000-3-2, the special wave shape refers to current waveforms similar to the one shown in Fig 3.3a. It should not be confused with the symmetrical waveform defined in this thesis.

The limits of the harmonics in classes A and B are specified with absolute values, whereas in classes C and D, relative limits are used. No limits have been determined for most of the even harmonics in classes C and D. The Equipment in these two classes has naturally low even harmonics. Thus, there was no need for specifications.

Figure 3.7 shows the limits of class A in a logarithmic plot. In many cases, the magnitudes of the harmonics decay faster than the limits as the frequency increases. In particular, this holds for the circuits discussed in this thesis. In single-phase cases, the third harmonic is the most difficult to meet. In three-phase cases with no neutral, it is the fifth harmonic as in this case no third harmonic is present (Appendix A.).

The theoretically highest allowed *THD* in class A is 19%. This value is evaluated assuming the rms-value of the current is 16A and all harmonics are present with their magnitudes at the allowed limit. This appears to be a high level of distortion. However,

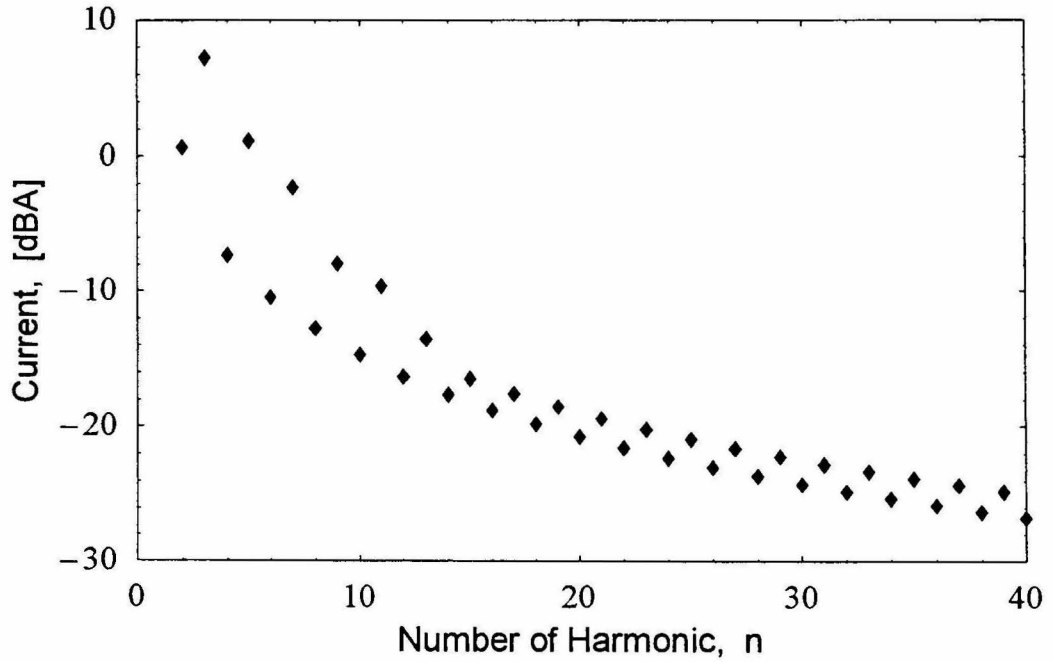

Figure 3.7: Limits for the current harmonics according to IEC 1000-3.2, class A.

in realistic cases, the even harmonics are typically very small, as are harmonics of order $3n$ in three-phase systems. If these harmonics are eliminated from the spectrum, the largest possible *THD* is reduced to 9.1%. Note that this value can not be reached in a practical case, as each individual harmonic must be below its specified limit. Thus, the realistically allowed maximum possible *THD* is significantly smaller than this value.

Because the limits for class A equipment are absolute, any signal can be reduced in magnitude to satisfy the standards. The rms-value of the quasi-rectangular signal in Fig. 3.6c must not exceed 2A. The 25^{th} harmonic reaches its limit at 2.06A. This would be an extremely low value for a three-phase system. (These limits apply to equipment with input currents as large as 16A.)

Chapter 4

A Single Active Switch Three-Phase Power Factor Corrector

In this chapter a power factor correction circuit for the three-phase utility line is investigated. The current shaping occurs naturally in this circuit; therefore, no extra control circuit is necessary in order to achieve a good current waveform. Thus, it is an automatic power factor corrector according to Chapter 3.1.4. This fact and the simplicity of the circuit make this a favorable topology for the lower power three-phase power range, i.e., approximately 2kW to 5kW. Because the circuit works in discontinuous inductor current mode (DICM), the topology might not be very well suited for applications in the high power range.

With the converter discussed in this chapter, a unity power factor can not be achieved. There is always a limited amount of distortion remaining in the input currents. Several operation schemes are investigated which lead to different results concerning the harmonic distortion. It is the goal of this chapter to establish which of these operational schemes is the most favorable solution.

4.1 The Topology

The circuit investigated here is shown in Fig. 4.1. It is a boost-derived topology suitable for connection to a three-phase source, e.g., the utility line. All three input inductors operate in DICM. This must be accomplished by proper design of the circuit. The analysis of the converter is based on the following assumptions.

1) The three line voltage source v_1, v_2 and v_3 are ideal sine waves, equal in magnitude and with 120° mutual phase. Thus, the converter is connected to an ideal three-phase source as defined in Appendix A.1.

2) The capacitance C_o is sufficiently large to allow the six times the line frequency ripple of V_o to be neglected.

3) The inductance values of the three inductors L_1, L_2 and L_3 are equal.

4) The three inductors L_1, L_2 and L_3 operate in DICM.

5) For the waveform analysis during one switching cycle, the input voltages are considered to be constant, i.e., the line frequency is assumed to be much lower than the switching frequency.

6) The input filter eliminates the switching ripple of the input current, but it does not affect line frequency related variations.

7) The converter is loss-less.

In accordance with the above assumptions, the following definitions are made:

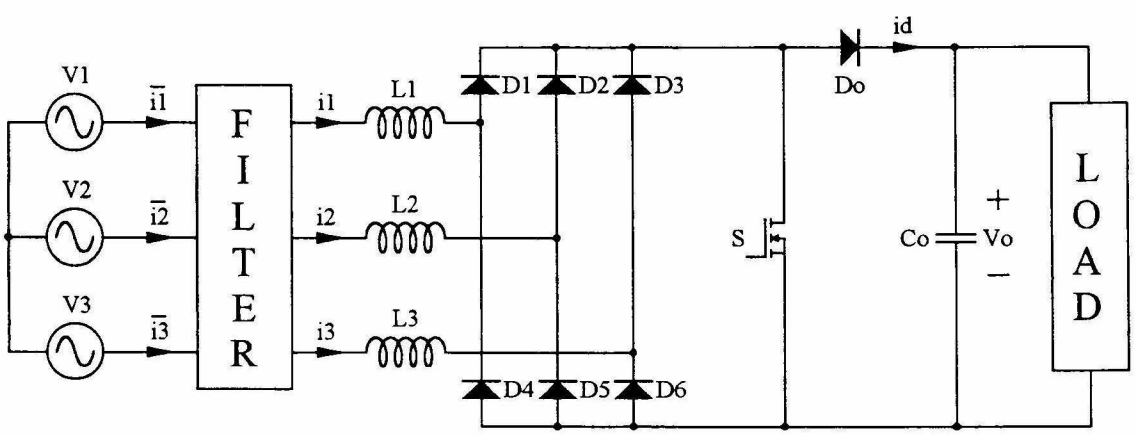

Figure 4.1: The boost derived single active switch three-phase power factor corrector connected to a three-phase source.

$$v_1(\theta) = V_L\sqrt{2}\sin(\theta) \tag{4.1.1}$$

$$v_2(\theta) = V_L\sqrt{2}\sin\left(\theta - \frac{2\pi}{3}\right) \tag{4.1.2}$$

$$v_3(\theta) = V_L\sqrt{2}\sin\left(\theta - \frac{4\pi}{3}\right) \tag{4.1.3}$$

and

$$M = \frac{V_o}{\sqrt{6}\cdot V_L} \tag{4.1.4}$$

$$R_e = \frac{2L}{T_s} \tag{4.1.5}$$

where V_L is the rms-value of the line to neutral voltage. It should be pointed out that the conversion ratio M is defined by the ratio of the output voltage to the peak line to line voltage.

Firstly, the line voltage dependence of relevant currents will be found, namely the three input currents i_1, i_2 and i_3 and the current i_d in the output diode D_o. The three input voltage sources satisfy the symmetrical waveform condition as defined in Appendix A.2 and they also satisfy (A.3.1). Moreover, due to the symmetry of the circuit the input of the converter appears identical at each phase. Therefore, the three currents $\bar{i}_1$, $\bar{i}_2$ and $\bar{i}_3$ must satisfy the condition (A.3.2). It turns out that in addition the current waveform satisfies the special waveform condition according to Appendix A.4. Thus, only the first 30° of one line period must be analyzed and the rest of the current waveform can be derived using these symmetry properties. The fact that the special waveform condition is fulfilled will be apparent after the results for the first 30° are obtained. Therefore, in the following analysis it is assumed that the phase angle θ is somewhere between 0 and 30°. Concerning the phase voltages this means

$$0 \le v_1(\theta) \le v_3(\theta) \le -v_2(\theta) \tag{4.1.6}$$

Each switching cycle can be divided into four subintervals. The four equivalent circuits for each subinterval are shown in Fig. 4.2. Since the output voltage is considered to be constant, the load together with C_o is replaced by a voltage source. The four equivalent circuits in Fig. 4.2 are valid for every θ with the range from 0 to 30° because (4.1.6) holds for any possible θ in this range.

The first subinterval is defined by the ON-time T_1 of the switch S. Due to the symmetry of the circuit, during this interval each inductor is exposed to the corresponding phase voltage. The three input currents are given by

$$i_{11}(t) = \frac{v_1}{L}t \tag{4.1.7}$$

$$i_{21}(t) = \frac{v_2}{L}t \tag{4.1.8}$$

$$i_{31}(t) = \frac{v_3}{L}t \tag{4.1.9}$$

The diode D_o is reversed biased during the first interval, thus

$$i_{d1}(t) = 0 \tag{4.1.10}$$

The second interval starts when the switch S turns off. The two positive input currents (i.e., i_1 and i_3) start to flow through the diode D_o to the output whereas phase 2 provides the return path. The initial values of the second subinterval are the same as the final values of the first subinterval. For simplicity it is assumed that the time variable is reset to zero at the beginning of each subinterval. Thus, the currents during the second subinterval are given by

$$i_{12}(t) = \frac{v_1}{L}T_1 + \frac{3v_1 - V_o}{3L}t \tag{4.1.11}$$

$$i_{22}(t) = \frac{v_2}{L}T_1 + \frac{3v_2 + 2V_o}{3L}t \tag{4.1.12}$$

$$i_{32}(t) = \frac{v_3}{L}T_1 + \frac{3v_3 - V_o}{3L}t \tag{4.1.13}$$

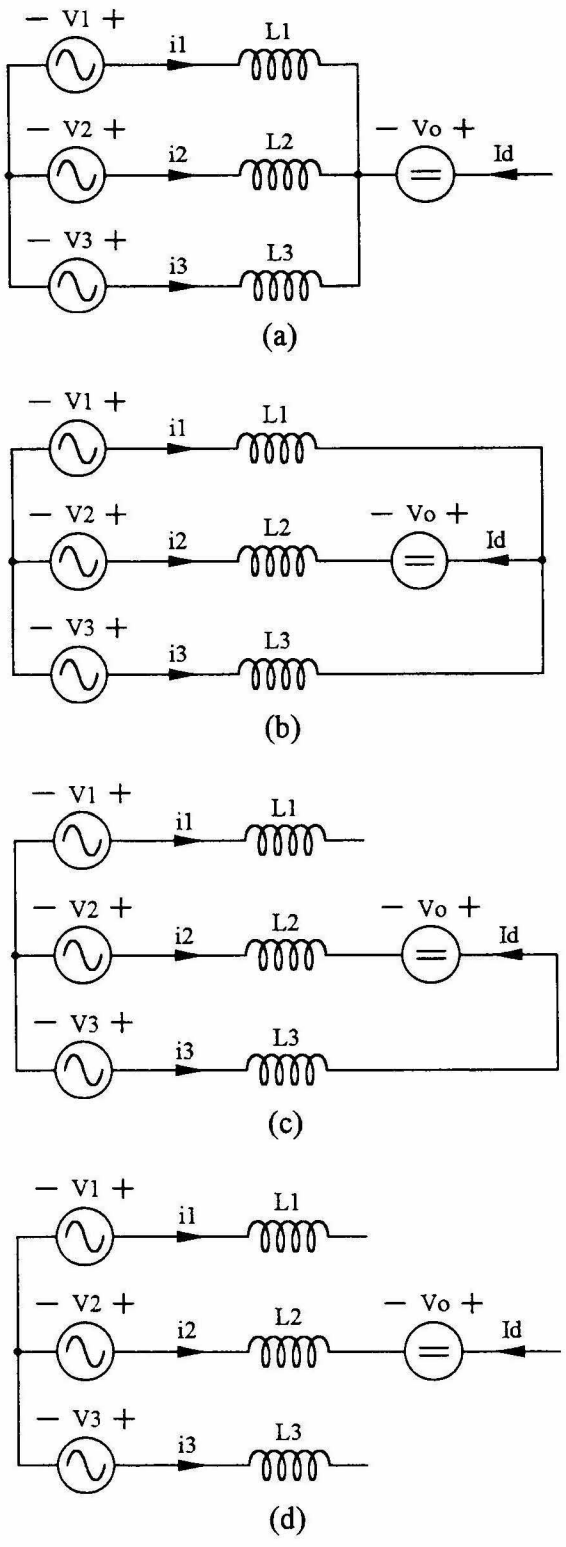

Figure 4.2: The four equivalent circuits during one switching cycle.

$$i_{d2}(t) = -i_{22}(t) \tag{4.1.14}$$

The output voltage must be sufficient to decrease the magnitude of all currents. Since v_1 has the smallest absolute value of all three-phase voltages, $i_1(t)$ becomes zero first. This instant concludes the second interval. To find the length T_2 of this subinterval, the following equation must be solved:

$$i_{12}(T_2) = 0 \tag{4.1.15}$$

This yields

$$T_2 = T_1 \frac{3v_1}{V_o - 3v_1} \tag{4.1.16}$$

During the third subinterval i_1 stays zero because the diode D_1 prevents it from becoming negative. According to Fig. 4.2c the currents can be found to be

$$i_{13}(t) = 0 \tag{4.1.17}$$

$$i_{23}(t) = \frac{T_1}{L} V_o \frac{v_1 - v_3}{V_o - 3v_1} + \frac{V_o + v_2 - v_3}{2L} t \tag{4.1.18}$$

$$i_{33}(t) = \frac{T_1}{L} V_o \frac{v_3 - v_1}{V_o - 3v_1} - \frac{V_o + v_2 - v_3}{2L} t \tag{4.1.19}$$

$$i_{d3}(t) = i_{33}(t) \tag{4.1.20}$$

The end of this subinterval is reached when the remaining currents become zero. Thus, the length T_3 of this interval can be found by solving

$$i_{23}(T_3) = 0 \tag{4.1.21}$$

This leads to

$$T_3 = T_1 \frac{2V_o(v_3 - v_1)}{(V_o - 3v_1)(V_o + v_2 - v_3)} \tag{4.1.22}$$

Through the remainder of the switching cycle, all currents stay at zero. Therefore,

$$i_{14}(t) = i_{24}(t) = i_{34}(t) = i_{d4}(t) = 0 \tag{4.1.23}$$

The length of the fourth subinterval T_4 is given by

$$T_4 = T_s - T_1 - T_2 - T_3 \tag{4.1.24}$$

This can be simplified using (4.1.16) and (4.1.22)

$$T_4 = T_s - T_1 \frac{V_o}{V_o + v_2 - v_3} \tag{4.1.25}$$

Typical waveforms of the currents i_1, i_2 and i_3 are shown in Fig. 4.3. It is again assumed that the line voltage phase angle is somewhere between zero and 30°.

Both T_2 and T_3 must be positive. Using (4.1.6), (4.1.16) and (4.1.22), it can be concluded that

$$V_o - 3v_1(\theta) > 0 \tag{4.1.26}$$

$$V_o + v_2(\theta) - v_3(\theta) > 0 \tag{4.1.27}$$

This provides a lower limit for V_o for a given set of phase voltages. It turns out that if (4.1.27) is satisfied, (4.1.26) is also satisfied for any θ in the 0 to 30°. The worst case occurs at $\theta = 0$ which leads to

$$V_o > \sqrt{6} V_L \tag{4.1.28}$$

or equivalently using (4.1.4)

$$M > 1 \tag{4.1.29}$$

In addition, the fourth subinterval must be equal to or greater than zero, i.e., $T_4 \geq 0$. This provides an upper limit to the length of the first interval T_1 and thus, to the maximum possible duty ratio. Using (4.1.25) the following restriction on T_1 can be found:

$$T_1 \leq T_s \frac{V_o + v_2(\theta) - v_3(\theta)}{V_o} \tag{4.1.30}$$

The duty ratio has to satisfy

$$D_1 \leq \frac{V_o + v_2(\theta) - v_3(\theta)}{V_o} \tag{4.1.31}$$

This equation must be satisfied for every possible θ. The worst case appears again at $\theta = 0°$. Under the assumption that the duty ratio is constant, i.e., D_1 is not a function of θ, the equation (4.1.31) reduces to

$$D_1 \leq \left(1 - \frac{1}{M}\right) \tag{4.1.32}$$

or equivalently

$$M \geq \frac{1}{1 - D_1} \tag{4.1.33}$$

This equation requires again that M is greater than unity because D_1 is a positive number. Moreover, M can not be close to 1 because this would require a duty ratio of approximately zero.

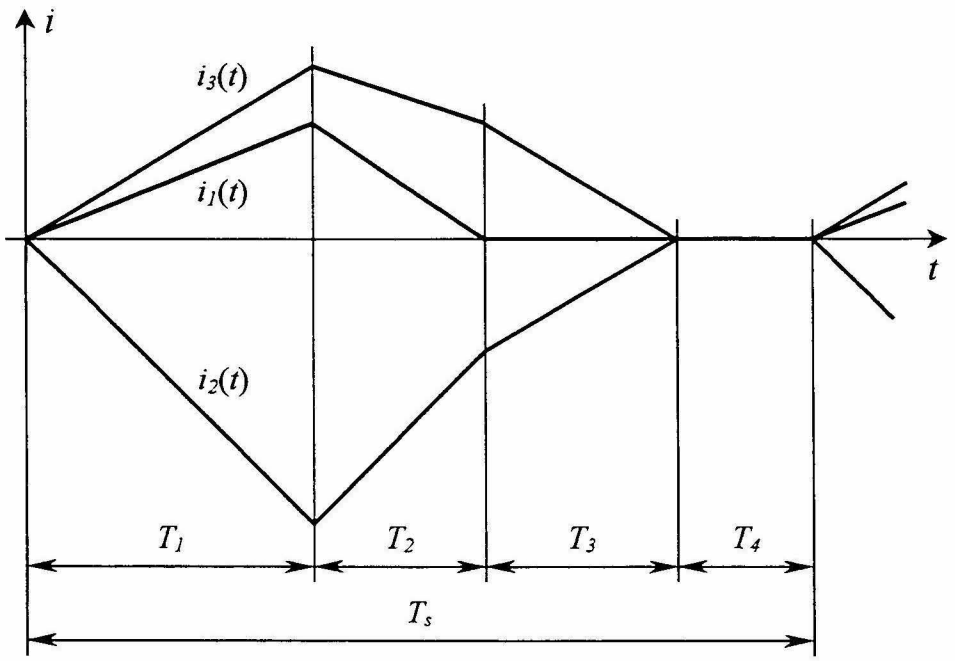

Figure 4.3: Typical current waveforms under the assumption that the input voltage phase angle is between 0 and 30°.

In order to reduce the voltage stress on the switches a small conversion ratio M is preferred. On the other hand, a large duty ratio is preferred because this reduces the current stress in most components of the converter. Equation (4.1.33) shows that there is a trade off between a low conversion ratio and a large duty ratio.

The next step is to find the currents averaged over one switching cycle. These quantities will still be a function of the phase angle θ; with the switching ripple removed. In the real circuit the input filter accomplishes this effect. The three inductor currents are given by

$$\bar{i}_1 = \frac{i_{12}(0)}{2} \cdot \frac{T_1 + T_2}{T_s} \tag{4.1.34}$$

$$\bar{i}_2 = \frac{i_{22}(0)}{2} \cdot \frac{T_1 + T_2}{T_s} + \frac{i_{23}(0)}{2} \cdot \frac{T_2 + T_3}{T_s} \tag{4.1.35}$$

$$\bar{i}_3 = -\bar{i}_1 - \bar{i}_2 \tag{4.1.36}$$

The diode current i_d averaged over one switching cycle can be written as

$$\bar{i}_d = \frac{i_{d2}(0)}{2} \cdot \frac{T_2}{T_s} + \frac{i_{d3}(0)}{2} \cdot \frac{T_2 + T_3}{T_s} \tag{4.1.37}$$

Substitution of the previously derived expressions and simplifications using (A.1.5) and (A.1.6) lead to

$$\bar{i}_1 = \frac{D_1^2 T_s}{2L} \cdot \frac{V_o v_1}{V_o - 3v_1} \tag{4.1.38}$$

$$\bar{i}_2 = \frac{D_1^2 T_s}{2L} \cdot \frac{V_o^2 v_2 + V_o\left(v_2^2 - v_3^2\right)}{(V_o - 3v_1)(V_o + v_2 - v_3)} \tag{4.1.39}$$

$$\bar{i}_3 = \frac{D_1^2 T_s}{2L} \cdot \frac{V_o^2 v_3 + V_o\left(v_3^2 - v_2^2\right)}{(V_o - 3v_1)(V_o + v_2 - v_3)} \tag{4.1.40}$$

$$\bar{i}_d = \frac{D_1^2 T_s}{2L} \cdot \frac{3V_o V_L^2 + 3v_2\left(v_2^2 - v_3^2\right)}{(V_o - 3V_1)(V_o + v_2 - v_3)} \tag{4.1.41}$$

The phase angle dependence of these equations is directly related to the three input voltages v_1, v_2 and v_3. No other phase angle dependent quantities and no derivatives are involved. It can therefore be concluded that the current $\bar{i}_1$ at 180°-θ is the same as at θ since a look at the voltage diagram in Fig. A.2 confirms that the input voltages are the same at both instants except that the positions of v_2 and v_3 are interchanged. This does not affect the current $\bar{i}_1$ due to the symmetry of the input of the circuit. The same can be said for any other interval between 0 and 180°.

By a similar reasoning, the negative half wave must be equivalent to the positive one except for the inverted sign since all the voltages are inverted. This establishes the fact that the current exhibits the symmetrical waveform as defined in Appendix A.2.

Equations (4.1.38) through (4.1.41) can be further simplified using the definitions (4.1.1) through (4.1.5).

$$\bar{i}_1(\theta) = D_1^2 \frac{\sqrt{2}V_L}{R_e} \cdot \alpha_1(\theta) \tag{4.1.42}$$

$$\bar{i}_2(\theta) = D_1^2 \frac{\sqrt{2}V_L}{R_e} \cdot \alpha_2(\theta) \tag{4.1.43}$$

$$\bar{i}_3(\theta) = D_1^2 \frac{\sqrt{2}V_L}{R_e} \cdot \alpha_3(\theta) \tag{4.1.44}$$

$$\bar{i}_d(\theta) = D_1^2 \frac{\sqrt{2}V_L}{R_e} \cdot \alpha_d(\theta) \tag{4.1.45}$$

where

$$\alpha_1(\theta) = \frac{M \sin(\theta)}{M - \sqrt{3}\sin(\theta)} \tag{4.1.46}$$

$$\alpha_2(\theta) = \frac{M^2 \sin\left(\theta - \frac{2\pi}{3}\right) + M \sin(2\theta)}{\left(M - \sqrt{3}\sin(\theta)\right)\left(M - \cos(\theta)\right)} \tag{4.1.47}$$

$$\alpha_3(\theta) = \frac{M^2 \sin\left(\theta - \frac{4\pi}{3}\right) - \frac{1}{2} M \sin(2\theta)}{\left(M - \sqrt{3}\sin(\theta)\right)\left(M - \cos(\theta)\right)} \tag{4.1.48}$$

$$\alpha_d(\theta) = \frac{\sqrt{3}}{2} \cdot \frac{M + \sin(2\theta)\sin\left(\theta - \frac{2\pi}{3}\right)}{\left(M - \sqrt{3}\sin(\theta)\right)\left(M - \cos(\theta)\right)} \tag{4.1.49}$$

This set of equations (i.e., (4.1.42) through (4.1.49)) describes the current waveforms as a function of the phase angle θ for a given input voltage V_L and a conversion ratio M. Even though the expressions are valid only for the range $0 \le \theta \le 30°$, the remainder can be found according to the discussion in Appendix A.4 since the necessary conditions have been established. It is important to note that the duty ratio D_1 can be a function of θ, thus, the above expressions are not restricted to the case of a constant D_1. The current $\bar{i}_1$ over one quarter line cycle is, therefore, given by

$$\bar{i}_{1_{90°}}(\theta) = \begin{cases} \bar{i}_1(\theta) & \text{for } 0 \le \theta \le \frac{\pi}{6} \\ \bar{i}_3\left(\frac{\pi}{3} - \theta\right) & \text{for } \frac{\pi}{6} \le \theta \le \frac{\pi}{3} \\ -\bar{i}_2\left(\theta - \frac{\pi}{3}\right) & \text{for } \frac{\pi}{3} \le \theta \le \frac{\pi}{2} \end{cases} \tag{4.1.50}$$

Over one full line period the input current of phase 1 becomes

$$\bar{i}_{1_{360°}}(\theta) = \begin{cases} \bar{i}_{1_{90°}}(\theta) & \text{for } 0 \le \theta \le \frac{\pi}{2} \\ \bar{i}_{1_{90°}}(\pi - \theta) & \text{for } \frac{\pi}{2} \le \theta \le \pi \\ -\bar{i}_{1_{90°}}(\theta - \pi) & \text{for } \pi \le \theta \le \frac{3\pi}{2} \\ -\bar{i}_{1_{90°}}(2\pi - \theta) & \text{for } \frac{3\pi}{2} \le \theta \le 2\pi \end{cases} \tag{4.1.51}$$

As shown in Appendix A.5 the output power of this converter contains only harmonics of order six and multiples thereof (besides a constant part). Since the output voltage is

assumed to be constant, the same must apply to the diode current $\bar{i}_d$. Consequently, the ripple frequency of the diode current is equal to six times the line frequency, or equivalently, the period length of that ripple is 60° of one line period. Therefore, one full period of $\bar{i}_d$ is given by

$$\bar{i}_{d_{60^\circ}}(\theta)=\begin{cases}\bar{i}_d(\theta) & \text{for } 0\le\theta\le\dfrac{\pi}{6}\\ \bar{i}_d\left(\dfrac{\pi}{3}-\theta\right) & \text{for } \dfrac{\pi}{6}\le\theta\le\dfrac{\pi}{3}\end{cases} \tag{4.1.52}$$

In this converter the only energy storage element on the line frequency scale is the output capacitor. Since the inductors operate in DICM, they can not contribute to any energy storage lasting longer than one switching cycle. This means that the instantaneous power (or more precisely the power averaged over one switching cycle) at the input $\bar{p}_i$ must be the same as $\bar{p}_o$ (the power provided to the output capacitor and load). The input power is given by the sum of the voltage and current products at each individual phase, whereas the output power is the product of the diode current and the output voltage. They are given by

$$\bar{p}_i=\bar{i}_1 v_1+\bar{i}_2 v_2+\bar{i}_2 v_2 \tag{4.1.53}$$

$$\bar{p}_o=\bar{i}_d V_o \tag{4.1.54}$$

Using (4.1.1) through (4.1.4) and (4.1.42) through (4.1.45), the above two equations can be written as

$$\bar{p}_i=D_1^2\frac{2V_L^2}{R_e}\left(\alpha_1(\theta)\sin(\theta)+\alpha_2(\theta)\sin\left(\theta-\frac{2\pi}{3}\right)+\alpha_3(\theta)\sin\left(\theta-\frac{4\pi}{3}\right)\right) \tag{4.1.55}$$

$$\bar{p}_o=D_1^2\frac{2\sqrt{3}MV_L^2}{R_e}\alpha_d(\theta) \tag{4.1.56}$$

Equating these two expressions leads to

$$\alpha_1(\theta)\sin(\theta)+\alpha_2(\theta)\sin\left(\theta-\frac{2\pi}{3}\right)+\alpha_3(\theta)\sin\left(\theta-\frac{4\pi}{3}\right)=\sqrt{3}M\alpha_d(\theta) \qquad (4.1.57)$$

This equality is used to simplify some expressions in the following sections of this chapter. This result was derived using the power conservation theorem. Of course, the same conclusion can be obtained using trigonometric identities.

In the case of a constant duty ratio, the currents satisfy the symmetrical waveform condition as defined in Appendix A.2 and exhibit three-phase symmetry as defined in Appendix A.3. These properties are preserved if the duty ratio is a function of θ and satisfies the following conditions

$$D_1(\theta)=D_1\left(\theta+\frac{\pi}{3}\right) \qquad (4.1.58)$$

$$D_1(\theta)=D_1\left(\frac{\pi}{3}-\theta\right) \qquad (4.1.59)$$

The duty ratio D_1 must be periodic with a frequency that is six times higher than the line frequency. Each period is symmetrical with respect to the vertical line at its center. Once D_1 is known over the range from 0 to 30°, then it is determined for any θ, whereas any arbitrary function in the interval from 0 to 30° can be expanded to satisfy the above conditions. Therefore, the simplified expressions due to the special waveform and symmetrical three-phase condition still apply even for an arbitrary D_1.

The formulas derived below will be useful in the following sections. The output power and thus, by assumption 7 in Section 4.1, the processed power P averaged over one line cycle can be found by averaging (4.1.56) over the first 30° of the line period.

$$P=\frac{2\sqrt{3}MV_L^{\,2}}{R_e}\cdot\frac{6}{\pi}\int_0^{\pi/6}D_1^{\,2}(\theta)\alpha_d(\theta)\,d\theta \qquad (4.1.60)$$

The rms-value of the current can be found using (A.4.10)

$$I_{rms} = \sqrt{\frac{2}{\pi}\int_0^{\pi/6} \bar{i}_1^{\,2}(\theta) + \bar{i}_2^{\,2}(\theta) + \bar{i}_3^{\,2}(\theta)\, d\theta} \tag{4.1.61}$$

Using (4.1.42) through (4.1.49) this can be written as

$$I_{rms} = 2\frac{V_L}{R_e}\sqrt{\frac{1}{\pi}\int_0^{\pi/6} D_1^{\,4}(\theta)\alpha_s(\theta)\, d\theta} \tag{4.1.62}$$

where

$$\alpha_s(\theta) = \alpha_1^{\,2}(\theta) + \alpha_2^{\,2}(\theta) + \alpha_3^{\,2}(\theta) \tag{4.1.63}$$

Since the input currents exhibit the symmetrical waveform and are part of a symmetrical three-phase system according to Appendix A.4, the fundamental component of the input currents can be found using (A.4.15). A much simpler way is to realize that only the fundamental component is contributing to the energy processing since the input voltages are ideal sine waves. According to (A.4.11) there are only sine terms, thus, the fundamental harmonic is in phase with the voltage. Therefore, the rms-value of the fundamental component I_1 of any of the input currents can be found simply using

$$I_1 = \frac{P}{3V_L} \tag{4.1.64}$$

Using (A.4.14) each individual odd harmonic is given by

$$I_k = \frac{2\sqrt{2}}{\pi}\int_0^{\pi/6} \bar{i}_1 \sin(k\theta) + \bar{i}_2 \sin\left(k\theta - \frac{2\pi k}{3}\right) + \bar{i}_3 \sin\left(k\theta - \frac{4\pi k}{3}\right) d\theta \tag{4.1.65}$$

where $|I_k|$ is the rms value of the k^{th} harmonic. All even harmonics are zero. For the purpose of comparison, a more useful quantity is the value of each individual harmonic relative to the fundamental. Thus,

$$I_{k_{rel}} = \frac{I_k}{I_1} \tag{4.1.66}$$

Using the previously derived formulas in this chapter $I_{k_{rel}}$ can be written as

$$I_{k_{rel}} = \begin{cases} \dfrac{12V_L^{\,2}}{\pi R_e P}\displaystyle\int_0^{\pi/6} D_1^{\,2}(\theta)\beta_k(\theta)d\theta & \text{for } k = 1,3,5,\ldots \\ 0 & \text{for } k = 2,4,6,\ldots \end{cases} \tag{4.1.67}$$

where β_k is defined as

$$\beta_k(\theta) \equiv \alpha_1(\theta)\sin(k\theta) + \alpha_2(\theta)\sin\left(k\theta - \frac{2\pi k}{3}\right) + \alpha_3(\theta)\sin\left(k\theta - \frac{4\pi k}{3}\right) \tag{4.1.68}$$

By substituting (4.1.46) through (4.1.48) into (4.1.68), it can be shown that the harmonics of order 3 and its multiples are indeed zero as it was generally derived for symmetrical three-phase three-wire systems in Appendix A.3. The final result after this substitution has been performed is reported in Appendix B.2.

It is important to understand the duty ratio variation for a particular control scheme. In this thesis the modulation depth ΔD_1 is defined as the maximum value minus the minimum value of $D_1(\theta)$, i.e.,

$$\Delta D_1 = D_{1_{max}} - D_{1_{min}} \tag{4.1.69}$$

Another quantity of interest is the ripple of the current $\bar{i}_d(\theta)$ in the diode D_o. This ripple is ideally zero in order to have a constant output voltage. In this thesis the relative ripple is defined by the absolute value of the peak to peak ripple divided by the average value. The average value of $\bar{i}_d(\theta)$ over one period is given by

$$\bar{I}_d = \frac{P}{V_o} = \frac{P}{\sqrt{6}MV_L} \tag{4.1.70}$$

Thus, the relative ripple current Δi_d is given by

$$\Delta I_d = \frac{\sqrt{6}MV_L}{P}\left(\bar{i}_{d_{max}} - \bar{i}_{d_{min}}\right) \tag{4.1.71}$$

This concludes the derivation of a basic set of equations that will be used for the analysis of the different cases in the following sections.

4.2 Constant Duty Ratio Operation

When this topology was first introduced it was assumed to work with a constant duty ratio in the steady state condition [3] (i.e., D_1 does not depend on the phase angle θ). Several authors have extended the topology in order to introduce galvanic separation or soft- or resonant switching [4-7]. However, in all these cases, the constant duty ratio operation was kept in place. This case is reviewed here for two reasons. First it serves as a reference against which any improved scheme can be compared. Second, to the best of the author's knowledge, formulas this simple describing the current quality for this case have not been previously published.

If the duty ratio is constant the processed power P averaged over one line cycle as given in (4.1.60) can be simplified to

$$P = \frac{12\sqrt{3}V_L^2 M D_1^2}{\pi R_e} \cdot \int_0^{\pi/6} \alpha_d(\theta)\, d\theta \tag{4.2.1}$$

This equation can be solved for the required duty ratio D_1 to process a certain power level

$$D_1 = \sqrt{\frac{R_e P}{12 V_L^2 A_1}} \tag{4.2.2}$$

where the constant A_1 is defined as

$$A_1 \equiv \frac{\sqrt{3}M}{\pi} \int_0^{\pi/6} a_d(\theta)\, d\theta \tag{4.2.3}$$

Using (4.1.62) and (4.2.2) the rms-value of the currents can be written as

$$I_{rms} = \frac{P}{6V_L} \cdot \frac{A_2}{A_1} \tag{4.2.4}$$

where the constant A_2 is defined by

$$A_2 \equiv \sqrt{\frac{1}{\pi}\int_0^{\pi/6} \alpha_s(\theta)\,d\theta} \tag{4.2.5}$$

Using (2.7.4), (2.7.5) and (4.1.64) the expected power factor and *THD* can be expressed as

$$PF = 2\frac{A_1}{A_2} \tag{4.2.6}$$

$$THD = \sqrt{\frac{A_2^{\,2}}{4A_1^{\,2}} - 1} \tag{4.2.7}$$

In the constant duty ratio case, the formulas for each individual harmonic relative to the fundamental given in (4.1.67) becomes

$$I_{k_{rel}} = \begin{cases} \dfrac{1}{\pi A_1} \cdot \displaystyle\int_0^{\pi/6} \beta_k(\theta)\,d\theta & \text{for } k = 1,3,5,\ldots \\ 0 & \text{for } k = 2,4,6,\ldots \end{cases} \tag{4.2.8}$$

where β_k is defined in (4.1.68). At $k = 1$ β_k reduces to the left-hand side of (4.1.57) and by comparing the right-hand side of the same equation with the definition of A_1 in (4.2.3), it can be concluded that the integral in (4.2.8) equals to $A_1\pi$ and thus I_{1rel} is unity. This can be used to support the reasoning preceding (4.1.64).

The modulation depth is of course zero in constant duty ratio case. Thus,

$$\Delta D_1 = 0 \tag{4.2.9}$$

If D_1 is constant it can be shown that the maximum value of $\bar{i}_d$ appears at $\theta = 0$ and the minimum value appears at $\theta = 30°$. Therefore, using (4.1.71) the relative ripple is given by

$$\Delta I_d = \frac{\sqrt{6}MV_L}{P}\left(\bar{i}_d(0) - \bar{i}_d\left(\frac{\pi}{6}\right)\right) \tag{4.2.10}$$

After substitutions and simplifications this can be written as

$$\Delta I_d = \frac{M}{4A_1}\cdot\frac{2-\sqrt{3}}{(M-1)\left(2M-\sqrt{3}\right)} \tag{4.2.11}$$

All the quantities derived above were evaluated using Mathematica®. Fig. 4.4 shows the expected input current shape and the expected ripple in the diode current $\bar{i}_d$ for different conversion ratios, including plots of the magnitude of each harmonic component of the input currents. As predicted in Appendix A.3 there are no harmonics of order $3n$, and of course, there are no even harmonics.

The above-mentioned ripple in the diode current is undesirable because it causes a ripple in the output voltage ruling out this topology as a single-stage converter. A large capacitor C_o is necessary to alleviate this problem. By comparing Fig. 4.4a through 4.4c it becomes obvious that increasing the conversion ratio simultaneously reduces the distortion of the input current and the ripple at the output of the converter. Since in most applications the input voltage is given (e.g., the utility line), a higher conversion ratio means a higher output voltage. On the other hand, this also increases the voltage stress in the switches and in the output capacitor. This is not desirable since this topology operates with high voltages even with M close to unity. (As previously stated, the circuit requires a conversion ratio greater than unity.)

Figure 4.5a shows how the expected *THD* is related to the conversion ratio, whereas Fig. 4.5b shows the dependence of the lowest order non-zero harmonics on the conversion ratio. The 5th harmonic is clearly the worst for any value of M. Figure 4.5c shows the diode current ripple normalized with respect to its average value as a function of the conversion ratio. This ripple is evaluated from peak to peak, and therefore, it can be greater than 100%.

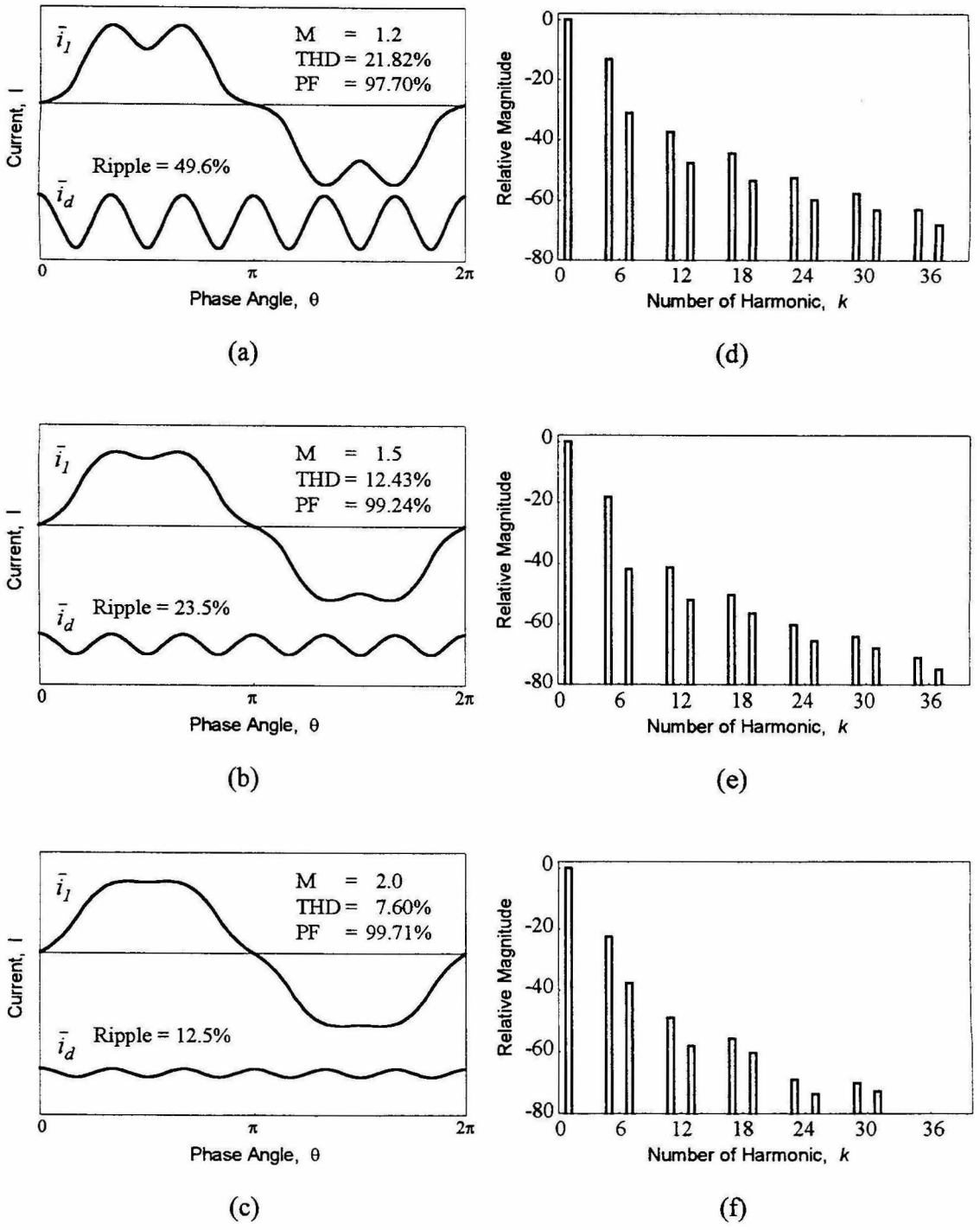

Figure 4.4: Constant duty ratio with different conversion ratios: (a), (b) and (c) Calculated input current waveform and output voltage ripple. (d), (e) and (f) Harmonic content of the input current in dB normalized with respect to the fundamental component.

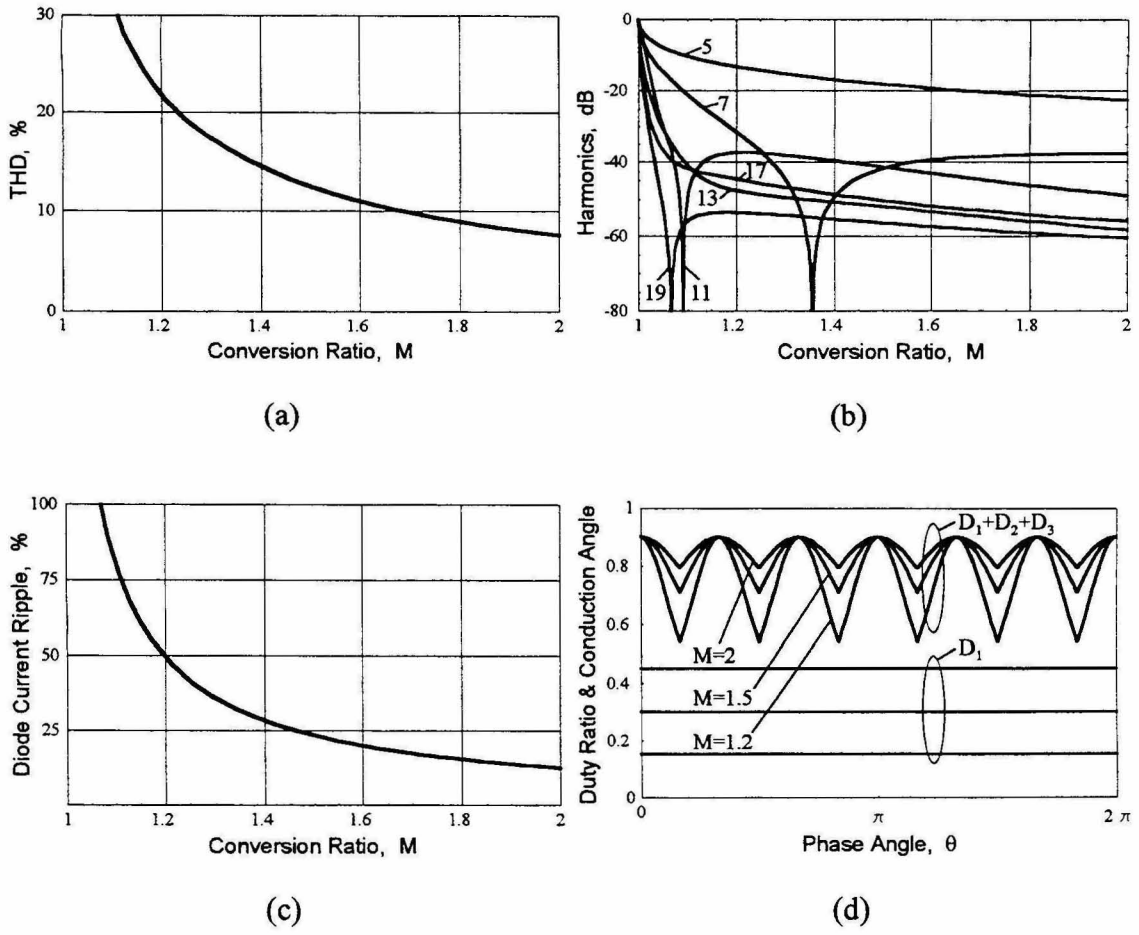

Figure 4.5: Constant duty ratio: (a) The calculated THD versus the conversion ratio. (b) The magnitudes of the lower order harmonics versus the conversion ratio. (c) Six times the line frequency ripple of the diode current i_d as a function of the conversion ratio normalized with respect to the average value of i_d. (d) The calculated conduction angle of the inductors L_1, L_2, or L_3 and the necessary duty ratio to achieve a maximal conduction angle of 0.9 for three conversion ratios. (One of the 3 inductors becomes discontinuous first. This shorter conduction angle is not shown here.)

Finally, Fig. 4.5d shows the conduction angle of the inductors L_1, L_2, or L_3 for 3 different conversion ratios. The conduction angle is defined as the fraction of the duty cycle while the inductor current is non-zero. Thus, referring to Fig. 4.3 the conduction angle is given by

$$D_{123} = \frac{T_1 + T_2 + T_3}{T_s} \tag{4.2.12}$$

One out of the three inductor currents becomes discontinuous before the other two. Because this shorter conduction angle is not important for design purposes, it is not shown in the graph. The necessary duty ratio to achieve a maximum conduction angle of 0.9 again for three different values for M is also shown.

As mentioned above, it is very undesirable to increase the conversion ratio in order to improve the performance of this topology. This gave rise to the question whether it is possible to improve the current shape and possibly reduce the output voltage ripple without increasing the conversion ratio. Probably the most promising idea is to give up the constant duty ratio operation and find schemes to modulate the duty ratio such that the overall behavior of the converter is improved. Several of such schemes are discussed in the subsequent sections.

4.3 Optimal Duty Ratio

In the previous section it was assumed that the duty ratio D_1 is constant. The question arises, can the input current shape be improved by modulating the D_1 in a certain manner? It should be pointed out that there are three input currents but only two of them are independent. The third is always the negative sum of the other two. On the other hand, there is only one active switch whose duty ratio can be varied. Every duty ratio change affects both independent currents, and thus, all three input currents. Therefore, there are not enough degrees of freedom to shape the currents into any desired form. In the ideal case, all three input currents are pure sine waves in phase with the corresponding voltages. This converter operating under the conditions stated in

Section 4.1 possesses no duty ratio modulation scheme that provides these ideal input currents. Moreover, in this section a duty ratio modulation scheme is found which optimizes all three current waveforms simultaneously. A similar approach as introduced here has been published recently [8] without stating analytical results.

In order to find the optimal duty ratio, the following ideal reference currents are defined:

$$i_{R1}(\theta) \equiv I_R \sin(\theta) \tag{4.3.1}$$

$$i_{R2}(\theta) \equiv I_R \sin\left(\theta - \frac{2\pi}{3}\right) \tag{4.3.2}$$

$$i_{R3}(\theta) \equiv I_R \sin\left(\theta - \frac{4\pi}{3}\right) \tag{4.3.3}$$

where the value of I_R remains to be determined.

Next, the quantity Δ is defined as the square of the sum of the differences between the actual currents and the ideal reference currents as indicated in Fig. 4.6.

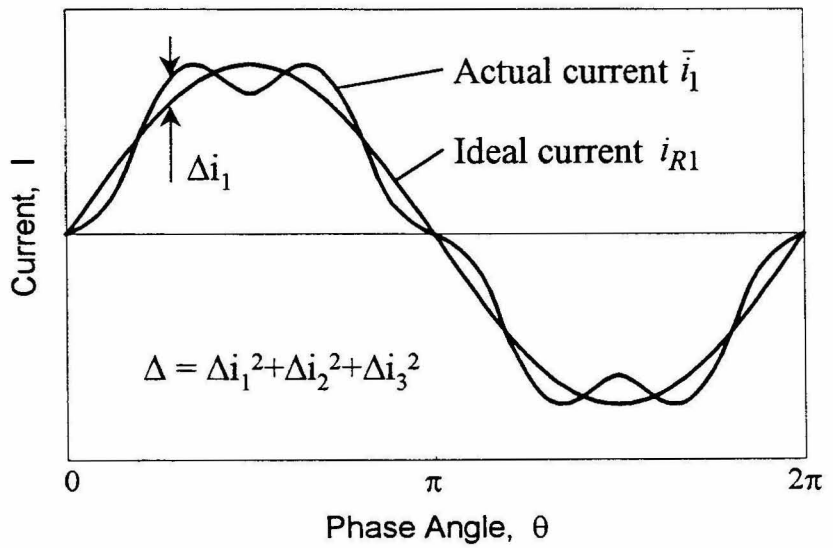

Figure 4.6: Definition of Δ which is minimized with respect to the duty ratio to optimize the input current shape.

$$\Delta(D_1,\theta)=(\bar{i}_1(\theta)-i_{R1}(\theta))^2+(\bar{i}_2(\theta)-i_{R2}(\theta))^2+(\bar{i}_3(\theta)-i_{R3}(\theta))^2 \tag{4.3.4}$$

Now, the goal is to find $D_1(\theta)$ which minimizes Δ for every phase angle θ. This D_1 optimizes the input current shape in the time domain in the least square sense. The derivative of Δ with respect to D_1 must be found in order to solve the following equation for D_1.

$$\frac{d\Delta(D_1,\theta)}{dD_1}=0 \tag{4.3.5}$$

The result is found to be

$$D_1(\theta)=I_R\frac{R_e}{\sqrt{2}V_L}\cdot\frac{\alpha_1(\theta)\sin(\theta)+\alpha_2(\theta)\sin\left(\theta-\frac{2\pi}{3}\right)+\alpha_3(\theta)\sin\left(\theta-\frac{4\pi}{3}\right)}{\alpha_1^{\,2}(\theta)+\alpha_2^{\,2}(\theta)+\alpha_3^{\,2}(\theta)} \tag{4.3.6}$$

Using (4.1.57) and (4.1.63) this can be simplified to

$$D_1(\theta)=\sqrt{I_R\frac{\sqrt{6}MR_e}{2V_L}\cdot\frac{\alpha_d(\theta)}{\alpha_s(\theta)}} \tag{4.3.7}$$

This optimal duty ratio can be substituted into the expression for the averaged processed power given in (4.1.60). After some substitutions and simplifications this can be written as

$$P=6\sqrt{2}I_RV_LA_3^{\,2} \tag{4.3.8}$$

where A_3 is defined as

$$A_3\equiv\sqrt{\frac{3M^2}{\pi}\cdot\int_0^{\pi/6}\frac{\alpha_d^{\,2}(\theta)}{\alpha_s(\theta)}d\theta} \tag{4.3.9}$$

Equation (4.3.8) can be solved for the unknown coefficient I_R for a given power level

$$I_R=\frac{P}{6\sqrt{2}V_LA_3^{\,2}} \tag{4.3.10}$$

With this the optimal duty ratio in (4.3.7) can be expressed as

$$D_1(\theta) = \sqrt{\frac{MPR_e}{4\sqrt{3}V_L{}^2 A_3{}^2} \cdot \frac{\alpha_d(\theta)}{\alpha_s(\theta)}} \tag{4.3.11}$$

Assuming the converter is operated with this optimal duty ratio the rms value of the resulting input current can be found using (4.1.62) which can now be simplified to

$$I_{rms} = \frac{P}{6V_L} \cdot \frac{1}{A_3} \tag{4.3.12}$$

The power factor and the *THD* can be found using (2.7.4) and (2.7.5) respectively where I_1 is given in (4.1.64)

$$PF = 2A_3 \tag{4.3.13}$$

$$THD = \sqrt{\frac{1}{4A_3{}^2} - 1} \tag{4.3.14}$$

The general formula for each individual harmonic is given in (4.1.67). Using the optimal duty ratio as given in (4.3.11) the coefficients of each harmonic relative to the fundamental can be expressed as

$$I_{k_{rel}} = \begin{cases} \dfrac{\sqrt{3}M}{\pi A_3{}^2} \displaystyle\int_0^{\pi/6} \frac{\alpha_d(\theta)}{\alpha_s(\theta)} \beta_k(\theta)\, d\theta & \text{for } k = 1,3,5,\ldots \\ 0 & \text{for } k = 2,4,6,\ldots \end{cases} \tag{4.3.15}$$

where β_k is defined in (4.1.68). It is again easy to show that I_{1rel} is unity.

It can be shown that the maximum value of the duty ratio appears at $\theta = 30°$ whereas the minimum value appears at $\theta = 0°$. Therefore, the modulation depth ΔD_1 can be expressed as

$$\Delta D_1 = D_1\left(\frac{\pi}{6}\right) - D_1(0) \tag{4.3.16}$$

Using (4.3.11) and (4.1.46) through (4.1.49) and some algebra ΔD_1 leads to

$$\Delta D_1 = \sqrt{\frac{PR_e}{12MV_L{}^2A_3{}^2}}\left(\sqrt{M-\frac{\sqrt{3}}{2}}-\sqrt{M-1}\right) \tag{4.3.17}$$

Finally, the relative ripple of the output diode current $\bar{i}_d$ remains to be evaluated. Substituting $\theta = 0°$ and $\theta = 30°$ into the equation for $\bar{i}_d$, i.e., (4.1.45), shows that the values of $\bar{i}_d$ are identical in both cases. It can be shown that these are the maximum values. The minimum occurs somewhere within the 30° interval. There is no closed form expression for the phase angle at the minimum value of $\bar{i}_d$.

It can be shown that the phase angle θ that satisfies

$$\sin\left(\theta+\frac{\pi}{6}\right)-3\sin\left(3\theta-\frac{\pi}{6}\right)+\frac{2}{M}\sin^2(2\theta)=0 \quad \text{AND} \quad 0<\theta<\frac{\pi}{6} \tag{4.3.18}$$

is the phase angle at the minimum value of $\bar{i}_d$. This equation can be solved numerically for an arbitrary M. Assuming θ_o is the solution of (4.3.18), then the relative ripple of $\bar{i}_d$ can be found using (4.1.71)

$$\Delta I_d = \frac{\sqrt{6}MV_L}{P}\left(\bar{i}_d(0)-\bar{i}_d(\theta_o)\right) \tag{4.3.19}$$

By substituting the corresponding expressions into (4.3.19), the following form can be found:

$$\Delta I_d = \frac{1}{4A_3{}^2}\left(1-2M^2\frac{\alpha_d{}^2(\theta_o)}{\alpha_s(\theta_o)}\right) \tag{4.3.20}$$

All the quantities derived above have been evaluated and the results are presented in Figs. 4.7 through 4.9. The current waveform has improved primarily due to a reduction of the 5th harmonic. This improvement is most visible in Fig. 4.8b when compared with Fig. 4.5b. Moreover, at low conversion ratios the reduction of the *THD* is more relevant than for higher values of M.

Furthermore, the ripple in the diode current has almost disappeared as it can be seen in Figs. 4.7a through 4.7c. This current ripple versus the conversion ratio is plotted in Fig. 4.8c. The value is roughly 15 times lower than in the constant duty ratio case, which is shown in Fig. 4.5c. This greatly enhances the usefulness of this control scheme. Unlike the single-phase case, this topology does not require a large energy storage / output capacitor for the ac-to-dc conversion and power factor correction function.

Figure 4.9a shows the duty ratio modulation at a frequency that is six times higher than the line frequency. In addition, the conduction angle of inductors L_1, L_2 and L_3 is less varying as a function of the phase angle (i.e., as a function of the time). This means the intervals with zero inductor current are shorter. Thus, the rms-values of the currents are lower for the same processed power and it allows a better utilization of the magnetic components.

The required modulation depth ΔD_1 versus the conversion ratio is shown in Fig. 4.9b. It is evident that only a very weak modulation is necessary to obtain the optimal duty ratio.

The major problem with this control scheme is its difficult implementation. The duty ratio function as stated in (4.3.11) is rather complicated and, thus, not very practical to accomplish. This control method requires constant monitoring of the output voltage as well as the instantaneous values of at least two of the input voltages. These quantities are necessary to evaluate (4.1.49) and (4.1.63), which are needed to calculate the optimal duty ratio given in (4.3.11). This is a complex algorithm involving a lot of computation and is therefore difficult to implement.

However, the fact that in the optimal duty ratio case the diode current $\bar{i}_d$ is almost ripple free provides an interesting simple means to approximate the optimal duty ratio. All that is required is a fast feedback loop that keeps the diode current completely constant. This much simpler control method is investigated in the next section.

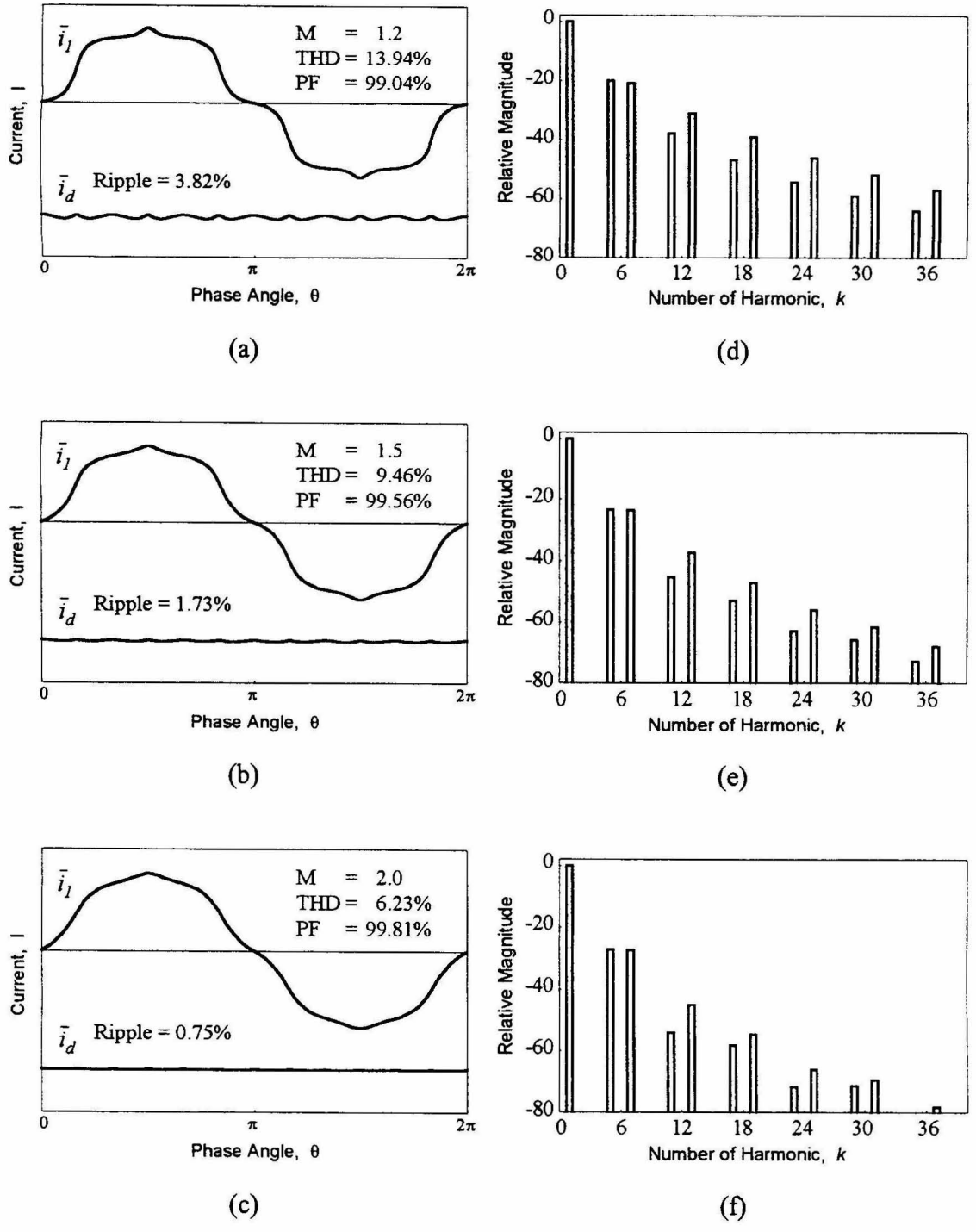

Figure 4.7: Optimal duty ratio with different conversion ratios: (a), (b) and (c) Calculated input current waveform and output voltage ripple. (d), (e) and (f) Harmonic content of the input current in dB normalized with respect to the fundamental component.

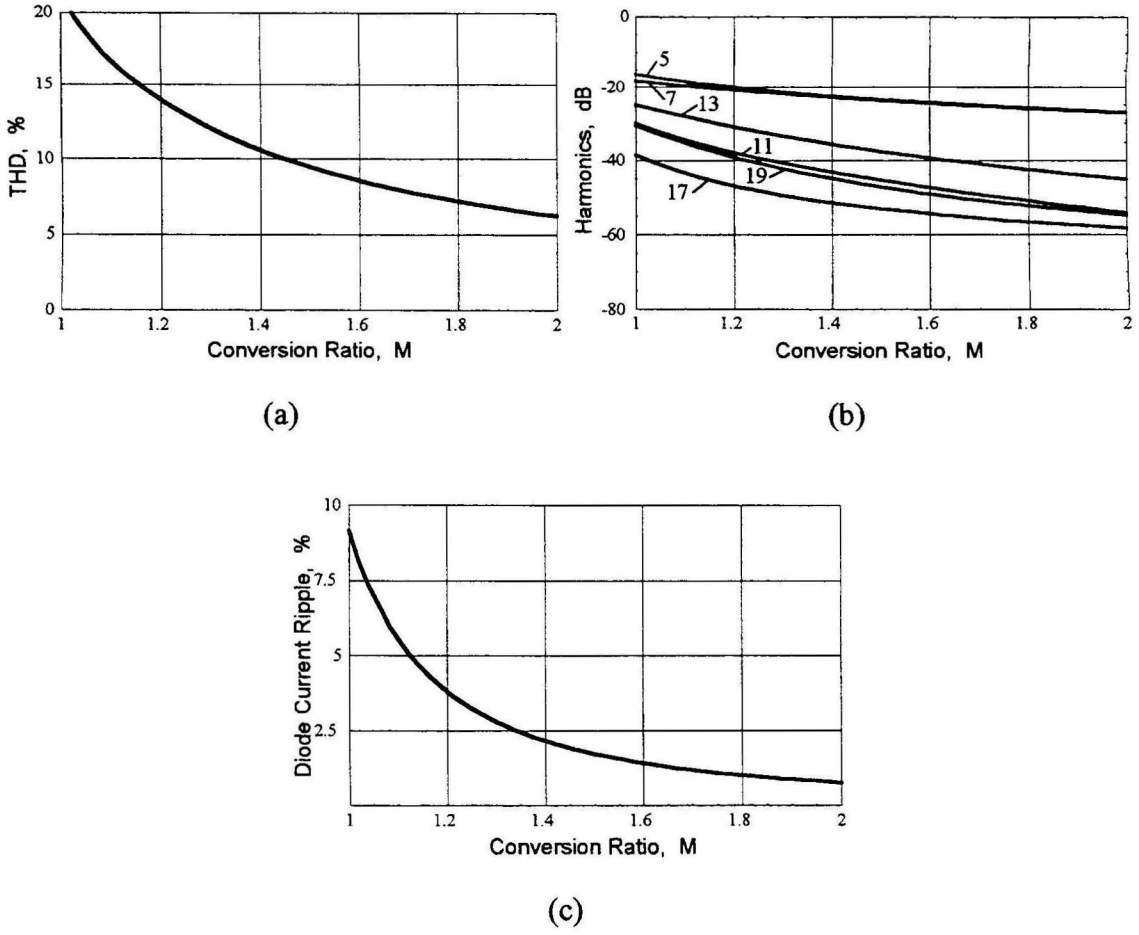

Figure 4.8: Optimal duty ratio: (a) The calculated THD versus the conversion ratio. (b) The magnitudes of the lower order harmonics versus the conversion ratio. (c) Six times the line frequency ripple of the diode current i_d as a function of the conversion ratio normalized with respect to the average value of i_d.

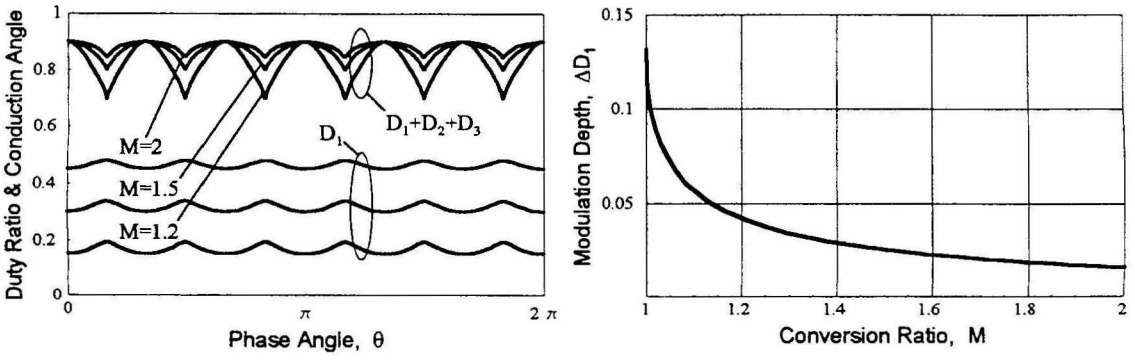

(a) (b)

Figure 4.9: Optimal duty ratio: (a) The calculated conduction angle of the inductors L_1, L_2, or L_3 and the necessary duty ratio to achieve a maximal conduction angle of 0.9 for three conversion ratios (One of the 3 inductors becomes discontinuous first. This shorter conduction angle is not shown here.) and (b) the modulation depth ΔD_1 as a function of the conversion ratio.

4.4 Controlled Diode Current Operation

Figure 4.4a through 4.4c shows the diode current waveform for the constant duty ratio case whereas the same information for the optimal duty ratio is shown in Figs. 4.7a through 4.7c. The percentage of the peak to peak current ripple compared with the average value of $\bar{i}_d$ is shown in Fig. 4.8c for the optimal duty ratio case and in Fig. 4.5c for the constant duty ratio case. It is of note that the six times the line frequency ripple, observed with constant D_1, almost disappears if the optimal duty ratio is applied. (The ripple is reduced by a factor of approximately 15). Therefore, there is no need to artificially generate the optimal duty ratio. Closer scrutiny of (4.3.11) reveals that this is not a simple task, in any event, since $\alpha_s(\theta)$ and $\alpha_d(\theta)$ are complicated phase angle dependent functions.

An alternative and simpler approach is to control the diode current $\bar{i}_d$ such that it remains entirely constant. By doing so, it can be expected that the input current is only slightly different from the optimal case. In this scenario there is exactly one

current to control and there is exactly one duty ratio available to exercise proper control. This problem is well defined and much simpler to solve.

Furthermore, if the control loop is ideal, the output voltage will not have a line frequency related ripple. Realistically and desirably, the ripple is at least drastically reduced. The necessary feedback loop must have a bandwidth well above six times the line frequency. For further considerations an entirely constant diode current $\bar{i}_d$ is assumed.

Since in this case both V_o and $\bar{i}_d$ are constant the instantaneous power $\bar{p}_o$ and the averaged processed power P are the same. Thus, (4.1.56) can be written as

$$P = D_1^2 \frac{2\sqrt{3}MV_L^2}{R_e}\alpha_d(\theta) \tag{4.4.1}$$

This can be solved for the necessary duty ratio to achieve a constant $\bar{i}_d$.

$$D_1 = \sqrt{\frac{R_e P}{2\sqrt{3}MV_L^2\alpha_d(\theta)}} \tag{4.4.2}$$

To find the rms-value of the resulting input current D_1 can be substituted into (4.1.62).

$$I_{rms} = \frac{P}{3V_L}A_4 \tag{4.4.3}$$

where the constant A_4 is defined by

$$A_4 \equiv \sqrt{\frac{3}{\pi M^2}\int_0^{\pi/6}\frac{\alpha_s(\theta)}{\alpha_d^2(\theta)}d\theta} \tag{4.4.4}$$

Using (2.7.4), (2.7.5) and (4.1.64) the power factor and the *THD* are found to be

$$PF = \frac{1}{A_4} \tag{4.4.5}$$

$$THD = \sqrt{A_4^2 - 1} \tag{4.4.6}$$

Using (4.1.67) the expressions for each individual harmonic becomes

$$I_{k_{rel}} = \begin{cases} \dfrac{2\sqrt{3}}{\pi M} \displaystyle\int_0^{\pi/6} \frac{\beta_k(\theta)}{\alpha_d(\theta)} d\theta & \text{for } k = 1,3,5,... \\ 0 & \text{for } k = 2,4,6,... \end{cases} \tag{4.4.7}$$

where β_k is defined in (4.1.68). Using (4.1.57) it is again easy to show that I_{1rel} is unity.

Similar as in the case of the optimal duty ratio the maximum value of the duty ratio appears at $\theta = 30°$ and the minimum appears at $\theta = 0°$. Thus, ΔD_1 is given by

$$\Delta D_1 = D_1\left(\frac{\pi}{6}\right) - D_1(0) \tag{4.4.8}$$

Using (4.4.2) and (4.1.46) through (4.1.49), the following expression can be found:

$$\Delta D_1 = \sqrt{\frac{PR_e}{3MV_L{}^2}}\left(\sqrt{M - \frac{\sqrt{3}}{2}} - \sqrt{M-1}\right) \tag{4.4.9}$$

By assumption the relative ripple of $\bar{i}_d$ is zero in this case. Thus,

$$\Delta I_d = 0 \tag{4.4.10}$$

Figure 4.10 shows the current waveforms and the corresponding harmonic components for the constant diode current controlled case. As expected, the input current waveforms are very similar to the ones of the optimal duty ratio case. The calculated values for the *THD* and the power factor differ only slightly from the previous case. The graphs for the *THD* versus the conversion ratio shown in Fig. 4.11a and Fig. 4.8a are virtually identical.

It comes as no surprise that the duty ratio function, the conduction angle and the modulation depth are very similar in the optimal case and in the constant diode current case. This can be concluded by comparing Fig. 4.11c and 4.11d with Fig. 4.9.

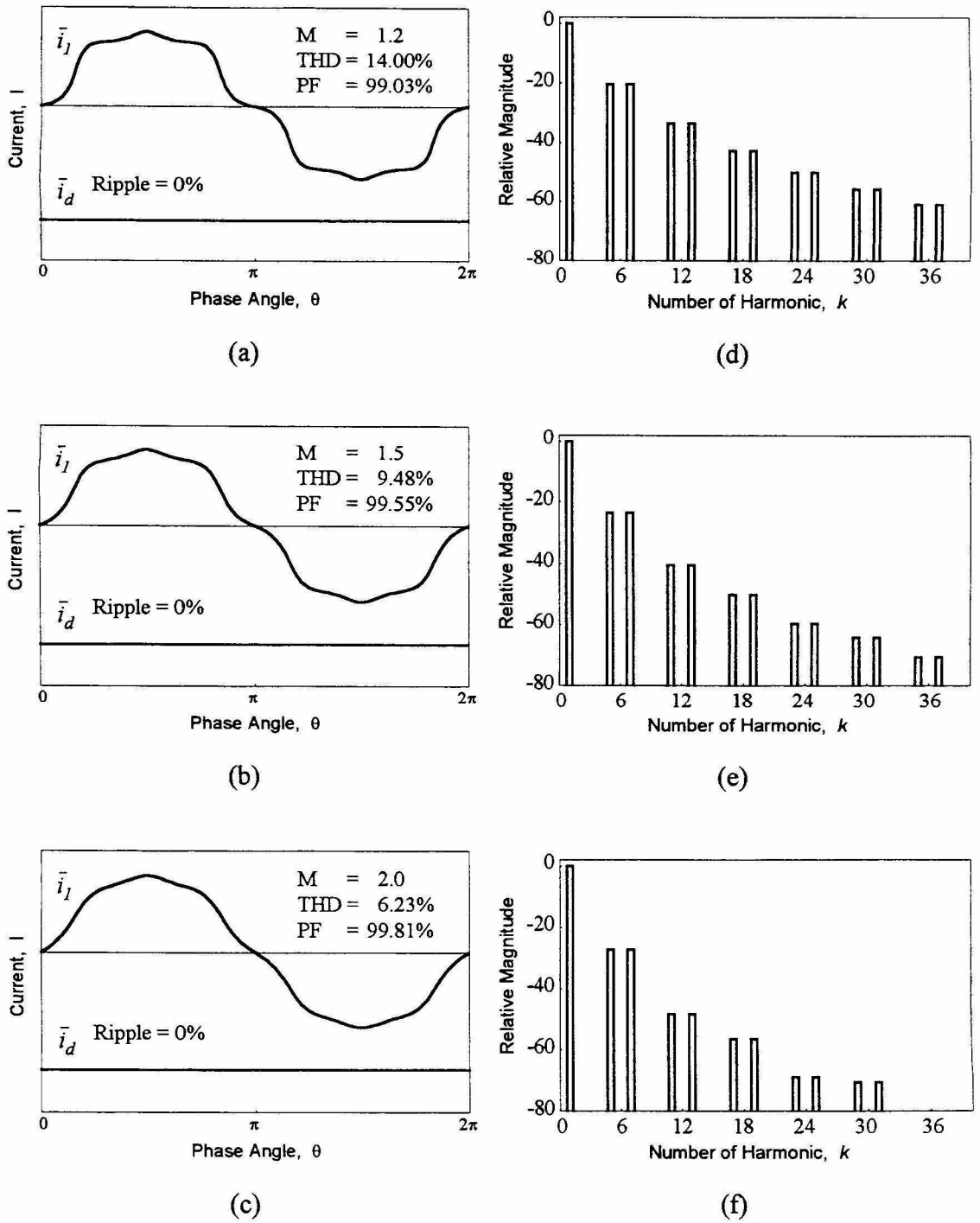

Figure 4.10: Constant diode current with different conversion ratios: (a), (b) and (c) Calculated input current waveform and output voltage ripple. (d), (e) and (f) Harmonic content of the input current in dB normalized with respect to the fundamental component.

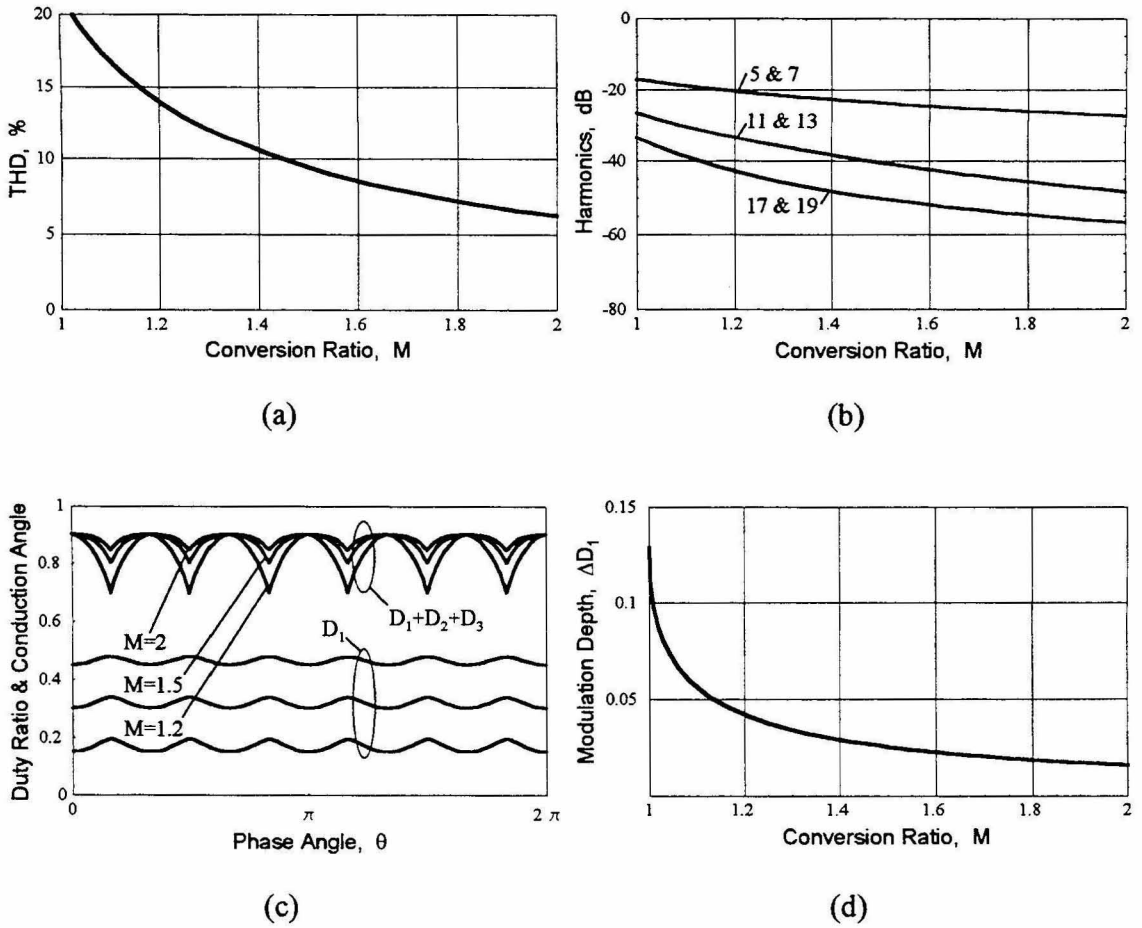

Figure 4.11: Constant diode current controlled: (a) The calculated THD versus the conversion ratio. (b) The magnitudes of the lower order harmonics versus the conversion ratio. (c) The calculated conduction angle of the inductors L_1, L_2, or L_3 and the necessary duty ratio to achieve a maximal conduction angle of 0.9 for three conversion ratios. (One of the 3 inductors becomes discontinuous first. This shorter conduction angle is not shown here.) (d) The modulation depth ΔD_1 as a function of the conversion ratio.

In this case the instantaneous power $\bar{p}$ is constant since $\bar{i}_d$ and by assumption V_o is constant. As derived in Appendix A.5 this requires the harmonics to appear in pairs of equal magnitude. Figure 4.10d through 4.10f confirms this behavior.

The constant diode current control method approximates the optimal duty ratio so closely that any attempt to realize the precisely optimal case can never be justified. The analytical evaluation of the optimal case, however, is very useful since it reveals that there is no justification to search for a control method that is better than the constant diode current method. Firstly, because the difference from the optimal case is so slim that an improvement is hardly possible. Secondly, this control method also removes the twice the line frequency ripple at the output of the converter. This is another beneficial effect that can be achieved by applying this control method.

Results similar to the ones discussed here were presented in [9]. However, only approximate expressions were used to characterize the currents, and it has not been shown that the constant output control very closely approximates the optimal duty ratio. Due to its simplicity and to its advantageous effect at the input and output of the converter, the constant diode current control method appears to be the control method of choice.

Several other schemes have been suggested, to improve the input current waveform over the constant duty ratio case, one of which is presented in [10]. The objective is to inject an easy to generate function into the duty ratio. The resulting function approximates to the optimal duty ratio to some degree. The next section deals with these methods in a more generic form than [10].

4.5 Arbitrarily Modulated Duty Ratio

An alternative method to improve the input current waveform is to approximate the optimal duty ratio given in (4.3.11) with easier to generate functions. The optimal duty ratio for $M = 1.5$ is plotted in Fig. 4.12 over one-sixth of a line cycle, which is one full

period for this signal. This curve might be approximated with a triangular signal of six times the line frequency and an improved current shape can be expected. Potentially a modulation of the duty ratio with a cosine of the same frequency could be more effective.

To remain generic, suppose the duty ratio is given by the following formula:

$$D_1 = D_{1o}(1 + \delta \cdot f(\theta)) \tag{4.5.1}$$

where $f(\theta)$ can be an arbitrary function for $0 \le \theta \le 30°$. For all values outside this range, $f(\theta)$ has to satisfy

$$f(\theta) = f\left(\theta + \frac{\pi}{3}\right) \tag{4.5.2}$$

$$f(\theta) = f\left(\frac{\pi}{3} - \theta\right) \tag{4.5.3}$$

in order for the duty ratio to satisfy (4.1.58) and (4.1.59). Without loss of generality $f(\theta)$ can by scaled such that the maximum value minus the minimum value equals 1. With this choice the modulation depth ΔD_1 as defined in (4.1.69) will simply be

$$\Delta D_1 = D_{1o} \cdot |\delta| \tag{4.5.4}$$

The objective now is to find the optimal value of δ for a given function f such that the *THD* of the resulting input current is minimized. D_{1o} can then be adjusted to obtain a desired power level. From (2.4.2) it is evident that this is the same as minimizing the following function.

$$\frac{I_{rms}^{\ 2}}{I_1^{\ 2}} \tag{4.5.5}$$

Using (4.1.62) I_{rms} is given by

$$I_{rms} = 2\frac{V_L}{R_e} D_{1o}^{\ 2} \sqrt{\frac{1}{\pi} \int_0^{\pi/6} (1 + \delta \cdot f(\theta))^4 \alpha_s(\theta)\, d\theta} \tag{4.5.6}$$

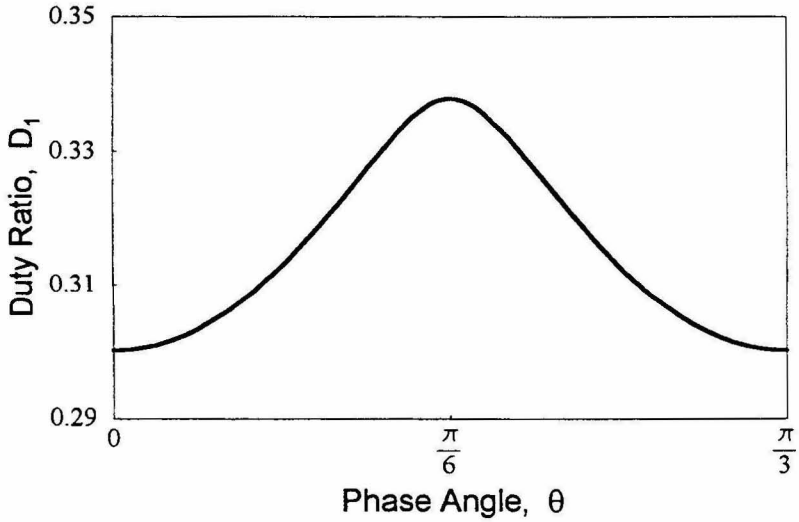

Figure 4.12: Optimal duty ratio over one-sixth of a line cycle with a conversion ratio of $M = 1.5$.

whereas (4.1.65) in conjunction with (4.1.57) can be used to find I_1

$$I_k = 4\sqrt{3}\frac{V_L M}{\pi R_e} D_{1o}{}^2 \int_0^{\pi/6} (1+\delta \cdot f(\theta))^2 \alpha_d(\theta)\, d\theta \tag{4.5.7}$$

Minimizing (4.5.5) is the same as minimizing $F(\delta)$ where

$$F(\delta) = \frac{\int_0^{\pi/6} (1+\delta \cdot f(\theta))^4 \alpha_s(\theta)\, d\theta}{\left(\int_0^{\pi/6} (1+\delta \cdot f(\theta))^2 \alpha_d(\theta)\, d\theta \right)^2} \tag{4.5.8}$$

Equation (4.5.8) can be written as

$$F(\delta) = \frac{P_o + 4\delta P_1 + 6\delta^2 P_2 + 4\delta^3 P_3 + \delta^4 P_4}{(Q_o + 2\delta Q_1 + \delta^2 Q_2)^2} \tag{4.5.9}$$

where

$$P_i = \int_0^{\pi/6} \alpha_s(\theta) f^i(\theta) d\theta \tag{4.5.10}$$

$$Q_i = \int_0^{\pi/6} \alpha_d(\theta) f^i(\theta) d\theta \tag{4.5.11}$$

P_i and Q_i are all constants which can be numerically evaluated for a given conversion ratio M. The next step is to solve

$$\frac{\partial F(\theta)}{\partial \delta} = 0 \tag{4.5.12}$$

Even though it is complex it is straightforward to show that solving (4.5.12) is equivalent to solving

$$0 = K_o + \delta K_1 + \delta^2 K_2 + \delta^3 K_3 + \delta^4 K_4 \tag{4.5.13}$$

where the constant coefficients are given by

$$\begin{aligned} K_o &= P_o Q_1 - P_1 Q_o \\ K_1 &= P_o Q_2 + 2P_1 Q_1 - 3P_2 Q_o \\ K_2 &= 3(P_1 Q_2 - P_3 Q_o) \\ K_3 &= 3P_2 Q_2 - 2P_3 Q_1 - P_4 Q_o \\ K_4 &= P_3 Q_2 - P_4 Q_1 \end{aligned} \tag{4.5.14}$$

The solution for δ must be in the range of $0 < |\delta| < 1$ (typically δ approximately 0.1 and it decreases as M increases). In general a polynomial as the one given in (4.5.13) might have none or more than one real roots in the specified range. But from a physical point of view it can be argued that for a function $f(\theta)$, which even only roughly approximates the optimal duty ratio, there will be a solution δ which minimizes the *THD* and if the D_1 is over or under modulated the current shape becomes monotonically worse. This can be verified for a particular function $f(\theta)$ by plotting the corresponding polynomial (i.e., the right-hand side of (4.5.13), as δ runs from 0 to 1).

Once δ is known D_1 given in (4.5.1) can be substituted into (4.1.60). The expression for the processed power then becomes

$$P = \frac{12{V_L}^2}{R_e}{D_{1o}}^2 A_5 \tag{4.5.15}$$

where the constant A_5 is defined as

$$A_5 \equiv \frac{\sqrt{3}M}{\pi}\int_0^{\pi/6}(1+\delta\cdot f(\theta))^2\alpha_d(\theta)d\theta \tag{4.5.16}$$

Equation (4.5.15) can be solved for D_{1o}.

$$D_{1o} = \sqrt{\frac{R_e P}{12{V_L}^2 A_5}} \tag{4.5.17}$$

This can be substituted into (4.5.1)

$$D_1(\theta) = \sqrt{\frac{R_e P}{12{V_L}^2 A_5}}(1+\delta\cdot f(\theta)) \tag{4.5.18}$$

The rms value of the input currents given (4.5.6) can now be expressed as

$$I_{rms} = \frac{P}{6V_L}\cdot\frac{A_6}{A_5} \tag{4.5.19}$$

where the constant A_6 is defined as

$$A_6 \equiv \sqrt{\frac{1}{\pi}\int_0^{\pi/6}(1+\delta\cdot f(\theta))^4\alpha_s(\theta)d\theta} \tag{4.5.20}$$

Using (2.7.4), (2.7.5) and (4.1.64), the power factor and the *THD* can be found to be

$$PF = 2\frac{A_5}{A_6} \tag{4.5.21}$$

$$THD = \sqrt{\frac{A_6^{\,2}}{4A_5^{\,2}} - 1} \tag{4.5.22}$$

To get an expression for each individual harmonic relative to the fundamental, (4.1.67) can be used

$$I_{k_{rel}} = \begin{cases} \dfrac{1}{\pi A_5} \displaystyle\int_0^{\pi/6} (1+\delta \cdot f(\theta))^2 \beta_k(\theta)\, d\theta & \text{for } k = 1,3,5,\ldots \\ 0 & \text{for } k = 2,4,6,\ldots \end{cases} \tag{4.5.23}$$

where β_k is defined in (4.1.68). Using (4.1.57) it is again easy to show that I_{1rel} is unity. To find the modulation depth, (4.5.17) can be substituted into (4.5.4)

$$\Delta D_1 = |\delta| \cdot \sqrt{\frac{R_e P}{12 V_L^{\,2} A_5}} \tag{4.5.24}$$

There are no formulas for the ripple in $\bar{i}_d$ derived in this thesis. There is no simple description of ΔI_d for a general $f(\theta)$. Even with a known function $f(\theta)$ there can be local maxima and minima. The global maximum or minimum can be either one of these depending on the conversion ratio M.

In this thesis, the following four functions for $f(\theta)$ are considered:

$$f_1(\theta) = \frac{6}{\pi}\theta \tag{4.5.25}$$

$$f_2(\theta) = -\frac{1}{2}\cos(6\theta) \tag{4.5.26}$$

$$f_3(\theta) = -\cos(3\theta) \tag{4.5.27}$$

$$f_4(\theta) = -\frac{1}{2}\cos\left(\pi^{(1-b)} \cdot (6\theta)^b\right) \tag{4.5.28}$$

where b was chosen to be 1.5. The best value for b depends on the conversion ratio. For the range of M under consideration, $b = 1.5$ appears to be a reasonable choice. The minus sign in the last three cases was chosen in order to make δ a positive number.

Henceforth, the four approximation functions stated above will be called as follows:

- Equation (4.5.25): The linear modulation of the duty ratio.
- Equation (4.5.26): The cosine modulation of the duty ratio.
- Equation (4.5.27): The rectified cosine modulation of the duty ratio.
- Equation (4.5.28): The modified cosine modulation of the duty ratio.

The cosine modulation of the duty ratio is also called sixth harmonic injection. It was introduced in [10] where a different approach was used to find the optimal modulation depth than the one presented in this section.

The obtained duty ratio functions for all four cases optimized according to the above discussion (i.e., using (4.5.13) and (4.5.18)) are shown in Fig. 4.13. The conversion ratio in these examples is 1.5. The dotted line represents the optimal duty ratio as discussed in Section 4.3.

The analytically obtained current waveforms and their harmonic components are shown in Figs 4.14 through 4.17. All these modulation functions improve the current waveform significantly. It is noteworthy that even the linear approximation of the optimal duty ratio yields very good results.

It should be mentioned that these are analytically obtained results. Two obstacles must be overcome in order to realize these schemes. Firstly, the desired modulation function must be generated and synchronized with the utility line. Secondly, the appropriate modulation depth δ for any given conversion ratio must be found. This is potentially even more difficult.

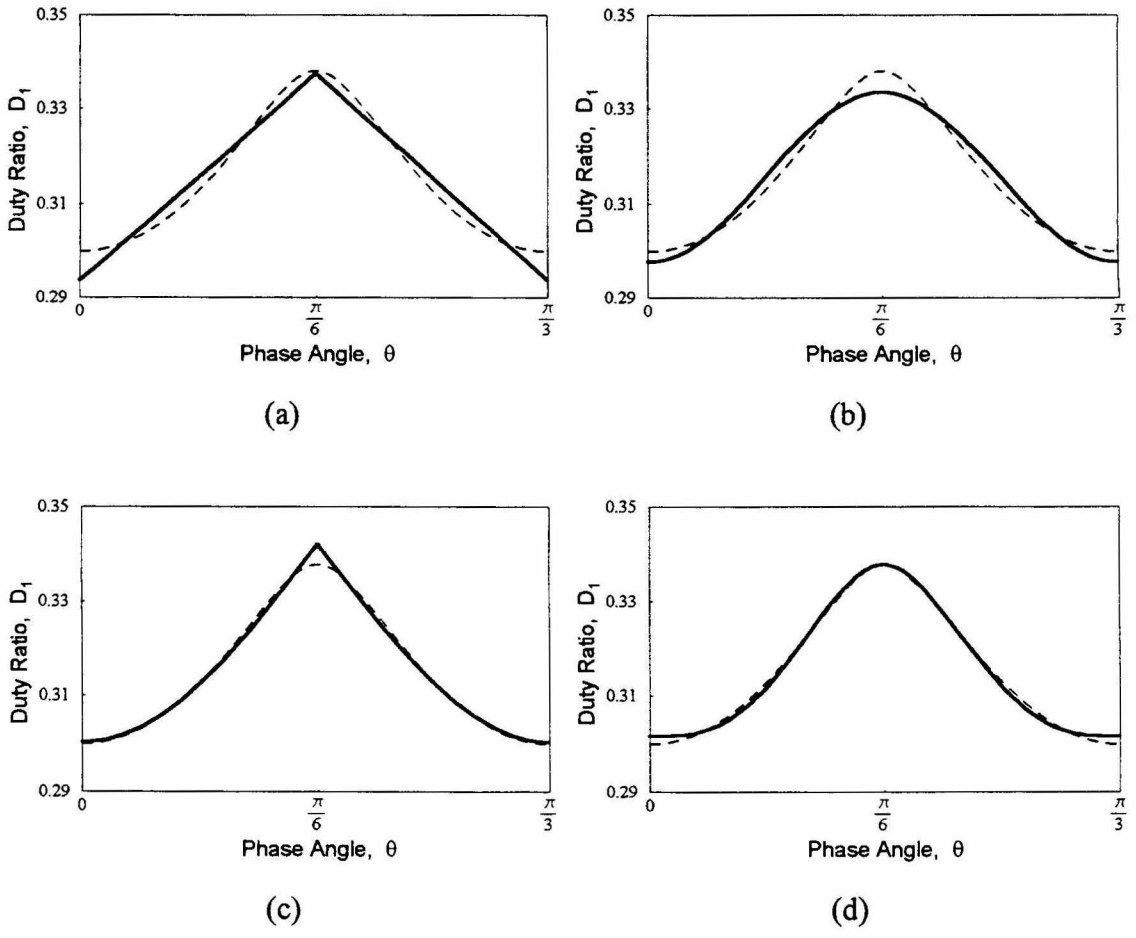

Figure 4.13: Solid line: duty ratio modulation function; dotted line: optimal duty ratio. (a) Linear modulation, (b) cosine modulation, (c) rectified cosine modulation and (d) modified cosine modulation.

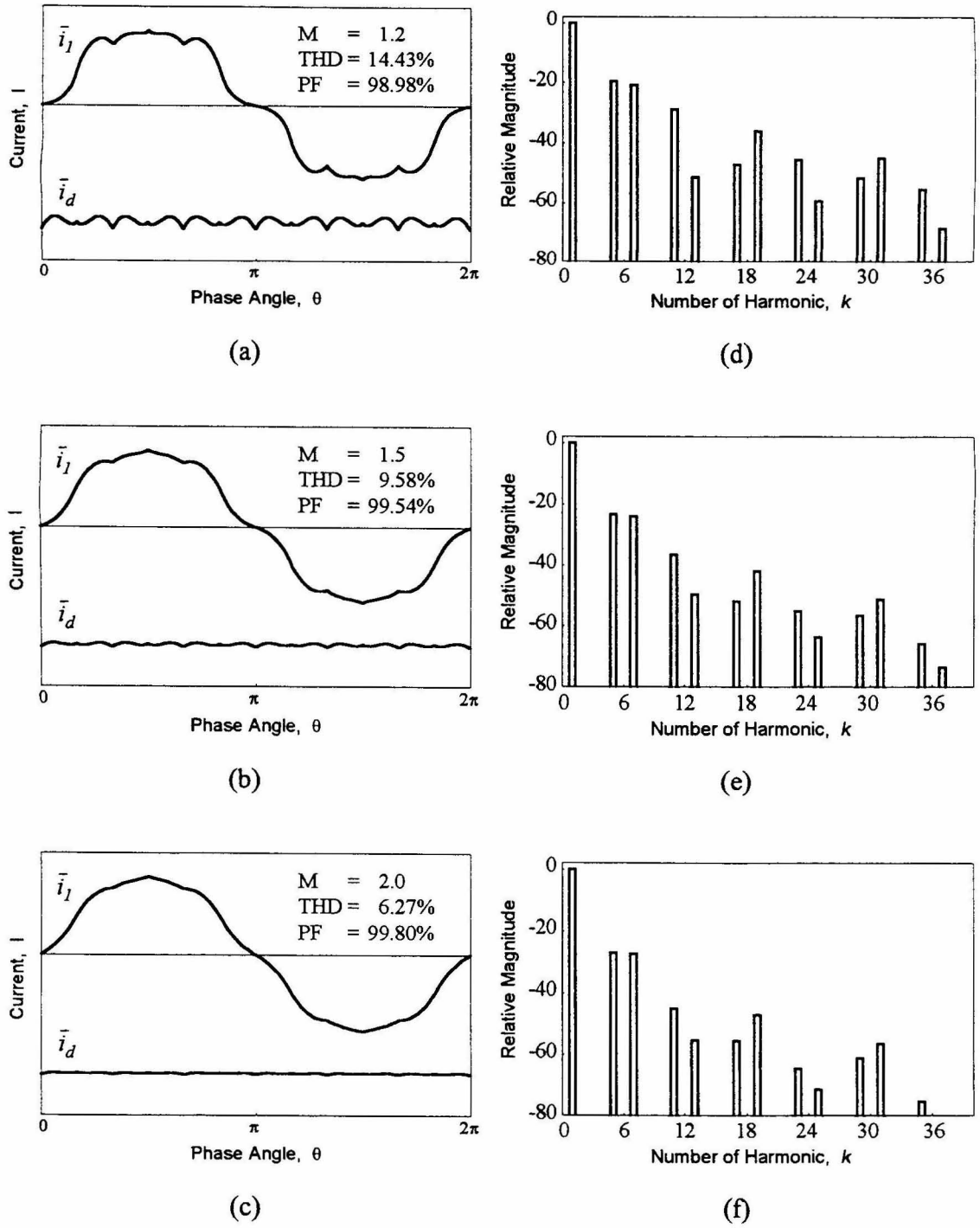

Figure 4.14: Linear modulation of the duty ratio with different conversion ratios: (a), (b) and (c) Calculated input current waveform and output voltage ripple. (d), (e) and (f) Harmonic content of the input current in dB normalized with respect to the fundamental component.

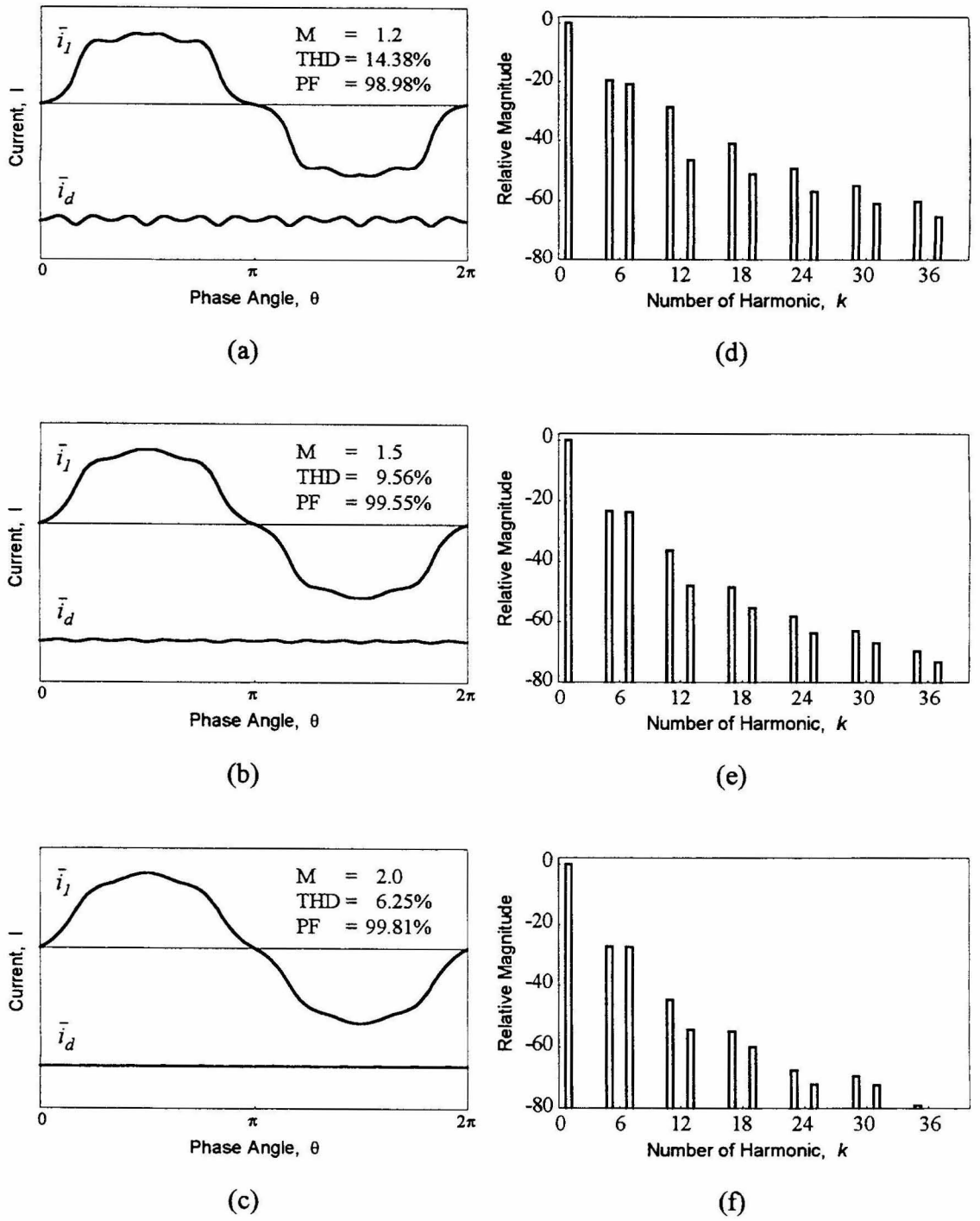

Figure 4.15: Cosine modulation of the duty ratio with different conversion ratios: (a), (b) and (c) Calculated input current waveform and output voltage ripple. (d), (e) and (f) Harmonic content of the input current in dB normalized with respect to the fundamental component.

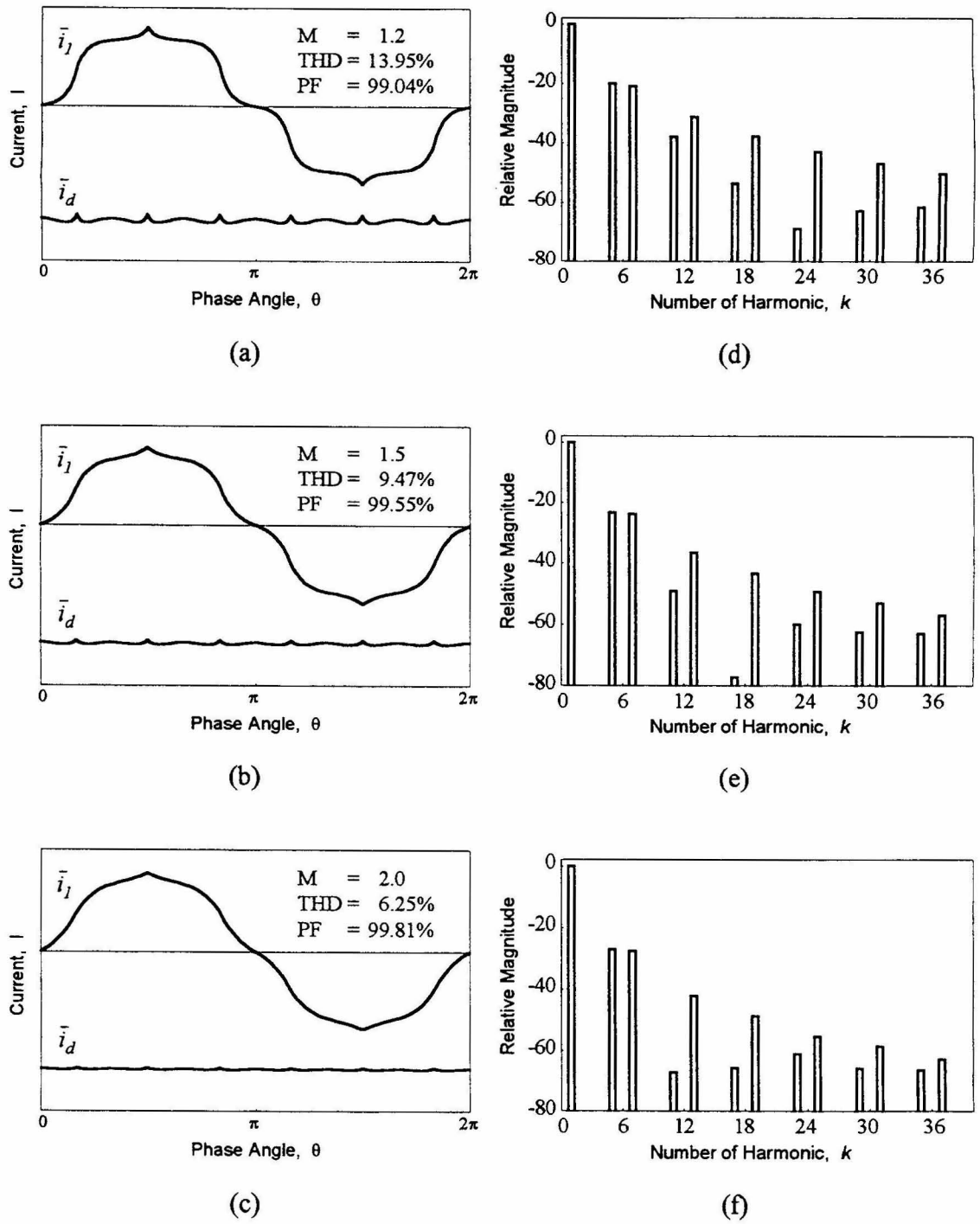

Figure 4.16: Rectified cosine modulation of the duty ratio with different conversion ratios: (a), (b) and (c) Calculated input current waveform and output voltage ripple. (d), (e) and (f) Harmonic content of the input current in dB normalized with respect to the fundamental component.

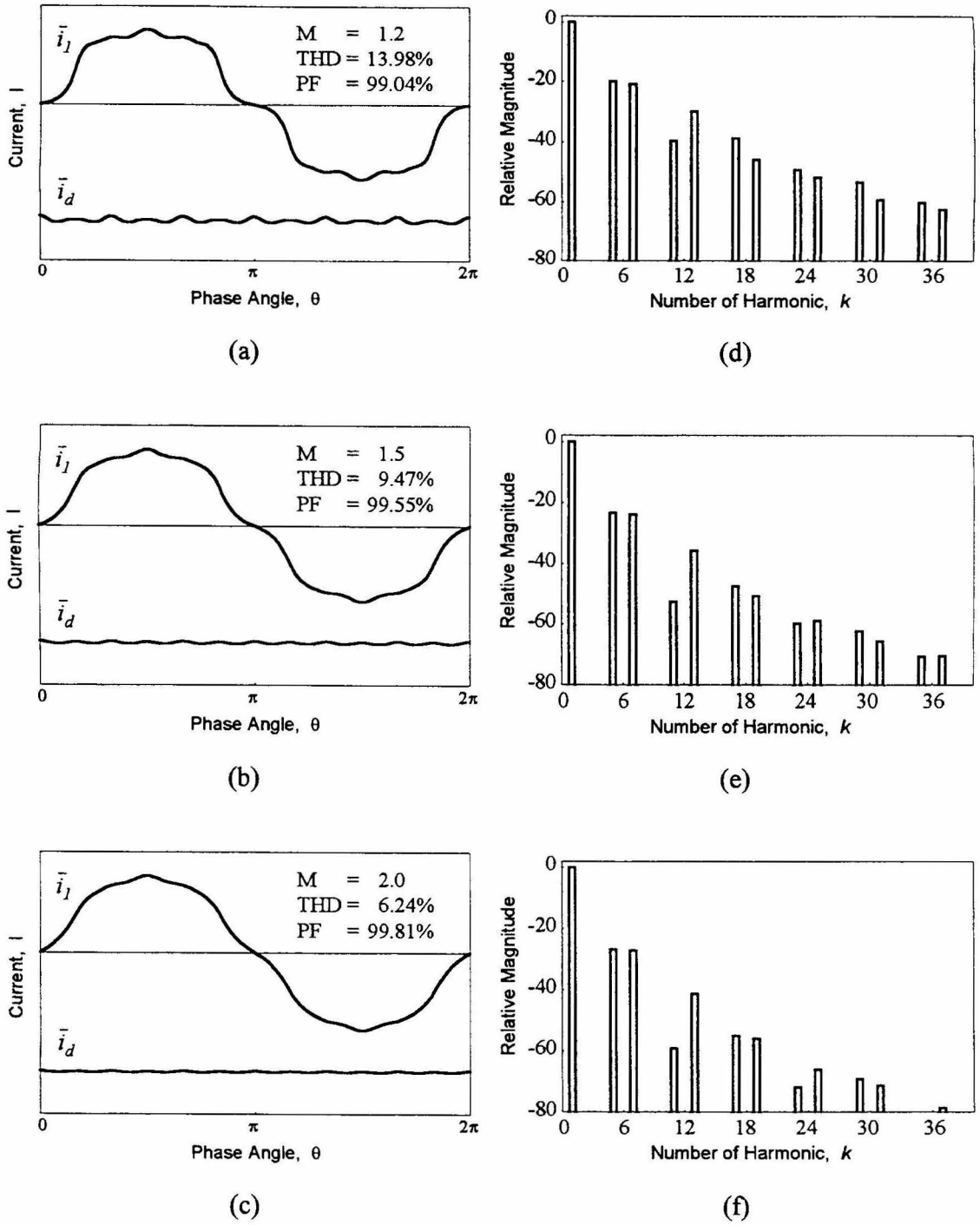

Figure 4.17: Modified cosine modulation of the duty ratio with different conversion ratios: (a), (b) and (c) Calculated input current waveform and output voltage ripple. (d), (e) and (f) Harmonic content of the input current in dB normalized with respect to the fundamental component.

However, if in a particular application the conversion ratio is fixed, or only slightly changing, then δ can be fixed without sacrificing performance. These modulation schemes have one advantage over the constant diode current control method. International standards such as IEC1000-3-2 set limits for the maximum allowed value of each individual harmonic. These limits decrease as the order of the harmonic increases, but not by the same rate as the actual magnitudes of the current harmonics decrease. This behavior is shown in Fig. 4.18 for a $380V_{ac}/800V_{dc}/8kW$ converter. The stars mark the limits according to IEC1000-3-2. That means, the requirements for the lower order harmonics are more difficult to meet. The most critical harmonics in this particular topology are the 5^{th} and the 7^{th}.

If the converter is operated with constant duty ratio, the magnitude of the 5^{th} harmonic will be larger than the 7^{th} and will clearly exceed the limit as shown in Fig. 4.18a. Conversely, if the constant current control method is applied, the magnitudes of the 5^{th} and 7^{th} harmonic are equal. In this case the 7^{th} harmonic exceeds the limit as shown in Fig. 4.18b.

However, if the linearly modulated duty ratio is applied, then the modulation depth δ can be varied from zero (i.e., constant duty ratio) to the optimal value of δ which yields almost identical magnitudes for the 5^{th} and 7^{th} harmonic (Figs. 4.14d through 4.14f). The harmonic content changes gradually from the constant duty ratio case to approximately the constant diode current controlled case (i.e., from Fig. 4.18a to Fig. 4.18c). Somewhere in between there is a range of values for δ that retains all the harmonics below the limit; even though it does not minimize the harmonic distortion. This situation is shown in Fig. 4.18d where the modulation depth was chosen to be 80% of the optimal value.

Therefore, these modulation schemes provide a means to play with the values of individual harmonics. If this is of importance in a practical example, then these methods might be applied.

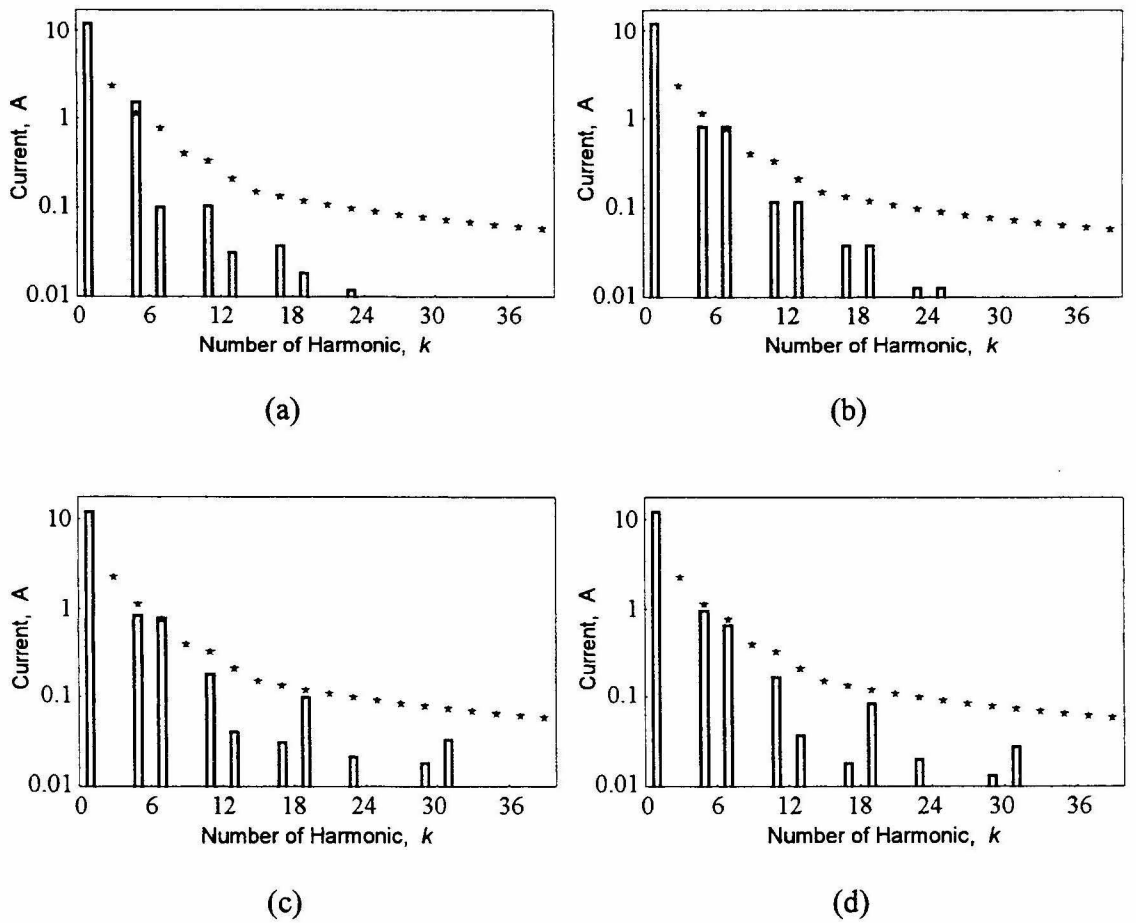

Figure 4.18: Input current spectrum for a $380V_{ac}$ /$800V_{dc}$ / 8kW rectifier: (a) Constant duty ratio, (b) constant diode current controlled, (c) linearly modulated duty ratio using the optimal δ and (d) linearly modulated using a modulation depth of 80% of the optimal value. The stars mark the limits according to IEC1000-3-2.

Another means to improve the current shape has been presented in [9,11]. The converter was operated at the boundary of DCM. The interval T_4 in Fig. 4.3 is omitted. This is achieved by turning on the active switch S as soon as all inductor currents (or the diode current i_d) reach the zero level. The consequence is a variable switching frequency.

This control scheme is not investigated in this thesis. It has been reported in [9,11] that this method does not provide a significant reduction of the *THD*, however, it shifts the distortion to harmonics at higher frequencies. This reduces the filtering effort. At low conversion ratios the total harmonic distortion appears to be even worse than with the constant duty ratio.

4.6 Summary of the Results and Practical Realization

In this section the most important results of the preceding analysis are summarized and the most significant formulas describing the performance of the converter are stated again. Table 4.1 contains key expressions for all the analyzed cases in terms of the processed power P, the line to neutral input voltage V_L and the conversion ratio M.

In order to evaluate the expressions in Table 4.1, the following equations are necessary:

$$M = \frac{V_o}{\sqrt{6} \cdot V_L} \tag{4.6.1}$$

$$R_e = \frac{2L}{T_s} \tag{4.6.2}$$

$$\alpha_1(\theta) = \frac{M \sin(\theta)}{M - \sqrt{3}\sin(\theta)} \tag{4.6.3}$$

$$\alpha_2(\theta) = \frac{M^2 \sin\left(\theta - \frac{2\pi}{3}\right) + M \sin(2\theta)}{\left(M - \sqrt{3}\sin(\theta)\right)\left(M - \cos(\theta)\right)} \tag{4.6.4}$$

	Constant D_1	Optimal D_1	Constant I_d	Modulated D_1
$D_1(\theta)$	$\sqrt{\frac{R_e P}{12 V_L^2 A_1}}$	$\sqrt{\frac{MPR_e}{4\sqrt{3} V_L^2 A_3^2} \cdot \frac{\alpha_d(\theta)}{\alpha_s(\theta)}}$	$\sqrt{\frac{R_e P}{2\sqrt{3} M V_L^2 \alpha_d(\theta)}}$	$\sqrt{\frac{R_e P}{12 V_L^2 A_5}(1+\delta f(\theta))}$
I_{rms}	$\frac{P}{6V_L} \cdot \frac{A_2}{A_1}$	$\frac{P}{6V_L} \cdot \frac{1}{A_3}$	$\frac{P}{3V_L} A_4$	$\frac{P}{6V_L} \cdot \frac{A_6}{A_5}$
I_1	$\frac{P}{3V_L}$	$\frac{P}{3V_L}$	$\frac{P}{3V_L}$	$\frac{P}{3V_L}$
PF	$2\frac{A_1}{A_2}$	$2A_3$	$\frac{1}{A_4}$	$2\frac{A_5}{A_6}$
THD	$\sqrt{\frac{A_2^2}{4A_1^2}-1}$	$\sqrt{\frac{1}{4A_3^2}-1}$	$\sqrt{A_4^2-1}$	$\sqrt{\frac{A_6^2}{4A_5^2}-1}$
$I_{k_{rel}}$ $k=odd$	$\frac{1}{\pi A_1}\int_0^{\pi/6}\beta_k(\theta)d\theta$	$\frac{\sqrt{3}M}{\pi A_3^2}\int_0^{\pi/6}\frac{\alpha_d(\theta)}{\alpha_s(\theta)}\beta_k(\theta)d\theta$	$\frac{2\sqrt{3}}{\pi M}\int_0^{\pi/6}\frac{\beta_k(\theta)}{\alpha_d(\theta)}d\theta$	$\frac{1}{\pi A_5}\int_0^{\pi/6}(1+\delta f(\theta))^2\beta_k(\theta)d\theta$
ΔD_1	0	$\sqrt{\frac{PR_e}{12MV_L^2A_3^2}}\left(\sqrt{M-\frac{\sqrt{3}}{2}}-\sqrt{M-1}\right)$	$\sqrt{\frac{PR_e}{3MV_L^2}}\left(\sqrt{M-\frac{\sqrt{3}}{2}}-\sqrt{M-1}\right)$	$\lvert\delta\rvert\cdot\sqrt{\frac{R_eP}{12V_L^2A_5}}$
ΔI_d	$\frac{M}{4A_1}\cdot\frac{2-\sqrt{3}}{(M-1)(2M-\sqrt{3})}$	$\frac{1}{4A_3^2}\left(1-2M^2\frac{\alpha_d^2(\theta_o)}{\alpha_s(\theta_o)}\right)$	0	No simple expression available

Table 4.1: Key expressions for the analyzed cases in terms of the power P, the line voltage V_L and conversion ratio M.

$$\alpha_3(\theta)=\frac{M^2\sin\left(\theta-\frac{4\pi}{3}\right)-\frac{1}{2}M\sin(2\theta)}{\left(M-\sqrt{3}\sin(\theta)\right)\left(M-\cos(\theta)\right)} \tag{4.6.5}$$

$$\alpha_d(\theta)=\frac{\sqrt{3}}{2}\cdot\frac{M+\sin(2\theta)\sin\left(\theta-\frac{2\pi}{3}\right)}{\left(M-\sqrt{3}\sin(\theta)\right)\left(M-\cos(\theta)\right)} \tag{4.6.6}$$

$$\alpha_s(\theta)=\alpha_1{}^2(\theta)+\alpha_2{}^2(\theta)+\alpha_3{}^2(\theta) \tag{4.6.7}$$

$$\beta_k(\theta)=\alpha_1(\theta)\sin(k\theta)+\alpha_2(\theta)\sin\left(k\theta-\frac{2\pi k}{3}\right)+\alpha_3(\theta)\sin\left(k\theta-\frac{4\pi k}{3}\right) \tag{4.6.8}$$

$$A_1=\frac{\sqrt{3}M}{\pi}\int_0^{\pi/6}\alpha_d(\theta)\,d\theta \tag{4.6.9}$$

$$A_2=\sqrt{\frac{1}{\pi}\int_0^{\pi/6}\alpha_s(\theta)\,d\theta} \tag{4.6.10}$$

$$A_3=\sqrt{\frac{3M^2}{\pi}\int_0^{\pi/6}\frac{\alpha_d{}^2(\theta)}{\alpha_s(\theta)}\,d\theta} \tag{4.6.11}$$

$$A_4=\sqrt{\frac{3}{\pi M^2}\int_0^{\pi/6}\frac{\alpha_s(\theta)}{\alpha_d{}^2(\theta)}\,d\theta} \tag{4.6.12}$$

$$A_5=\frac{\sqrt{3}M}{\pi}\int_0^{\pi/6}(1+\delta f(\theta))^2\alpha_d(\theta)\,d\theta \tag{4.6.13}$$

$$A_6=\sqrt{\frac{1}{\pi}\int_0^{\pi/6}(1+\delta f(\theta))^4\alpha_s(\theta)\,d\theta} \tag{4.6.14}$$

$$\sin\left(\theta_o+\frac{\pi}{6}\right)-3\sin\left(3\theta_o-\frac{\pi}{6}\right)+\frac{2}{M}\sin^2(2\theta_o)=0 \quad \text{AND} \quad 0<\theta_o<\frac{\pi}{6} \tag{4.6.15}$$

$$0 = K_o + \delta K_1 + \delta^2 K_2 + \delta^3 K_3 + \delta^4 K_4 \tag{4.6.16}$$

$$\begin{aligned} K_o &= P_o Q_1 - P_1 Q_o \\ K_1 &= P_o Q_2 + 2P_1 Q_1 - 3P_2 Q_o \\ K_2 &= 3(P_1 Q_2 - P_3 Q_o) \\ K_3 &= 3P_2 Q_2 - 2P_3 Q_1 - P_4 Q_o \\ K_4 &= P_3 Q_2 - P_4 Q_1 \end{aligned} \tag{4.6.17}$$

$$P_i = \int_0^{\pi/6} \alpha_s(\theta) f^i(\theta) d\theta \tag{4.6.18}$$

$$Q_i = \int_0^{\pi/6} \alpha_d(\theta) f^i(\theta) d\theta \tag{4.6.19}$$

This is all that is needed to evaluate the expressions in Table 4.1. Note that the equations (4.6.13) and higher are exclusively used for the arbitrarily modulated duty ratio case (i.e., for column four in Table 4.1). All formulas were expressed in the simplest possible form that was found. Nevertheless, after some algebra, alternative forms can be found for (4.6.7) through (4.6.12) and for I_{krel} in the first three columns of Table 4.1. These new formulas, which are stated in Appendix B, do not appear to be simpler, but the calculation speed is drastically reduced if they are used in numerical calculations instead of those stated above.

The current waveforms are given by

$$\bar{i}_1(\theta) = D_1^2 \frac{\sqrt{2}V_L}{R_e} \cdot \alpha_1(\theta) \tag{4.6.20}$$

$$\bar{i}_2(\theta) = D_1^2 \frac{\sqrt{2}V_L}{R_e} \cdot \alpha_2(\theta) \tag{4.6.21}$$

$$\bar{i}_3(\theta) = D_1^2 \frac{\sqrt{2}V_L}{R_e} \cdot \alpha_3(\theta) \tag{4.6.22}$$

$$\bar{i}_d(\theta) = D_1^2 \frac{\sqrt{2}V_L}{R_e} \cdot \alpha_d(\theta) \tag{4.6.23}$$

for the interval $0 \le \theta \le 30°$. The waveforms for the rest of the line cycle can be found using the permutation of subscripts and time reversal as explained in Section 4.1.

There are very few design constraints associated with this converter. To assure a proper operation, the following must be satisfied:

$$D_1(0) \le 1 - \frac{1}{M} \tag{4.6.24}$$

This equation implies that M must be greater than unity since the ratio must have a positive value. Assuming the power level P and the input voltage V_L are given and a value for M has been chosen, the only possibility to influence D_1 is by altering R_e. Equation (4.6.24) provides a tool to determine R_e and thus the inductance L and the switching frequency T_s. In order to reduce the current stress in all the elements of the converter, the left-hand side of (4.6.24) should only be marginally smaller than the right-hand side. For example,

$$D_1(0) = 0.9\left(1 - \frac{1}{M}\right) \tag{4.6.25}$$

Table 4.2 contains a comparison of the predicted values of the *THD* in % between the previously discussed cases. As previously mentioned, the constant diode current method approximates the optimal case very closely. This approach has the additional advantageous property that the output voltage ripple is eliminated. Therefore, this circuit can be used as a single-stage converter if a high output voltage is required. The constant diode current control only requires a fast feedback loop to achieve the reduction in the harmonic content and a good output regulation. The optimal duty ratio (i.e., case 2) is only marginally better and is so complicated to generate that an implementation in a real circuit is neither justified nor realistic. However, analysis is useful because it serves as a reference against which other methods can be compared.

Case	Duty ratio function	$M = 1.2$	$M = 1.5$	$M = 2.0$
1	Constant duty ratio	21.82	12.43	7.597
2	Optimal duty ratio	13.94	9.456	6.228
3	Constant diode current controlled	14.00	9.476	6.234
4	Linearly modulated duty ratio	14.43	9.580	6.266
5	Cosine modulated duty ratio	14.38	9.556	6.251
6	Rectified cosine modulated duty ratio	13.95	9.473	6.247
7	Modified cosine modulated duty ratio	13.98	9.471	6.244

Table 4.2: The Predicted THD for all cases and for 3 different conversion ratios.

The other approximations of the optimal duty ratio (i.e., cases 4 through 7) have the following disadvantages:

1) The desired function must be artificially generated or derived from somewhere.

2) The optimal modulation depth depends on the conversion ratio and the load current. For example, if the input voltage changes, the magnitude of the injected signal to the duty ratio must be adjusted. This requires constant monitoring of the conversion ratio and load current plus an additional circuitry, which provides the proper modulation depth.

3) The diode current and hence the output voltage still suffer from some low frequency ripple.

The most favorable solution, therefore, is case 3, i.e., the diode current control method. The following graph compares the improvement of the *THD* versus the conversion ratio M for the constant duty ratio case and the constant diode current control method. It is evident that the most significant reduction of the *THD* occurs at low conversion ratios where the distortion is large if a constant duty ratio is applied. In most cases a low

conversion ratio is desired in order to reduce the voltage stress on the switches and in the output capacitor. The primary reason for designing the converter with an increased M is to achieve a lower harmonic distortion.

The proposed control method provides an alternative method to obtain the same goal without adding voltage stress to the components. The horizontal distance between the two curves in Fig. 4.19a is approximately 0.22; therefore, if the constant diode current control method is applied, the conversion ratio can be reduced by a factor of 0.22 to achieve the same *THD* as with a constant duty ratio. This approximation is quite accurate over the whole range of interest (see Fig. 4.19b). The difference in M translates to a variance in output voltage of 60V with a 110V input (rms-value phase to neutral) and 120V with a 220V input. An additional advantage of this control scheme is the well-regulated output voltage.

Depending on the particular application, it might be enough to use a fast voltage feedback loop as suggested in [9] and shown in Fig. 4.20a to achieve the desired duty ratio modulation. This requires a time invariant load. The necessary bandwidth of the feedback loop must be much higher than six times the line frequency. An excellent load step responses can be achieved with this solution. Experimental results, however, indicate that the performance concerning the input currents is better if the diode current is controlled directly and the output voltage is used in an outer loop as shown in Fig. 4.20b. With this second control method, the residual output voltage ripple is also smaller.

Since the diode current is discontinuous, a simple high frequency current sense transformer can be used to realize the current measurement. The bandwidth of the inner loop must be much higher than six times the line frequency, whereas the outer loop requires a bandwidth clearly below six times the line frequency.

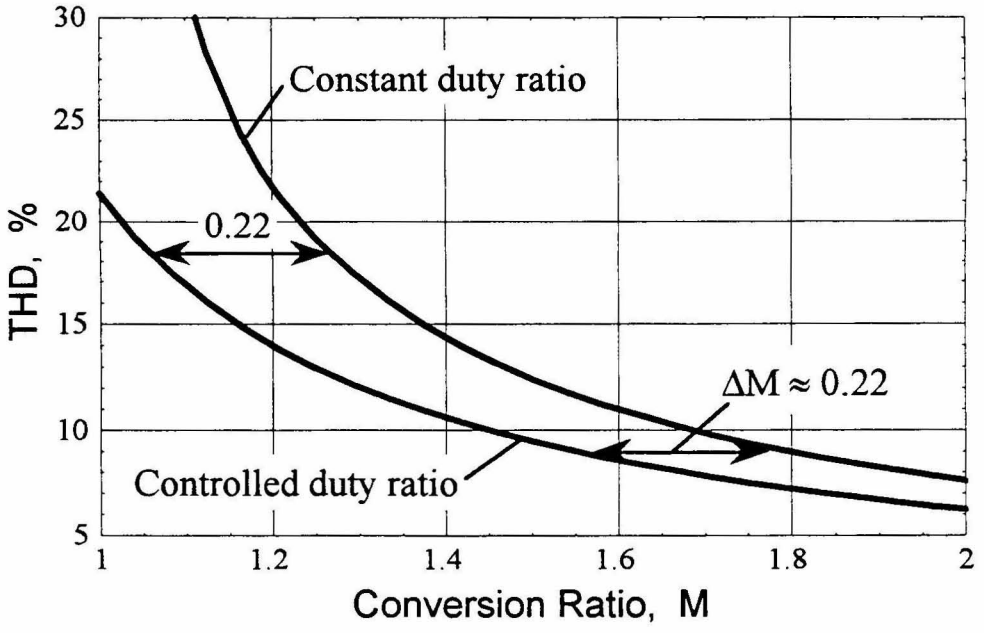

(a)

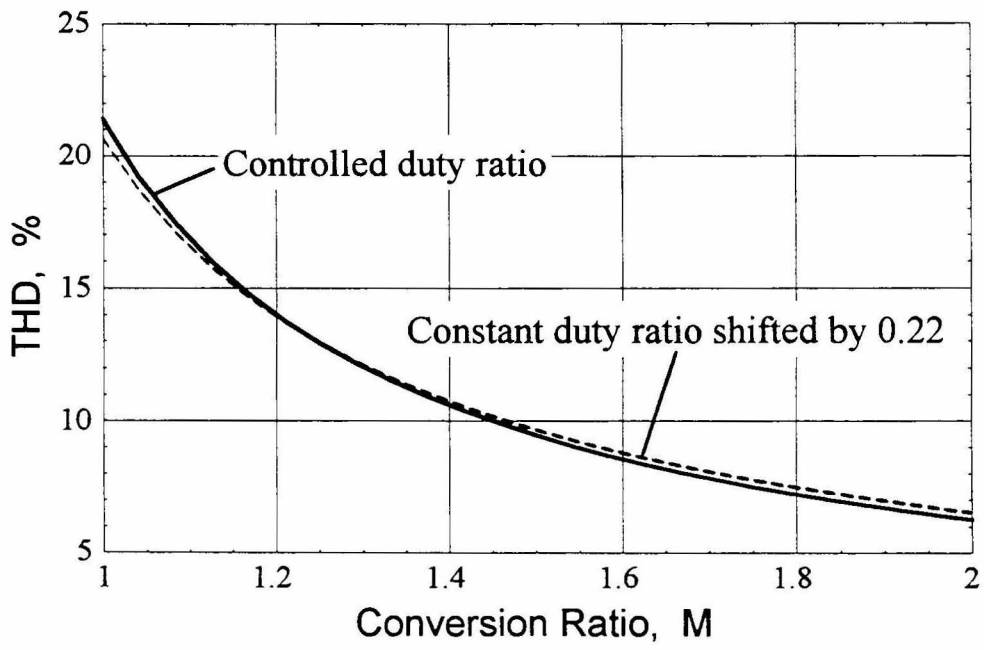

(b)

Figure 4.19: (a) Comparison of the predicted THD between the constant duty ratio case and the diode current control method. (b) The graph for the constant duty ratio case is shifted to the left by 0.22.

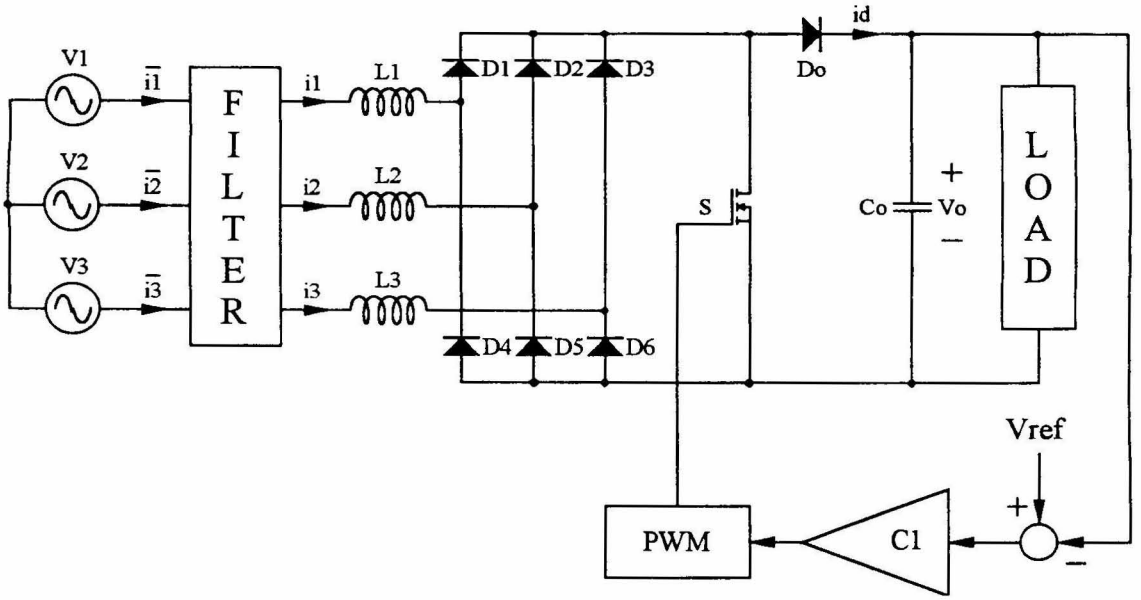

(a)

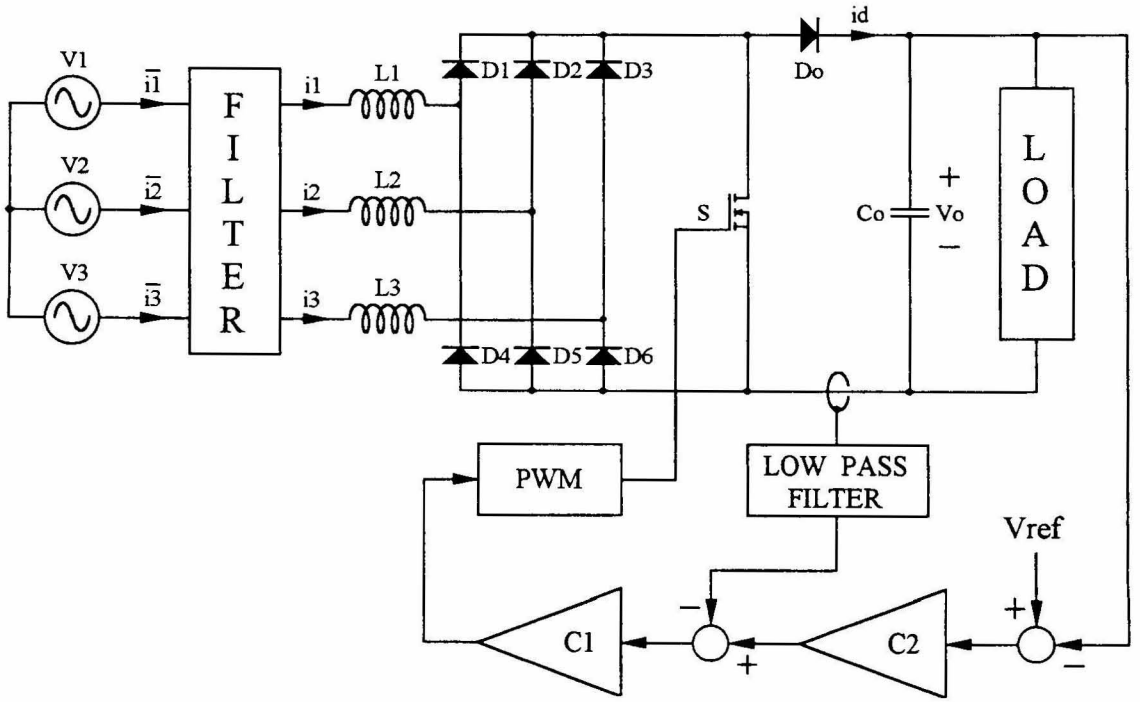

(b)

Figure 4.20: The two proposed control structures. (a) The single loop structure with a high bandwidth loop and (b) the two loop structure with a high bandwidth current loop and a low bandwidth voltage loop.

4.7 Experimental Results

The validity of the analysis of this converter was tested on an experimental circuit with the following element values: L_1=L_2=L_3=310μH, C_o=40μF and a resistive load of 500Ω (Fig. 4.1). Throughout the analysis the input voltage was assumed to be an ideal three-phase system. However, the real utility line voltage contains some distortion in the voltage waveform. In order to be able to compare the measurement with the prediction the experimental circuit was connected to a power supply with nearly ideal voltage waveforms. The input voltage was 80V phase to neutral and the output voltage was 280V, which corresponds to a conversion ratio of 1.43. The control method shown in Fig. 4.20b was applied. In addition, an input filter was designed as shown in Fig. 4.21, where L_{f1}=3.5mH, L_{f2}=1.2mH, C_{f1}=0.1μF, C_{f2}=0.5μF and R_d=47Ω.

The constant duty ratio case is considered first. The measured input current together with the ac-component of the output voltage is shown in Fig. 4.22a whereas the magnitudes of the current spectrum are depicted in Fig. 4.22b. The measurement is slightly better than the prediction. This can be explained by the presence of the input filter, which also takes part in reducing the harmonic content. This effect is not

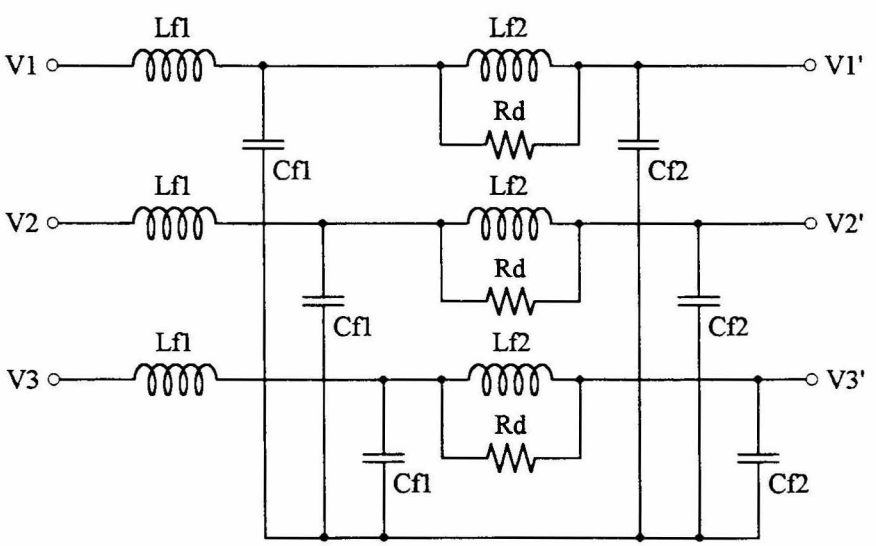

Figure 4.21: Three-phase input filter.

accounted for in the analysis. The measured waveforms in Fig. 4.22 can be compared with the prediction as shown in Fig. 4.4b and 4.4e. (Note that the conversion ratio is slightly different.)

The same information for the controlled diode current case is shown in Fig. 4.23a and Fig. 4.23b respectively. It is evident that the harmonic distortion dropped and the output voltage ripple almost disappeared. It is shown that the harmonics appear in pairs of equal magnitude as predicted. This waveforms compare very well with the prediction as shown in Fig. 4.10b and 4.10c.

In the real world, however, the circuit will be connected to the non-ideal line voltage. It is important to observe how the circuit behaves in this more realistic situation. The input voltage was chosen to be 100V phase to neutral and the output was 350V, which leads to the same conversion ratio as in the previous case. At the time the measurement was taken, the harmonic distortion of the line voltage was measured to be 4.5%. The resulting waveforms and spectrum are shown in Fig. 4.24a and Fig. 4.24b respectively, whereas the same plots for the constant diode current control method are shown in Fig. 4.25.

It is evident that the line current waveform does not agree as well with the prediction as in the previous case, even though the general shape appears still fairly close. The measured *THD* for the constant duty ratio case is significantly worse than the prediction (i.e., 20.4% versus 13.7%). (Note that the prediction is still based on ideal voltage waveforms.) In the controlled case the measurement and prediction are much closer together, i.e., 12.4% versus 10.2%. Consequently, if the constant diode current control method is applied, the actual reduction of the *THD* is 8% and not only 3.5% as suggested by the prediction.

The exact values depend on the nature of the distortion and its severity. A voltage *THD* of 4.5%, however, is quite typical in a 110V system. The main reason for the distortion is the "peak detector" type of power inputs as discussed in Chapter 3.1.2, which causes the voltage waveform to appear trapezoidal rather than sinusoidal. As a

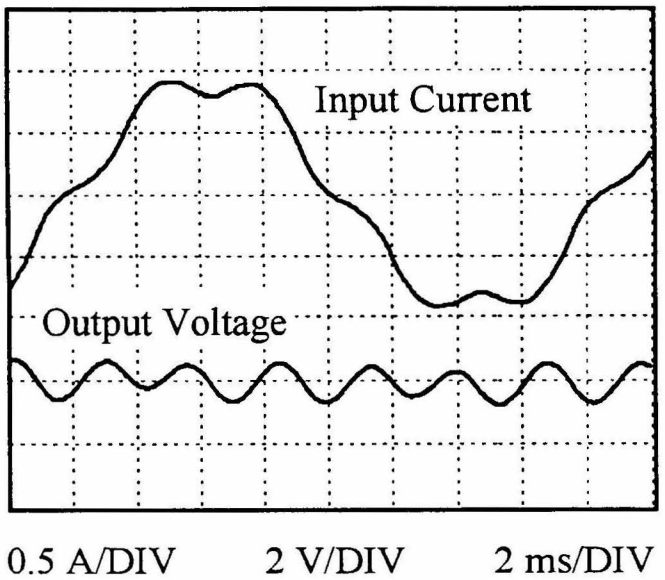

(a)

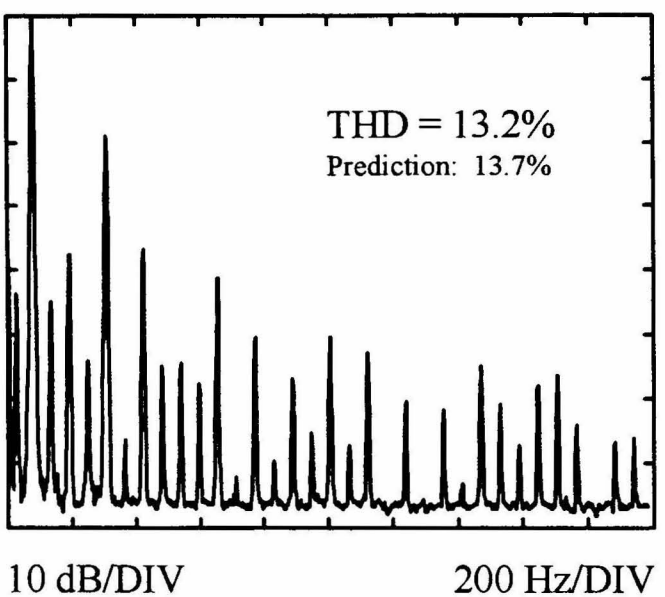

(b)

Figure 4.22: Ideal input voltage source, constant duty ratio: (a) Measured input current shape together with the ac-component of the output voltage and (b) measured spectrum and THD of the input current.

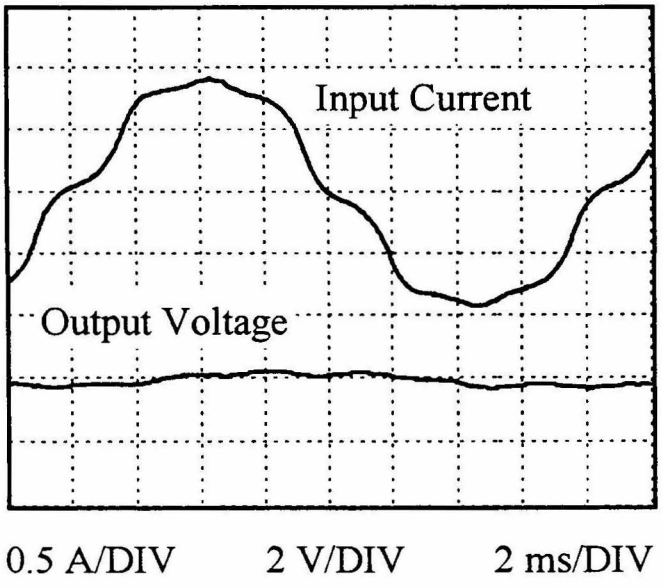

(a)

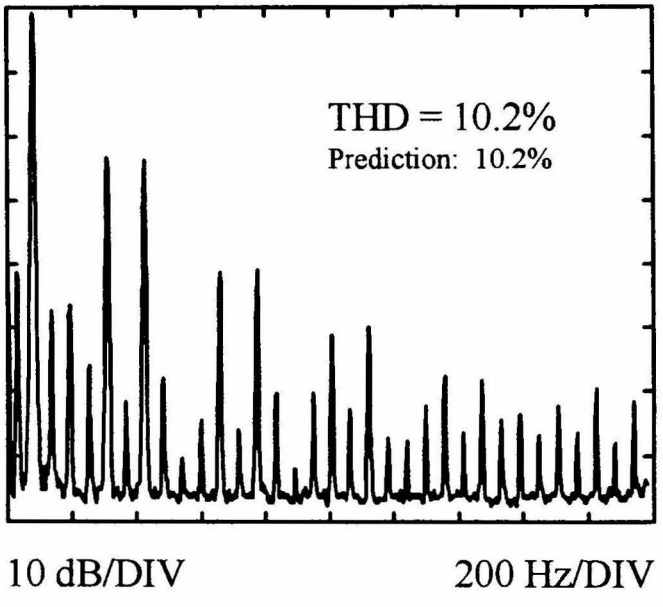

(b)

Figure 4.23: Ideal input voltage source, constant diode current controlled: (a) Measured input current shape together with the ac-component of the output voltage and (b) measured spectrum and THD of the input current.

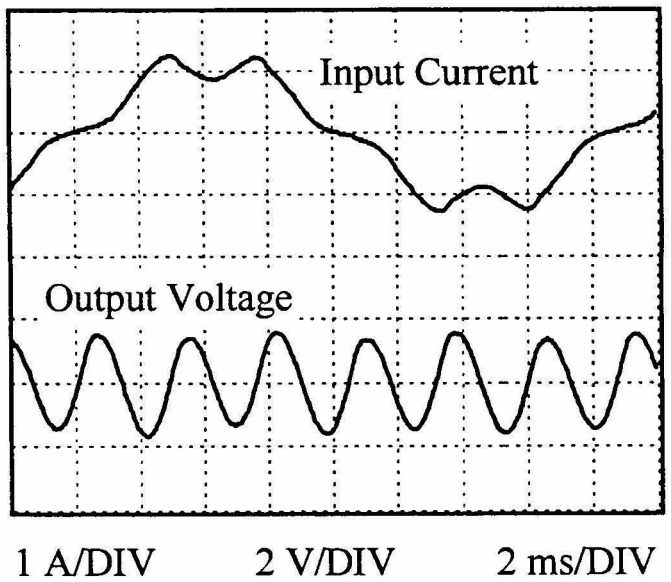

(a)

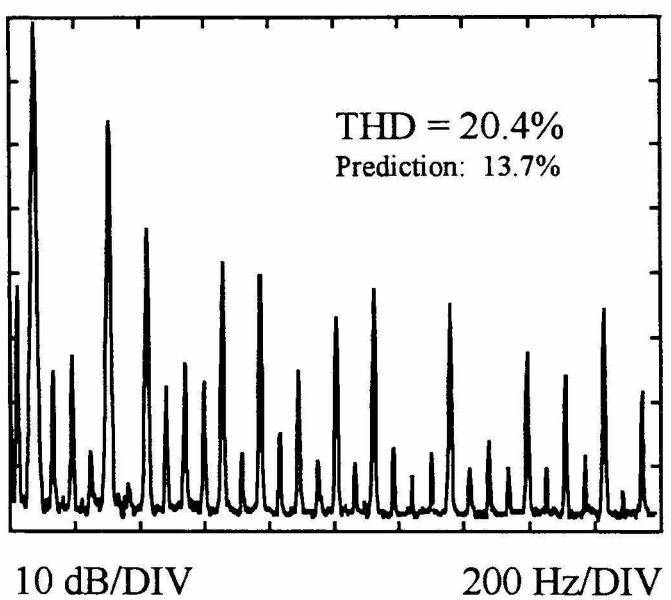

(b)

Figure 4.24: Working off the utility line with 4.5% voltage THD, constant duty ratio: (a) Measured input current shape together with the ac-component of the output voltage and (b) measured spectrum and THD of the input current.

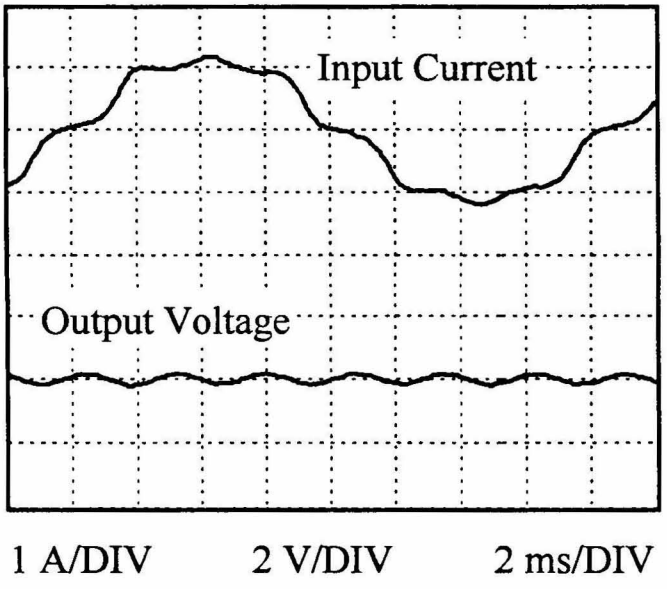

(a)

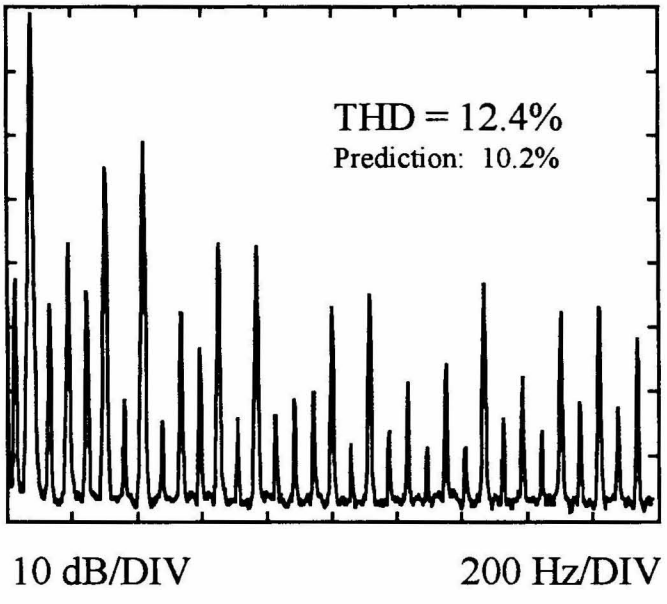

(b)

Figure 4.25: Working off the utility line with 4.5% voltage THD, constant diode current controlled: (a) Measured input current shape together with the ac-component of the output voltage and (b) measured spectrum and THD of the input current.

result of this uniform distortion mechanism the nature of the distortion can be expected to remain the same. This allows generalizing the results stated in the previous paragraph.

4.8 Final Remarks

In this chapter the non-isolated single active switch three-phase power factor corrector was investigated. In a first step the previously known constant duty ratio operation was analyzed. The achieved results motivated the search for the optimal duty ratio. Results were derived for a duty ratio modulation, which optimizes the input current waveforms in the time domain in a least square sense. Unfortunately, this duty ratio is not practical to realize, since it is described by a rather complicated expression. It depends on each of the instantaneous input voltages and the conversion ratio.

Nevertheless, the current shape can be analytically evaluated for the optimal duty ratio. By doing so, it can be observed that the current in the boost diode becomes almost constant with the optimal duty ratio. This offers an interesting chance to achieve a nearly optimal duty ratio by controlling this current so that it becomes entirely constant. It has been shown that this control strategy provides results that are indeed very close to the optimal case. In addition, it also provides simultaneously a well-regulated output voltage. This is a very desirable feature. Applying a simple control loop improves the input current distortion as well as the output voltage regulation.

On a final note, the way the analysis chronologically was performed was the following: The constant duty ratio case was investigated first. Then the optimum duty ratio was defined and analyzed. Since it turned out to be unpractical to realize, the next best option was using an approximation. Based on the actual shape of the optimal duty ratio the linear, the cosine and the cosine half wave approximations were analyzed.

In a real circuit these functions must be generated somehow. In the light of that the cosine approximation appeared to be the most promising choice. Since the diode current carried a nearly cosine shaped ripple, the idea occurred to derive the duty ratio modulation from this current. In the process of exploring that option, it so happens that

this does not work because as soon as the duty ratio was modulated using this ripple current, it almost vanished. Yet, what at first appeared to be a dead end led to the discovery of the simple diode current control method, which approximates the optimum duty ratio very closely and additionally provides a full output regulation.

Some of the results reported in this chapter have meanwhile been published by other sources is a similar way. To the best of the author's knowledge, such a complete analysis allowing an easy comparison between different cases and providing simple expression for all quantities of interest for all these cases has not yet been published.

Chapter 5

Isolated Extension of the Three-Phase Power Factor Corrector

The converter presented and analyzed in the preceding chapter has interesting properties concerning the input current distortion and the output voltage regulation. However, there are two major drawbacks: Firstly, the converter requires a high output voltage, which must be larger than the peak line to line voltage. Secondly, this topology does not provide galvanic isolation. In this chapter, two isolated extensions are presented and analyzed. Any desired output voltage can now be achieved by designing a transformer with the appropriate turns ratio.

The proposed converters are depicted in Fig. 5.1a and 5.1b respectively. Several authors [4-6, 9] have mentioned these circuits before, providing only little analysis, or none at all. In all the cases except in [9], the duty ratio was always assumed to be constant. One goal of this chapter is to investigate if the overall performance of these converters can be improved using similar control schemes as in the non-isolated case. In [9] it has been claimed that by simply applying a fast feedback loop to the isolated converter the same improvements are achieved as in the non-isolated case. It will be shown that the situation in the isolated converter is more complex. The results from the previous chapter do not generally apply in the isolated case.

The combination of power factor correction and isolation in one stage is most useful if, in addition, the output voltage is well-regulated. If operated with constant duty ratio, the circuits in Fig. 5.1 suffer from an output voltage ripple at six times the line frequency. Therefore, in most cases, they do not qualify as single-stage solutions. In this chapter the output ripple problem is analyzed, and a solution is presented.

5.1 The Topologies

The converters under consideration are the Cuk-derived and the Sepic-derived topologies shown in Fig. 5.1a and Fig. 5.1b respectively. The analysis is based on the assumptions listed below:

1) The input side is equivalent to the non-isolated case. That means that the inductors L_1, L_2 and L_3 operate in DCIM.

2) The capacitors C_1, C_2 and C_o are sufficiently large to ensure that any line frequency related voltage ripple can be neglected for the evaluation of the input current waveform.

3) All the assumptions stated in Chapter 4.1 still apply.

With these assumptions the input current waveforms are equivalent to those found in Chapter 4 given that the duty ratio function is the same. This can easily be explained as follows: during the ON time of switch S, the three input inductors are shorted on their right-hand side, exactly as in the non-isolated version. During the OFF time of S the energy stored in the three inductors is released into a constant voltage source, exactly as before. This means that the equivalent circuits for each subinterval remain the same. As far as the input of the converter is concerned, nothing has changed.

In particular, if the duty ratio is constant, the formulas found in Chapter 4.2 still apply. Nevertheless, one word of caution is necessary. The conversion ratio M, which is defined as the ratio of the output voltage to the peak value of the input voltage measured from phase to phase, is now different. M is no longer restricted to values greater than unity. Every M in the formulas in Chapter 4 must be substituted by a new quantity M_1, which is defined as follows:

$$M_1 = \frac{V_{s_{off}}}{\sqrt{6}V_L} \tag{5.1.1}$$

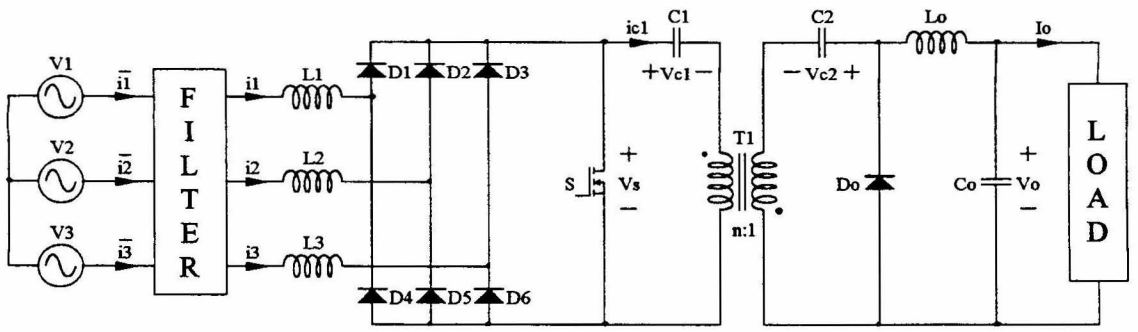

(a)

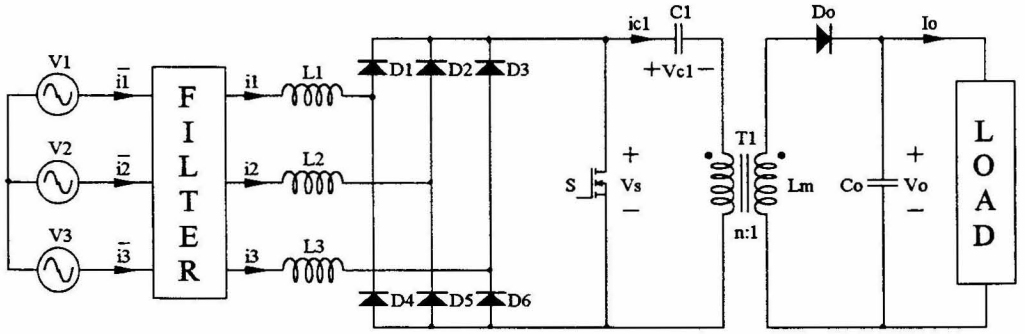

(b)

Figure 5.1: Isolated extensions of the single active switch three-phase power factor corrector: (a) Cuk-derived converter and (b) Sepic-derived converter.

where Vs_{off} is the voltage across switch S in its off-state. The same restrictions apply for M_1 as for M in Chapter 4.

The following question arises: Is there an equivalent control method as in the non-isolated case; does a fast output voltage feedback loop simultaneously solve the output ripple problem and improve the input current waveform? Since the converters in Fig. 5.1 possess additional reactive elements, a fast voltage feedback loop unfortunately does not have the same effect on the input current distortion. For the same reason, a fast control of the currents in L_o in Fig. 5.1a or in D_o in Fig. 5.1b does not solve the problem either. In order to achieve an improvement of the input current waveform, the output voltage V_o or the diode current $\bar{i}_d$ was controlled in the non-isolated case (Fig. 4.20). The equivalent quantities must be identified in the isolated converters.

In the non-isolated converter, V_o is the off-voltage of the active switch. The equivalent voltage in the converters of Fig. 5.1 is Vs_{off}, as defined above. In the converter of Fig. 5.1a Vs_{off} is the sum of V_{c1} and V_{c2} reflected to the primary of the transformer. In the converter of Fig. 5.1b Vs_{off} is given by the sum of V_{c1} and V_o reflected to the primary of the transformer. Nevertheless, keeping these voltages constant does not yield the desired result because the currents in the capacitors C_1 and C_2 contain also the output inductor current during the OFF time of the active switch. Thus, the current and voltage relation is not the same as in the non-isolated case.

However, a method exists which achieves the same effect on the input currents as in the diode current controlled case (Chapter 4.4). The proposed method for the non-isolated converter is to keep the diode current $\bar{i}_d$ constant as shown in Fig. 4.20b. This current is not directly available in the circuits of Fig. 5.1 because the diode D_o has been replaced with the capacitor C_1. The current $\bar{i}_{c1}$ in this branch is bi-directional whereas $\bar{i}_d$ is unidirectional due to the presence of D_o. The part of $\bar{i}_{c1}$ flowing into C_1 during the OFF time of switch S is equivalent to $\bar{i}_d$ of the non-isolated version of the converter. The fraction of the current discharging C_1 during the ON time was not present before. Fig. 5.2 illustrates the relation between $\bar{i}_{c1}$ and $\bar{i}_d$. This is not

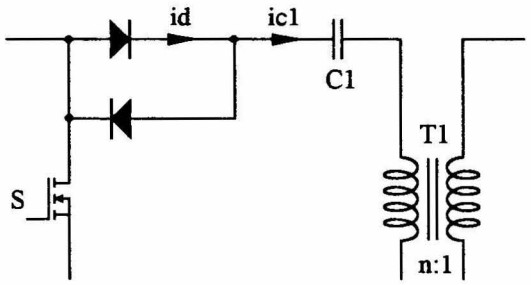

Figure 5.2: Identification of $\bar{i}_d$ in the isolated versions of the converters.

necessarily a suggestion for the practical implementation of the measurement of $\bar{i}_d$. There are more efficient ways to accomplish this task.

Controlling $\bar{i}_d$ in Fig. 5.2 so that it stays constant results in the same improvement of the input current waveform as in the non-isolated converter. Unfortunately, unlike in the non-isolated case, this control method does not suppress the output voltage ripple. On the contrary, the ripple can be much worse. This effect is studied in the next two sections.

5.2 The Cuk-Derived Topology

5.2.1 Steady State Analysis

The most relevant steady state equations of this converter shown in Fig. 5.1a are derived first. As opposed to the input inductors, the output inductor L_o operates in continuous conduction mode. The voltage across D_o during the ON time of the active switch must be V_{soff} reflected to the secondary of the transformer. (V_{soff} is the voltage across the main switch during its OFF time.) Volt-second balance applied to L_o yields

$$D_1\left(\frac{V_{soff}}{n} - V_o\right) = (1 - D_1)V_o \tag{5.2.1}$$

Thus,

$$V_{s_{off}} = \frac{n}{D_1} V_o \tag{5.2.2}$$

V_{soff} can also be described by

$$V_{s_{off}} = V_{c1} + nV_{c2} \tag{5.2.3}$$

The loop formed by L_o, C_o, C_2 and the secondary of T_1 contains only capacitors and inductors. The average voltage across an inductor must be zero. Thus, for steady state considerations, the inductors can be considered as short circuits. Consequently, the values for V_{c2} and V_o must be equal.

$$V_{c2} = V_o \tag{5.2.4}$$

V_{c1} can be found by substituting (5.2.2) and (5.2.4) into (5.2.3)

$$V_{c1} = nV_o\left(\frac{1}{D_1} - 1\right) \tag{5.2.5}$$

The output current is given by

$$I_o = \frac{P}{V_o} \tag{5.2.6}$$

These equations are sufficient to perform a first order design. The design algorithm is briefly out lined assuming that the power level P, the input voltage V_L and the output voltage V_o are given. Initially, a value for M_1 must be chosen based on the desired *THD* of the input current. The relation between *THD* and M_1 is discussed in detail in Chapter 4. (There, M was used instead of M_1.) The resulting duty ratio D_1 can be found in Table 4.1. The voltage V_{soff} can be determined according to (5.1.1). Equation (5.2.2) can now be used to find the required turns ratio n. The voltages V_{c1} and V_{c2} are found using (5.2.4) and (5.2.5). The input inductors must be designed in the same fashion as in the non-isolated case. The values for C_1, C_2, C_o and L_o must be designed so that the switching ripple voltage or current is sufficiently low. No formulas are stated at this point, because their values also strongly influence the output voltage ripple at six times

the line frequency. Knowing the relation between that ripple and the circuit element values is very important in order to accomplish a good design. This subject is investigated below.

5.2.2 Output Voltage Ripple

In order to understand and predict the behavior of the output of this converter, a series of circuit transformations were performed. The original circuit without the input filter is shown in Fig. 5.3a. As a first step, the transformer is eliminated. This is achieved by reflecting the secondary side to the primary as shown in Fig. 5.3b. The capacitor C_1 and the reflected capacitor C_2 can be represented by an equivalent capacitor C_e', which is given by

$$C_e' = \frac{C_1 C_2}{n^2 C_1 + C_2} \tag{5.2.7}$$

Figure 5.3c shows the non-inverting version of the same circuit, which is realized by adding two extra switches. Apart from the polarity, the circuit is equivalent to the previous one. The diode current i_d, which was not directly accessible in the original circuit, reappears. The nature of this current is very well known from the analysis of the non-isolated version in Chapter 4. Therefore, the whole input part of the converter can just be replaced by a current source that represents i_d. In addition, circuit averaging is applied as introduced in [12]. The switch pair S_2 and D_2 can be replaced by dependent sources, carrying the average currents and voltages of the switches. This step is shown in Fig. 5.4a.

At this point, a perturbation of the voltages, currents and the duty ratio is introduced. All these quantities are now represented by a dc-part plus a small signal ac-part. The dc-part is denoted by capital letters and the perturbation is denoted by lower case letters with a hat (e.g., $U + \hat{u}$). This step is shown in Fig. 5.4b. After neglecting all second order terms (i.e., terms that include $\hat{d}_1 \hat{i}_o$ and $\hat{d}_1 \hat{v}_e$), the dependent sources can be separated as shown in Fig. 5.4c. Lower case letters now denote the sum of the dc and

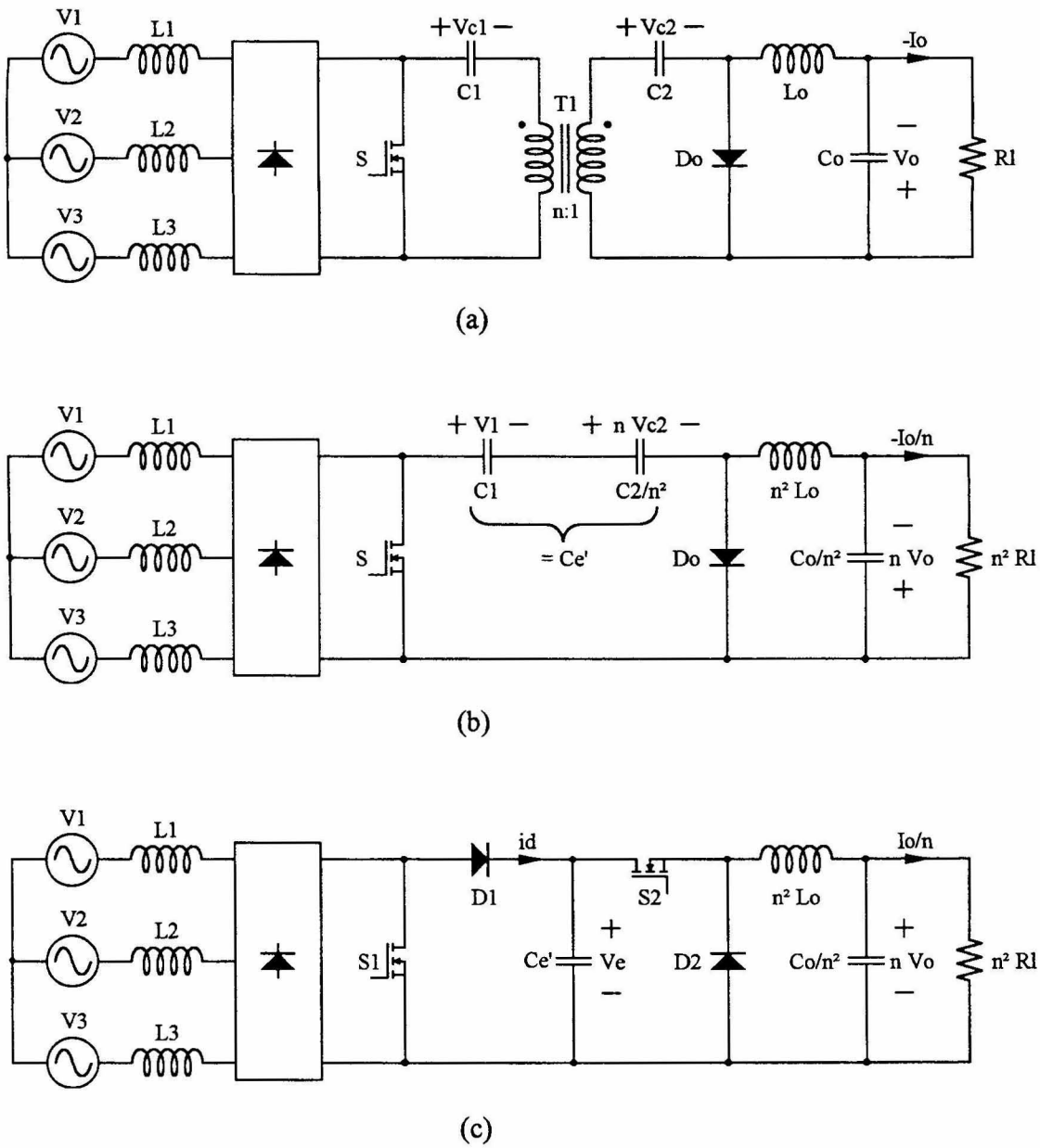

Figure 5.3: Circuit transformations on the Cuk-derived converter: (a) The original circuit, (b) the secondary side of the transformer is reflected to the primary and (c) modification to the non-inverting but otherwise equivalent topology.

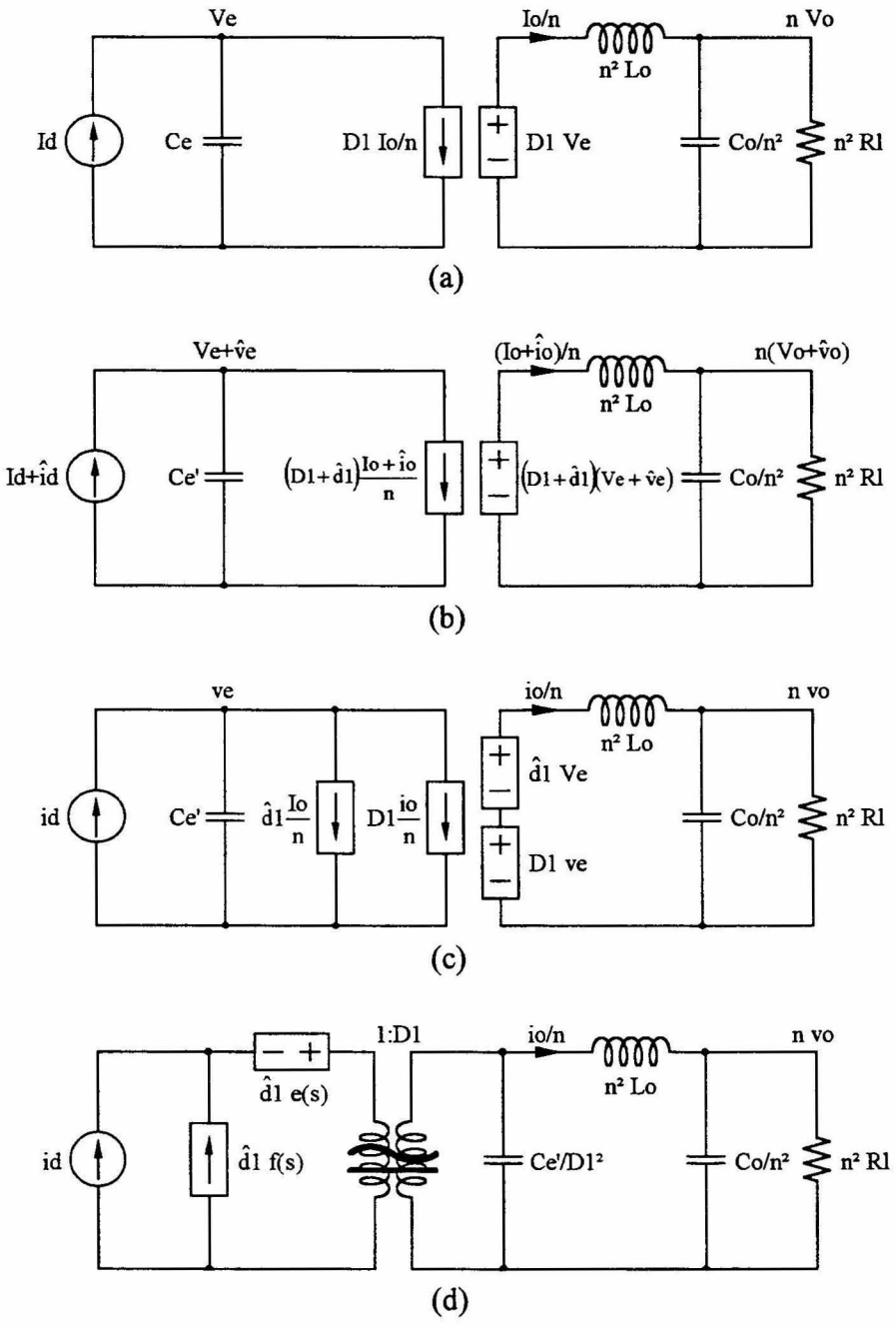

Figure 5.4: The input part is replaced by equivalent current source: (a) The switch pair S_2 and D_2 is replaced by dependent sources, (b) small signal perturbation is applied, (c) divided into dc and small signal sources, neglecting second order terms and (d) dc sources are replaced with ideal transformer and dependent sources are moved to the left.

ac signal (e.g., $u = U + \hat{u}$). The two dependent sources, which depend on D_1, can be replaced by an ideal transformer. In addition, the other dependent sources are moved to the primary side and all circuit elements are moved to the secondary side of this transformer. This leads to the circuit shown in Fig. 5.4d, where

$$e(s) = \frac{nV_o}{D_1^2} \tag{5.2.8}$$

$$f(s) = V_o\left(\frac{n}{D_1^2} sC_e' - \frac{1}{nR_l}\right) \tag{5.2.9}$$

The circuit is now represented by the canonical model according to [13]. In order to find the output voltage, the dependent voltage source $\hat{d}_1 e(s)$ is of no consequence since it is in series with current sources. It can be replaced by a short circuit. Furthermore, V_e is the same as V_{soff}, which is given in (5.2.2). This can be used to further simplify the circuit.

For the purposes of the present analysis, it is more useful to reflect the primary side of the ideal transformer to the secondary. Furthermore, the whole circuit can be reflected through a virtual n:1 transformer. This, plus a conversion of the current sources to voltage sources, lead to the final circuit shown in Fig. 5.5, where

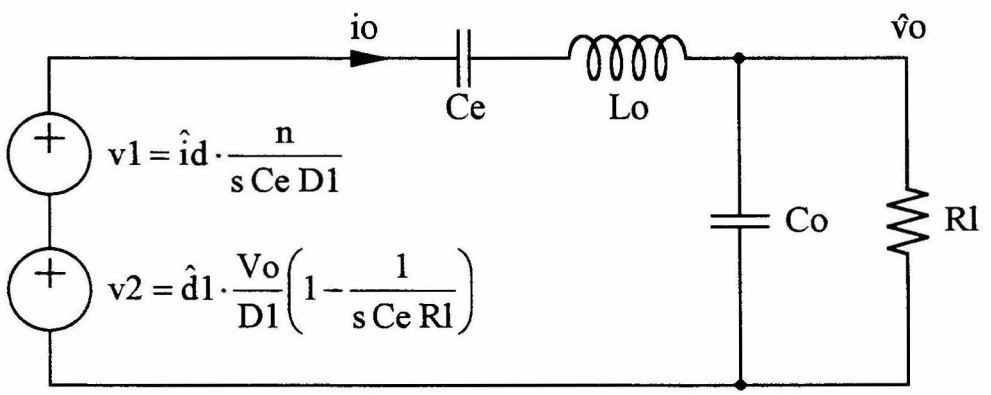

Figure 5.5: Equivalent small signal model: v_1 depends on the ripple of the diode current i_d and v_2 depends on the duty ratio modulation.

$$C_e = \frac{n^2}{D_1^2} C_e' = \frac{n^2}{D_1^2} \cdot \frac{C_1 C_2}{n^2 C_1 + C_2} \tag{5.2.10}$$

This circuit has the following two input sources:

$$v_1 = \hat{i}_d \cdot \frac{n}{sC_e D_1} \tag{5.2.11}$$

$$v_2 = \hat{d}_1 \frac{V_o}{D_1} \left(1 - \frac{1}{sC_e R_l} \right) \tag{5.2.12}$$

The first source, v_1, depends on the ripple of diode current i_d. Since this ripple was analyzed in Chapter 4, it is well-known. The second source, v_2, depends on the duty ratio modulation. Also the modulation depth was analyzed for different control schemes in Chapter 4.

The only cases of interest in this chapter are the constant duty ratio case and the constant diode current control method. If the duty ratio is constant, then v_2 is zero. The only contribution to the output voltage ripple is due to v_1, and consequently, due to the diode current ripple $\hat{i}_d$. Based on the graphs in Fig. 4.4a through Fig. 4.4c this ripple can be assumed to be sinusoidal at six times the line frequency. In order to find the output voltage ripple for the constant duty ratio case, the transfer function from $\hat{i}_d$ to $\hat{v}_o$ must be found.

If the constant diode current control method is applied, then v_1 is zero because this control method eliminates $\hat{i}_d$. As the duty ratio is no longer constant, the output voltage ripple is caused by v_2 in this second case. It is again reasonable to assume that the duty ratio is modulated with a sinusoidal function (Fig. 4.11c). The transfer function from $\hat{d}_1$ to $\hat{v}_o$ must be known in order to calculate the output voltage ripple. Using Fig. 5.5, the two required transfer functions are found to be

$$\frac{\hat{v}_o}{\hat{i}_d} = \frac{R_l \frac{n}{D_1}}{1 + sR_l(C_e + C_o) + s^2 L_o C_e + s^3 R_l L_o C_e C_o} \tag{5.2.13}$$

$$\frac{\hat{v}_o}{\hat{d}_1} = \frac{-\frac{V_o}{D_1}(1 - sR_l C_e)}{1 + sR_l(C_e + C_o) + s^2 L_o C_e + s^3 R_l L_o C_e C_o} \tag{5.2.14}$$

If the following inequality holds (which is very likely),

$$R_l^2 >> \frac{L_o C_e^2}{(C_e + C_o)^3} \tag{5.2.15}$$

then (5.2.13) and (5.2.14) can be approximated as follows:

$$\frac{\hat{v}_o}{\hat{i}_d} = R_l \frac{n}{D_1} \cdot \frac{1}{\left(1 + \frac{s}{\omega_1}\right)\left(1 + \frac{1}{Q} \cdot \frac{s}{\omega_o} + \left(\frac{s}{\omega_o}\right)^2\right)} \tag{5.2.16}$$

$$\frac{\hat{v}_o}{\hat{d}_1} = \frac{-V_o}{D_1} \cdot \frac{1 - \frac{s}{\omega_z}}{\left(1 + \frac{s}{\omega_1}\right)\left(1 + \frac{1}{Q} \cdot \frac{s}{\omega_o} + \left(\frac{s}{\omega_o}\right)^2\right)} \tag{5.2.17}$$

where

$$\omega_1 = \frac{1}{R_l(C_e + C_o)} \tag{5.2.18}$$

$$\omega_o = \frac{1}{\sqrt{L_o C_x}} \tag{5.2.19}$$

$$Q = \omega_o R_l \frac{C_o^2}{C_x} \tag{5.2.20}$$

$$\omega_z = \frac{1}{R_l C_e} \tag{5.2.21}$$

$$C_x = \frac{C_e C_o}{C_e + C_o} \tag{5.2.22}$$

D_1 in the above formulas must be a constant. This is naturally given in the constant duty ratio case. In the constant diode current controlled case, the average value of the duty ratio function should be used. From the discussion in Chapter 4.4 it can be concluded that the average value can be approximated by the value of D_1 at 15°. Thus, in this case, $D_1(\pi/12)$ should be used.

The value of the transfer function at six times the line frequency is of particular interest. Whether the circuit operates with constant duty ratio or with the constant diode current control method, the circuit is exposed to an excitation at this frequency. In order to find the peak to peak voltage ripple at the output of the converter, the expressions for the peak to peak value of the diode current ripple ΔI_d and the modulation depth ΔD_1 can be used. These expressions were derived in Chapter 4 and stated in Table 4.1. Since the current ΔI_d is a normalized quantity, it must be multiplied by its average value, which is given by

$$\bar{I}_d = \frac{P}{V_{s_{off}}} = \frac{D_1}{n} \cdot \frac{P}{V_o} = \frac{P}{\sqrt{6} M_1 V_L} \tag{5.2.23}$$

This leads to

$$\hat{i}_d = \Delta I_d \frac{P}{\sqrt{6} M_1 V_L} = \frac{P}{4\sqrt{6} V_L A_1} \cdot \frac{2-\sqrt{3}}{(M_1 - 1)(2M_1 - \sqrt{3})} \tag{5.2.24}$$

$$\hat{d}_1 = \Delta D_1 = \sqrt{\frac{PR_e}{3 M_1 {V_L}^2}} \left(\sqrt{M_1 - \frac{\sqrt{3}}{2}} - \sqrt{M_1 - 1} \right) \tag{5.2.25}$$

The peak to peak value of the output voltage ripple is plotted in Fig. 5.6 for the constant duty ratio case and for the controlled diode current case. In order to understand the behavior of the circuit, it was assumed that $\hat{i}_d$ and $\hat{d}_1$ sweep with constant magnitude through the displayed frequency range. In the practical circuit only the value at 360Hz

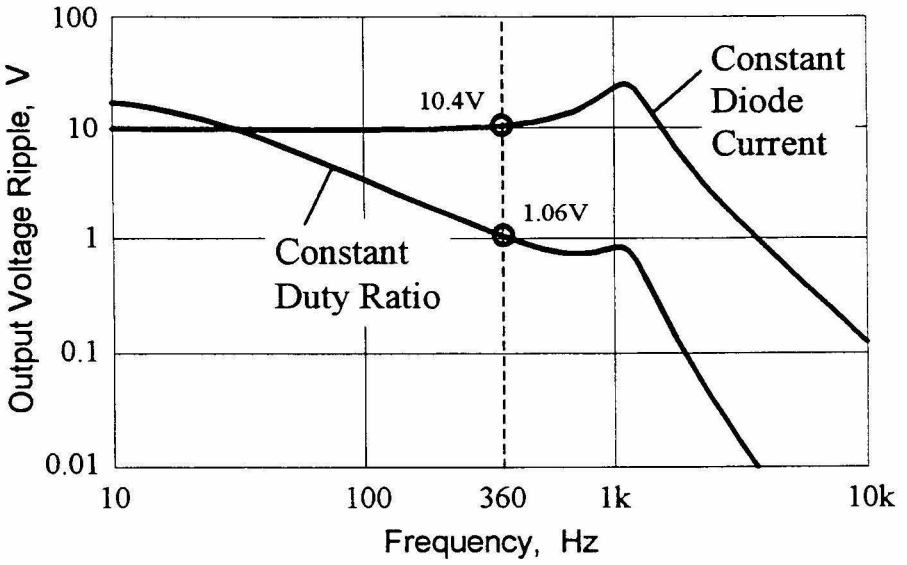

(a)

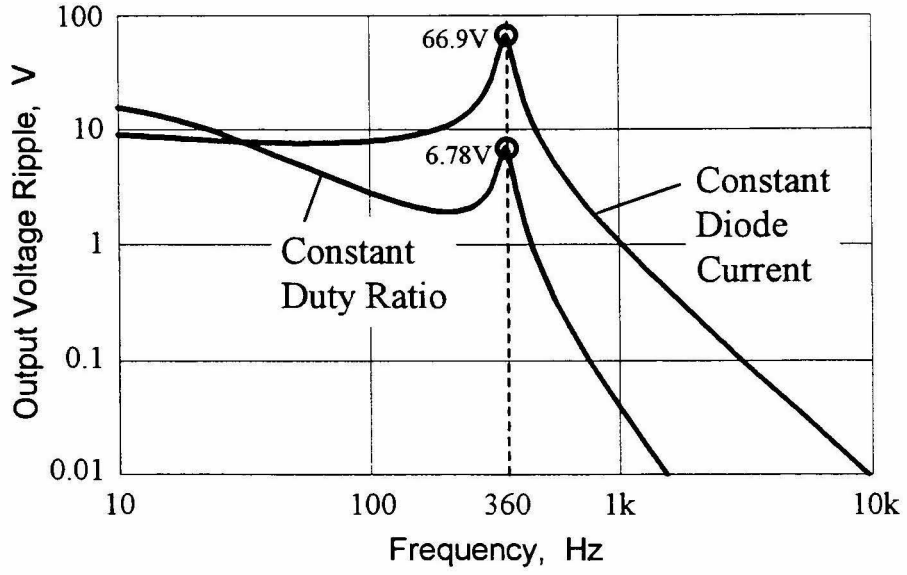

(b)

Figure 5.6: Cuk-derived converter: Transfer functions corresponding to the circuit in Fig. 5.5 with different values for the capacitor C_o and the inductor L_o: (a) C_o and L_o are small and (b) C_o and L_o are large.

(i.e., six times the line frequency) is of interest. This frequency is marked with a dotted vertical line.

The curves in Fig. 5.6a are based on a 200W converter with an input voltage $90V_{RMS}$ (line to neutral) and an output voltage $75V_{DC}$. In addition, M_1 is assumed to be 1.5. The component values are the following: $L_1=L_2=L_3=320\mu H$, $C_1=C_2=40\mu F$, $C_o=10\mu F$, $L_o=2mH$ and n=1.25 and the switching frequency is assumed to be 50kHz (these are the element values of the real circuit that was used to obtain the experimental data).

It is evident that the diode current controlled case is much more problematic than the constant duty ratio case. The predicted ripple of the output voltage is about 10 times higher than in the first case. (The exactly calculated values are 10.4V versus 1.06V.) There is a temptation to decrease the bandwidth of the output filter to reduce the ripple. Figure 5.6b illustrates that this does not necessarily alleviate the problem. The capacitance of C_o was increased from 10 to 90μF and the inductance L_o from 2 to 3mH. The effect was catastrophic. The complex pole pair closely approached 360 Hz and the Q-factor was increased. It is interesting to note that the difference between the two predicted ripple voltages is still approximately a factor of 10. This choice of values is completely useless. It is evident that the equations (5.2.16) through (5.2.22) constitute an important collection of formulas. They serve as a tool that allows avoiding oscillatory designs.

5.2.3 Preventing the Output Voltage Ripple

However, even in a carefully designed converter, the output voltage ripple can not be completely avoided. The problem is much more serious in the constant diode current controlled case. If a well-regulated output voltage is required, the circuit can be modified as shown in Fig. 5.7. The body diode of the additional active switch, S_2, is shown because it is essential for the operation of the circuit. This class of circuits, which were introduced in [14], is called capacitive idling converters.

This modified converter can be controlled with at least three different control structures. The simplest one is shown in Fig. 5.8a. Switch S_1 is controlled by a

constant duty ratio with resulting input current waveforms according to Chapter 4.2. The other switch S_2 is controlled by a fast output voltage feedback loop. The bandwidth of this loop must be much higher than six times the line frequency. The advantages of this control scheme are its simplicity and its good load regulation capability.

If an improved current waveform at the input is required, the equivalent to the constant diode current control can be applied according to Fig. 5.8b. This structure is somewhat more complicated. The reference current for the first control loop, I_{ref}, must be generated by some means. One possibility is to implement a slow outer loop that keeps V_{c1} constant. The bandwidth of this outer loop must be lower than the line frequency. As in the non-isolated case, the diodes D_b and D_f are placed in the schematic only to illustrate the meaning of i_d. It is not a suggestion for a practical implementation. It is more efficient and less expensive to sense the current polarity on the signal side of the measurement than connect diodes in series with the power path.

If the control loop on the primary side is in place, the second switch can operate at constant duty ratio as shown in Fig 5.8c. This can be explained as follows: The first loop ensures that the diode current i_d is constant. That means $\hat{i}_d$ in Fig. 5.5 is zero and, thus, v_1 is zero. Note that the duty ratio modulation of the second switch is relevant for $\hat{d}_1$ in Fig. 5.5. Therefore, if the second switch is operated at constant duty ratio, $\hat{d}_1$ is

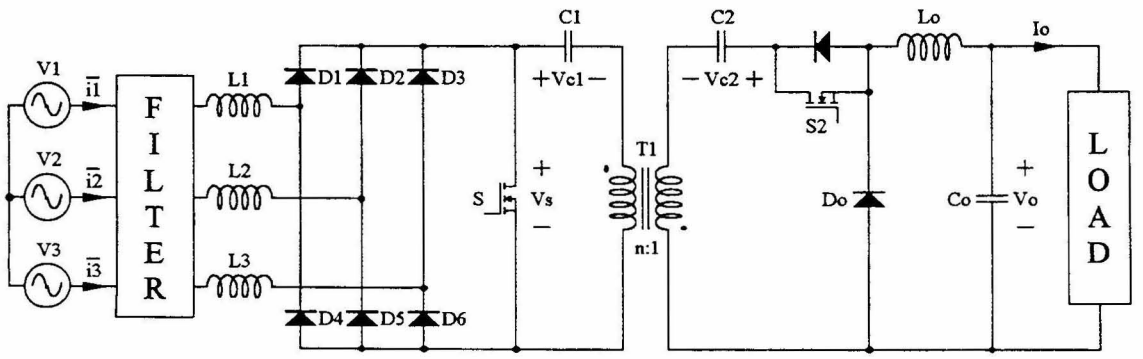

Figure 5.7: An extra switch S_2 is introduced to the Cuk- derived isolated extension. The anti parallel diode is shown here because it is essential for proper operation.

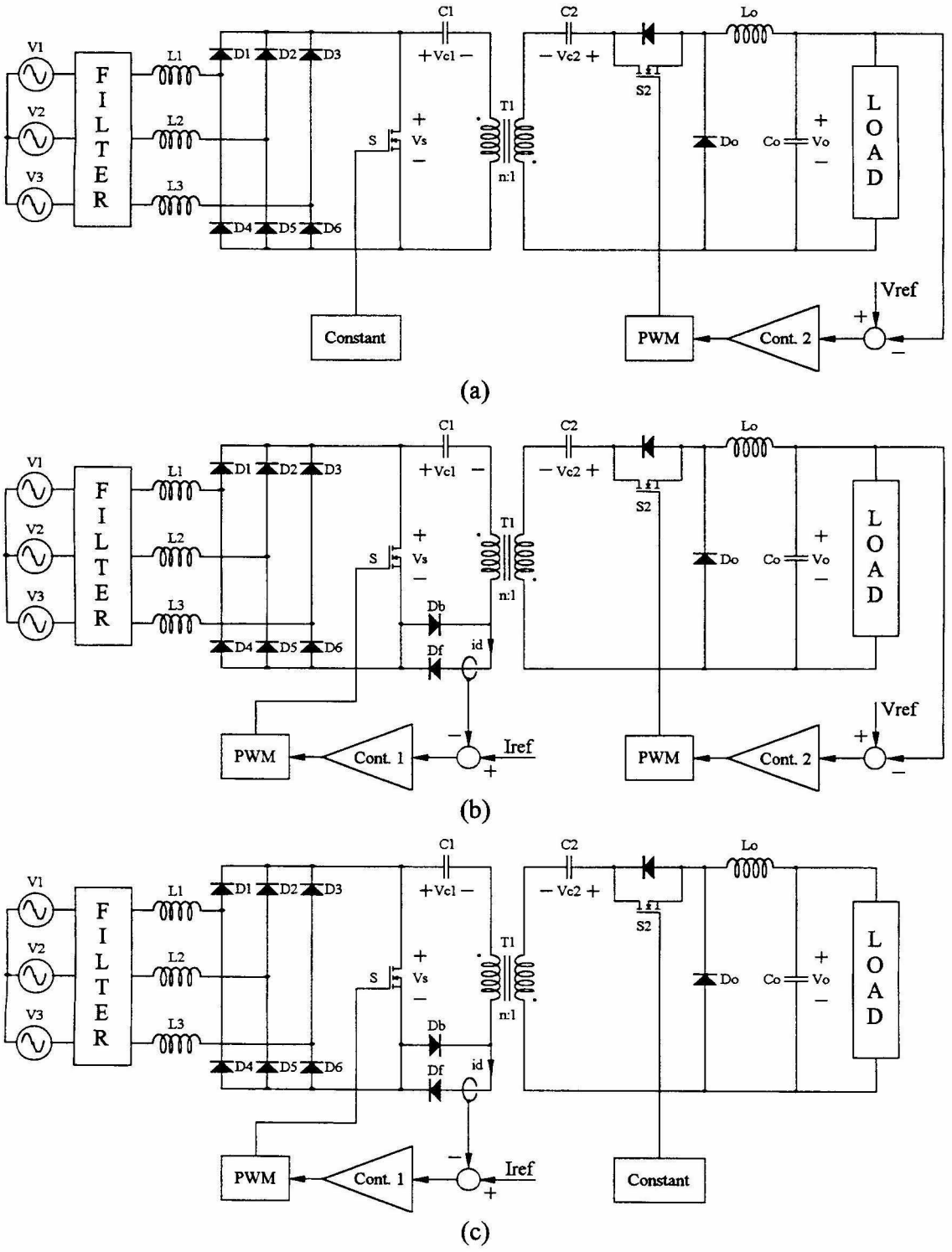

Figure 5.8: Control structures: (a) Independent output control loop, (b) including constant diode current control to reduce the THD at the input and (c) S_2 can operate with constant duty ratio if i_d is kept constant.

zero and so is v_2. Since under these conditions both sources, i.e., v_1 and v_2, are nulled, no output voltage ripple is expected. This result is obtained under somewhat idealized conditions. In a real circuit the control loop at the input side is not ideal, which leads to some ripple in i_d. This ripple propagates to the output of the converter. Nevertheless, this ripple is significantly reduced compared to the case when the constant i_d control method is implemented without adding S_2. A drawback of this control scheme is the reduced performance concerning the load regulation.

An interesting feature of this converter is that neither of the suggested control schemes requires a loop across the galvanic isolation. It is important to note that during the OFF time of S_1 the body diode of S_2 is conducting. During this interval switch S_2 is in the on-state by default. The only action S_2 can perform is to turn off while S_1 is on. Therefore, the two switches must be synchronized, which can be done by sensing the secondary voltage of the transformer [14]. In addition, the active duty ratio of S_2 is always smaller than the duty ratio of S_1. The simplest realization is to turn on both switches at the same time and to ensure that S_2 turns off before S_1. More detailed information about the design of capacitive idling converters can be found in [14].

5.2.4 Experimental Results

In order to confirm the above results experimentally, an isolated version of the Cuk-derived converter was built. It converted a power of 200W from $90V_{RMS}$ (line to neutral) to $75V_{DC}$ using an M_1 of 1.5. The component values were chosen to be L_1=L_2=L_3=320μH, C_1=C_2=40μF, C_o=10μF, L_o=2mH and n=1.25. The circuit was connected to the utility line as the input source while the measurements were taken (not to an ideal voltage source). The voltage THD was approximately 4.5%.

Figure 5.9 shows the input current waveform without the presence of the extra switch. The waveforms correspond to the circuit as shown in Fig. 5.1a. For the first measurement, the duty ratio was kept constant, which lead to the graph shown in Fig. 5.9a. The input current is very similar to the non-isolated case in Fig 4.24a. The output voltage ripple is reasonably close to 1V peak to peak as predicted in Fig. 5.6a.

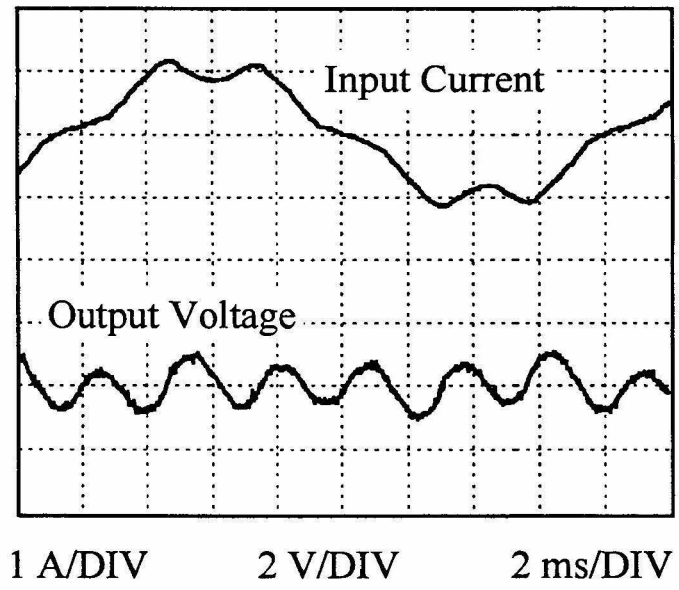

(a)

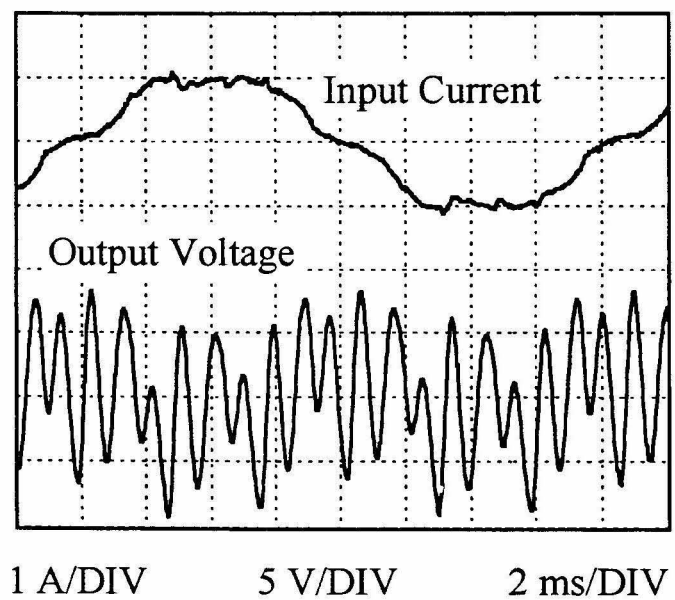

(b)

Figure 5.9: Input current waveform and output voltage ripple without extra switch S_2: (a) Constant duty ratio and (b) constant diode current controlled. (Notice the different voltage scale.)

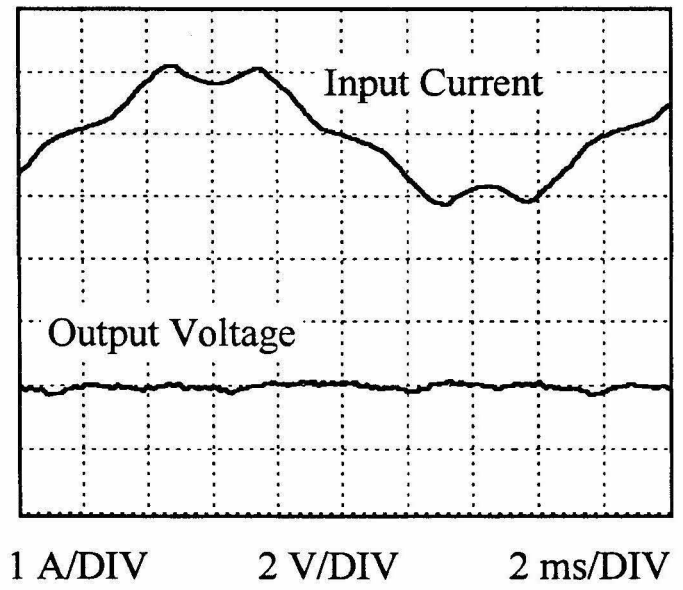

(a)

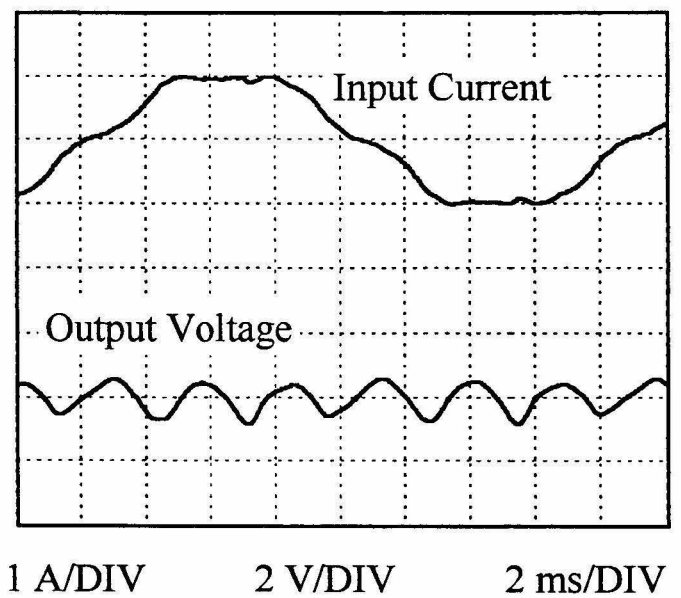

(b)

Figuer 9.10: Input current waveform and output voltage ripple when the circuit includes switch S_2: (a) S_1 constant, S2 controlled duty ratio (Fig. 5.8a) and (b) S_1 constant diode current controlled, S2 constant duty ratio (Fig. 5.8c).

If the constant diode current control method is applied, the input current appears to have less distortion (Fig 5.9b). However, the output voltage ripple is beyond any acceptable limit. The oscillation at the resonant frequency ω_o is worse than the one at 360Hz. Since the duty ratio modulation function is not exactly sinusoidal, as shown in Fig. 4.11c, it can excite various frequencies at the output. In this particular design, ω_o is close to three times 360Hz (i.e., close to the 3rd harmonic of the duty ratio function).

These results strongly suggest that if the constant diode current control method is applied, the capacitive idling converter must be used. The measurements taken with this topology are presented in Fig. 5.10. Initially, the control concept of Fig. 5.8a was applied. The switch S_1 operates with constant duty ratio whereas the second switch S_2 is controlled by means of an output voltage feedback loop with a high bandwidth. The result is shown in Fig. 5.10a. The presence of S_2 does not significantly affect the input current waveform. It is comparable with the one of Fig. 5.9a. However, the output voltage ripple has nearly vanished.

If a lower harmonic distortion of the input current is required, the constant diode current control method can now be applied. The last measurement, depicted in Fig. 5.10b, belongs to the control structure in Fig. 5.8c. The current waveform is improved. There is some noticeable output voltage ripple. This can be explained by the fact that the current loop controlling S_1 is not ideal and i_d itself has some residual ripple. Nevertheless, the ripple is significantly reduced compared to the situation in Fig. 5.9b. If a lower output ripple is required, the control method shown in Fig. 5.8b must be applied which combines the low distortion input with the well-regulated output.

5.3 The Sepic-Derived Topology

5.3.1 Steady State Analysis

The Sepic-derived converter shown in Fig. 5.1b is the second proposed topology to be used as an isolated extension of the single active switch three-phase power factor corrector. Many aspects are similar to the situation in the Cuk-derived converter. Therefore, this topology is treated without going into great detail. Subsequently, the

most important large-signal equations of the converter are derived. In the Cuk-derived converter, the component denoted with T_1 is a real transformer that does not need to have any energy storage capability. In the previous chapter, it was treated as an ideal transformer. This is different in a Flyback converter, where the "transformer" is actually an inductor carried out with two windings. Each of these windings carries the full current during one part of the switching cycle. In the Sepic-derived converter in Fig. 5.1b the transformer is a combination of the two previous cases. It should be pointed out that this is true for any isolated Sepic converter. This combination of transformer and inductor causes the primary side to have a continuous current whereas the secondary is discontinuous.

Based on the discussion above, it is clear that there must be a finite inductance associated with T_1. It will be called L_m, and its value refers to the secondary side. This inductance operates in continuous conduction mode. Volt-second balance applied to T_1 leads to

$$D_1 V_{c1} = (1 - D_1) n V_o \tag{5.3.1}$$

The voltage across the S during its OFF time can be expressed by

$$V_{s_{off}} = V_{c1} + n V_o \tag{5.3.2}$$

Thus,

$$V_{c1} = n V_o \left(\frac{1}{D_1} - 1 \right) \tag{5.3.3}$$

$$V_{s_{off}} = \frac{n}{D_1} V_o \tag{5.3.4}$$

The magnetizing current I_m (i.e., the current in the inductance L_m) must be the same as the output current reflected to the primary side of the transformer since all other branches connected to transformer contain capacitors.

$$I_m = I_o \tag{5.3.5}$$

The output current is given by

$$I_o = \frac{P}{V_o} = \frac{V_o}{R_l} \tag{5.3.6}$$

This concludes the steady state analysis.

5.3.2 Output Voltage Ripple

Similarly to the previous topology, this converter suffers from an output voltage ripple. In order to understand and predict this behavior, a small signal model for the Sepic-derived converter is derived. The procedure to find it is similar to the previous case where the derivation is outlined in greater detail. The only major obstacle in this case is to find an equivalent topology containing pairs of switches which can be replaced by controlled sources. A solution is presented in Fig. 5.11a. This circuit is equivalent to the original circuit except that it is realized with a considerably larger number of switches. The diode current i_d, which was not directly available in the original circuit, appeared in this schematic. Applying the same techniques to this circuit as used in Chapter 5.2 leads to the canonical model shown in Fig. 5.11b, where

$$e_i(s) = \frac{sL_m n^2}{D_1(1-D_1)} \tag{5.3.7}$$

$$e_d(s) = \frac{nV_o}{D_1^2}\left(1 - \frac{sL_m D_1}{R_l(1-D_1)}\right) \tag{5.3.8}$$

$$f_i(s) = \frac{1}{1-D_1}\left(1 + \frac{s^2 L_m C_1 n^2}{D_1}\right) \tag{5.3.9}$$

$$f_d(s) = \frac{-V_o}{R_l n(1-D_1)}\left(1 - \frac{sR_l C_1 n^2(1-D_1)}{D_1^2} + \frac{s^2 L_m C_1 n^2}{D_1}\right) \tag{5.3.10}$$

The equivalent capacitance C_e and inductance L_e are defined as

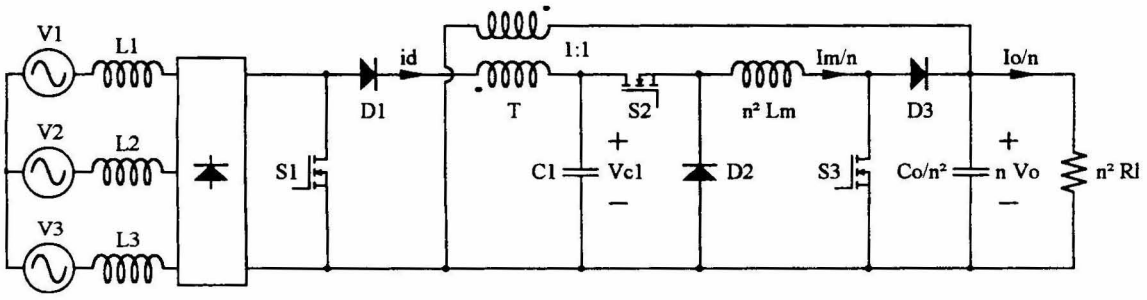

(a)

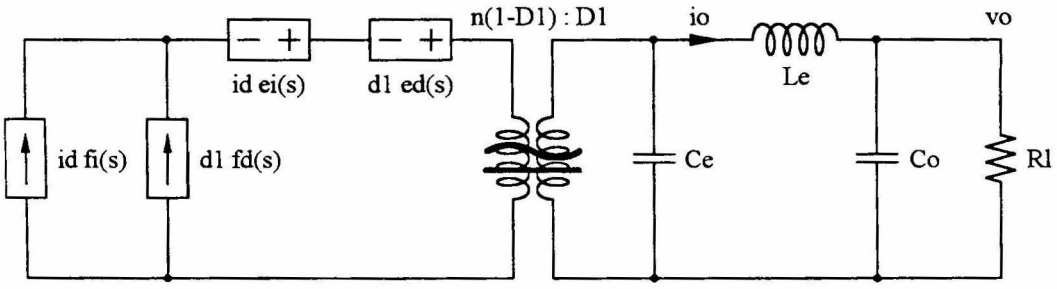

(b)

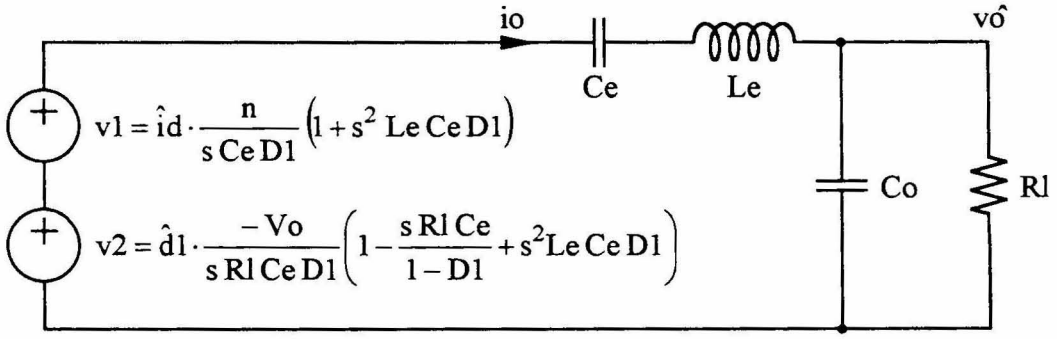

(c)

Figure 5.11: Sepic-derived converter: (a) Equivalent topology suitable to perform circuit averaging, (b) canonical model and (c) final model to calculate output voltage ripple.

$$C_e = C_1\left(\frac{n(1-D_1)}{D_1}\right)^2 \tag{5.3.11}$$

$$L_e = \frac{L_m}{(1-D_1)^2} \tag{5.3.12}$$

This circuit is somewhat more complex than the Cuk-derived topology. An additional voltage source appears that depends on i_d. Both voltage sources are in series with current sources and have no impact on the output voltage. Eliminating these sources leads to the small signal model shown in Fig. 5.11c. The two voltages sources v_1 and v_2 are given by

$$v_1 = \hat{i}_d \cdot \frac{n}{sC_eD_1}(1+sL_eC_eD_1) \tag{5.3.13}$$

$$v_2 = \hat{d}_1 \cdot \frac{-V_o}{sR_1C_eD_1}\left(1-\frac{sR_1C_e}{1-D_1}+s^2L_eC_eD_1\right) \tag{5.3.14}$$

With this, the two transfer functions from the diode current ripple to the output voltage and from the duty ratio to the output voltage becomes

$$\frac{\hat{v}_o}{\hat{i}_d} = \frac{R_1\frac{n}{D_1}\left(1+s^2L_eC_eD_1\right)}{1+sR_1(C_e+C_o)+s^2L_eC_e+s^3R_1L_eC_eC_o} \tag{5.3.15}$$

$$\frac{\hat{v}_o}{\hat{d}_1} = \frac{-\frac{V_o}{D_1}\left(1-\frac{sR_1C_e}{(1-D_1)}+s^2L_eC_eD_1\right)}{1+sR_1(C_e+C_o)+s^2L_eC_e+s^3R_1L_eC_eC_o} \tag{5.3.16}$$

It is likely that the following inequality holds as in the previous topology:

$$R_1^2 >> \frac{L_oC_e^2}{(C_e+C_o)^3} \tag{5.3.17}$$

If so, then the transfer functions in (5.3.15) and (5.3.16) can be approximated as follows:

$$\frac{\hat{v}_o}{\hat{i}_d} = R_l \frac{n}{D_1} \cdot \frac{1-\left(\frac{s}{\omega_z}\right)^2}{\left(1+\frac{s}{\omega_1}\right)\left(1+\frac{1}{Q_p}\cdot\frac{s}{\omega_p}+\left(\frac{s}{\omega_p}\right)^2\right)} \tag{5.3.18}$$

$$\frac{\hat{v}_o}{\hat{d}_1} = \frac{-V_o}{D_1} \cdot \frac{1-\frac{1}{Q_z}\cdot\frac{s}{\omega_z}+\left(\frac{s}{\omega_z}\right)^2}{\left(1+\frac{s}{\omega_1}\right)\left(1+\frac{1}{Q_p}\cdot\frac{s}{\omega_p}+\left(\frac{s}{\omega_p}\right)^2\right)} \tag{5.3.19}$$

where

$$\omega_1 = \frac{1}{R_l(C_e + C_o)} \tag{5.3.20}$$

$$\omega_p = \frac{1}{\sqrt{L_p C_x}} \tag{5.3.21}$$

$$Q_p = \omega_p R_l \frac{C_o^2}{C_x} \tag{5.3.22}$$

$$\omega_z = \frac{1}{\sqrt{L_e C_e D_1}} \tag{5.3.23}$$

$$Q_z = \frac{1-D_1}{R_l}\sqrt{\frac{L_e D_1}{C_e}} \tag{5.3.24}$$

$$C_x = \frac{C_e C_o}{C_e + C_o} \tag{5.3.25}$$

Q_z is often much less than unity. Should this be true, the numerator of (5.3.19) can be factorized simply and the equation can be approximated as

$$\frac{\hat{v}_o}{\hat{d}_1} = \frac{-V_o}{D_1} \cdot \frac{\left(1-\frac{s}{\omega_{z1}}\right)\left(1-\frac{s}{\omega_{z2}}\right)}{\left(1+\frac{s}{\omega_1}\right)\left(1+\frac{1}{Q_p}\cdot\frac{s}{\omega_p}+\left(\frac{s}{\omega_p}\right)^2\right)} \tag{5.3.26}$$

where

$$\omega_{z1} = \frac{1-D_1}{R_l C_e} \tag{5.3.27}$$

$$\omega_{z2} = \frac{R_l}{L_e D_1 (1-D_1)} \tag{5.3.28}$$

The calculated peak to peak output voltage ripples for two different cases are shown in Fig. 5.12a and 5.12b respectively. These graphs are based on a converter with component values similar to the ones in Fig. 5.6 of the Cuk-derived converter. The input voltage was chosen to be $90V_{rms}$ (line to neutral), the output voltage $75V_{DC}$ and the conversion ratio 1.5. The voltage and current stress of the components of the isolated Sepic converter are similar to the those of the isolated Cuk converter. The only major difference is that the capacitor C_2 is missing in the Sepic converter. A simple analysis reveals that the output capacitor C_o of that converter carries the same ripple current as C_2 and C_o combined in the Cuk converter. Since the voltages across the C_2 and C_o are the same, their values must be combined and used to determine the capacitance C_o of the Sepic converter. This ensures an equivalent situation in both converters. Therefore, in order to achieve a similar situation as in Fig. 5.6a, the component values are chosen to be as follows: L_1=L_2=L_3=320μH, C_1=40μF, C_o=50μF, L_m=2mH and n=1.25.

Unlike in the Cuk converter case, this is not a good choice since the resonant frequency as almost precisely at 360Hz. A significant ripple of 3.41V must be expected. According to (5.3.18) the Q-factor of the numerator is infinity. Therefore, at $\omega = \omega_z$ the transfer function is zero. This behavior can also be observed in Fig. 5.12. An interesting possibility is to place the ω_z exactly at six times the line frequency.

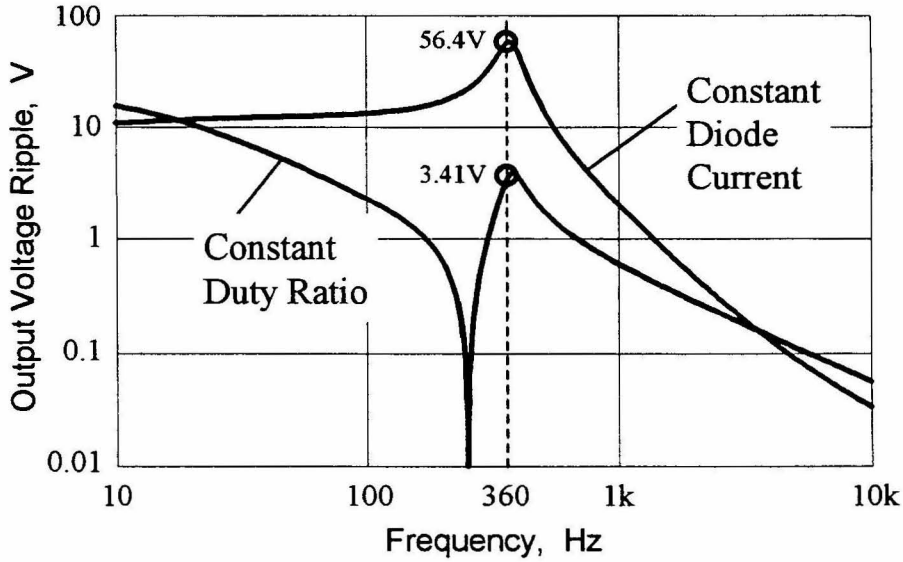

(a)

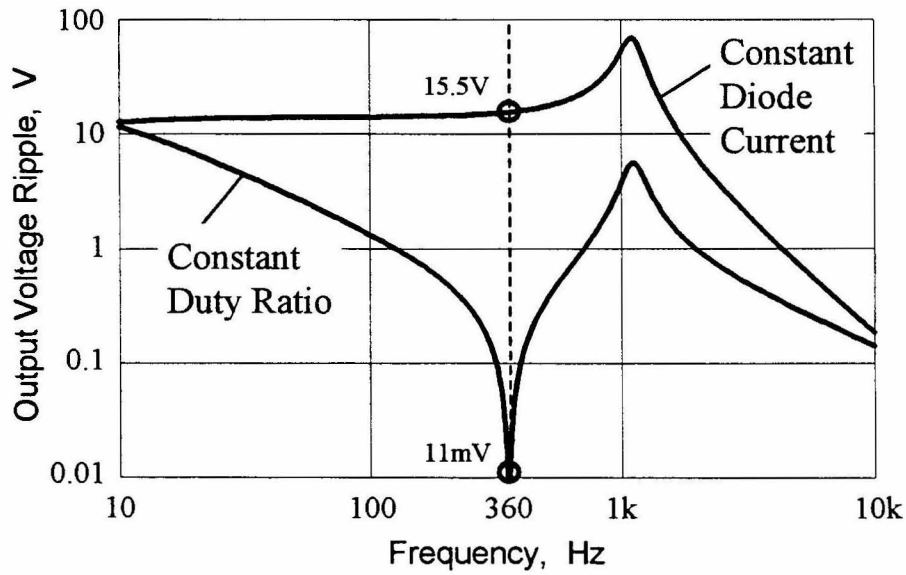

(b)

Figure 5.12: Sepic-derived converter: Transfer functions corresponding to the circuit in Fig. 5.11 with different values for the capacitors C_1 and C_o and the inductor L_m: (a) The values are chosen based on the ones that resulted in Fig. 5.6a and (b) optimized choice of values.

Using (5.3.23), it can be concluded that the following equation must hold in order to achieve the desired zero placement

$$L_e C_e = \frac{1}{(12\pi f_L)^2 D_1} \tag{5.3.29}$$

where f_L is the line frequency. Using (5.3.11) and (5.3.12), the same relation can be rewritten as

$$L_m C_1 = \frac{D_1}{(12\pi f_L n)^2} \tag{5.3.30}$$

Conversely, the resonant frequency ω_p should be moved away from six times the line frequency. This widens the range where the magnitude is low. This is important as all components have tolerances, and a converter usually operates over a certain duty ratio range. Moving ω_p to higher frequencies is achieved by choosing L_m or C_o low. The following inequality is very likely to be satisfied:

$$C_e >> C_o \tag{5.3.31}$$

If so, the following approximate relation holds:

$$L_m C_o \approx \left(\frac{1 - D_1}{2\pi f_p} \right)^2 \tag{5.3.32}$$

where f_p is the resonant frequency that corresponds to ω_p, i.e.,

$$f_p = \frac{\omega_p}{2\pi} \tag{5.3.33}$$

Lowering C_o also tends to decrease Q_p, a very desirable feature. However, it increases the switching ripple at the output of the converter, which puts a lower limit on C_o. Decreasing L_m increases the rms-value of the currents in the switches and the magnetizing current in the transformer. The price is higher power losses in these elements. Eventually, L_m will go into discontinuous conduction mode and the whole

analysis will not apply anymore. These are the main design restrictions placed on C_1, C_o and L_m.

Based on these considerations, new values were assigned to these components: C_1=80μF, C_o=20μF and L_m=0.5mH. This results in zero magnitude at 356Hz and the complex pole pair shifted from 373Hz to 1.11kHz. The corresponding transfer functions are shown in Fig. 5.12b. The 360Hz output voltage ripple is now expected to be negligible (i.e., 11mV) and the switching ripple will be increased.

5.3.3 Simulated Results

In order to verify this behavior, the circuit as shown in Fig. 5.1b was simulated using PSpice. The resulting output voltages over one line cycle are presented in Fig. 5.13. In the original design with C_1=40μF, C_o=50μF and L_m=2mH, the 360Hz ripple is reasonably close to the predicted 3.4V from peak to peak. The simulated value is about 3V. By adjusting the component values to C_1=80μF, C_o=20μF and L_m=0.5mH, a drastic reduction of the 360 Hz ripple is achieved. As predicted, the switching ripple has significantly increased.

5.3.4 Preventing the Output Voltage Ripple

Until now, only the constant duty ratio case was considered. The analysis reveals that the output voltage ripple is not reduced if the constant i_d control method is applied. Hence, if this control method is applied, an extra switch can be added to the circuit similar as in the Cuk-derived topology. Two versions of the capacitive idling converters are considered. The extra switch S_2 can be placed at the primary side of the transformer since the Sepic-derived converter in Fig. 5.1b has no capacitor connected to the secondary side. This version is shown in Fig. 5.14a. This solution has the disadvantage that the control loop must cross the galvanic isolation. A solution to this problem can be obtained by separating the transformer and inductor function into two different elements. This circuit is shown in Fig. 5.14b. The disadvantage is the higher number of components.

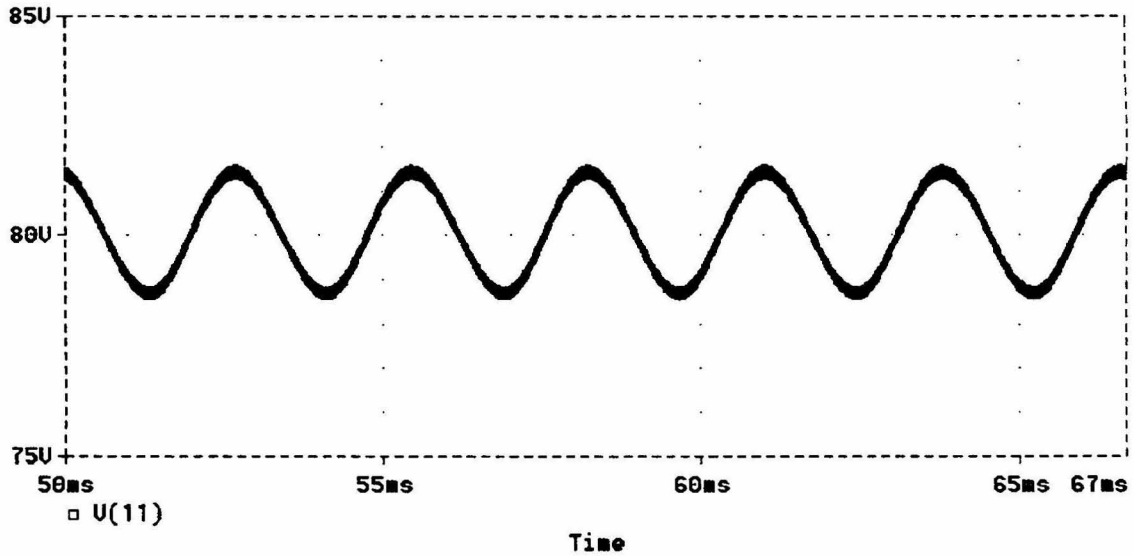

(a)

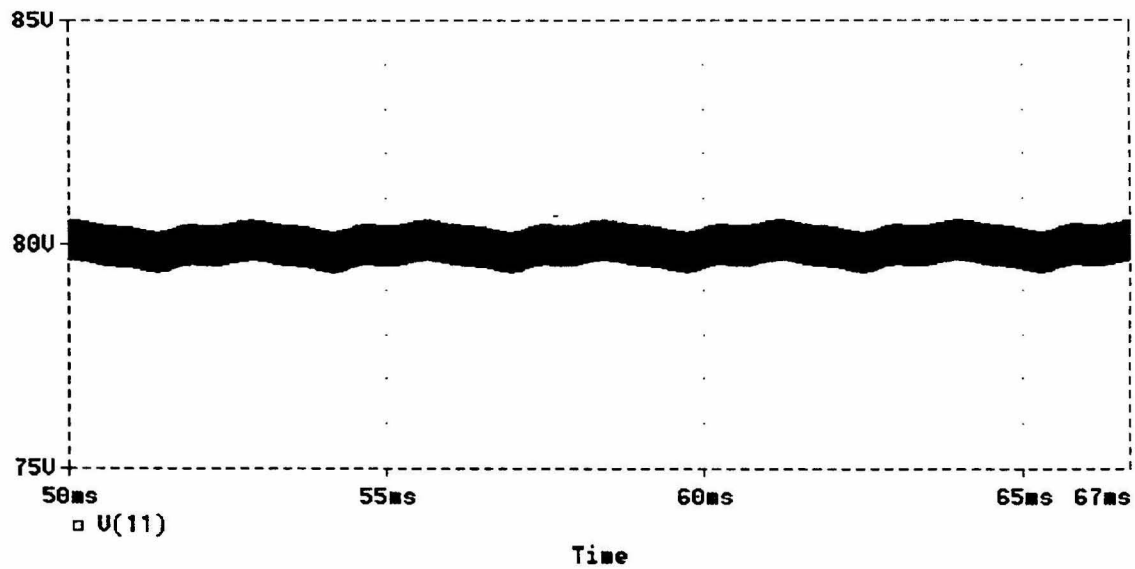

(b)

Figure 5.13: Simulation of the output voltage ripple of the Sepic-derived converter: (a) Initial choice of circuit values corresponding to Fig. 5.12a and (b) optimized design according to Fig. 5.12b.

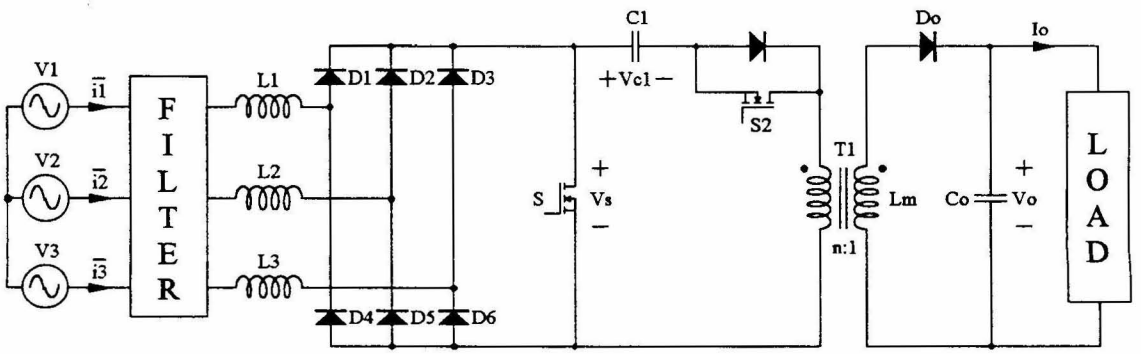

(a)

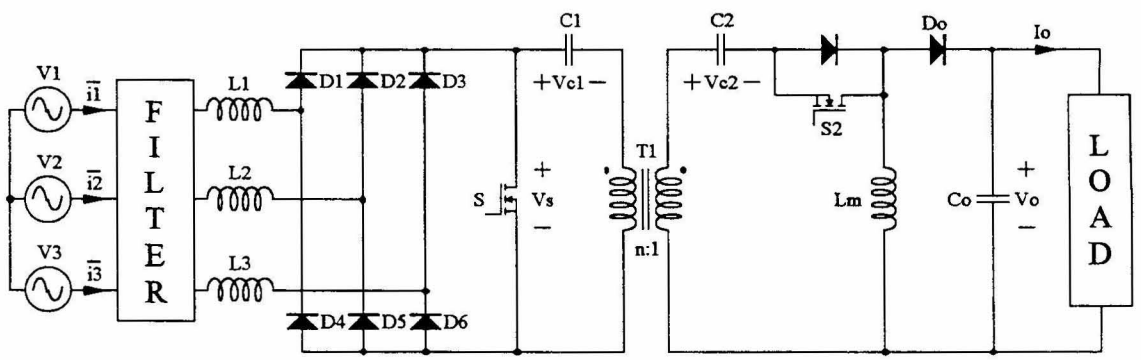

(b)

Figure 5.14: Capacitive idling Sepic converter: (a) The extra switch S_2 is at the primary side of the transformer and (b) S_2 can be placed on the secondary if the inductor L_m is realized as a separate component.

For the Cuk-derived topology, three different control methods were presented in Fig. 5.8. The same three concepts can be applied to the Sepic derived converter with the same restriction to the duty ratio of S_2. These methods are:

1) S_1 Constant duty ratio
   S_2 Controlled with fast output voltage feedback loop
2) S_1 Controlled such that i_d of Fig. 5.2 is constant
   S_2 Controlled with fast output voltage feedback loop
3) S_1 Controlled such that i_d of Fig. 5.2 is constant
   S_2 Constant duty ratio

Switch S_2 must be synchronized with S_1 and its duty ratio must always be less than that of S_1 for the same reason as discussed in conjunction with the Cuk-derived converter.

Chapter 6

A Single Active Switch Single-Phase Power Factor Corrector with High Quality Input and Output

In this chapter, a single-phase power factor corrector topology is investigated. This converter qualifies as an automatic current shaper. The current shaping function is a natural property of this circuit. Therefore, no extra control loop is necessary to achieve a low harmonic distortion. An output feedback loop with a high bandwidth is essential to obtain a good input current waveform. As a result, a well-regulated output voltage is provided at no extra cost.

6.1 The Topology

The circuit investigated in this chapter is shown in Fig. 6.1. It was introduced in [15] as Bifred (Boost Integrated with Flyback Rectifier/Energy storage/Dc-dc converter). Similarly, as in the Sepic-derived isolated extension of the three-phase converter in Chapter 5.3, the element denoted as L_2 is a combination of transformer and inductor. It must have a finite and properly designed magnetizing inductance. When the converter was first introduced, it was assumed that the inductor L_1 worked in discontinuous conduction mode (DCM), whereas, L_2 operated in continuous conduction mode (CCM). In this configuration, the voltage V_1 is strongly load dependent. For the converter to operate properly, there is a minimum value required for this voltage. The fact that V_1 varies over a wide range results in extremely high voltage stress in the switches.

In addition, the duty ratio was assumed to be constant over one line cycle. The resulting input current exhibits the well-known bell shape of the automatic power factor corrector based on the DCM boost converter operated with constant duty ratio [16]. This can be explained by the fact that the input of this converter is equivalent to a boost converter with an output voltage equal to the sum of V_I and V_o reflected to the transformer primary. A *THD* of about 20% is a typical value for this waveform. The constant duty ratio operation is commonly achieved with a low bandwidth feedback loop. Thus, an output voltage ripple of twice the line frequency must be expected.

In this chapter, a new mode of operation is investigated. Both inductors are operating in DCM, and the duty ratio is no longer constant over one switching cycle. It

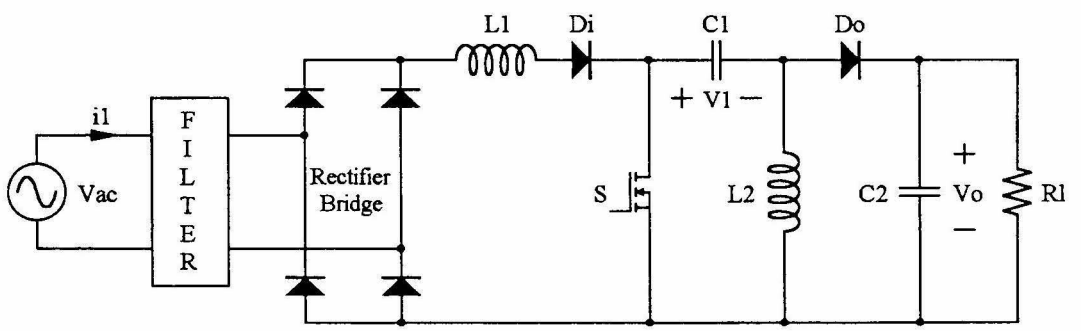

(a)

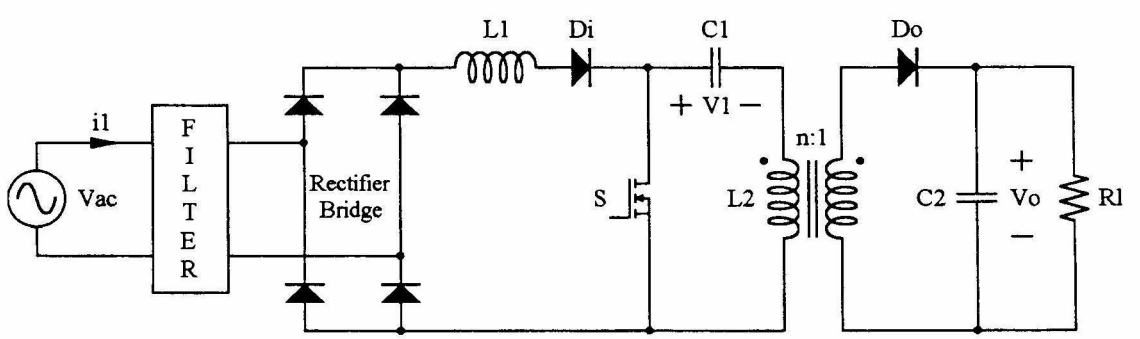

(b)

Figure 6.1: The Bifred Converter: (a) Non-isolated version and (b) including galvanic isolation.

is controlled by means of a fast feedback loop with a bandwidth much higher than twice the line frequency. This new mode leads to an improved overall behavior of the circuit. **By implementing a high bandwidth control loop, two goals are achieved simultaneously: namely, a very low harmonic content in the input current and a well-regulated output voltage with no line frequency related ripple.** All this is achieved without excessively high voltage stress on the switches since the voltage V_1 is no longer load dependent.

6.2 Large-Signal Analysis

In order to make the large-signal analysis of the converter more transparent, the non-isolated converter shown in Fig. 6.1a is considered. The final results can easily be modified to fit the isolated converter with a turns ratio n, shown in Fig. 6.1b. All line frequency dependent quantities are expressed in terms of the normalized frequency θ (i.e., $\omega t \rightarrow \theta$). The analysis is based on the assumptions listed below.

1) The input voltage is considered to be an ideal sine wave, thus $v_{ac}(\theta) = V_g \sin(\theta)$.

2) The capacitors C_1 and C_2 are sufficiently large to ensure that the low frequency ripple (twice the line frequency) of V_1 and V_o can be neglected.

3) Both inductors, L_1 and L_2, operate in DCM.

4) The current in L_1 reaches zero prior to the current in L_2.

5) For the analysis of the waveforms during one switching cycle, the input voltage v_{ac} is considered to be constant (i.e., the switching frequency is assumed to be much higher than the line frequency).

6) The input filter eliminates the switching ripple of the input current, but it does not affect line frequency related variations.

7) The converter is loss-less.

As far as the converter is concerned, both half waves of the line period are equivalent. It is therefore sufficient to investigate only the positive half wave. Based on that and assumption 6, the ac source, the input filter, and the rectifier bridge can be replaced by an equivalent rectified ac source in order to perform the analysis. This modified circuit is shown in Fig. 6.2. The input voltage v_g is represented by

$$v_g = V_g \sin(\theta) \tag{6.2.1}$$

The following definitions will be used throughout the analysis:

$$M \equiv \frac{V_o}{V_g} \tag{6.2.2}$$

$$M_1 \equiv \frac{V_1 + V_o}{V_g} \tag{6.2.3}$$

$$M_2 \equiv \frac{V_o}{V_1 + V_o} \tag{6.2.4}$$

$$M_3 \equiv \frac{V_1}{V_g} \tag{6.2.5}$$

$$M_4 \equiv \frac{V_o}{V_1} \tag{6.2.6}$$

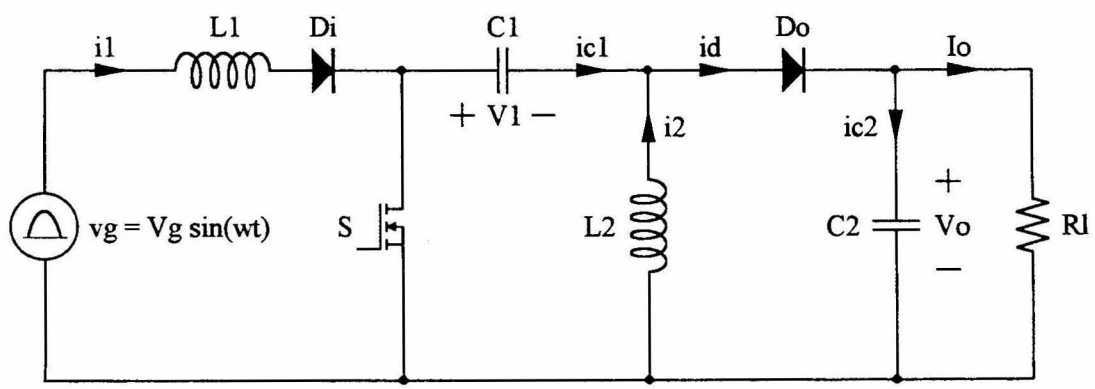

Figure 6.2: The equivalent circuit on which the analysis is based.

Every switching cycle can be divided into four subintervals. Each subinterval lasts for D_iT_s, where the subscript i runs from 1 through 4 and T_s is the length of the switching cycle. The equivalent circuits of each of these subintervals are shown in Fig. 6.3. The currents i_1, i_2 and i_d have the time dependent waveforms as sketched in Fig. 6.4.

The first subinterval is defined by the on-time of switch S. The currents i_1 and i_2 in the two inductors are increasing starting from zero. For the rest of the switching cycle, switch S is turned off. Both inductor currents now must flow through the diode D_o to the output and decrease in magnitude. The end of the second subinterval is reached when current i_1 becomes zero. It remains zero for the rest of the period as diode D_i prevents it from becoming negative. At the end of the third subinterval, i_2 also reaches zero and it remains zero together with i_1 during the fourth subinterval forced by the diode D_o.

Both inductor currents i_1 and i_2 reach their peak values at the end of the first interval. These values can be found using the equivalent circuit in Fig. 6.3a. At any point during the line half-cycle they are represented by

$$i_{1p} = v_g \frac{D_1 T_s}{L_1} \tag{6.2.7}$$

$$i_{2p} = V_1 \frac{D_1 T_s}{L_2} \tag{6.2.8}$$

The peak value of the diode current i_d is the sum of the i_{1p} and i_{2p}.

$$i_{dp} = v_g \frac{D_1 T_s}{L_1} + V_1 \frac{D_1 T_s}{L_2} \tag{6.2.9}$$

The values for D_2 and D_3 must be found and expressed in terms of D_1 and the voltages v_g, V_1 and V_o. At this point, it is assumed that V_1 is known. Later, it will be shown how to choose the inductors to obtain the desired V_1 for a given v_g and V_o. Using this approach the analysis is much simpler than by starting with the input voltage, the load and all the circuit elements as known parameters. In addition, from a design point

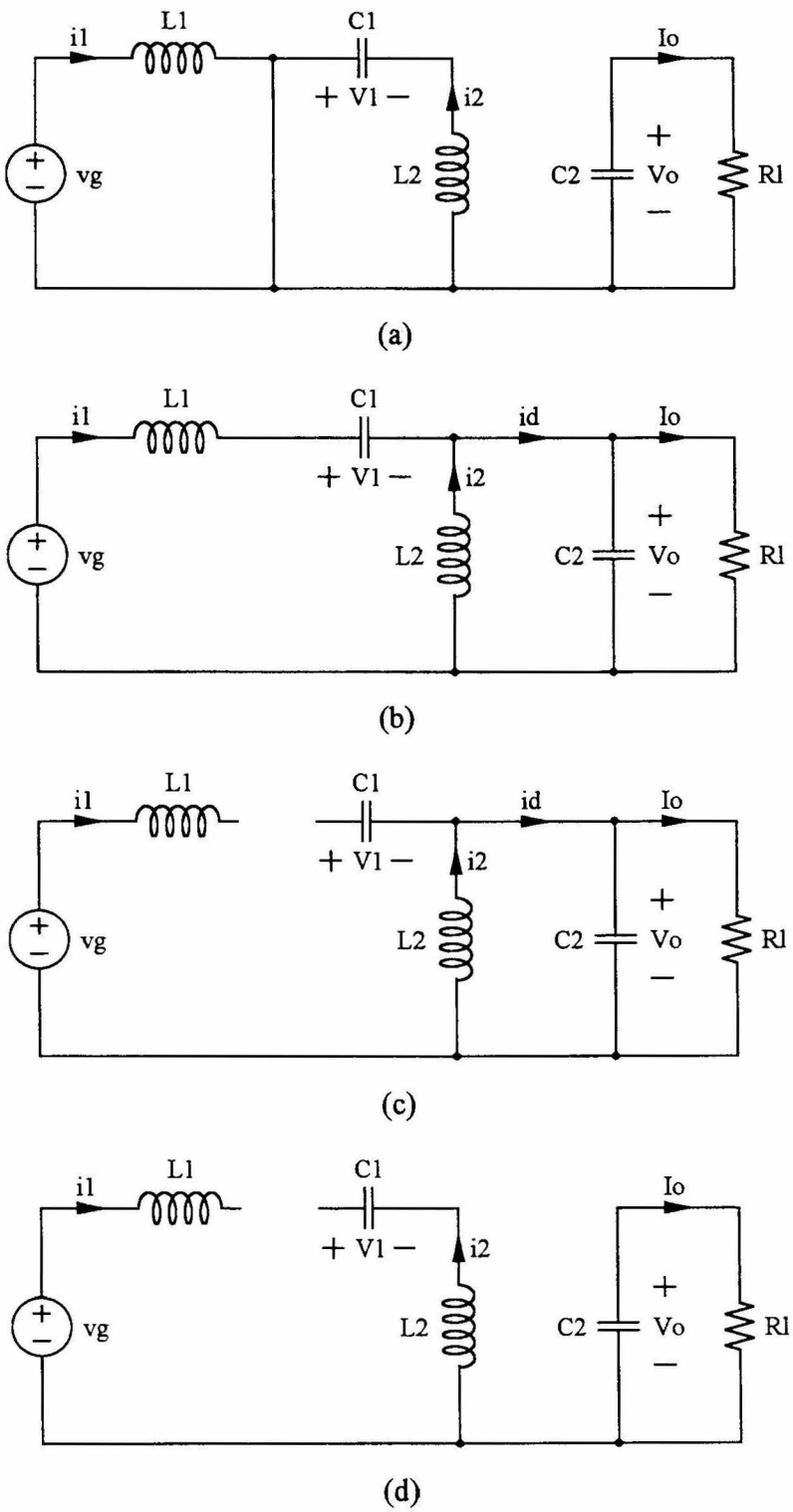

Figure 6.3: The four equivalent circuits during one switching cycle.

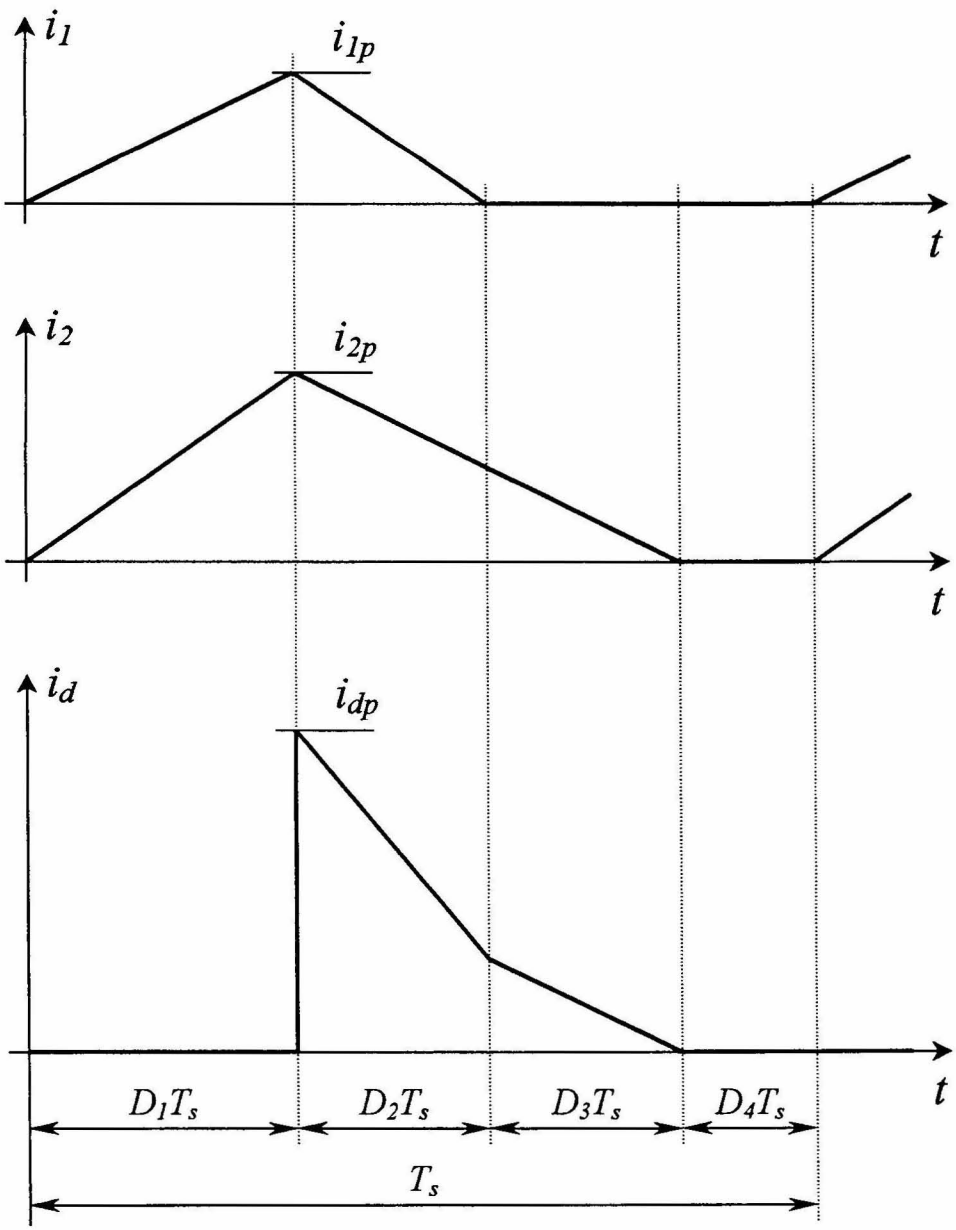

Figure 6.4: Typical current waveforms.

of view, this approach is more useful as the salient features of the converter directly depend on the ratios V_1 to V_g and V_1 to V_o. It is, therefore, desirable to choose V_1 at the beginning. The alternative is to choose all the circuit elements, work through transcendental equations to find V_1, and then decide whether or not that value is acceptable.

D_2 is found using volt-second balance on L_1, whereas volt-second balance on L_2 is used to determine D_3. The volt-second balance for L_1 and L_2 leads to

$$v_g D_1 = (V_1 + V_2 - v_g) D_2 \tag{6.2.10}$$

and

$$V_1 D_1 = V_2 (D_2 + D_3) \tag{6.2.11}$$

respectively. These two equations, together with (6.2.1), (6.2.3) and (6.2.4), can be used to find

$$D_2 = D_1 \frac{\sin(\theta)}{M_1 - \sin(\theta)} \tag{6.2.12}$$

$$D_3 = D_1 \left(\frac{1}{M_2} - \frac{\sin(\theta)}{M_1 - \sin(\theta)} - 1 \right) \tag{6.2.13}$$

Expressions for the currents averaged over one switching cycle can now be found by averaging the triangular waveforms in Fig. 6.4. Equations (6.2.7) and (6.2.12) are used to solve for the input current $\bar{i}_1$. (6.2.8), (6.2.12) and (6.2.13) are used to find $\bar{i}_2$, whereas $\bar{i}_d$ can be calculated by using (6.2.9), (6.2.12) and (6.2.13). The results are as follows:

$$\bar{i}_1 = \frac{D_1^2 T_s}{2L_1} V_g \frac{M_1 \sin(\theta)}{M_1 - \sin(\theta)} \tag{6.2.14}$$

$$\bar{i}_2 = \frac{D_1^2 T_s}{2L_2} \cdot \frac{V_1}{M_2} \tag{6.2.15}$$

$$\bar{i}_d = \frac{D_1^2 T_s}{2}\left(\frac{V_g}{L_1}\cdot\frac{\sin^2(\theta)}{M_1 - \sin(\theta)} + \frac{V_1}{L_2}\cdot\frac{1}{M_4}\right) \tag{6.2.16}$$

In the next step, the requirements to ensure discontinuous conduction mode are derived. There are two conditions to meet. Firstly, both inductor currents must reach zero before the end of the switching cycle at any input voltage (i.e., for every phase angle θ). Secondly, by assumption, L_1 must first become discontinuous, then L_2. These two conditions can be stated as follows:

$$D_1 + D_2 + D_3 \le 1 \tag{6.2.17}$$

$$D_3 \ge 0 \tag{6.2.18}$$

The equations can be simplified using (6.2.12) and (6.2.13). The results are

$$D_1 \le M_2 \tag{6.2.19}$$

$$1 \le M_3 \tag{6.2.20}$$

These are necessary and sufficient conditions to guarantee the proper mode of operation. The inequality (6.2.19) ensures that for any phase angle θ the current i_2 falls back to the zero level before or at the end of each switching cycle. The inequality (6.2.20) ensures that the current i_1 becomes zero before or together with i_2.

In most cases, a well-regulated output voltage is required. V_o is not allowed to have a low frequency ripple. In this topology, avoiding this ripple is equivalent to not allowing a low frequency ripple in the averaged diode current $\bar{i}_d$. This can be realized by controlling the duty ratio so that $\bar{i}_d$ is constant. If this control method is applied, the diode current is the same as the output current, i.e.,

$$\bar{i}_d = I_o \tag{6.2.21}$$

Using (6.2.16), the required duty ratio $D_1(\theta)$ that keeps $\bar{i}_d$ constant can be obtained.

$$D_1(\theta) = \sqrt{\frac{2I_o}{T_s} \cdot \frac{1}{\frac{V_g}{L_1} \cdot \frac{\sin^2(\theta)}{M_1 - \sin(\theta)} + \frac{V_1}{L_2} \cdot \frac{1}{M_4}}} \tag{6.2.22}$$

D_{123} represents the fraction of the switching cycle where at least one inductor current is non-zero and is defined by

$$D_{123}(\theta) \equiv D_1(\theta) + D_2(\theta) + D_3(\theta) \tag{6.2.23}$$

This can be simplified using (6.2.12) and (6.2.13).

$$D_{123}(\theta) = \frac{D_1(\theta)}{M_2} \tag{6.2.24}$$

From (6.2.22) it can be concluded that the maximum value occurs at $\theta = 0$, and therefore, D_{123max} becomes

$$D_{123max} = \sqrt{\frac{2I_o L_2}{T_s V_1 M_2 (1 - M_2)}} \tag{6.2.25}$$

To ensure that the inductors are operated in DCM over the entire line period, D_{123max} must be chosen to be smaller than unity. In order to obtain the best possible efficiency it should be close to one. Equation (6.2.25) can be solved for the required L_2.

$$L_2 = \frac{T_s}{2I_o} V_1 M_2 (1 - M_2) D_{123max}^2 \tag{6.2.26}$$

The next step is to find an expression for L_1 using charge balance on C_1. Q_{C1} represents the charge, which is released from C_1 during the first subinterval of the switching cycle (i.e., during the on-time of the active switch), whereas Q_{C2} stands for the charge stored in C_1 during the second subinterval. No currents are flowing in C_1 during the third and the fourth subinterval (Fig. 6.3). Before Q_{C1} and Q_{C2} can be equated, they must be averaged over a half of a line period (or a multiple thereof). Due to the waveform symmetry, the integral can run only from 0 to $\pi/2$. Q_{C1} can be expressed as

$$Q_{C1} = \frac{2}{\pi} \int_0^{\pi/2} i_{1p} \frac{D_2(\theta) T_s}{2} d\theta \tag{6.2.27}$$

The substitution of (6.2.7) and (6.2.12) into the above equation leads to

$$Q_{C1} = \frac{V_g T_s^2}{\pi L_1} \int_0^{\pi/2} D_1^2(\theta) \frac{\sin^2(\theta)}{M_1 - \sin(\theta)} d\theta \tag{6.2.28}$$

The expression for Q_{C2} is found to be

$$Q_{C2} = \frac{2}{\pi} \int_0^{\pi/2} i_{2p} \frac{D_1(\theta) T_s}{2} d\theta \tag{6.2.29}$$

Using (6.2.8) this can be expressed as

$$Q_{C2} = \frac{V_1 T_s^2}{\pi L_2} \int_0^{\pi/2} D_1^2(\theta) d\theta \tag{6.2.30}$$

In steady state Q_{C1} and Q_{C2} must be equal. Thus, (6.2.28) and (6.2.30) can be equated and solved for L_1

$$L_1 = \frac{L_2}{M_3} \cdot \frac{\int_0^{\pi/2} D_1^2(\theta) \frac{\sin^2(\theta)}{M_1 - \sin(\theta)} d\theta}{\int_0^{\pi/2} D_1^2(\theta) d\theta} \tag{6.2.31}$$

This equation contains $D_1(\theta)$ on the right-hand side. After substituting it by (6.2.22) and performing some algebra, (6.2.31) becomes

$$L_1 = \frac{\int_0^{\pi/2} \frac{d\theta}{\frac{M_3}{L_2} \cdot \frac{M_1 - \sin(\theta)}{\sin^2(\theta)} + \frac{M_4}{L_1}}}{\int_0^{\pi/2} \frac{d\theta}{\frac{L_2}{L_1} \cdot \frac{M_4}{M_3} \cdot \frac{\sin^2(\theta)}{M_1 - \sin(\theta)} + 1}} \tag{6.2.32}$$

This is a transcendental equation for L_1. It can only be solved numerically. One possibility is to apply the following iterative process: the result for L_1 of the current iteration step is used in the right-hand side of the next iteration. This process must be repeated until L_1 no longer changes its value. As initial value, L_1 can be set equal to L_2. This is not the fastest algorithm, but it probably is the easiest one to program.

Equation (6.2.32) is used to find the necessary L_1 that yields a desired V_1. Once a converter is designed for its nominal point of operation, L_1 and L_2 are fixed. In this case, it is interesting to know to what extent V_1 depends on input or output voltage variations or on load changes. For this purpose, (6.2.32) can be rearranged as follows:

$$V_1 = \frac{\int_0^{\pi/2} \frac{d\theta}{\frac{L_1}{L_2}\cdot\frac{V_1+V_2-V_g\sin(\theta)}{V_g{}^2\sin^2(\theta)}+\frac{V_2}{V_1{}^2}}}{\int_0^{\pi/2} \frac{d\theta}{\frac{L_2}{L_1}\cdot\frac{V_2}{V_1^2}\cdot\frac{V_g{}^2\sin^2(\theta)}{V_1+V_2-V_g\sin(\theta)}+1}} \tag{6.2.33}$$

This equation can be solved in a similar way as (6.2.32), starting with the nominal value for V_1. However, in this case the algorithm converges very slowly. A much faster method is as follows: the right-hand side of (6.2.33) is considered to be a function $f(V_1)$. Using this, the iteration can be carried out as stated below.

$$V_{1_{i+1}} = \frac{f(V_{1_i}) + f(f(V_{1_i}))}{2} \tag{6.2.34}$$

The expression for the duty ratio (6.2.22) can be substituted into (6.2.14) to get a final expression for the input current.

$$\bar{i}_1 = I_o \cdot \frac{\frac{M_4}{M_3}\cdot\frac{L_2}{L_1}\cdot\sin(\theta)}{1-\frac{\sin(\theta)}{M_1}+\frac{M_2}{M_3{}^2}\cdot\frac{L_2}{L_1}\sin^2(\theta)} \tag{6.2.35}$$

The harmonic distortion of this current and the resulting power factor can now be analyzed according to the definitions stated in Chapter 2. The results are reported in the next section. It should be pointed out that the current is in phase with the voltage since $i_1(\theta) = i_1(180 - \theta)$. Thus, the displacement factor is unity and (2.7.6) can be used to evaluate the power factor.

6.3 Results of the Large-Signal Analysis

The main topic of this chapter is to provide an overview of the improvement in the *quality* of the input current waveform of this converter under the special conditions proposed (both inductor currents discontinuous and in the presence of the constant output voltage control). The waveforms and their distortions are analyzed under various conditions. The results are compared with the same topology operated with constant duty ratio. This reference topology is designed so that the voltage stress in the switches is the same in both, the controlled duty ratio and in the constant duty ratio converter. The Bifred and the Boost converter in DCM generate the same input current waveform if both are operated with constant duty ratio and if both are designed to work with the same switch voltage stress. The output of the Boost converter must be equivalent to V_1+V_o in the Bifred. Therefore, the improvement of the current waveform due to the constant diode current control can be compared with the Bifred or DCM Boost converter.

6.3.1 Comparison with the Constant Duty Ratio Case

In the DCM Boost and Boost-like power factor correctors, increasing the switch voltage stress reduces the distortion of the input current [16] at the cost of a lower efficiency. In addition, components with higher voltage rating tend to be more expensive. A compromise must be found between a low switch voltage stress and a low harmonic distortion. The switch voltage stress V_s in the Bifred converter is given by

$$V_s = V_1 + V_o = (M_3 + M)V_g \tag{6.3.1}$$

Commonly, the input and output voltage of a converter are given quantities, and thus, M is given. However, the value of M_3 can be chosen by design, where the restriction (6.2.20) must be satisfied (M_3 must be larger or equal to unity) in order to ensure proper operation.

Fig. 6.5a and 6.5b shows the calculated harmonic distortion of the input current of this converter for different values of M_3. For the constant duty ratio DCM Boost or Bifred converter it can be clearly seen in Fig. 6.5b that increasing the switch voltage stress (or M_3 respectively) gradually reduces the *THD*. **If the constant output control is applied, an interesting observation can be made. At the conversion ratio M = 0.45, a very low *THD* can be achieved even with the lowest possible value of M_3.** (For M_3 = 1 the exact value of the optimal conversion ratio is M = 0.4435.) In Figs. 6.5c and 6.5d the same information is presented in terms of the power factor. At M = 0.45 it is nearly unity for any value of M_3. (Note the different scale on the vertical axis of these graphs.) A comparison of both cases for M_3 = 1 is displayed in Fig. 6.6a for the THD and in Fig 6.6b for the power factor.

It is evident that with the proposed control method there is no need for a high M_3 (i.e., a high switch voltage stress). The current distortion can be drastically reduced if the conversion ratio is appropriately chosen. As stated above, the conversion ratio can not usually be freely chosen. However, from Fig. 6.6 it can be concluded that even if the converter operates with an M other than 0.45, a significant improvement is achieved over a wide range of M. Furthermore, in many cases an isolation transformer is required. For an arbitrary output voltage the turns ratio in L_2 can be chosen in order that the reflected voltage at the primary has the optimal value.

The input current obtained with M_3 = 1 at the optimal conversion ratio is shown in Fig. 6.6c together with the value of the power factor and the *THD*. For comparison the current waveform of the constant duty ratio case is shown as a dashed line. The harmonic distortion is reduced by more than a factor of 10. Fig. 6.6d shows the frequency spectrum of these currents. The values of the harmonics are normalized with respect to the fundamental. Due to the symmetry of the current shape, there are, ideally, no even harmonics.

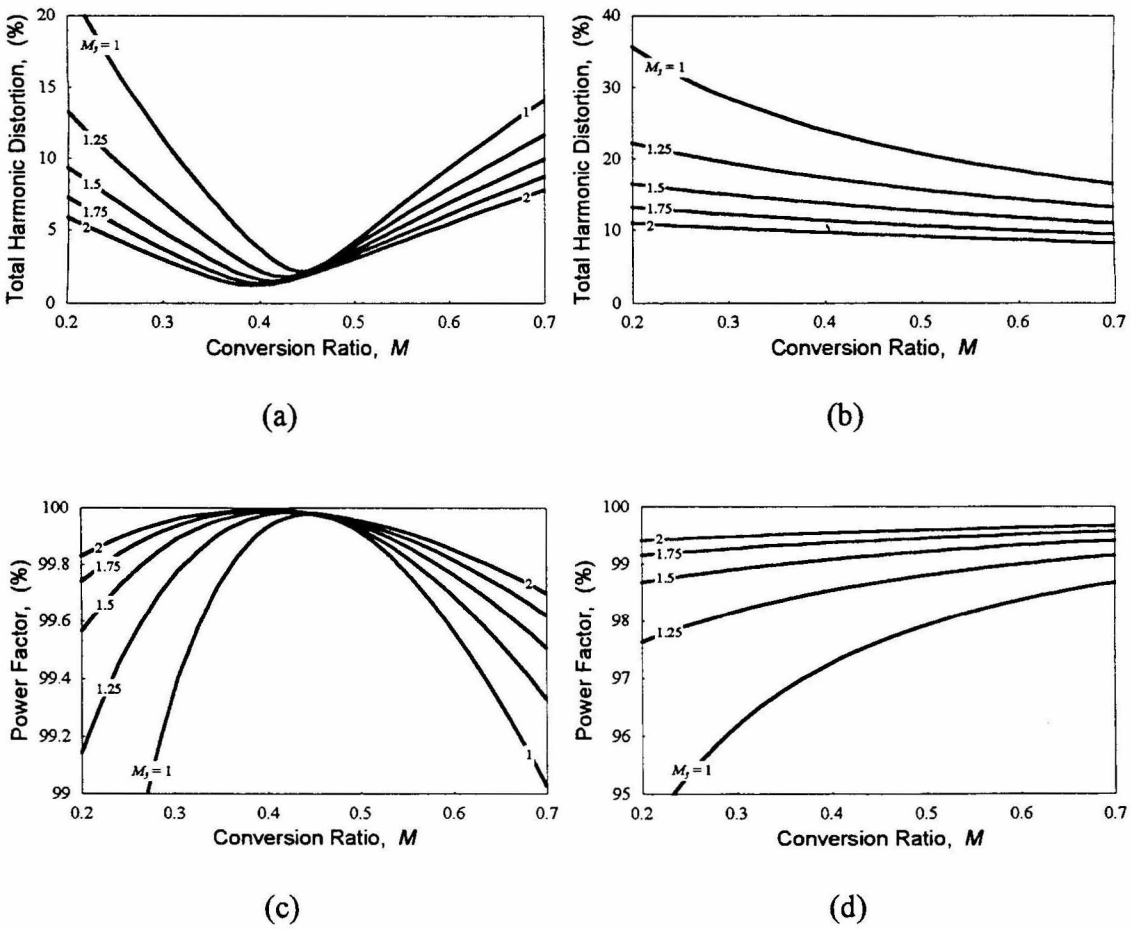

Figure 6.5: The calculated total harmonic distortion versus the conversion ratio M: (a) Bifred with constant diode current control and (b) Boost or Bifred with conventional mode of operation (constant duty ratio) and same switch voltage stress. The calculated power factor versus the conversion ratio M: (c) Controlled Bifred and (d) constant duty ratio Bifred or Boost. (Note the different vertical scales on the vertical axes.)

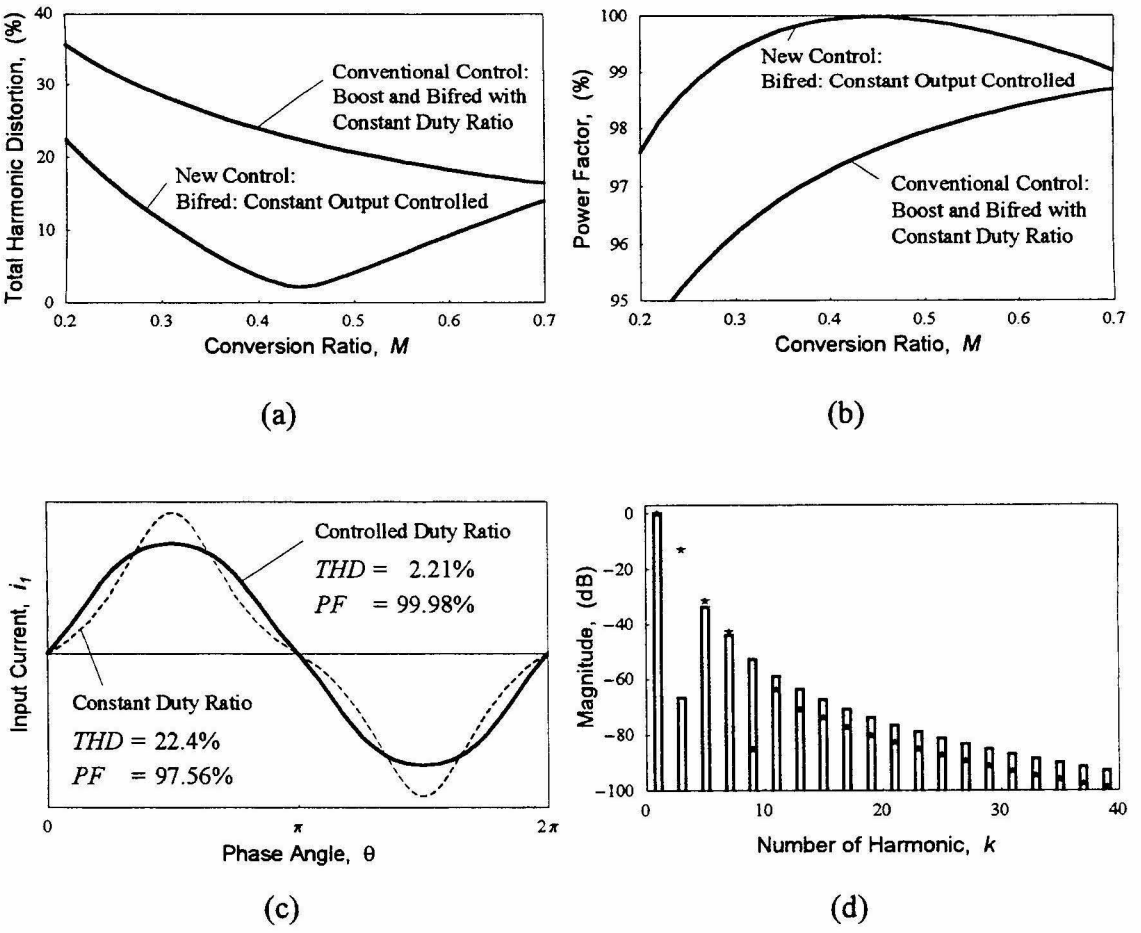

Figure 6.6: Comparison between constant diode current control method and the conventional mode of operation with constant duty ratio at M_3=1 (i.e., at the lowest possible voltage stress for the Bifred). (a) The total harmonic distortion versus the conversion ratio M. (b) The power factor versus the conversion ratio. (c) The input current. (d) The harmonic content of the input current: bars controlled diode current; stars: constant duty ratio Bifred or Boost.

From Fig. 6.6c it becomes apparent what this control method accomplishes. It virtually eliminates the third harmonic, whereas the rest of the spectrum is not significantly affected. The low value of the ninth harmonic in the constant duty ratio case is merely a coincidence for this particular conversion ratio. It is not generally low. It has been shown in [1] that for certain conversion ratios certain harmonics become zero. A similar behavior was encountered in Fig. 4.5b in Chapter 4.2. The higher order harmonics are in fact worse if the constant diode current control method is applied. This is not a problem because the values are very low in both cases. The second order effects observed in a real circuit at higher order harmonics are much more significant than the difference between the two predictions.

6.3.2 Universal Input Voltage

Until now, one single point of operation has been considered. The waveform shown in Figs. 6.6c and 6.6d are obtained by optimizing the converter for this point. In many cases the input voltage and the output voltage varies over a certain range. One important case is the universal input voltage range from $90V_{RMS}$ to $270V_{RMS}$. Even if the circuit is designed to work over this range, the harmonic distortion is significantly reduced compared to a converter operating with constant duty ratio.

The value of M_3 depends on the ratio of the inductances L_1 and L_2 and on the conversion ratio M. This can be concluded using (6.2.33) and the definitions (6.2.2) through (6.2.6). In order to plot the *THD* or the *PF* versus M at a constant M_3, as in Fig. 6.5 and 6.6, the ratio L_1 to L_2 must be adjusted for each point in the graph. Once a converter is designed, the values of L_1 and L_2 are fixed and M_3 changes as M changes. The inductors must be designed in such a way that the inequalities (6.2.19) and (6.2.20) are satisfied under all possible conditions.

Figure 6.7a shows the prediction of the total harmonic distortion and Fig. 6.7b the power factor in a design for the universal input voltage range (90V to 270V). The output voltage (reflected to the primary side of the transformer in the isolated version) was fixed at 85V. To some degree, this is an arbitrary choice. Increasing the output

voltage improves the current waveform at high input voltages with some penalty at the low end and vice-versa. The expected values of the *THD* and the *PF* are marked on the plots for a few interesting points.

Figure 6.7c shows the most relevant voltages of the converter as a function of the input voltage. M_3 (i.e., V_1/V_g) is unity only at 90V. This leads to the conclusion that (6.2.20) must be satisfied at the largest possible conversion ratio, in order to be satisfied in all cases. The fact that M_3 is larger than unity at higher input voltages adds some extra stress on the switches. Despite the large input voltage range, the switch stress remains in acceptable limits. The increased M_3 also has a positive effect. It widens the input voltage range with a low distortion of the input current. It is important to mention that (6.2.20), and thus, V_1 does not depend on the load. This can be concluded from (6.2.33). In the original version of the Bifred, as it was presented in [15], V_1 did strongly depend on the load level.

The necessary duty ratio modulation over one half of a line cycle is shown in Fig. 6.7d together with the conduction angle of the two inductors. This graph illustrates the division of one switching cycle into the four subintervals as a function of the phase angle. The inequality (6.2.19) ensures that the conduction angle of L_2 is always less than one. This sets an upper limit on the power processing capability of a given converter at a given set of values for the input and output voltage. The second inequality, (6.2.20), guarantees that the conduction angle of L_1 is less than the one of L_2 for every phase angle θ.

The expected current waveforms of a converter that is designed to operate over the universal input voltage range are shown in Figs. 6.8a and 6.9b for nominal voltages and in Figs. 6.8c and 6.8d for the two extreme cases. Under nominal conditions, the *THD* is expected to remain well below 10%.

6.3.3 Limited Input Voltage Range

As it has been demonstrated, this converter is entirely suitable to operate over the universal input range. If the input voltage range can be limited, the performance can be

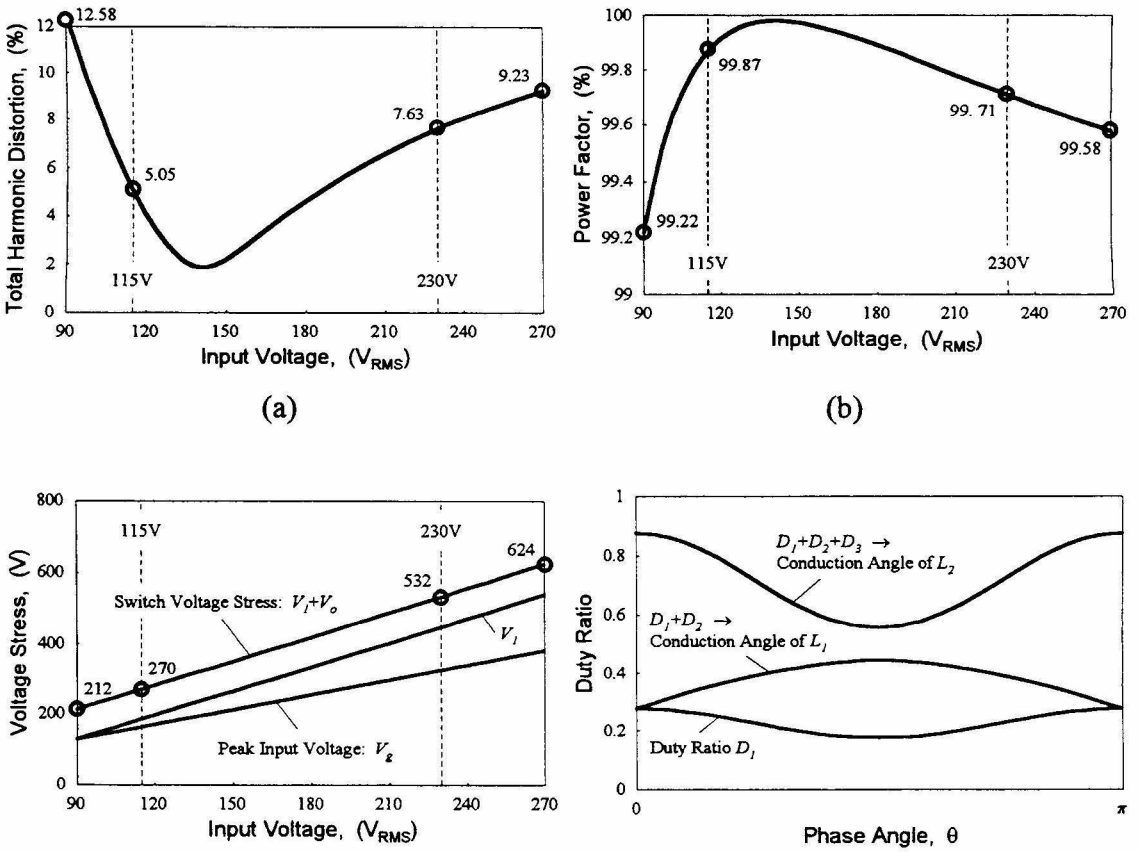

Figure 6.7: Universal input voltage range: predicted behavior based on an output voltage of 85V (reflected to the primary in the isolated version). (a) Total harmonic distortion versus the input voltage. (b) Power factor versus the input voltage. (c) Dependence of the voltages in the converter as a function of the input voltage. (d) Length of each subinterval of a switching cycle as a function of the phase angle. (In this example V_{ac}=90V, V_o=85V.)

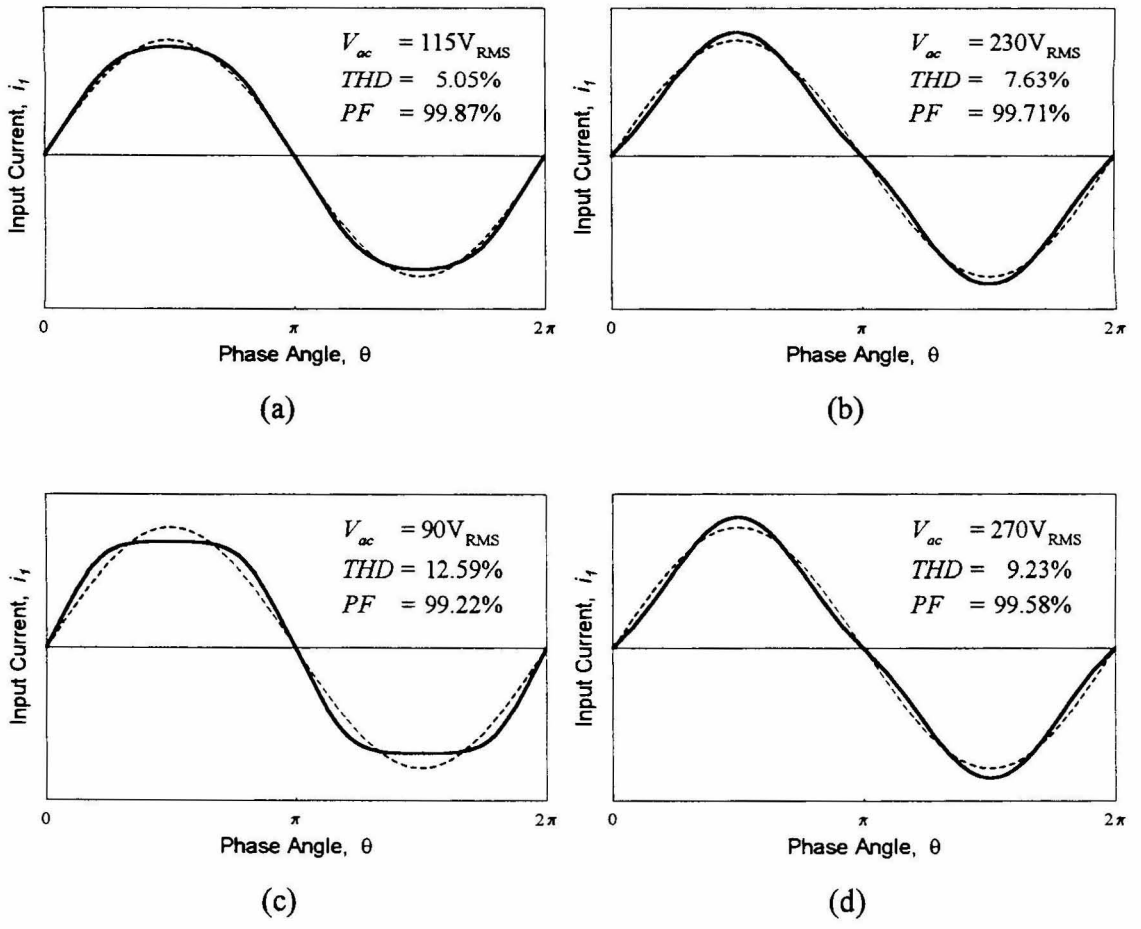

Figure 6.8: Universal input voltage range: predicted input current waveforms, THD and PF based on an output voltage of 85V (reflected to the primary in the isolated version) (a) and (b) Nominal input voltages. (c) and (d) Extreme input voltage values. The dashed line represents the fundamental component.

improved even further as demonstrated by the European input voltage range from 185V to 265V. The output voltage was fixed at 135V. Figures 6.9a and 6.9b show the predicted *THD* and *PF* as the input varies over the above mentioned range. The expected distortion is again significantly reduced. An additional benefit is the smaller difference between V_1 and V_g which results in a lower switch voltage stress. The stress is predicted to be 565V at most as opposed to 624V in the previous case (Figs. 6.9c and 6.7c). The resulting input current at nominal input voltage is nearly ideal as shown in Fig. 6.10c. The waveforms at low and high line voltage are shown in Figs. 6.10a and 6.10b. They still contain very low distortion (less than 5%).

6.3.4 Variable Output Voltage

Finally, the input voltage was fixed and the output voltage was varied over a range from one to two. As this does not refer to a particular case, all voltages are normalized with respect to the peak line voltage V_g. The expected *THD* and *PF* are shown in Figs. 6.11a and 6.11.b respectively. The optimal conversion ratio is slightly shifted to M = 0.43 since M_3 is not exactly unity. As shown in Fig. 6.11c, the switch voltage stress is nearly independent of the conversion ratio. The lowest value of M_3 occurs at the highest conversion ratio. The slightly distorted input currents at low and high output voltage are shown in Fig. 6.12a and 6.12b, whereas Fig. 6.12c exhibits the nearly ideal current waveform at M = 0.43.

In order to verify the analytical results presented so far, an experimental circuit was built. The measurements taken are supplied in the following section.

6.4 Experimental Results

The presented results must be achieved with a control strategy that ensures a constant diode current $\bar{i}_d$. In many cases, where the load is time invariant, it is sufficient to have an output voltage feedback and a fast controller (i.e., a controller with a bandwidth well above twice the line frequency). In some cases, it is better to sense the diode current $\bar{i}_d$

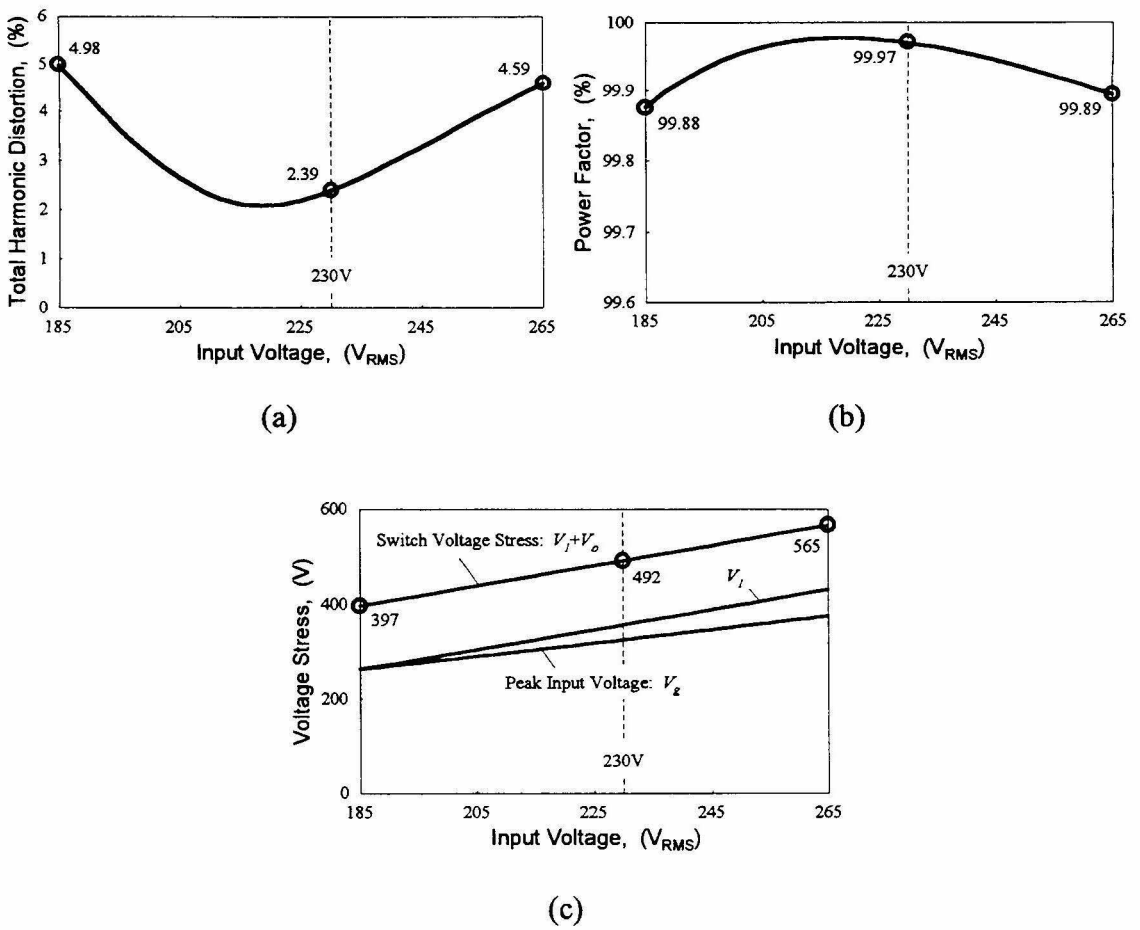

Figure 6.9: European input voltage range: predicted behavior based on an output voltage of 135V (reflected to the primary in the isolated version). (a) Total harmonic distortion versus the input voltage. (b) Power factor versus the input voltage. (c) Dependence of the voltages in the converter as a function of the input voltage.

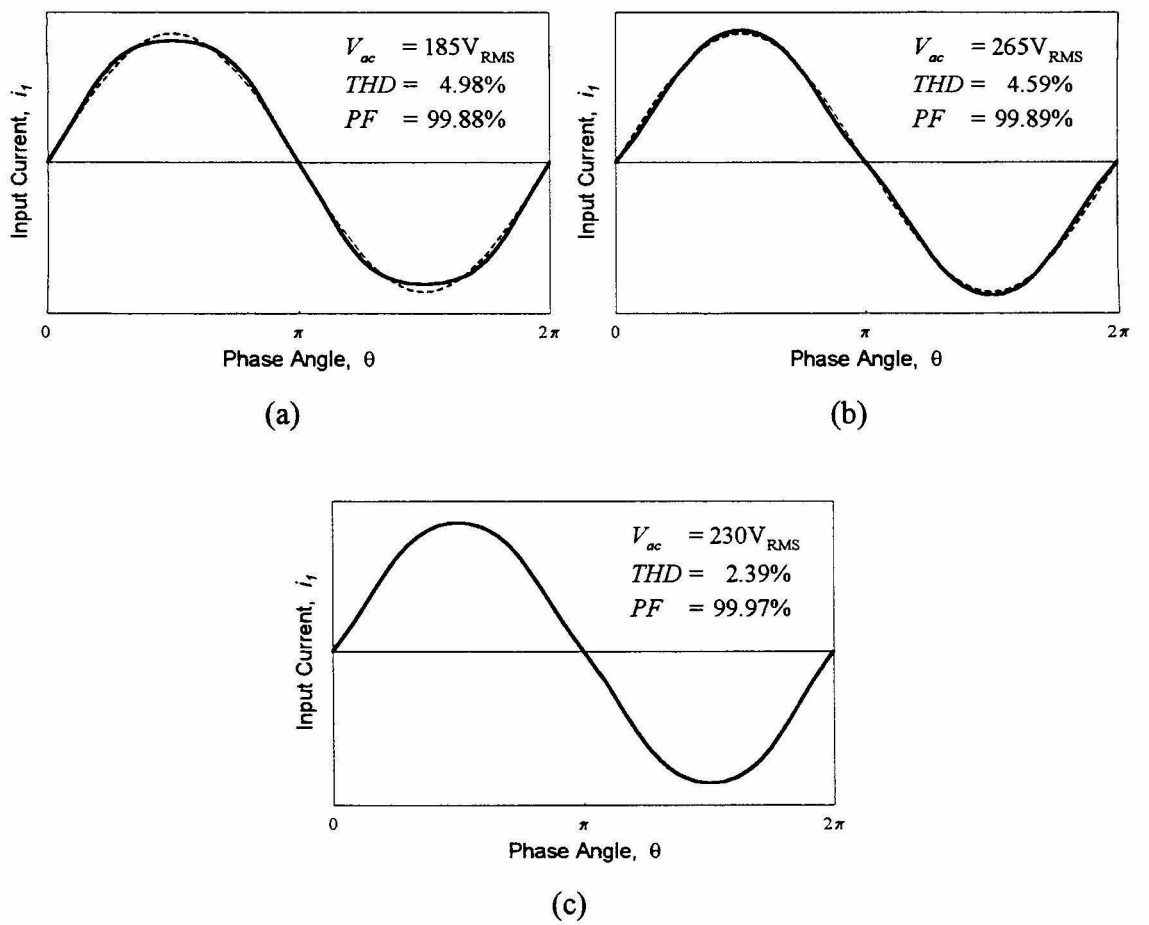

Figure 6.10: European input voltage range: predicted input current waveforms, THD and PF based on an output voltage of 135V (reflected to the primary in the isolated version). (a) and (b) Extreme input voltage values. The dashed line represents the fundamental component. (c) At the nominal input voltage.

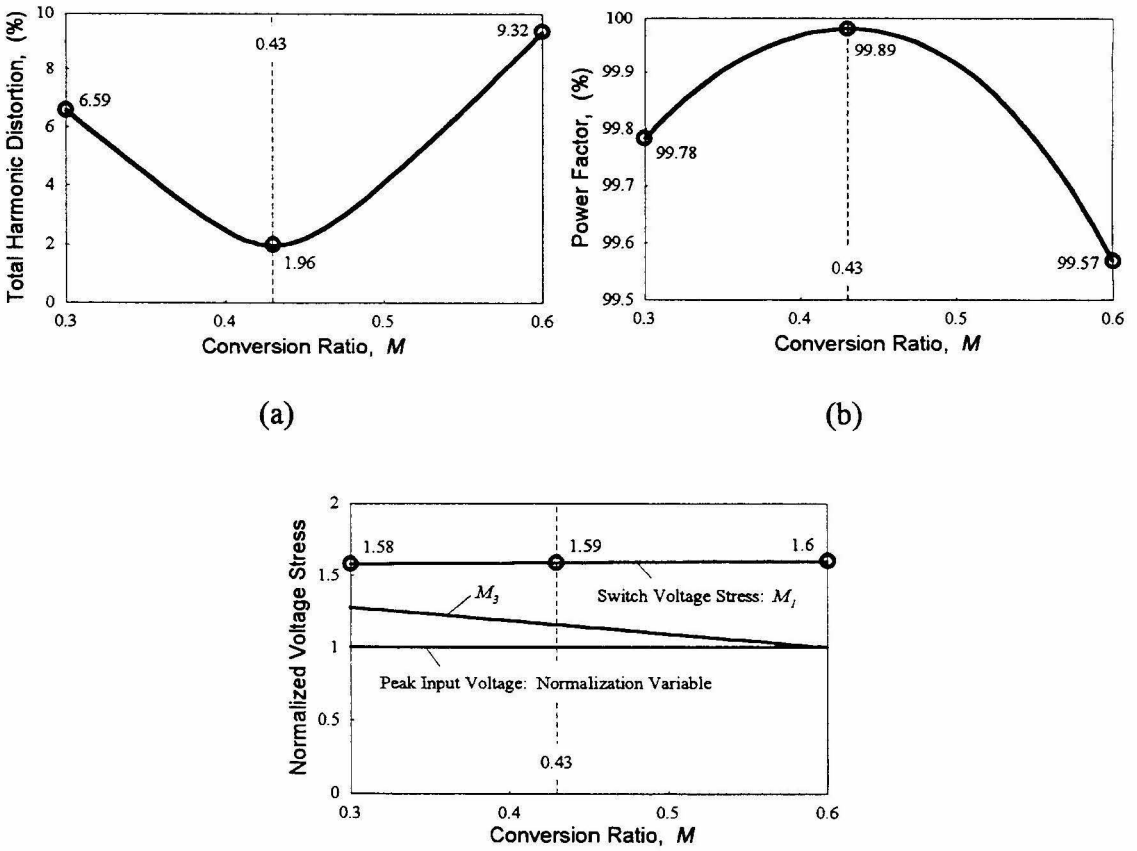

Figure 6.11: Variable output voltage range: predicted behavior. (a) Total harmonic distortion versus the conversion ratio. (b) Power factor versus the conversion ratio. (c) Dependence of the voltages in the converter as a function of the conversion ratio.

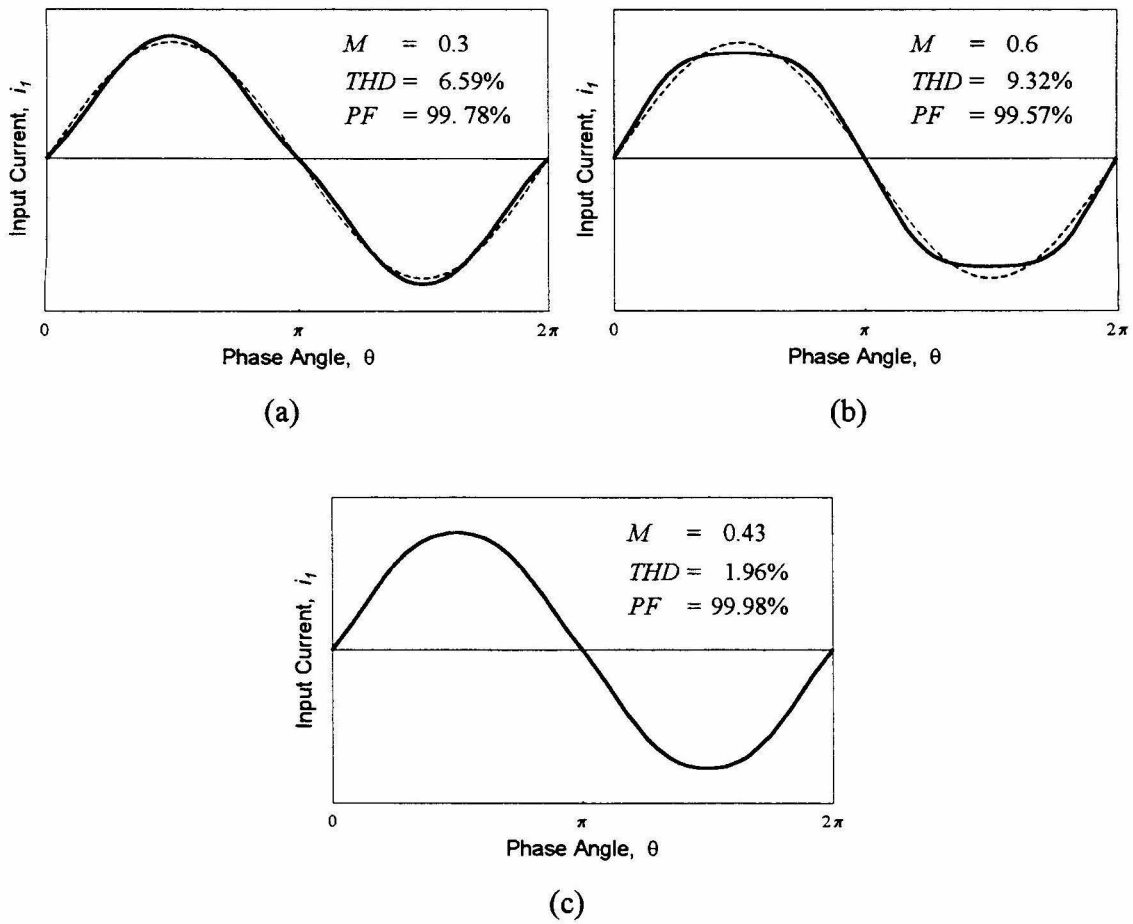

Figure 6.12: Variable output voltage range: predicted input current waveforms, THD and PF. (a) and (b) Extreme conversion ratios. The dashed line represents the fundamental component. (c) At the optimal conversion ratio.

and control this quantity with a feedback loop. Since $\bar{i}_d$ is discontinuous, a simple current transformer can be used. As a matter of fact, the control problem is closely related to the one described for the three-phase case in Chapter 4.6. The two control methods are illustrated in Figs. 4.20. The validity of the analysis was tested on an experimental circuit without isolation transformer. It converted a power level of 120W from $80V_{AC}$ into $50V_{DC}$.. The two-loop control method was applied, similar to the one shown in Fig. 4.20b. The values of the circuit elements were L_1=57μH, L_2=95μH, C_1=1mF, C_2=470μF and R_l=25Ω. A simple L-C-filter was connected between the input of the converter and the ac voltage source. The component values were C_f=1μF and L_f=227μH.

To have a reference a measurement with constant duty ratio was taken. The measured input current together with the output voltage ripple is shown in Fig. 6.13a. The frequency spectrum of the same current is presented in Fig. 6.13b. The current waveform definitely resembles the prediction shown in Fig. 6.6c. In addition, a severe output voltage ripple is observed. The measured frequency spectrum confirms that the 9th harmonic almost vanishes as predicted in Fig. 6.6d. The *THD* is found be 21.4%, which is close to the prediction of 22.4%.

The same waveforms with the fast loop in place are shown in Fig. 6.14a, and the corresponding frequency spectrum is depicted in Fig. 6.14b. Again, the current waveform predicted in Fig. 6.6c can be verified. The output voltage ripple has nearly vanished. The measured *THD* dropped to 3.5%. The difference from the predicted 2.2% can be partially explained by the non-ideality of the control loop. The diode current contains a certain amount of residual ripple. For the same reason, the 3rd harmonic is not as low as predicted. It should be noted that this is displayed in a semi logarithmic scale. This means that for low magnitudes, differences between the measurement and the prediction have little significance. The overall agreement between the measurement and the prediction is satisfactory.

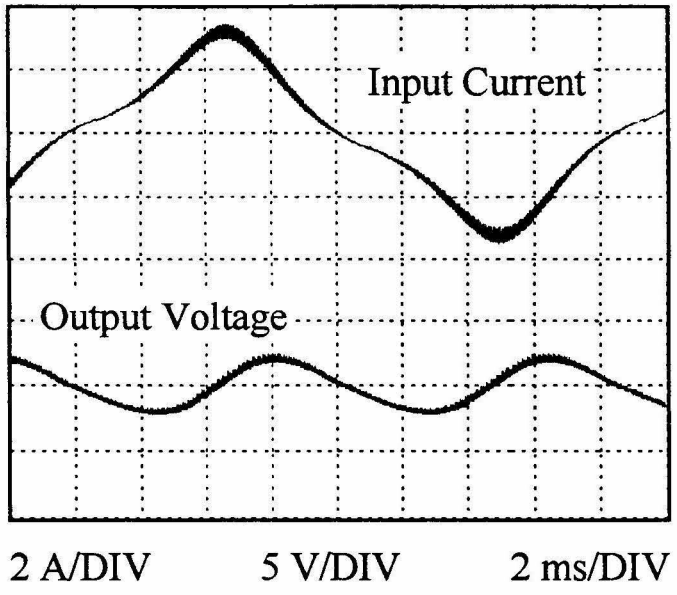

(a)

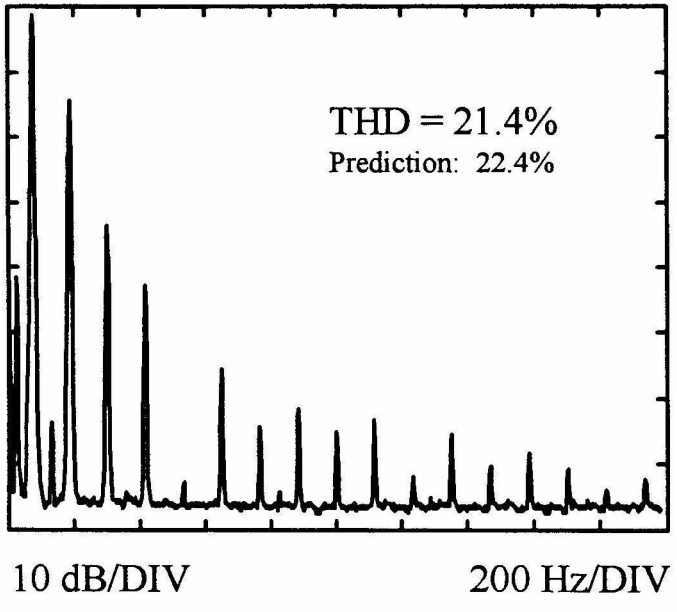

(b)

Figure 6.13: Constant duty ratio controlled Bifred converter: (a) Input current and ac component of the output voltage and (b) measured frequency spectrum and THD.

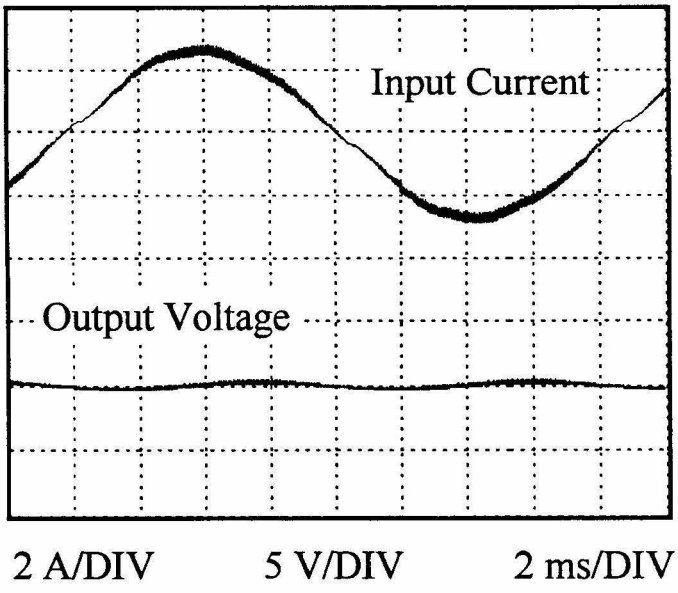

(a)

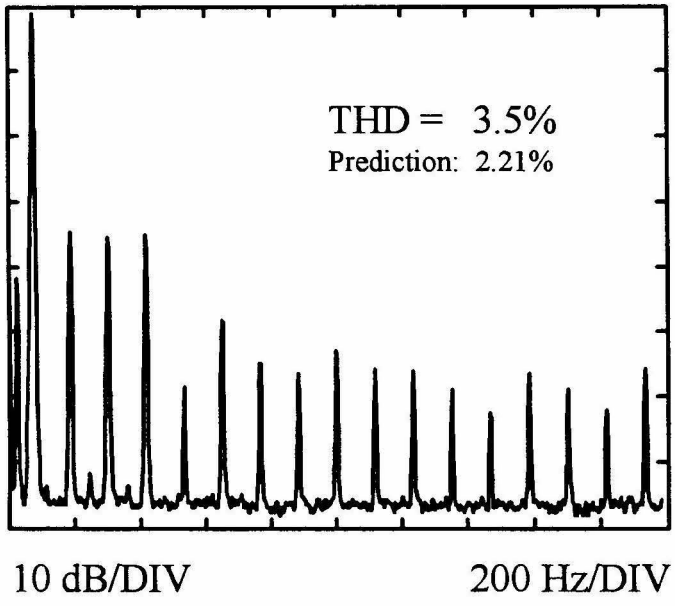

(b)

Figure 6.14: Constant diode current controlled Bifred converter: (a) Input current and ac component of the output voltage and (b) measured frequency spectrum and THD.

Chapter 7

Conclusion

This part of the thesis discusses the power quality of ac-to-dc rectifiers. These rectifiers often introduce harmonic distortion into the utility line. Two main reasons have been identified that explain why harmonic distortion must be limited. Firstly, the components of power generation and transmission systems must be over-rated in order to handle the distortion and the extra losses associated with it. Secondly, the current distortion can cause other equipment connected to the same line to malfunction.

Besides the distortion, the power factor is also used to describe the power quality. It has been shown that the power factor is closely related to the harmonic distortion, particularly if the input voltage is an ideal sine wave. In this case, the power factor directly depends on the total harmonic distortion and the phase displacement between the fundamental current component and the voltage. A unity power factor requires zero harmonic distortion.

The principal sources of the harmonic distortion have been identified for the single-phase and three-phase ac-to-dc rectification. In the single-phase case, it is the "peak detector" circuit at the input of the rectifier, which generates a large amount of harmonic distortion (THD>100%). In the three-phase rectifiers, it is the six-pulse diode bridge which is connected to a constant power sink. The result is a quasi-rectangular current waveform with a THD of 32%.

A single active switch three-phase power factor corrector was presented. The current shaping is a natural property of this converter. The simplicity of the circuit and the great performance make this a favorable topology. If the converter is operated with a constant switching frequency, the achieved THD is reasonably low. However, the

performance can further be improved if a fast output feedback loop is implemented. This loop removes the six times the line frequency ripple in the output voltage and simultaneously enhances the input current shape.

It has been shown that there exists an optimal duty ratio for this converter. Moreover, the constant output control mentioned above approximates the optimal duty ratio so closely that any attempt to implement the optimal duty ratio can not be justified. Four additional control laws for this converter were investigated and compared with the optimal and the constant duty ratio case.

The converter was extended using a Cuk and Sepic-derived isolated version. The reason for this extension is twofold: it allows an isolation transformer to be introduced, and the converter can be designed for an arbitrary conversion ratio. The non-isolated version requires a conversion ratio greater than unity (since it is a Boost derived topology). The problem that arises is the six times the line frequency ripple at the output of the converter. The introduction of a second switch provides a solution. This switch decouples the input and the output of the converter and enables an independent control of the output voltage.

A set of small-signal equations has been derived which make it possible to predict the expected output voltage ripple, and even more importantly, serve as a tool to avoid oscillatory designs. Experimentally obtained results of the isolated and non-isolated version of the three-phase ac-to-dc-rectifier are in good agreement with the prediction.

Finally, a single-phase converter was discussed which exhibits a similar behavior. It can be operated with a constant duty ratio over one line cycle. The achieved *THD* is approximately 20%. When the converter has an appropriate conversion ratio, a fast output feedback loop can reduce the *THD* to almost 2% without increasing the switch voltage stress. Again, the feedback loop solves two problems at the same time. It removes the output voltage ripple at twice the line frequency and it drastically reduces the harmonic distortion in the input current.

Even though there is an optimal conversion ratio, as far as the current shaping function is concerned, it has been demonstrated that the results are highly satisfactory over the whole universal input range.

In order to verify the analysis with measurements, an experimental circuit was built. The excellent agreement between the prediction and measurement confirms the interesting properties of the converter.

Part II

Small-Signal Analysis of Converters in Discontinuous Conduction Mode

Chapter 8

Introduction

Small-signal modeling has been a part of power electronics research for more than a quarter of a century. During this time, several methods have been developed to predict the small-signal behavior of switched mode converters. The principal difficulty is that a switched-mode converter represents a highly non-linear system. This system is to be approximated around a point of operation using linear techniques.

Switched-mode converters can operate in two different modes: the continuous conduction mode (CCM) and the discontinuous conduction mode (DCM). In many respects the CCM is easier to handle. This particularly applies to the small-signal analysis. Several methods have been developed to analyze the small-signal behavior of converters in CCM. Even though these methods might appear to be different; the majority of these lead to exactly the same result. The standard method is the so-called state-space averaging.

The situation is different with regard to converters in DCM. Not all models do agree. One can distinguish between so called full-order models and reduced-order models. Given the same converter, the full-order models in DCM are of the same order as their counterparts in CCM. The order of reduced-order models is decreased by the number of components in DCM. At low frequencies, all models generally give the same result. When the frequency approaches half the switching frequency, a significant difference can be observed. Measurements seem to suggest that the full order models are correct.

This part of the thesis is focused solely on the DCM case. The reason for introducing yet another model is twofold. The model is simple to apply, and it leads to

extremely accurate results. Some full-order models are difficult to apply if the circuit is complicated. State-space averaging is the widely accepted standard method to perform the small-signal analysis. However, it leads to a reduced-order model which is inaccurate at higher frequencies. The new theory, developed in Chapter 9, demonstrates that the result of state-space averaging can be modified in order to account for the effects at higher frequencies.

Chapter 9 starts with a line of arguments supporting the claim that there is an alternative way to deal with the DCM. This is followed by the derivation of an expression which accurately accounts for the mechanism encountered in DCM. The result can then be approximated using a simple delay term. This term can be added to the transfer function obtained by a reduced order model (e.g., state-space averaging). The results gained by this method are compared to a series of measurements, and are indeed satisfactory.

State-space averaging in DCM is more difficult to accomplish than in CCM. The complexity of the method is even further increased, if more than one element operates in DCM. In Chapter 10 an algorithm is introduced, which allows the performance of state-space averaging in DCM in a simple manner, even if there is more than one element in DCM. The procedure is standardized and therefore user and computer friendly.

Chapter 9

Alternative Approach to Model the Small-Signal Behavior of Converters in Discontinuous Conduction Mode

Switch mode converters are inherently nonlinear devices. For several purposes it is of great help to have linear small-signal models. They can be used to design a feedback loop using well-known linear control techniques. They serve to determine the input and output impedance of a converter, which are necessary to predict the interaction with the surrounding circuitry. Another case for the use of the small-signal model is the response at the output of a converter to an incremental change at the input.

All switch mode topologies can potentially operate in two different modes, which are called continuous conduction mode (CCM) and discontinuous conduction mode (DCM). A lot of effort has been invested in order to find suitable small-signal models for both modes of operation. Models for converters in CCM are presented in [12,13,17]. Even though the methods to arrive at the desired result are different, most of the suggested models are equivalent.

In DCM the suggested small-signal models differ considerably. They can be divided into two groups. The first group contains models that are of the same order as the corresponding CCM model. Hence, the number of reactive components in the converter determines the order of the model. These models are also called *Full-Order Models*. Examples of these type of models are given in [18-20] as well as the loss-free resistor concept in [21]. The second group consists of the models of lower order than the corresponding CCM model. In most cases, each discontinuous component reduces the

order by one. These models are referred to as *Reduced-order Models*, where examples can be found in [22-24].

The model derived in this chapter can not be allocated to either one of the described groups. The order is given by the number of discontinuous components plus one. Thus, with one element in DCM, the new model is a full-order model and with more than one element in DCM it becomes a reduced-order model.

9.1 Motivation for a New Model

Existing full-order models as [18-21] predict the behavior of the transfer function very well for frequencies lower than half the switching frequency. The behavior at higher frequencies than these is of little practical interest. Therefore, the question might be asked; why is another model introduced? The most standard method to evaluate the transfer function is by using state-space averaging. This method is presented in [13] for converters in CCM and in [22] for DCM. In the latter case a reduced-order model is obtained. It is well known that the predicted transfer function does not provide accurate results close to half of the switching frequency. In this chapter a correction term is derived that can be added to the transfer function obtained by a reduced-order model to account for the effects observed at higher frequencies. This correction term can be determined in a very simple manner. Therefore, the transfer function can be obtained using the well-known state-space averaging technique. If accurate results are required at higher frequencies, the simple correction term can be added.

If one element is in DCM, the resulting transfer function corresponds to a full-order model. However, it is different from the transfer function obtained by the previously suggested methods. If more than one element is in DCM, the resulting transfer function corresponds to a reduced-order model.

One argument often used to support the validity of the full-order model is the following: From a physical point of view the characteristics of a system can not change abruptly. The order of a converter has to be maintained as it enters DCM. This is not a valid argument for small-signal considerations. Fig. 9.1 shows a two port network with

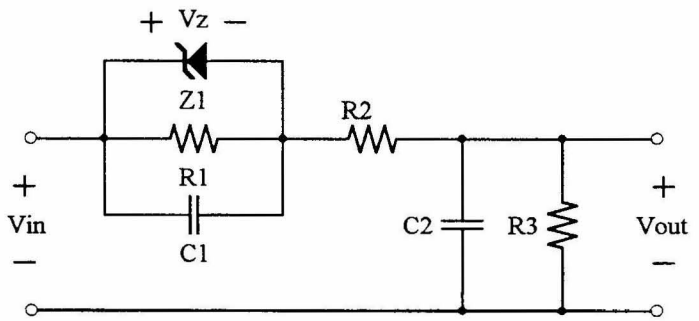

Figure 9.1: Simple two port network.

two reactive components. V_z is the zener voltage. The input to output transfer function is not the same for all input voltages. Clearly, if

$$V_{in} < V_z \frac{R_1 + R_2 + R_3}{R_1} \tag{9.1.1}$$

then the transfer function is of second order. Conversely, if

$$V_{in} > V_z \frac{R_1 + R_2 + R_3}{R_1} \tag{9.1.2}$$

then the transfer function is of first order. This is a simple, physically realizable network, which illustrates that the small-signal behavior can change abruptly. The small-signal expressions depend on the derivatives of the large-signal quantities. Even though some large-signal values must be continuous functions due to the laws of physics, their derivatives can be discontinuous.

Another point of interest is the existence of a right half plane zero in the control-to-output transfer function. For example, they appear in the Boost and the Buck-Boost converter in CCM. Both of these converters are second order systems. A second order system without any zeros is represented by the following transfer function:

$$H(s) = H_o \frac{1}{1 + \frac{1}{Q}\frac{s}{\omega_o} + \left(\frac{s}{\omega_o}\right)^2} \tag{9.1.3}$$

The shape of the unit step response in the time domain of a system that is described by $H(s)$ depends on the Q-factor. It is represented by a well-documented set of curves, which can be found in any fundamental textbook on linear control, for example in [25]. In converters operating in CCM, the Q-factor is always greater than 0.5. In that case the expressions for the unit step response $h(t)$ and its time-derivative are given by

$$h(t) = H_o\left(1 - e^{-\alpha t}\left(\cos(\omega t) + \frac{\alpha}{\omega}\sin(\omega t)\right)\right) \tag{9.1.4}$$

$$\frac{dh(t)}{dt} = H_o\left(\frac{\alpha^2 + \omega^2}{\omega}\right)e^{-\alpha t}\sin(\omega t) \tag{9.1.5}$$

where

$$\alpha = \frac{\omega_o}{2Q} \tag{9.1.6}$$

$$\omega = \omega_o\sqrt{1 - \frac{1}{4Q^2}} \tag{9.1.7}$$

For the purpose here it is important to notice that the step response is always positive at any value for t. In addition, during the initial phase, i.e., for

$$t < \frac{\pi}{\omega}, \tag{9.1.8}$$

the step response has a positive time derivative.

As mentioned above several second order converters have a right half plane zero in their transfer function. To represent such a converter, (9.1.1) must be modified to

$$G(s) = H_o\frac{1 - \frac{s}{\omega_z}}{1 + \frac{1}{Q}\frac{s}{\omega_o} + \left(\frac{s}{\omega_o}\right)^2} \tag{9.1.9}$$

This can be written as

$$G(s) = H(s) - \frac{s}{\omega_z} H(s) \tag{9.1.10}$$

The term $sH(s)$ represents the time derivative of $H(s)$. Therefore, the step response and its derivative can now easily be found using (9.1.4) and (9.1.5).

$$g(t) = h(t) - \frac{1}{\omega_z} \cdot \frac{dh(t)}{dt} \tag{9.1.11}$$

$$g(t) = H_o \left(1 - e^{-\alpha t} \left(\cos(\omega t) + \frac{\alpha^2 + \omega^2 + \omega_z \alpha}{\omega_z \omega} \sin(\omega t) \right) \right) \tag{9.1.12}$$

$$\frac{dg(t)}{dt} = H_o \left(\frac{\alpha^2 + \omega^2}{\omega_z \omega} \right) e^{-\alpha t} \left((\alpha + \omega_z) \sin(\omega t) - \omega \cos(\omega t) \right) \tag{9.1.13}$$

The value of the derivative of $g(t)$ at $t = 0$, which is the initial slope of the unit step response, is given by

$$\frac{dg(0)}{dt} = -H_o \frac{\alpha^2 + \omega^2}{\omega_z} \tag{9.1.14}$$

Using (9.1.6) and (9.1.7) this can be expressed as

$$\frac{dg(0)}{dt} = -H_o \frac{\omega_o^{\,2}}{\omega_z} \tag{9.1.15}$$

This value is always negative. This means a second order converter (or any second order system) with a right half plane zero starts to respond in the wrong direction if a step is applied at the control input. Equation (9.1.15) was obtained under the assumption that the Q-factor is greater than 0.5. A similar analysis reveals that if the Q-factor is equal or smaller than 0.5, the initial slope of the unit step response is still given by (9.1.15).

It is interesting to understand what the physical reason for this right half plane zero is in switch mode converters. The Boost converter shown in Fig. 9.2 is used to explain this phenomenon. The inductor current I_L and the diode current I_D for the CCM case are

shown in Fig. 9.3a. If a step ΔD is applied to the duty ratio, the inductor current changes from the solid to the dashed line, and it will eventually assume a new steady state on a higher level. The result will be a higher output voltage. The diode current also changes from the solid to the dashed line. Since the I_L can not change immediately to a higher value, the charge denoted by Q_1 is larger than Q_2. Therefore, the average diode current directly after the step is smaller than before. The output capacitor C receives less charge and the output voltage drops initially.

The situation is different if the inductor L operates in DCM and a step is applied to the duty ratio. The charge Q_1 in Fig. 9.3b is always smaller than Q_2. Thus, the charge below the solid line is always smaller than the one below the dashed line. Consequently, the average diode current never decreases and the same applies to the output voltage. This seems to imply that there is no right half plane zero in the control-to-output transfer function if the Boost converter operates in DCM. The same line of argument can be made for the Buck-Boost, Cuk and other converters possessing a right half plane zero in the control-to-output transfer function.

In contrast, the Buck converter and similar topologies operating in CCM do not behave according to the above discussion. Evidently, the output voltage increases immediately after the step is applied. That is why their small-signal transfer functions have no right half plane zero even in CCM.

Finally, one more remark. It has been argued that a converter in DCM must be of the same order as the number of reactive components in the circuit. However, it must be noted that a switch mode converter is a highly nonlinear system, and therefore, it is of

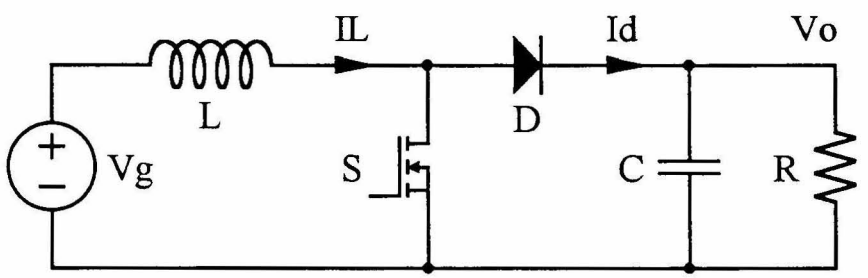

Figure 9.2: Simple Boost converter.

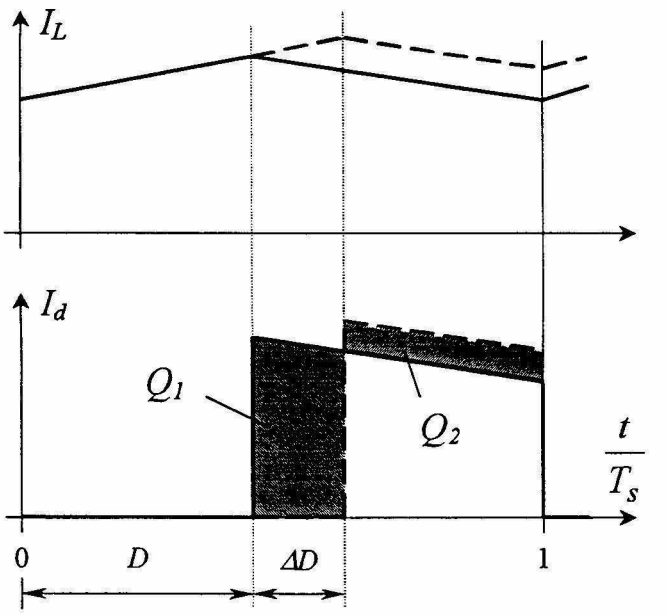

(a)

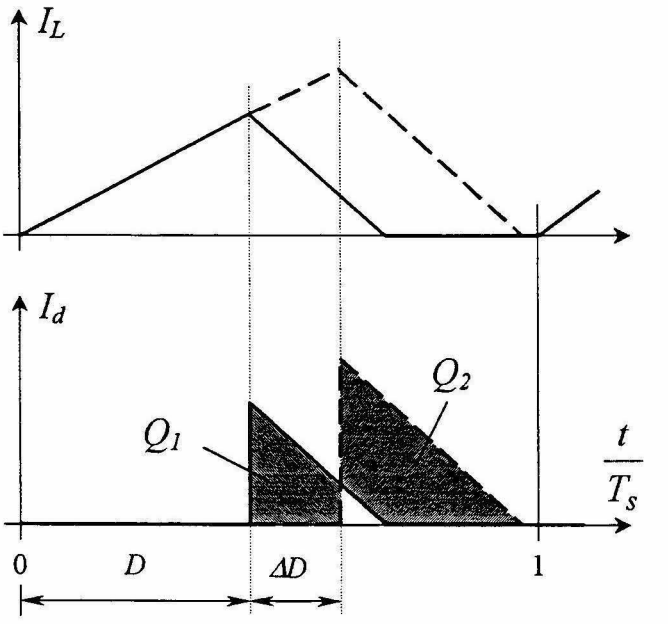

(b)

Figure 9.3: Inductor and diode current waveforms of a Boost converter (a) in continuous conduction mode and (b) in discontinuous conduction mode.

infinite order. The question should be, what order is necessary to approximate its behavior with sufficient accuracy? Most models agree that in the CCM case it is indeed the same as the number of reactive components. Nevertheless, this might not necessarily be true for converters in DCM, particularly if more than one state operates in DCM. This topic (i.e., multiple discontinuous conduction modes) is treated in Chapter 10.

9.2 The Description of the Discontinuous Current

In the previous section the diode current of a Boost converter was used to illustrate that there is a fundamental difference between the two modes of operation if an incremental change at the control input is applied. This suggests that the analysis must be focused on that current in order to understand the involved mechanisms. The characteristics of this current are investigated below.

9.2.1 Validity of the Model

The considerations are restricted to converters with the following configuration. The diode, which carries the discontinuous current, is connected to a linear circuit. The diode current i_d decreases linearly. This requires that the input voltage of the linear circuit must be approximately constant. This situation is illustrated in Fig. 9.4. For example, in the Boost and Buck-Boost converter this requirement is satisfied. During the first subinterval (i.e., while the active switch is on) the current i_d is zero. It starts to flow with its peak value at the beginning of the second subinterval. This interval ends when i_d reaches zero again. Thus, the input of the linear network is a pulsating current where the pulses have triangular shape.

9.2.2 Analysis of the Diode Current

If the duty ratio is perturbed in a small-signal sense, the triangles in Fig. 9.4 move their position and size accordingly. This was indicated in Fig. 9.3b. For the transfer function only the harmonic component of the output voltage at the same frequency as

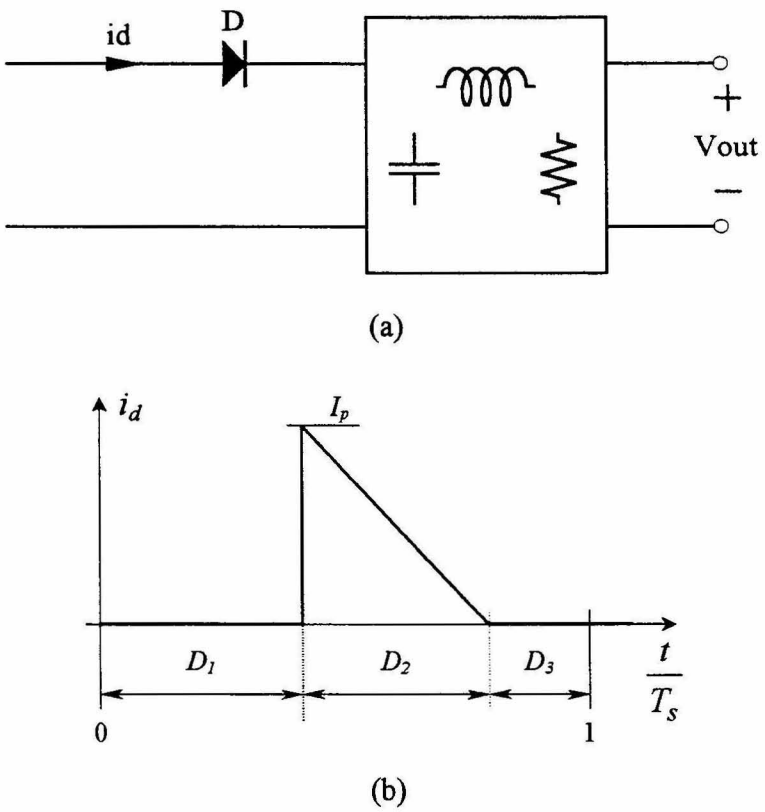

Figure 9.4: (a) A discontinuous diode current is supplying a linear network and (b) the diode current shape during one switching cycle.

the input perturbation is relevant. Due to the linearity of the output network, the triangular input current can be replaced by its harmonic component at this frequency without changing the output voltage reading.

The switching frequency is denoted by f_s and the duty ratio is perturbed at the frequency f. If these two frequencies satisfy

$$\frac{f}{f_s} = \frac{\omega}{\omega_s} = \frac{T_s}{T} = \frac{N}{M} \tag{9.2.1}$$

where M and N are positive integers, then the series of generated triangles is a periodic signal with a period length of M switching cycles or equivalently N perturbation cycles. In the example shown in Fig. 9.5 M is 5 and N is 1. Since the current i_d is periodic, a simple Fourier analysis can be applied to find its harmonic component at f. The same

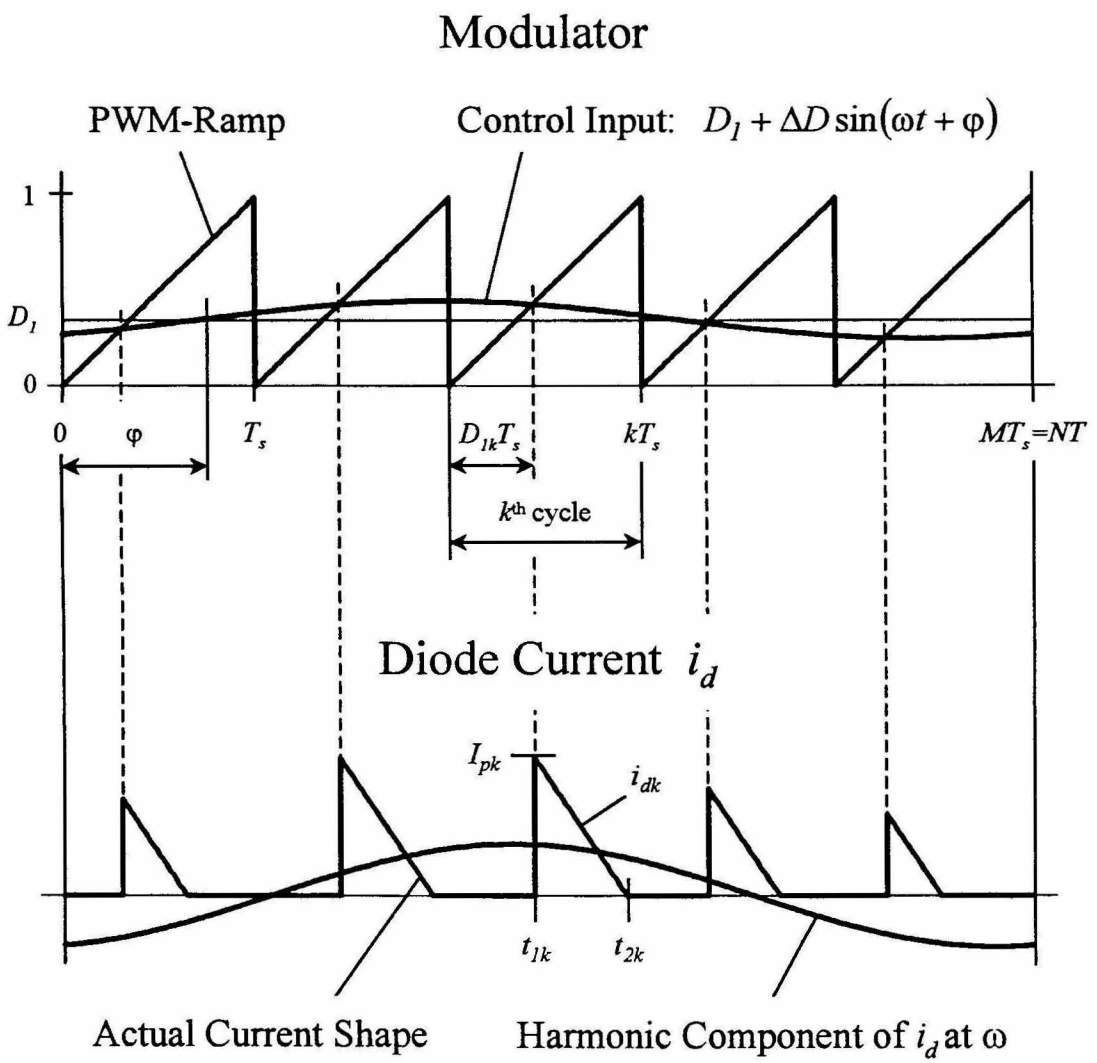

Figure 9.5: Upper traces: PWM modulator with a sinusoidal perturbation at the input. Lower traces: Resulting diode current i_d. The size and the position of the triangular pulses are changing. The calculated harmonic component of i_d at ω is shown with its magnitude scaled by a factor of 5 compared to the actual current waveform.

component could be found for an arbitrary frequency ratio using more difficult mathematical methods. This is not really necessary since every arbitrary ratio is as close as desired to a rational number if M and N are chosen sufficiently large. In addition, the desired frequency component is expected to be a smooth function of f (at least below half of the switching frequency).

A very similar analysis has been performed in [26] where the objective was to determine the delay of different types of pulse with modulators. The analysis follows in general the same steps with the added complication that the current i_d is triangular and the modulation affects the leading edge, the trailing edge, and the magnitude of i_d. In [26] only the trailing edge of a rectangular pulse train with constant magnitude was modulated.

As mentioned above, the analysis is based on the assumption that the input voltage of the linear network is constant. This is justified, since a small voltage ripple on top of the dc-value hardly affects the shape of the current triangles. The control input (the input of the modulator) is of the general form

$$d(t) = D_1 + \Delta D \sin(\omega t - \varphi) \tag{9.2.2}$$

where D_1 is the steady state duty ratio, ΔD is the magnitude of the perturbation, and φ is an arbitrary phase-shift. The intersections of this signal with the PWM-ramp can be described by the following equation:

$$D_{1k} = D_1 + \Delta D \sin(\omega(T_s(k-1) + D_{1k}T_s) - \varphi) \tag{9.2.3}$$

where k runs from 1 to N and enumerates the switching cycles. Since the perturbation must be small around the steady state point, the following inequality holds:

$$|D_{1k} - D_1| <<< \frac{2\pi}{\omega T_s} \tag{9.2.4}$$

Thus, D_{1k} can be replaced by D_1 inside the argument of the sine function. With that, (9.2.3) becomes

$$D_{1k} = D_1 + \Delta D \sin(\omega T_s(k - 1 + D_1) - \varphi) \tag{9.2.5}$$

This is an expression for the relative length of the first subinterval of the k^{th} switching cycle in terms of the control input.

Next, let μ be defined as

$$\mu \equiv \frac{V_{D2}}{V_{D1}} \tag{9.2.6}$$

where V_{D1} is the voltage across the inductor carrying the discontinuous current during the first subinterval of the switching cycle (i.e., during $D_1 T_s$) and V_{D2} is the same voltage during the second subinterval. Both voltages are assumed to be constant. In a Buck-Boost converter μ coincides with the conversion ratio; in a Boost converter the conversion ratio is $\mu + 1$.

Applying volt-second balance to this inductor leads to

$$D_{2k} = \frac{D_{1k}}{\mu} \tag{9.2.7}$$

The current during the second subinterval of the k^{th} switching cycle is given by

$$i_{dk}(\tau) = I_{pk} - \frac{I_{pk}}{D_{2k} T_s} \tau \tag{9.2.8}$$

where τ is zero at the beginning of each second subinterval. The peak current of the k^{th} switching cycle can be expressed as

$$I_{pk} = \frac{V_{D1}}{L} D_{1k} T_s \tag{9.2.9}$$

where L is the inductance value of the discontinuous inductor. This, together with (9.2.7), can be substituted into (9.2.8).

$$i_{dk}(\tau) = \frac{V_{D1}}{L} (D_{1k} T_s - \mu \tau) \tag{9.2.10}$$

The time variable τ can now be replaced by t which is zero at the beginning of the first switching cycle. This leads to

$$i_{dk}(t) = \frac{V_{D1}}{L} (D_{1k} T_s + \mu T_s (k - 1 + D_{1k}) - \mu t) \tag{9.2.11}$$

during the second subinterval of the k^{th} switching cycle. i_{dk} is zero during the other subintervals of each switching cycle. The starting time t_{1k} and using (9.2.7), the ending time t_{2k} of this second subinterval in the k^{th} switching cycle can be expressed as:

$$t_{1k} = (k-1+D_{1k})T_s \tag{9.2.12}$$

$$t_{2k} = \left(k-1+D_{1k}\left(1+\frac{1}{\mu}\right)\right)T_s \tag{9.2. 13}$$

Now, the harmonic component of $i_d(t)$ at the same frequency as the input signal must be found. This current component will be denoted by i_{dn}. A possible form of the Fourier representation of a signal is given by

$$f(t) = K_o + \sum_{i=1}^{\infty} |K_i| \sin(i\omega_f t + \mathrm{Arg}(K_i)) \tag{9.2.14}$$

where

$$K_o = \frac{1}{\tau}\int_0^{\tau} f(t)\,dt \tag{9.2.15}$$

$$K_i = \frac{2\mathrm{j}}{\tau}\int_0^{\tau} f(t)\,e^{-\mathrm{j}i\omega_f t}\,dt \tag{9.2.16}$$

(similarly as in (2.2.5) through (2.2.9)). The fundamental frequency ω_f in this example is given by

$$\omega_f = \frac{\omega}{N} \tag{9.2.17}$$

Only K_N is of interest here, since the frequency associated with K_N coincides with the perturbation frequency f. Substituting (9.2.11) into (9.2.16) and using the appropriate integration limits given in (9.2.12) and (9.2. 13) leads to

$$K_N = \frac{V_{D1}}{L}\cdot\frac{2\mathrm{j}}{NT}\cdot\sum_{k=1}^{M}\int_{(k-1+D_{1k})T_s}^{\left(k-1+D_{1k}\left(1+\frac{1}{\mu}\right)\right)T_s}\left(D_{1k}T_s+(k-1+D_{1k})\mu T_s-\mu t\right)e^{-\mathrm{j}\omega t}\,dt \tag{9.2.18}$$

This expression is somewhat easier to deal with if ωt is replaced by the phase angle θ. This requires a scaling of the magnitude and integration limits and by ω. $(T \to 2\pi)$. The modified equation is

$$K_N = \frac{V_{D1}}{L} \cdot \frac{\mathrm{j}}{N\pi} \cdot \sum_{k=1}^{M} \int_{(k-1+D_{1k})\omega T_s}^{\left(k-1+D_{1k}\left(1+\frac{1}{\mu}\right)\right)\omega T_s} \left((D_{1k}(\mu+1)+\mu(k-1))T_s - \mu\frac{\theta}{\omega} \right) e^{-\mathrm{j}\theta}\, d\theta \tag{9.2.19}$$

The integral inside the summation can be solved. The result is

$$K_N = \frac{V_{D1}}{L} \cdot \frac{1}{\omega N\pi} \cdot \sum_{k=1}^{M} \left(\omega T_s D_{1k} + \mathrm{j}\mu \left(1 - e^{-\mathrm{j}\omega T_s \frac{D_{1k}}{\mu}} \right) \right) e^{-\mathrm{j}\omega T_s (1-k+D_{1k})} \tag{9.2.20}$$

This expression can be multiplied out and rewritten as a sum of three different terms.

$$K_N = \frac{V_{D1}}{L} \cdot \frac{S_1 + S_2 + S_3}{\omega N\pi} \tag{9.2.21}$$

where

$$S_1 = \omega T_s \cdot \sum_{k=1}^{M} D_{1k} e^{-\mathrm{j}\omega T_s (D_{1k}-D_1)}\, e^{-\mathrm{j}\omega T_s (k-1-D_1)} \tag{9.2.22}$$

$$S_2 = \mathrm{j}\mu \cdot \sum_{k=1}^{M} e^{-\mathrm{j}\omega Ts (D_{1k}-D_1)} e^{-\mathrm{j}\omega Ts (k-1+D_1)} \tag{9.2.23}$$

$$S_3 = -\mathrm{j}\mu \cdot \sum_{k=1}^{M} e^{-\mathrm{j}\omega Ts (D_{1k}-D_1)\left(1+\frac{1}{\mu}\right)} e^{-\mathrm{j}\omega Ts \left(k-1+D_1\left(1+\frac{1}{\mu}\right)\right)} \tag{9.2.24}$$

The following is an often-used approximation if x is small.

$$e^x \approx 1 - x \tag{9.2.25}$$

Since it is assumed that the perturbation is small, the value of $D_{1k} - D_1$ is also small. The above approximation can be applied to (9.2.22) through (9.2.24).

$$S_1 = \omega T_s \cdot \sum_{k=1}^{M} (D_1 + D_{1k} - D_1)(1 - j\omega T_s (D_{1k} - D_1)) e^{-j\omega T_s (k-1-D_1)} \tag{9.2.26}$$

$$S_2 = j\mu \cdot \sum_{k=1}^{M} (1 - j\omega T_s (D_{1k} - D_1)) e^{-j\omega T_s (k-1+D_1)} \tag{9.2.27}$$

$$S_3 = j\mu \cdot \sum_{k=1}^{M} \left(1 - j\omega T_s (D_{1k} - D_1)\left(1 + \frac{1}{\mu}\right)\right) e^{-j\omega T_s \left(k-1+D_1\left(1+\frac{1}{\mu}\right)\right)} \tag{9.2.28}$$

These three sums can be rearranged in three new terms collecting the same powers of $(D_{1k} - D_1)$ separately, so that

$$S_1 + S_2 + S_3 = T_1 + T_2 + T_3 \tag{9.2.29}$$

where

$$T_1 = (\omega T_s D_1 + j\mu) \cdot \sum_{k=1}^{M} e^{-j\omega T_s (k-1+D_1)} - j\mu \cdot \sum_{k=1}^{M} e^{-j\omega T_s \left(k-1+D_1\left(1+\frac{1}{\mu}\right)\right)} \tag{9.2.30}$$

$$T_2 = \omega T_s \sum_{k=1}^{M} (D_{1k} - D_1) \left((1 - j\omega T_s D_1 + \mu) e^{-j\omega T_s (k-1+D_1)} - (\mu + 1) e^{-j\omega T_s \left(k-1+D_1\left(1+\frac{1}{\mu}\right)\right)} \right) \tag{9.2.31}$$

$$T_3 = -j\omega^2 T_s^2 \cdot \sum_{k=1}^{M} (D_{1k} - D_1)^2 e^{-j\omega T_s (k-1+D_1)} \tag{9.2.32}$$

The first of these sums (i.e., T_1) is zero for M bigger than 1. This immediately follows using

$$\omega T_s = \frac{2\pi N}{M} \tag{9.2.33}$$

which is a consequence of (9.2.1). It can be shown that the third sum T_3 is also zero except for the following frequency ratios:

$$\frac{N}{M} = \frac{1}{2},\ 1, \frac{3}{2}, 2, \frac{5}{2}, \ldots. \tag{9.2.34}$$

The measurement of the transfer function at half of the switching frequency is meaningless due to the aliasing problem. As pointed out in [26], the lower side band of the switching frequency coincides with frequency of the perturbation. The problem can easily be visualized in the time domain using Fig 9.5. At this particular frequency the modulation largely depends on the phase difference between the switching frequency and the injected signal. This signal can be shifted with respect to the PWM-ramp so that its crossings with the ramp always occur at the zero level of the injected sine wave or alternating at the positive and negative peak value. In the first case no modulation occurs whereas in the second case the modulation is certainly strong.

At exactly the switching frequency no modulation can appear with any phase-shift of the input signal. This can also be visualized by shifting the injected signal across the PWM-ramp. Therefore, the frequency ratios designated by (9.2.34) are not considered here, and T_3 is considered to be zero.

The only non-zero component is T_2, which can be reorganized as follows:

$$T_2 = \omega T_s \left((\mu+1)\left(1 - e^{-j\omega T_s \frac{D_1}{\mu}}\right) - j\omega T_s D_1 \right) \cdot \sum_{k=1}^{M} (D_{1k} - D_1) e^{-j\omega T_s (k-1+D_1)} \tag{9.2.35}$$

Using (9.2.3) D_{1k}-D_1 can be replaced in (9.2.31). After some algebra the following expression can be found:

$$T_2 = \frac{\Delta D \omega T_s}{2j} \left((\mu+1)\left(1 - e^{-j\omega T_s \frac{D_1}{\mu}}\right) - j\omega T_s D_1 \right) \left(M - \sum_{k=1}^{M} e^{-2j(\omega T_s (k-1+D_1) - \varphi)} \right) e^{-j\varphi} \tag{9.2.36}$$

The part that remains in the summation is again zero except for the frequency ratios defined in (9.2.34). Similarly as before, these frequencies are not considered. Equation (9.2.36) can now be substituted into (9.2.29) and that one into (9.2.21). This, together with the use of (9.2.33) leads to

$$K_N = \Delta D \frac{V_{D1}}{\omega L}\left(\mathrm{j}(\mu+1)\left(e^{-\mathrm{j}\frac{2\pi N D_1}{M\mu}} - 1 \right) - \frac{2\pi N}{M} D_1 \right) e^{-\mathrm{j}\varphi} \qquad (9.2.37)$$

The magnitude of K_N represents the magnitude of i_{dn} and the argument of K_N represents its phase. As it was to be expected, the phase has a component of -φ. This means the phase difference to the perturbation at the input does not depend on φ. (This does not apply at half of the switch frequency according to the above discussion.) Henceforth, it is assumed that φ is zero.

The expression (9.2.37) is a surprisingly simple result considering the problem that was to be solved. However, it is still far too complicated in order to be useful for design purposes. Approximations for the magnitude and phase are required. The case is considered first, where ω is chosen very low (i.e., if the converter is perturbed well below the switching frequency). In this case the ratio N/M is low. The exponential function in (9.2.37) can be approximated using (9.2.25). This leads to

$$K_N = \Delta D \frac{V_{D1}}{\omega L} \cdot \frac{2\pi N D_1}{M\mu} \qquad (9.2.38)$$

With the use of (9.2.33), this can be simplified to

$$K_N = \Delta D \frac{V_{D1} D_1 T_s}{L\mu} \qquad (9.2.39)$$

It should be mentioned that a perturbation at a low frequency requires an extremely large capacitor at the input of the linear network in Fig. 9.4a; otherwise, the assumption that V_{D2} is constant is violated. In a realistic case (9.2.39) may not offer the appropriate result, but it is used here for the sake of argument.

According to Fig. 9.4b in an unperturbed converter the average diode current $\bar{I}_d$ is given by

$$\frac{I_p}{2} D_2 \tag{9.2.40}$$

Using (9.2.7) and (9.2.9) this can be expressed as

$$\bar{I}_d = \frac{V_{D1} D_1^2 T_s}{2L\mu} \tag{9.2.41}$$

This is not a linear relation between the D_1 and $\bar{I}_d$. In accordance with the discussion above, it is again assumed that the capacitance at the input of the linear network is very large, or even infinite. If an incremental change ΔD at the duty ratio is applied, the linearized expression for the incremental change of $\bar{I}_d$ can be found using the following formula:

$$\Delta I_d = \frac{\partial \bar{I}_d}{\partial D_1} \Delta D \tag{9.2.42}$$

This leads to

$$\Delta I_d = \frac{V_{D1} D_1 T_s}{L\mu} \Delta D \tag{9.2.43}$$

The right-hand side of the above equation is precisely the same as in (9.2.39). Therefore, K_N at low frequencies is the same as ΔI_d. This result is not actually surprising, but it is useful for the further discussion.

It turns out that the magnitude of K_N is almost independent of the frequency in most cases. Figures 9.6a, through 9.6c show a comparison of the accurate value of $|K_N|$ (dashed lines) versus ΔI_d (solid lines) calculated using (9.2.43) at three different frequency values. The plots are normalized with respect to V_{D1}, T_s, L and ΔD. As expected, at 10% of the switching frequency ΔI_d approximates the exact of values $|K_N|$ closely for all duty ratios and μ-values. At half of the switching frequency, some discrepancy can be observed particularly if μ and D_1 are both large (Fig. 9.6c).

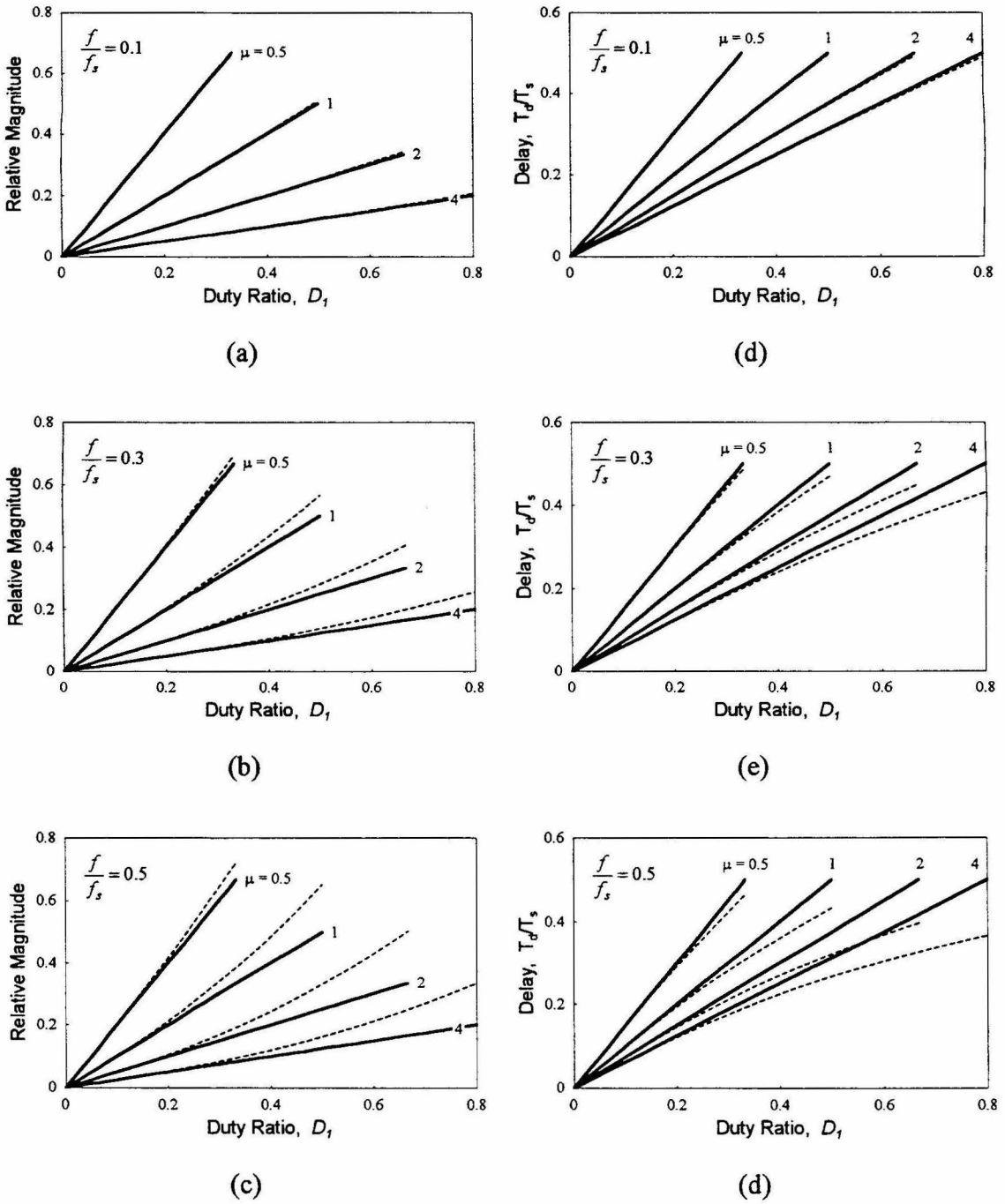

Figure 9.6: Comparison between the normalized value of K_n with the approximation. Dashed line: exact value, solid line approximation. (a), (b) and (c) Comparison of the magnitude at three different frequencies and (d), (e) and (f) comparison of the resulting time delay at the same frequencies.

The phase of K_N is investigated next. The low frequency perturbation case is considered first, as before. The exponential function must be expanded with the three first terms of the series expansion, otherwise all phase information is lost. Thus, the following approximation is used for a small x.

$$e^x \approx 1 + x + \frac{x^2}{2} \tag{9.2.44}$$

If this is applied in (9.2.37), it reduces to

$$\arg(K_N) = \Delta D \frac{V_{D1}}{\omega L}\left(-2j(\mu+1)\left(\frac{\pi N D_1}{M\mu}\right)^2 + \frac{2\pi N}{M\mu} D_1 \right) \tag{9.2.45}$$

The phase of K_N is given by

$$\tan^{-1}\left(-(\mu+1)\frac{\pi N D_1}{2M\mu} \right) \tag{9.2.46}$$

For small arguments the inverse tangent is nearly the same as its argument, i.e., if $x \approx 0$, then

$$\tan^{-1}(x) \approx x \tag{9.2.47}$$

Making use of this approximation and (9.2.33) leads to

$$\arg(K_N) = -\omega D_1 T_s \frac{\mu+1}{2\mu} \tag{9.2.48}$$

The current i_{dn} appears to be lagging with respect to the perturbation. This is in fact an expected behavior. The phase lag is proportional to the frequency. This holds at least at low frequencies since the derivation leading to (9.2.48) is based on the assumption that the frequency is low. Thus, it makes sense to express (9.2.48) normalized to the frequency, which is the corresponding time delay T_d between the input signal and i_{dn}. Thus,

$$T_d = D_1 T_s \frac{\mu+1}{2\mu} \tag{9.2.49}$$

At least at low frequencies the T_d does not depend on the frequency. It turns out that this approximately holds over a wide rage of frequencies. Figures 9.6d through 9.6f show a comparison between the accurately calculated delay according to (9.2.37) and the approximation stated above. Similarly as before with the magnitude, T_d closely approximates the accurate values, except if all three of the duty ratio, the conversion ratio and the frequency are high (Fig. 9.6d).

From the above discussion it can be concluded that the magnitude of i_{dn} stays approximately constant over the whole frequency range of interest. In addition, i_d is delayed with respect to the modulator input by an approximately constant time. The amount of delay depends on the steady state duty ratio D_1 and on the ratio μ, which is closely related to the conversion ratio.

As discussed earlier, reduced-order models accurately predict the transfer function at frequencies well below half of the switching frequency. Based on the preceding discussion, one possibility to improve these models is to add a delay term to the transfer function. The magnitude does not need to be adjusted since the contribution due to the DCM operation is constant over the whole frequency range, and at low frequency it is appropriately accounted for the magnitude by the reduced-order model. The amount of the delay is given in (9.2.49). A probably more useful and insightful version can be found by substituting (9.2.7) into (9.2.49). This leads to

$$T_d = T_s \frac{D_1 + D_2}{2} \tag{9.2.50}$$

This result is rather interesting since the delay is half as long as the conduction angle of the inductor in DCM. The transfer function of a delay $A_d(s)$ is given by

$$A_d(s) = e^{-sT_d} \tag{9.2.51}$$

For many purposes it is sufficient and much more convenient to use the Padé approximation [25] to account for a delay. The first order approximation is given by

$$A_d(s) = \frac{1 - \frac{sT_d}{2}}{1 + \frac{sT_d}{2}} \tag{9.2.52}$$

Using (9.2.50) this can be expressed in a more meaningful way as

$$A_d(s) = \frac{1 - \frac{s}{\omega_d}}{1 + \frac{s}{\omega_d}} \tag{9.2.53}$$

where

$$\omega_d = \frac{4}{T_s(D_1 + D_2)} \tag{9.2.54}$$

These last two equations are the only ones needed in order to improve reduced-order models such as the one obtained by state-space averaging.

Equation (9.2.53) has a pole and a right half plane zero in the neighborhood of the switching frequency. In Chapter 9.1 it has been pointed out that there is no physical reason for this zero to occur in DCM. In (9.2.53), it did not appear due to a physical necessity, but as a means to mathematically approximate the expression of a delay.

It is interesting to investigate how well the pole and the right half plane zero gained by the full-order models approximate the magnitude of and phase of K_N. For this purpose the values for the high frequency pole and zero given in [18] and [19] for the Boost converter were used. In order to allow an easy comparison with the delay approximation, the phase information was converted into the corresponding time delay at each particular frequency. The results are presented in Fig. 9.7 in the same fashion as the delay approximation was shown in Fig. 9.6. The dashed lines represent K_N whereas the solid lines are calculated using the full-order model.

In [18] and [19] it has been pointed out that the pole is always at lower frequency than the zero. This leads to a drop of the magnitude at high frequencies. This is best seen in Fig. 9.7c. Conversely, K_N predicts that the magnitude can be increasing with increasing frequency particularly if a high μ-value and at a high duty ratio coincide. It

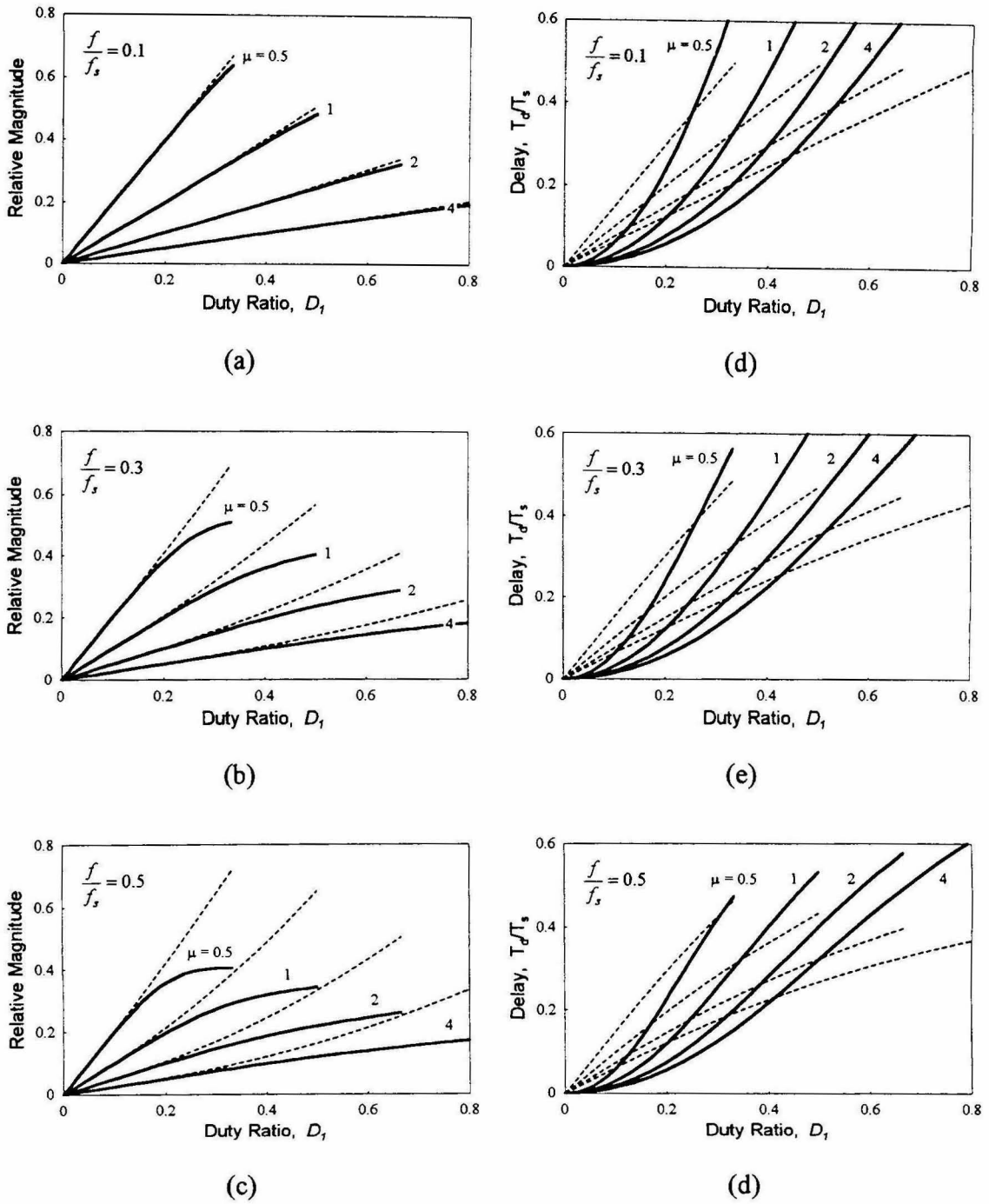

Figure 9.7: Comparison between the normalized value of K_n (dashed lines) with the high frequency pole and right half plane zero from the full-order model (solid lines). (a), (b) and (c) Comparison of the magnitude at three different frequencies and (d), (e) and (f) comparison of the resulting time delay at the same frequencies.

has been observed in measurements that this is in fact true. The experimental results are reported in the next section.

9.3 Experimental Results

In this section the experimentally obtained results are compared with the theory developed in the previous section. The measurements were taken on a Boost converter as shown in Fig. 9.8. The component values are given in Table 9.1. A foil capacitor with a very low equivalent series resistance was used for C. With this choice the additional left half plane zero lies far above the switching frequency and does not influence the measurement.

During the third subinterval in DCM the inductor current resonates with the parasitic capacitance of the two switches. The consequence is that at the time the active switch turns on, the current in the inductor is not zero as assumed in the analysis. This leads to misleading measurements. In order to prevent this situation, a damping resistor R_d was connected in parallel with the inductor. In addition, to reduce the parasitic capacitance seen by the inductor, an extra diode D_d was connected in series with the inductor.

Two quantities are necessary to characterize the nature of the discontinuous conduction mode. So far, D_1 and μ or D_1 and D_2 were used. It is sometimes helpful to use yet another pair, which is D_1 and the conduction parameter K, which is defined as

$$K = \frac{2L}{RT_s} \tag{9.3.1}$$

In the Boost converter the relations between K and μ, and K and D_2 is given by

$$\mu = \frac{\sqrt{1+\frac{4D_1^2}{K}}-1}{2} \tag{9.3.2}$$

$$D_2 = \frac{K}{D_1}\cdot\frac{\sqrt{1+\frac{4D_1^2}{K}}+1}{2} \tag{9.3.3}$$

The values of K at the boundary between DCC and CCM are called K_{crit}. A plot of K_{crit} for the Boost converter is shown in Fig. 9.9. All values of D_1 and K below the curve represent DCM operation. The seven crosses indicate the points where the measurements were taken. To present a complete picture the measurements are scattered over the whole DCM range. Table 9.2 lists some key values corresponding to the chosen points.

The results are presented in Fig. 9.10 through Fig. 9.13. The graphs at the top of each page show the comparison between the measured transfer function and the prediction using the simple delay approximation. The frequency ranges from 25Hz to 12.5 kHz. The upper limit is at half the switching frequency. The graphs below present an enlargement of the magnitude and phase respectively in the higher frequency range. The upper limit in these cases is the full switching frequency. The comparison also includes the more accurate prediction using K_N according to (9.2.37). In addition, the graphs also contain the prediction using the conventional full-order model as presented in [18,19].

The simple delay approximation provides good results at every measured point up to half the switching frequency. As expected the most severe discrepancy is observed in Fig. 9.11a. This point corresponds to the highest duty ratio and highest conversion ratio. Nevertheless, the prediction using K_N is still very accurate. A similar but smaller difference can be observed in Fig. 9.10d and Fig. 9.12d. From Table 9.2 it can be seen that these are the points with the next highest conversion ratios.

Over all, the delay approximation appears to be very useful in every case. As far as the magnitude is concerned, it is always closer to the measurement than the conventional full-order model. In two cases, namely Fig. 9.10f and Fig. 9.13c, the phase prediction of the conventional model is better than the simple delay. However, in the first case it is only marginally better and in the second case it only applies over a part of the frequency range.

The prediction of the phase lag using K_N is somewhat too small at high frequencies. The discrepancy is almost the same in each measurement. This might be due to the additional left half plane zero that appears as a result of the series resistance or

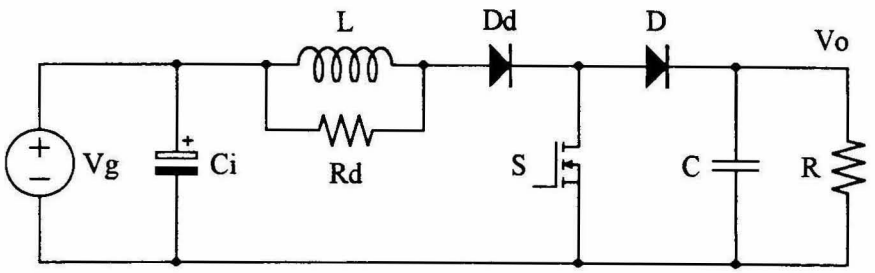

Figure 9.8: Experimental circuit.

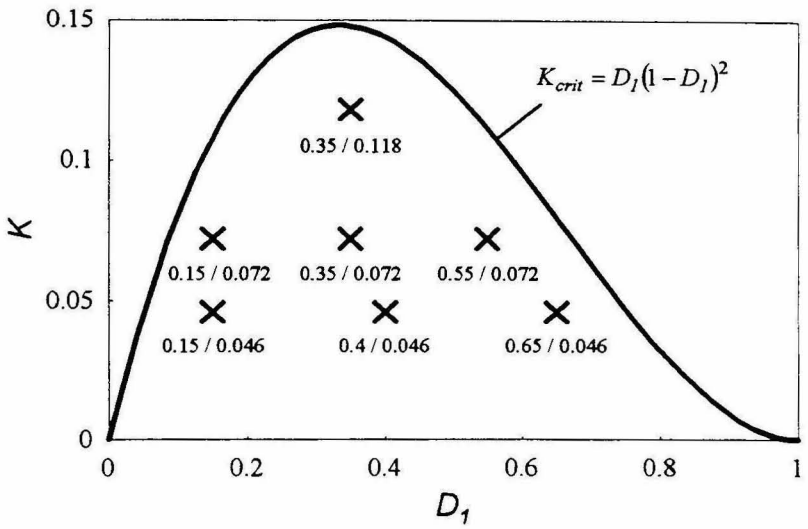

Figure 9.9: Points in the D - K plane where the measurements were taken.

V_g	f_s	L	C	C_i	R_d	R
15V	25kHz	294μH	8.13μF	470μF	2.7kΩ	320Ω, 205Ω, 125Ω

Table 9.1: Component values of the experimental circuit.

R	K	D_1	D_2	D_3	μ	V_o/V_g
320	0.046	0.15	0.42	0.43	0.36	1.36
		0.40	0.28	0.32	1.43	2.43
		0.65	0.25	0.10	2.57	3.57
205	0.072	0.15	0.60	0.25	0.25	1.25
		0.35	0.39	0.26	0.90	1.90
		0.55	0.34	0.11	1.61	2.61
125	0.118	0.35	0.55	0.10	0.64	1.64

Table 9.2: Relation between the characteristic values at the measurement points.

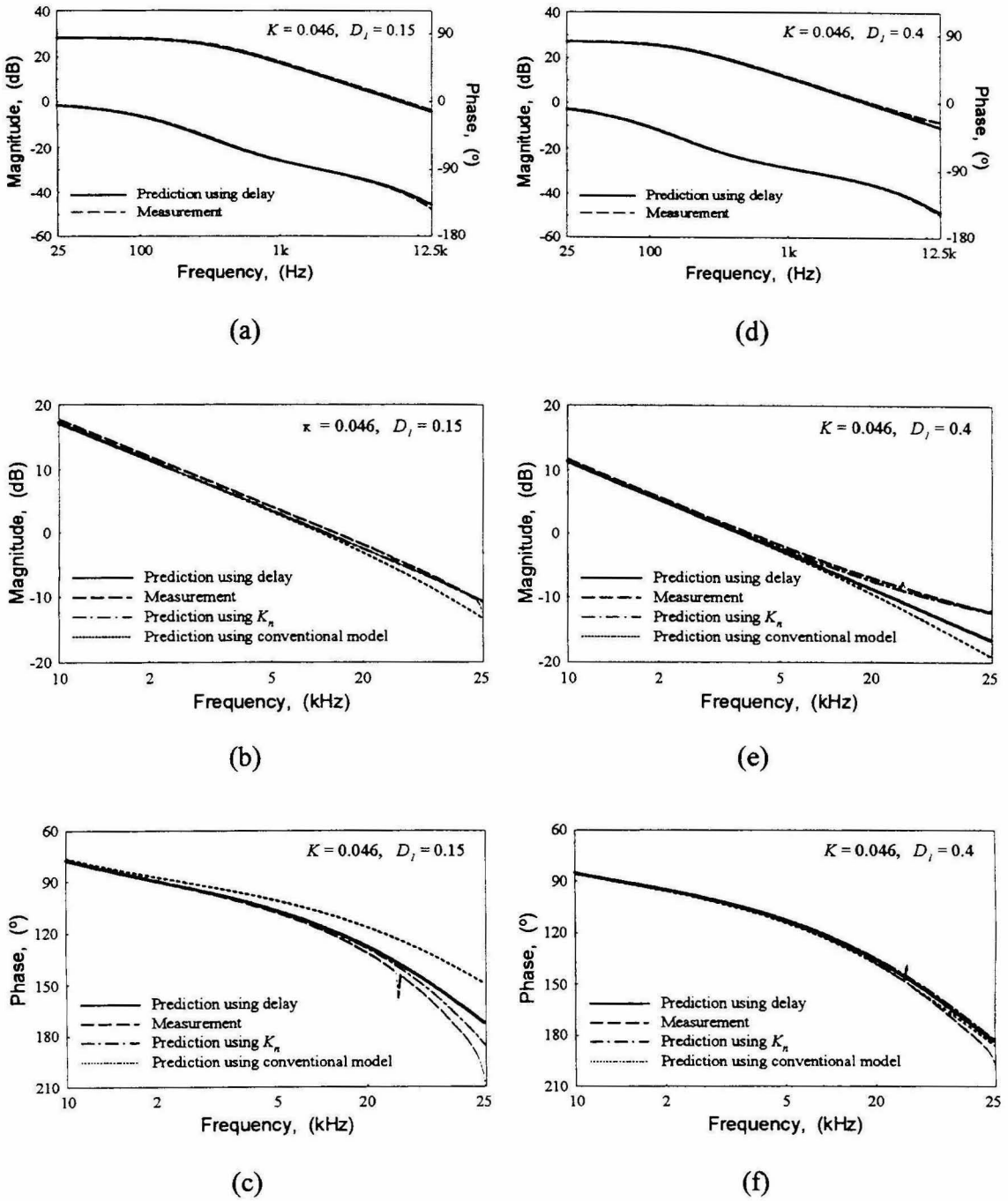

Figure 9.10: Comparison of the measurement with different predicted values: (a)-(c) Low K and low D_1. (d)-(f) Low K and intermediate D_1. (a) and (d) Prediction over two decades to half of the switching frequency using the simple delay formula. (b), (c), (e) and (f) Enlarged magnitude and phase respectively up to the full switching frequency.

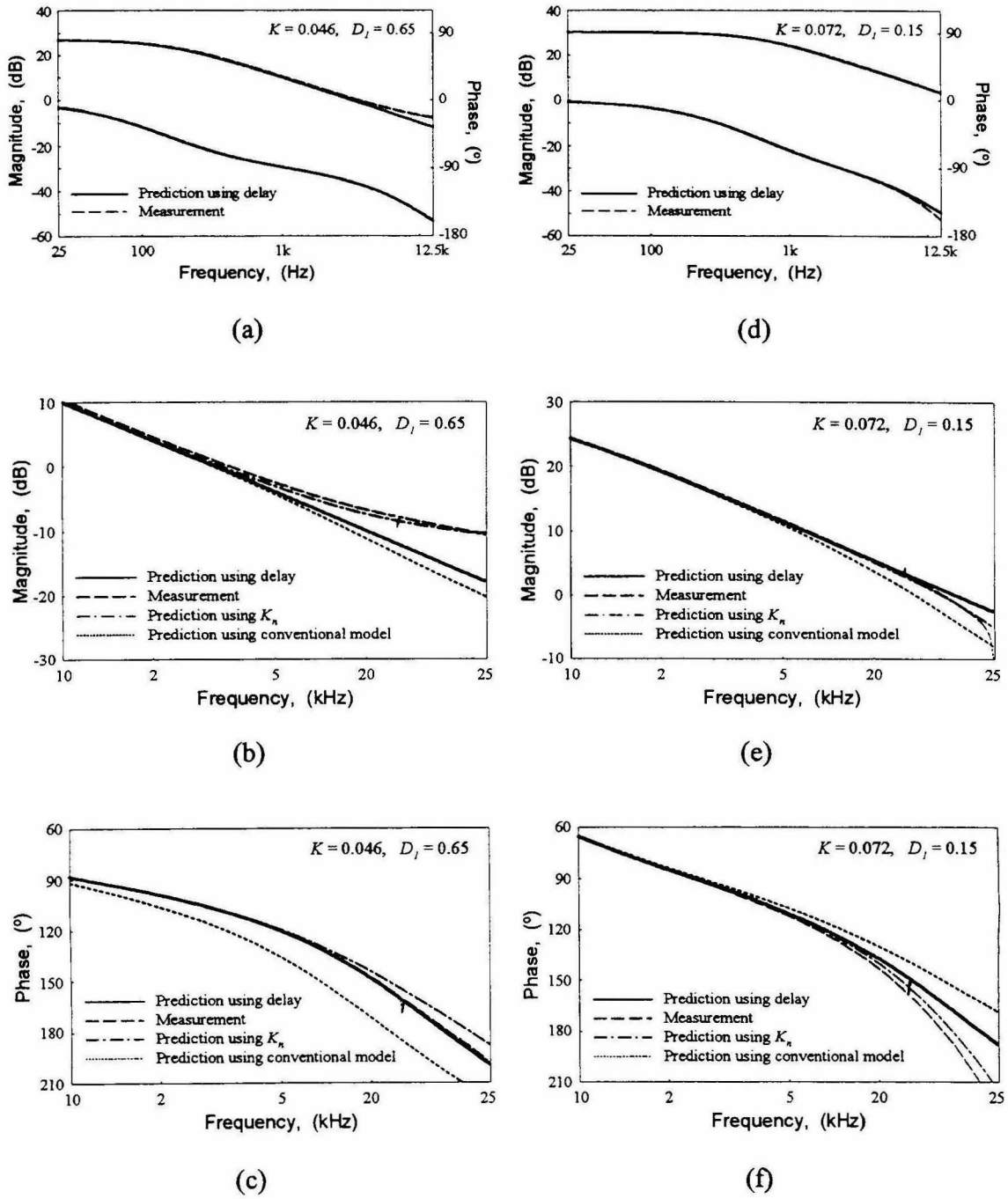

Figure 9.11: Comparison of the measurement with different predicted values: (a)-(c) Low K and high D_1. (d)-(f) Intermediate K and low D_1. (a) and (d) Prediction over two decades to half of the switching frequency using the simple delay formula. (b), (c), (e) and (f) Enlarged magnitude and phase respectively up to the full switching frequency.

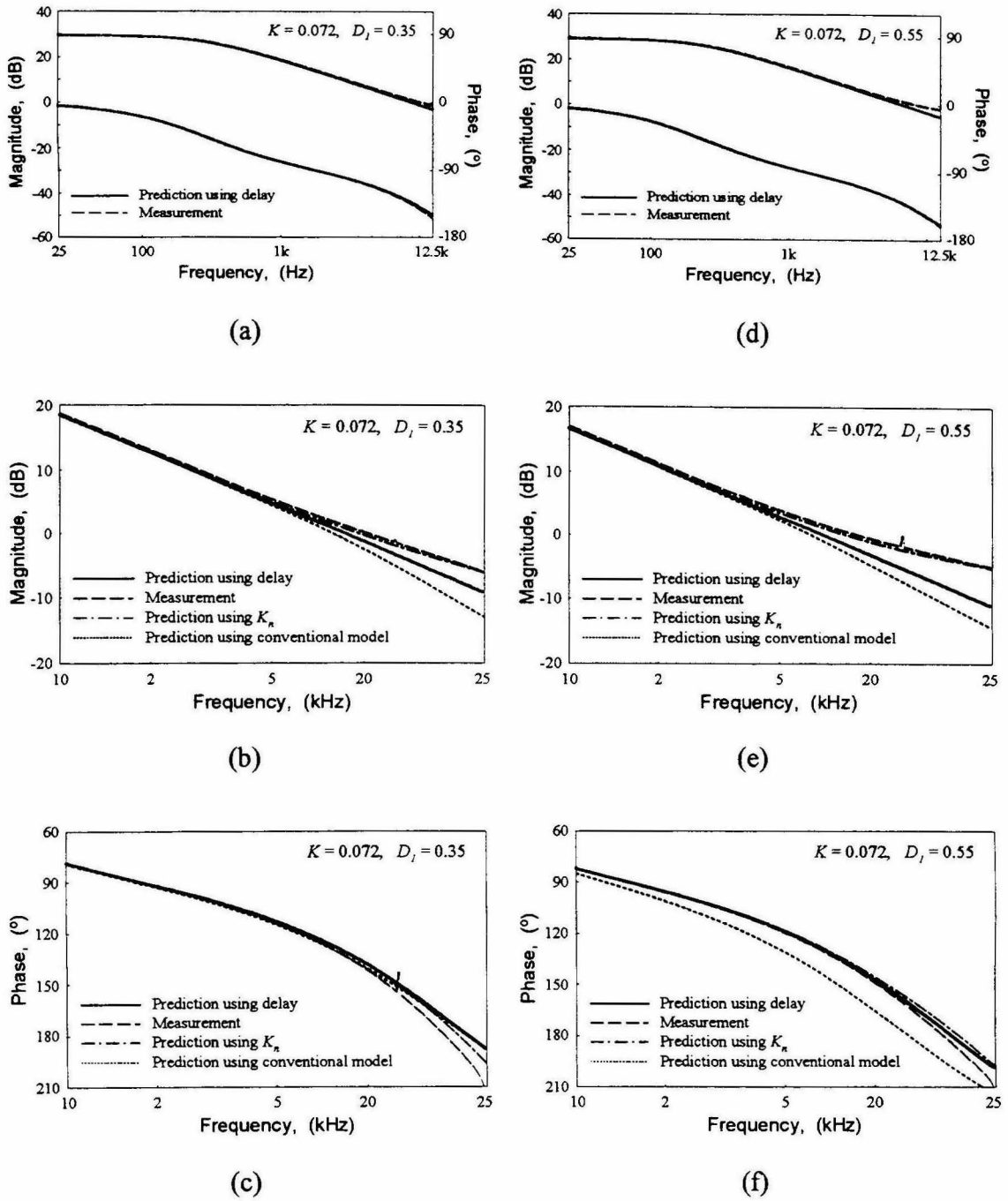

Figure 9.12: Comparison of the measurement with different predicted values: (a)-(c) Intermediate K and intermediate D_1. (d)-(f) Intermediate K and high D_1. (a) and (d) Prediction over two decades to half of the switching frequency using the simple delay formula. (b), (c), (e) and (f) Enlarged magnitude and phase respectively up to the full switching frequency.

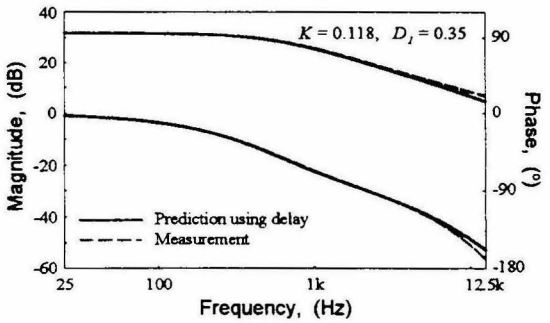

(a)

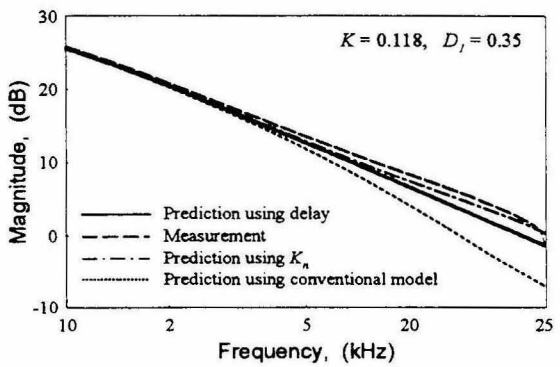

(b)

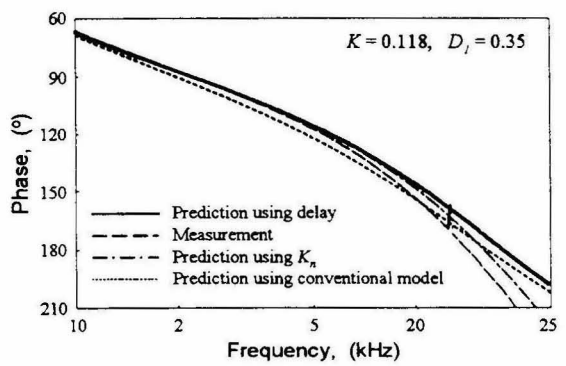

(c)

Figure 9.13: Comparison of the measurement with the prediction at high K-value. (a) Prediction over two decades to half of the switching frequency using the simple delay formula. (b) and (c) Enlarged magnitude and phase respectively up to the full switching frequency.

inductance of the capacitor. Even though no influence is visible in the magnitude, it might start to appear in the phase.

9.4 Final Remarks

The high level accuracy of the prediction using K_N suggests that the derivation in the preceding Section 9.2 is a valid approach. The principal query was the justification of the assumption that the voltage V_{D2} is constant. (In the Boost converter V_{D2} is V_o-V_g.) There are still some open issues. Firstly, what happens if the capacitor at the input of the linear network becomes so small the constant voltage assumption does not hold anymore? Secondly, there is a good chance that there is a more accurate yet still simple approximation in a pole-zero-form to model the behavior of K_N. Thirdly, the derivation is based on assumptions, which excludes some converters. It would be interesting if the idea was generalized so that it applies to a Buck and other converters.

It is clear, for any engineering purpose, no better model is needed than the conventional full-order model. However, the delay approximation is in many cases simpler to derive and is certainly no less accurate, particularly in conjunction with circuits treated in the next chapter with multiple discontinuous conduction modes. The next chapter introduces a straightforward way to perform state-space averaging for converters in DCM where an increasing number of discontinuous elements does not increase the complexity of the analysis. The result is a reduced-order model. If the converter satisfies the conditions stated in Chapter 9.2.1, this problem can easily be eradicated using the delay approximation.

Chapter 10

Small-Signal Analysis of Converters with Multiple Discontinuous Conduction Modes

The purpose of this chapter is to introduce a unified approach to perform the small-signal analysis of converters with more than one reactive element in discontinuous conduction mode. The technique is based on the well-known state-space averaging method. However, the procedure is standardized and thus, more user and computer friendly.

State-space averaging is a widely accepted method of evaluating the small-signal behavior of switch mode converters. This method was introduced in [13] for converters working in continuous conduction mode (CCM) and in [22] for converters working in discontinuous conduction mode (DCM). The latter becomes quite cumbersome if more than one reactive element works in DCM. This gave rise to the motivation for the search for a more efficient way of using state-space averaging for topologies with multiple discontinuous conduction modes. The presented procedure is not a new method of finding the small-signal behavior. The algorithm follows closely the method introduced in [22]. The major advancement is its simplicity, even if there is more than one element operating in DCM. Of course, it can be applied in case of a single reactor in DCM. Moreover, if no discontinuous element is present, the algorithm reduces to the CCM case as presented in [13]. In addition, the extra term introduced in Chapter 9 to account for the effects close to the switching frequency can be added. This term does not depend on the rest of the analysis; therefore, it can be omitted if there is no need for an accurate transfer function close to half of the switching frequency.

10.1 Derivation

The small-signal analysis presented in this paper applies to a large class of topologies operating in DCM. However, some assumptions must be stated in order to define clearly when the algorithm can be applied as described. In some of the cases excluded by the assumptions below, a few adjustments to the algorithm are necessary. These special cases will not be treated in this thesis.

10.1.1 Assumptions

The considerations in this chapter are restricted to converters satisfying the following assumptions:

1) There is only one control input, i.e., all active switches have the same on-time. (In this context an active switch is a switch that can not be implemented by a diode.)
2) The currents and voltages in the discontinuous elements have approximately triangular waveforms.

The second assumption requires a small ripple assumption in the elements operating in CCM. However, the state-space averaging method for CCM requires this anyway. Therefore, this is not an additional limitation. Topologies where the discontinuous reactors exhibit piece-wise linear waveforms, which are not triangular, are excluded from these considerations. An example of this class of waveforms is encountered in Fig. 4.3 of Chapter 4.1. A possible solution to the problem is to represent each of the currents $i_2(t)$ and $i_3(t)$ (in Fig. 4.3) with two separate triangular waveforms. These two currents are not independent; therefore, some additional adjustments to the procedure derived in this chapter are necessary. However, the discussion of these special cases is beyond the scope of this thesis.

10.1.2 State-Space Description

In the state-space description of an electrical circuit, the states are usually chosen to be the currents and voltages of the reactive components. For simplicity, in this thesis the discontinuous currents and voltages are referred to as discontinuous states, even though they are not actually state variables.

Let l be the number of states (i.e., the number of independent reactive elements) of a converter. If m is the number of discontinuous states and n is the number of continuous states, then

$$l = m + n \tag{10.1.1}$$

The number of subintervals during one switching cycle depends on the number of discontinuous states. In CCM the number of subintervals is two. Each element in DCM initiates an additional subinterval at the instant when its voltage or current value becomes zero. Generally, the number of subintervals, k, is equal to the number of discontinuous states plus two. Thus,

$$k = m + 2 \tag{10.1.2}$$

As demonstrated in [13,22] each of these subintervals has a state-space representation of the form

$$\dot{\mathbf{x}} = \mathbf{A_i}\mathbf{x} + \mathbf{b_i}V_g \tag{10.1.3}$$

where V_g is the input voltage, and the subscript i denotes the i^{th} subinterval ($i \in 1,\ldots,k$). The state vector $\mathbf{x}$ contains all the state variables (i.e., all the currents and voltages in the reactive elements). The algorithm derived in this section requires that $\mathbf{x}$ must contain the discontinuous states in the top part, whereas the continuous states are located in the lower part of $\mathbf{x}$. Therefore, $\mathbf{x}$ can be represented as

$$\mathbf{x} = \begin{bmatrix} \mathbf{x_d} \\ \mathbf{x_c} \end{bmatrix} \tag{10.1.4}$$

where $\mathbf{x_d}$ is a column vector of length m containing all discontinuous states and $\mathbf{x_c}$ is a column vector of length n with all the continuous state variables.

D_i denotes the length of the i^{th} subinterval relative to the length of one switching cycle. In accordance with the above assumptions D_1 is the duty cycle of the active switches, and consequently, it is the control input of the converter. Thus, D_1 is considered to be a known variable. The length of all other subintervals has yet to be determined. The state-space representation of the converter is found by averaging the equations of all the subintervals weighted with D_i. Thus,

$$\dot{\mathbf{x}} = \sum_{i=1}^{k} D_i \mathbf{A_i} \mathbf{x} + \sum_{i=1}^{k} D_i \mathbf{b_i} V_g \tag{10.1.5}$$

An additional equation is needed to describe the output, Y, of the system in terms of the state vector $\mathbf{x}$. Namely,

$$Y = \sum_{i=1}^{k} D_i \mathbf{c_i} \mathbf{x} \tag{10.1.6}$$

where the row vectors $\mathbf{c_i}$ have to be found for each subinterval separately, similar as $\mathbf{A_i}$ and $\mathbf{b_i}$. By using the definitions

$$\mathbf{A} \equiv \sum_{i=1}^{k} D_i \mathbf{A_i} \tag{10.1.7}$$

$$\mathbf{b} \equiv \sum_{i=1}^{k} D_i \mathbf{b_i} \tag{10.1.8}$$

$$\mathbf{c} \equiv \sum_{i=1}^{k} D_i \mathbf{c_i} \tag{10.1.9}$$

the equations (10.1.5) and (10.1.6) can be restated in a simpler form.

$$\dot{\mathbf{x}} = \mathbf{A}\mathbf{x} + \mathbf{b} V_g \tag{10.1.10}$$

$$Y = \mathbf{c}\mathbf{x} \tag{10.1.11}$$

In steady state, the left-hand side of (10.1.10) is zero. Thus,

$$\mathbf{0} = \mathbf{A}\mathbf{x} + \mathbf{b}V_g \tag{10.1.12}$$

With that the large-signal description of the converter is complete.

10.1.3 Small-Signal Perturbation

At this point the small-signal perturbation can be applied to the system given in (10.1.10) and (10.1.11) in much the same way as described in [13.22]. Two different quantities are usually considered as possible inputs. The first is the input voltage, and the second is the duty ratio. This thesis follows the same concept. In order to apply the small-signal perturbation, the following substitutions have to be made:

$$\begin{aligned} Vg &\rightarrow V_g + \hat{v}_g \\ D_i &\rightarrow D_i + \hat{d}_i \\ Y &\rightarrow Y + \hat{y} \\ \mathbf{x} &\rightarrow \mathbf{x} + \hat{\mathbf{x}} \end{aligned} \tag{10.1.13}$$

It is commonly understood that the magnitude of each individual perturbation is much smaller than the corresponding steady state value, i.e.,

$$\begin{aligned} \hat{v}_g &<< V_g \\ \hat{d}_i &<< D_i \\ \hat{y} &<< Y \\ \hat{\mathbf{x}} &<< \mathbf{x} \end{aligned} \tag{10.1.14}$$

It is easier to apply these substitutions to (10.1.5) and (10.1.6) rather than to (10.1.10) and (10.1.11). This leads to the following expressions:

$$\dot{\mathbf{x}} = \sum_{i=1}^{k}\left(D_i + \hat{d}_i\right)\mathbf{A_i}\left(\mathbf{x} + \hat{\mathbf{x}}\right) + \sum_{i=1}^{k}\left(D_i + \hat{d}_i\right)\mathbf{b_i}\left(V_g + \hat{v}g\right) \tag{10.1.15}$$

$$Y + \hat{y} = \sum_{i=1}^{k} \left(D_i + \hat{d}_i\right)\mathbf{c_i}\left(\mathbf{x} + \hat{\mathbf{x}}\right) \tag{10.1.16}$$

The expressions below can be found by substituting (10.1.7) and (10.1.8) into (10.1.15), and (10.1.9) into (10.1.16).

$$\dot{\mathbf{x}} = \mathbf{A}\mathbf{x} + \mathbf{A}\hat{\mathbf{x}} + \sum_{i=1}^{k} \hat{d}_i \mathbf{A_i}\mathbf{x} + \underbrace{\sum_{i=1}^{k} \hat{d}_i \mathbf{A_i}\hat{\mathbf{x}}}_{\approx 0} + \mathbf{b}V_g + \mathbf{b}\hat{v}_g + \sum_{i=1}^{k} \hat{d}_i \mathbf{b_i} V_g + \underbrace{\sum_{i=1}^{k} \hat{d}_i \mathbf{b_i}\hat{v}_g}_{\approx 0} \tag{10.1.17}$$

$$Y + \hat{y} = \mathbf{c}\mathbf{x} + \mathbf{c}\hat{\mathbf{x}} + \sum_{i=1}^{k} \hat{d}_i \mathbf{c_i}\mathbf{x} + \underbrace{\sum_{i=1}^{k} \hat{d}_i \mathbf{c_i}\hat{\mathbf{x}}}_{\approx 0} \tag{10.1.18}$$

As indicated in the two equations above, due to assumption (10.1.14), all second order terms (i.e., terms involving $\hat{d}_i\hat{\mathbf{x}}$ and $\hat{d}_i\hat{v}_g$) are very small compared to the other terms and can therefore be neglected. Furthermore, it is assumed that the converter operates in steady state in the large-signal sense. Thus (10.1.12) is satisfied and it can be subtracted from (10.1.17). Equation (10.1.6) always holds and thus can be subtracted from (10.1.18). The result is

$$\dot{\mathbf{x}} = \mathbf{A}\hat{\mathbf{x}} + \mathbf{b}\hat{v}_g + \sum_{i=1}^{k} \hat{d}_i \left(\mathbf{A_i}\mathbf{x} + \mathbf{b_i}V_g\right) \tag{10.1.19}$$

$$\hat{y} = \mathbf{c}\hat{\mathbf{x}} + \sum_{i=1}^{k} \hat{d}_i \mathbf{c_i}\mathbf{x} \tag{10.1.20}$$

These equations can be rearranged as

$$\dot{\mathbf{x}} = \mathbf{A}\hat{\mathbf{x}} + \mathbf{b}\hat{v}_g + \sum_{i=1}^{k-1} \hat{d}_i \left(\mathbf{A_i}\mathbf{x} + \mathbf{b_i}V_g\right) + \hat{d}_k \left(\mathbf{A_k}\mathbf{x} + \mathbf{b_k}V_g\right) \tag{10.1.21}$$

$$\hat{y} = \mathbf{c}\hat{\mathbf{x}} + \sum_{i=1}^{k-1} \hat{d}_i \mathbf{c_i}\mathbf{x} + \hat{d}_k \mathbf{c_k}\mathbf{x} \tag{10.1.22}$$

Independent of whether the system is perturbed or not the relative lengths of all the subintervals always add up to unity. Therefore,

$$\sum_{i=1}^{k} D_i = \sum_{i=1}^{k} D_i + \hat{d}_i = 1 \tag{10.1.23}$$

Using this it can be concluded that

$$\sum_{i=1}^{k} \hat{d}_i = 0 \tag{10.1.24}$$

or equivalently

$$\hat{d}_k = -\sum_{i=1}^{k-1} \hat{d}_i \tag{10.1.25}$$

The substitution of $\hat{d}_k$ in (10.1.21) and (10.1.22) using (10.1.25) leads to

$$\dot{\mathbf{x}} = \mathbf{A}\hat{\mathbf{x}} + \mathbf{b}\hat{v}_g + \sum_{i=1}^{k-1} \hat{d}_i \left((\mathbf{A_i} - \mathbf{A_k})\mathbf{x} + (\mathbf{b_i} - \mathbf{b_k})V_g \right) \tag{10.1.26}$$

$$\hat{y} = \mathbf{c}\hat{\mathbf{x}} + \sum_{i=1}^{k-1} \hat{d}_i (\mathbf{c_i} - \mathbf{c_k})\mathbf{x} \tag{10.1.27}$$

The following quantities are defined in order to simplify the expressions.

$$\mathbf{e_i} \equiv (\mathbf{A_i} - \mathbf{A_k})\mathbf{x} + (\mathbf{b_i} - \mathbf{b_k})V_g \tag{10.1.28}$$

$$\mathbf{E2} \equiv [\mathbf{e_2} \ , \ \mathbf{e_3} \ , \ \ldots \ , \ \mathbf{e_{k-1}}] \tag{10.1.29}$$

$$k_i \equiv (\mathbf{c_i} - \mathbf{c_k})\mathbf{x} \tag{10.1.30}$$

$$\mathbf{k_2} \equiv [k_2 \quad k_3 \quad \ldots \quad k_{k-1}] \tag{10.1.31}$$

$$\hat{\mathbf{d}}' \equiv \begin{bmatrix} d_2 \\ \vdots \\ d_{k-1} \end{bmatrix} \tag{10.1.32}$$

Equations (10.1.26) and (10.1.27) can now be written as

$$\dot{\mathbf{x}} = \mathbf{A}\hat{\mathbf{x}} + \mathbf{b}\hat{v}_g + \mathbf{e}_1\hat{d}_1 + \mathbf{E}_2\hat{\mathbf{d}}' \tag{10.1.33}$$

$$\hat{y} = \mathbf{c}\hat{\mathbf{x}} + k_1\hat{d}_1 + \mathbf{k}_2\hat{\mathbf{d}}' \tag{10.1.34}$$

These two equations describe the small-signal behavior of the whole system. Starting from here the discontinuous states and the continuous states must be treated differently. In order to do that (10.1.33) will be decomposed into DCM and CCM parts. The DCM part is represented by the upper row of (10.1.35), whereas the lower row stands for the CCM part. The matrices of (10.1.33) must be partitioned so that the submatrices in the upper line of (10.1.35) have the same number of rows, as there are DCM states. Similarly, the number of rows of the matrices in the lower line of (10.1.35) corresponds to the number of CCM states. The vertical separation of **A** is such that $\mathbf{A}_{11}$ and $\mathbf{A}_{22}$ are square matrices. Therefore, $\mathbf{A}_{11}$ is a $m \times m$, $\mathbf{A}_{12}$ is a $m \times n$, $\mathbf{A}_{21}$ is a $n \times m$ and $\mathbf{A}_{22}$ is a $n \times n$ matrix. The partitioning of the state vector x was already introduced in (10.1.4).

$$\underbrace{\begin{bmatrix}\dot{\mathbf{x}}_\mathbf{d}\\ \dot{\mathbf{x}}_\mathbf{c}\end{bmatrix}}_{=\dot{\mathbf{x}}} = \underbrace{\begin{bmatrix}\mathbf{A}_{11} & \mathbf{A}_{12}\\ \mathbf{A}_{21} & \mathbf{A}_{22}\end{bmatrix}}_{=\mathbf{A}} \cdot \underbrace{\begin{bmatrix}\hat{\mathbf{x}}_\mathbf{d}\\ \hat{\mathbf{x}}_\mathbf{c}\end{bmatrix}}_{=\hat{\mathbf{x}}} + \underbrace{\begin{bmatrix}\mathbf{b}_{11}\\ \mathbf{b}_{12}\end{bmatrix}}_{=\mathbf{b}}\hat{v}_g + \underbrace{\begin{bmatrix}\mathbf{e}_{11}\\ \mathbf{e}_{12}\end{bmatrix}}_{=\mathbf{e}_1}\hat{d}_1 + \underbrace{\begin{bmatrix}\mathbf{E}_{21}\\ \mathbf{E}_{22}\end{bmatrix}}_{=\mathbf{E}_2}\hat{\mathbf{d}}' \tag{10.1.35}$$

A similar decomposition of (10.1.34) results in

$$\hat{y} = \mathbf{c}_\mathbf{d}\hat{\mathbf{x}}_\mathbf{d} + \mathbf{c}_\mathbf{c}\hat{\mathbf{x}}_\mathbf{c} + k_1\hat{d}_1 + \mathbf{k}_2\hat{\mathbf{d}}' \tag{10.1.36}$$

where $\mathbf{c}_\mathbf{d}$ is a row vector of length m and $\mathbf{c}_\mathbf{c}$ is of length n, which are found by splitting **c** such that

$$\mathbf{c} = [\mathbf{c}_\mathbf{d} \ , \ \mathbf{c}_\mathbf{c}] \tag{10.1.37}$$

Equation (10.1.35) can now be written as two different equations.

$$\mathbf{0} = \mathbf{A}_{11}\hat{\mathbf{x}}_\mathbf{d} + \mathbf{A}_{12}\hat{\mathbf{x}}_\mathbf{c} + \mathbf{b}_{11}\hat{v}_g + \mathbf{e}_{11}\hat{d}_1 + \mathbf{E}_{21}\hat{\mathbf{d}}' \tag{10.1.38}$$

$$\dot{\mathbf{x}}_\mathbf{c} = \mathbf{A}_{21}\hat{\mathbf{x}}_\mathbf{d} + \mathbf{A}_{22}\hat{\mathbf{x}}_\mathbf{c} + \mathbf{b}_{12}\hat{v}_g + \mathbf{e}_{12}\hat{d}_1 + \mathbf{E}_{22}\hat{\mathbf{d}}' \tag{10.1.39}$$

As pointed out in [22] $\hat{\mathbf{x}}_\mathbf{d}$ must be set to zero. This is neither an approximation nor is something neglected. It is important to realize that (10.1.38) does not imply that the time derivative of the discontinuous states is zero in the perturbed system. The reason for this is that the discontinuous states are described by algebraic equations rather than by differential equations. Since this point often causes confusion, an alternative justification for $\hat{\mathbf{x}}_\mathbf{d}$ being set to zero is provided in Appendix C. Equation (10.1.38) is used to find $\hat{\mathbf{d}}'$, but it can not be used to find $\hat{\mathbf{x}}_\mathbf{d}$ (i.e., the perturbation of the discontinuous states).

Given the assumptions stated in Section 10.1.1, the average value of each discontinuous state can be expressed as a function of the continuous states, the input voltage and the duty ratio. They are of the general form

$$X_{d_i} = f\left(X_{c_1},\ldots,X_{c_n},V_g,D_1\right) \quad , \quad i \in 1,\ldots,m \tag{10.1.40}$$

where the scalars X_{j_i} are the elements of the state vector $\mathbf{x}$, such that

$$\mathbf{x} = \begin{bmatrix} X_{d_1} \\ \vdots \\ X_{d_m} \\ X_{c_1} \\ \vdots \\ X_{c_n} \end{bmatrix} \begin{matrix} \left.\begin{matrix} \\ \\ \\ \end{matrix}\right\}\mathbf{x_d} \\ \left.\begin{matrix} \\ \\ \\ \end{matrix}\right\}\mathbf{x_c} \end{matrix} \tag{10.1.41}$$

It should be stressed here that X_{d_i} must be averaged only over the conduction angle of the corresponding element and not over the whole switching cycle. Due to this, the expressions in (10.1.40) are very simple since the average value in the described sense is simply half the peak value of that particular voltage or current.

As mentioned above $\dot{\mathbf{x}}_\mathbf{d} = \mathbf{0}$, it does not mean that the discontinuous states are not time varying. Since they are described by algebraic equations, the linearized perturbation $\hat{\mathbf{x}}_\mathbf{d}$ can be found using partial derivatives of (10.1.41) with respect to the

continuous states, the input voltage and the duty ratio. In general, the m components of $\hat{\mathbf{x}}_\mathbf{d}$ have the following form:

$$\hat{x}_{d_i} = \sum_{j=1}^{n} \frac{\partial X_{d_i}}{\partial X_{c_j}} \hat{x}_{c_j} + \frac{\partial X_{d_i}}{\partial V_g} \hat{v}_g + \frac{\partial X_{d_i}}{\partial D_1} \hat{d}_1 \quad , \quad i \in 1,...,m \tag{10.1.42}$$

This can be written in matrix form as follows:

$$\hat{\mathbf{x}}_\mathbf{d} = \mathbf{D_1} \hat{\mathbf{x}}_\mathbf{c} + \mathbf{d_2} \hat{v}_g + \mathbf{d_3} \hat{d}_1 \tag{10.1.43}$$

where

$$\mathbf{D_{1_{ij}}} \equiv \frac{\partial X_{d_i}}{\partial X_{c_j}} \quad , \quad i \in 1,...,m \quad , \quad j \in 1,...,n \tag{10.1.44}$$

$$\mathbf{d_{2_i}} \equiv \frac{\partial X_{d_i}}{\partial V_g} \quad , \quad i \in 1,...,m\,; \tag{10.1.45}$$

$$\mathbf{d_{3_i}} \equiv \frac{\partial X_{d_i}}{\partial D_1} \quad , \quad i \in 1,...,m\,; \tag{10.1.46}$$

It may seem quite tedious to find all these derivatives. However, the expressions represented by (10.1.40) are usually very simple and many of the partial derivatives in (10.1.42) are zero.

Now, $\hat{\mathbf{d}}'$ can be found by substituting (10.1.43) into (10.1.38).

$$\hat{\mathbf{d}}' = -\mathbf{E_{21}}^{-1}\left(\left(\mathbf{A_{11}D_1} + \mathbf{A_{12}}\right)\hat{\mathbf{x}}_\mathbf{c} + \left(\mathbf{A_{11}d_2} + \mathbf{b_{11}}\right)\hat{v}_g + \left(\mathbf{A_{11}d_3} + \mathbf{e_{11}}\right)\hat{d}_1\right) \tag{10.1.47}$$

This equation together with (10.1.43) can be substituted into (10.1.39) and (10.1.36) to obtain

$$\dot{\hat{\mathbf{x}}}_\mathbf{c} = \mathbf{F}\hat{\mathbf{x}}_\mathbf{c} + \mathbf{G_1}\hat{v}_g + \mathbf{G_2}\hat{d}_1 \tag{10.1.48}$$

$$\hat{y} = \mathbf{H}\hat{\mathbf{x}}_\mathbf{c} + J_1\hat{v}_g + J_2\hat{d}_1 \tag{10.1.49}$$

where

$$\mathbf{F} \equiv \mathbf{A_{21}D_1} + \mathbf{A_{22}} - \mathbf{E_{22}E_{21}}^{-1}\left(\mathbf{A_{11}D_1} + \mathbf{A_{12}}\right) \tag{10.1.50}$$

$$\mathbf{G_1} \equiv \mathbf{A_{21}d_2} + \mathbf{b_{12}} - \mathbf{E_{22}E_{21}}^{-1}(\mathbf{A_{11}d_2} + \mathbf{b_{11}}) \tag{10.1.51}$$

$$\mathbf{G_2} \equiv \mathbf{A_{21}d_3} + \mathbf{e_{12}} - \mathbf{E_{22}E_{21}}^{-1}(\mathbf{A_{11}d_3} + \mathbf{e_{11}}) \tag{10.1.52}$$

$$\mathbf{H} \equiv \mathbf{c_d D_1} + \mathbf{c_c} - \mathbf{k_2 E_{21}}^{-1}(\mathbf{A_{11}D_1} + \mathbf{A_{12}}) \tag{10.1.53}$$

$$J_1 \equiv \mathbf{c_d d_2} - \mathbf{k_2 E_{21}}^{-1}(\mathbf{A_{11}d_2} + \mathbf{b_{11}}) \tag{10.1.54}$$

$$J_2 \equiv \mathbf{c_d d_3} + k_1 - \mathbf{k_2 E_{21}}^{-1}(\mathbf{A_{11}d_3} + \mathbf{e_{11}}) \tag{10.1.55}$$

After applying the Laplace transform to (10.1.48) and (10.1.49), the two equations can be written as

$$s\hat{\mathbf{x}}_\mathbf{c}(s) = \mathbf{F}\hat{\mathbf{x}}_\mathbf{c}(s) + \mathbf{G_1}\hat{v}_g(s) + \mathbf{G_2}\hat{d}_1(s) \tag{10.1.56}$$

$$\hat{y}(s) = \mathbf{H}\hat{\mathbf{x}}_\mathbf{c}(s) + J_1\hat{v}_g(s) + J_2\hat{d}_1(s) \tag{10.1.57}$$

Equation (10.1.56) can be solved for $\hat{\mathbf{x}}_\mathbf{c}(s)$, which leads to

$$\hat{\mathbf{x}}_\mathbf{c}(s) = (\mathbf{sI} - \mathbf{F})^{-1}\left(\mathbf{G_1}\hat{v}_g(s) + \mathbf{G_2}\hat{d}_1(s)\right) \tag{10.1.58}$$

where $\mathbf{I}$ is the $n \times n$ identity matrix. Using this result (10.1.57) can now be stated as

$$\hat{y}(s) = \mathbf{H}(\mathbf{sI} - \mathbf{F})^{-1}\left(\mathbf{G_1}\hat{v}_g(s) + \mathbf{G_2}\hat{d}_1(s)\right) + J_1\hat{v}_g(s) + J_2\hat{d}_1(s) \tag{10.1.59}$$

In order to find the input voltage to output voltage transfer function, $A_v(s)$, and the control-to-output voltage transfer function, $A_c(s)$, the perturbation of the second input (i.e., $\hat{d}_1$ and $\hat{v}_g$ respectively) has to be nulled. The two transfer functions are given by

$$A'_v(s) = \frac{\hat{y}}{\hat{v}_g} = \mathbf{H}(\mathbf{sI} - \mathbf{F})^{-1}\mathbf{G_1} + J_1 \tag{10.1.60}$$

$$A'_c(s) = \frac{\hat{y}}{\hat{d}_1} = \mathbf{H}(\mathbf{sI} - \mathbf{F})^{-1}\mathbf{G_2} + J_2 \tag{10.1.61}$$

This algorithm is a generalization of the method presented in [22]. Thus, the order of the frequency responses in (10.1.60) and (10.1.61) is equivalent to n (i.e., the same as the number of continuous states). As discussed in the previous chapter, this algorithm is not very accurate for frequencies close to half of the switching frequency. If the converter satisfies the conditions stated in Chapter 9.2.1, the extra delay term (9.2.52) can be added to the results obtained by the state-space averaging. The delay term is given by

$$A_d(s) = \frac{1 - \frac{s}{\omega_d}}{1 + \frac{s}{\omega_d}} \tag{10.1.62}$$

where

$$\omega_d = \frac{4}{T_S(D_1 + D_d)} \tag{10.1.63}$$

where D_d is the conduction angle of the diode carrying the discontinuous current according to Chapter 9.2.1. Equation (10.1.63) has been slightly modified from its original form (9.5.53) in order to accommodate the multiple discontinuous conduction mode. In addition, the current in the diode might not exhibit a triangular waveform as assumed in Chapter 9.2.1. It can change the slope each time a current becomes discontinuous. However, the general shape is still close to a triangle, which allows to use the results from Chapter 9.

The final form of the two transfer functions is then given by

$$A_v(s) = \frac{\hat{y}}{\hat{v}_g} = \left(\mathbf{H}(s\mathbf{I} - \mathbf{F})^{-1}\mathbf{G_1} + J_1\right) \cdot A_d(s) \tag{10.1.64}$$

$$A_c(s) = \frac{\hat{y}}{\hat{d}_1} = \left(\mathbf{H}(s\mathbf{I} - \mathbf{F})^{-1}\mathbf{G_2} + J_2\right) \cdot A_d(s) \tag{10.1.65}$$

This concludes the derivation of the algorithm. In the next section a summary of the necessary steps is presented to arrive at (10.1.64) and (10.1.65).

10.2 Summary of the Algorithm

The previous section contains a rather detailed derivation of the suggested procedure to evaluate the small-signal behavior of converters with multiple discontinuous conduction modes. However, once the equations are derived it is unnecessary to repeat the derivation for each new converter. In this section the required steps to perform the analysis are summarized. It is assumed that the steady state quantities of the converter are known. In addition, it must understood in what order the discontinuous states go into DCM. The presented algorithm does not provide this information.

Assuming this information is available, the state vector $\mathbf{x}$ can be defined with the only constraint that the discontinuous states must be allocated in the top part $\mathbf{x}$. Next, the system matrices $\mathbf{A_i}$, $\mathbf{b_i}$ and $\mathbf{c_i}$ for each subinterval must be derived in exactly the same way as in CCM, with the only difference that there are more than two subintervals. In addition, the expressions for the discontinuous states of the form given in (10.1.40) must be found. This part must be done for each converter individually. Even the sequences of the subintervals can change in one particular topology depending on the component values.

From this step, the procedure is always the same; and it can be programmed in a software package like Mathemetica®. The steps are as follows:

$$\mathbf{A} = \sum_{i=1}^{k} D_i \mathbf{A_i} \quad , \quad i \in 1,\ldots,k \tag{10.2.1}$$

$$\mathbf{b} = \sum_{i=1}^{k} D_i \mathbf{b_i} \quad , \quad i \in 1,\ldots,k \tag{10.2.2}$$

$$\mathbf{c} = \sum_{i=1}^{k} D_i \mathbf{c_i} \quad , \quad i \in 1,\ldots,k \tag{10.2.3}$$

$$\mathbf{e_i} = (\mathbf{A_i} - \mathbf{A_k})\mathbf{x} + (\mathbf{b_i} - \mathbf{b_k})V_g \quad , \quad i \in 1,\ldots,k-1 \tag{10.2.4}$$

$$\mathbf{E2} = [\mathbf{e_2} \ , \ \mathbf{e_3} \ , \ \ldots \ , \ \mathbf{e_{k-1}}] \tag{10.2.5}$$

$$k_i = (\mathbf{c_i} - \mathbf{c_k})\mathbf{x} \quad , \quad i \in 1,\ldots,k-1 \tag{10.2.6}$$

$$\mathbf{k_2} = [k_2 \quad k_3 \quad \ldots \quad k_{k-1}] \tag{10.2.7}$$

$$\mathbf{A} \rightarrow \begin{bmatrix} \mathbf{A_{11}} & \mathbf{A_{12}} \;\}m \\ \underbrace{\mathbf{A_{21}}}_{m} & \underbrace{\mathbf{A_{22}}}_{n} \;\}n \end{bmatrix} \tag{10.2.8}$$

$$\mathbf{b} \rightarrow \begin{bmatrix} \mathbf{b_{11}} \;\}m \\ \mathbf{b_{12}} \;\}n \end{bmatrix} \tag{10.2.9}$$

$$\mathbf{e_1} \rightarrow \begin{bmatrix} \mathbf{e_{11}} \;\}m \\ \mathbf{e_{12}} \;\}n \end{bmatrix} \tag{10.2.10}$$

$$\mathbf{E_2} \rightarrow \begin{bmatrix} \mathbf{E_{21}} \;\}m \\ \mathbf{E_{22}} \;\}n \end{bmatrix} \tag{10.2.11}$$

$$\mathbf{c} \rightarrow [\; \underbrace{\mathbf{c_d}}_{m} \quad \underbrace{\mathbf{c_c}}_{n} \;] \tag{10.2.12}$$

$$\mathbf{D_{1_{ij}}} = \frac{\partial X_{d_i}}{\partial X_{c_j}} \quad , \quad i \in 1,\ldots,m \quad , \quad j \in 1,\ldots,n \tag{10.2.13}$$

$$\mathbf{d_{2_i}} = \frac{\partial X_{d_i}}{\partial V_g} \quad , \quad i \in 1,\ldots,m \tag{10.2.14}$$

$$\mathbf{d_{3_i}} = \frac{\partial X_{d_i}}{\partial D_1} \quad , \quad i \in 1,\ldots,m \tag{10.2.15}$$

$$\mathbf{F} = \mathbf{A_{21}D_1} + \mathbf{A_{22}} - \mathbf{E_{22}E_{21}}^{-1}(\mathbf{A_{11}D_1} + \mathbf{A_{12}}) \tag{10.2.16}$$

$$\mathbf{G_1} = \mathbf{A_{21}d_2} + \mathbf{b_{12}} - \mathbf{E_{22}E_{21}}^{-1}(\mathbf{A_{11}d_2} + \mathbf{b_{11}}) \tag{10.2.17}$$

$$\mathbf{G_2} = \mathbf{A_{21}d_3} + \mathbf{e_{12}} - \mathbf{E_{22}E_{21}}^{-1}(\mathbf{A_{11}d_3} + \mathbf{e_{11}}) \tag{10.2.18}$$

$$\mathbf{H} = \mathbf{c_d D_1} + \mathbf{c_c} - \mathbf{k_2 E_{21}}^{-1}(\mathbf{A_{11}D_1} + \mathbf{A_{12}}) \tag{10.2.19}$$

$$J_1 = \mathbf{c_d d_2} - \mathbf{k_2 E_{21}}^{-1}(\mathbf{A_{11} d_2} + \mathbf{b_{11}}) \tag{10.2.20}$$

$$J_2 = \mathbf{c_d d_3} + k_1 - \mathbf{k_2 E_{21}}^{-1}(\mathbf{A_{11} d_3} + \mathbf{e_{11}}) \tag{10.2.21}$$

$$A'_v(s) = \frac{\hat{y}}{\hat{v}_g} = \mathbf{H}(\mathbf{sI} - \mathbf{F})^{-1}\mathbf{G_1} + J_1 \tag{10.2.22}$$

$$A'_c(s) = \frac{\hat{y}}{\hat{d}_1} = \mathbf{H}(\mathbf{sI} - \mathbf{F})^{-1}\mathbf{G_2} + J_2 \tag{10.2.23}$$

If a high level of accuracy close to half of the switching frequency is required and the topology satisfies the condition stated in Chapter 9.2.1, then the following steps may be added:

$$\omega_d = \frac{4}{T_S(D_1 + D_d)} \tag{10.2.24}$$

$$A_d(s) = \frac{1 - \dfrac{s}{\omega_d}}{1 + \dfrac{s}{\omega_d}} \tag{10.2.25}$$

$$A_v(s) = \frac{\hat{y}}{\hat{v}_g} = \left(\mathbf{H}(\mathbf{sI} - \mathbf{F})^{-1}\mathbf{G_1} + J_1\right) \cdot A_d(s) \tag{10.2.26}$$

$$A_c(s) = \frac{\hat{y}}{\hat{d}_1} = \left(\mathbf{H}(\mathbf{sI} - \mathbf{F})^{-1}\mathbf{G_2} + J_2\right) \cdot A_d(s) \tag{10.2.27}$$

10.3 Practical Example

This section demonstrates how the procedure is applied to a real circuit. The Bifred topology shown in Fig. 10.1 has been chosen for that. This is a Sepic derived circuit where an additional diode D_1 in series with the input inductor L_1 was inserted. The presence of this diode enables two independent discontinuous inductor currents. Thus, the converter is designed such that both inductors operate in DCM. R_s the equivalent

series resistance (ESR) of C_2 is included in the model. Since in the experimental circuit the ESR was present it was included in order to compare the prediction with measurements.

The small-signal behavior of a switched mode converter depends on the operation point. Therefore, the first step is to find the steady state equations of that converter. Unlike on the small-signal behavior the effect of the series resistance R_s on the steady state is insignificant. The following large-signal equations were derived assuming the converter is loss-less (i.e., $R_s = 0$).

Historically, steady state equations of converters are commonly given in terms of all circuit elements, the input voltage and the duty ratio. In converters in DCM, particularly with multiple discontinuous conduction modes, this leads to quite complicated functions for the output voltage. Very often the equations are transcendental. However, from a designer's point of view this is usually the wrong approach, even if the equations were simple. Nobody decides to use a certain set of component values, applies a given duty ratio, and uses the output voltage which is a result of the chosen combination.

A design almost always starts with a given input and output voltage (or current) and, in order to have control over the voltage stress of the components, even the voltages inside the converter itself. Given these voltages, equations can be derived, which determine which duty ratio and component values are necessary to obtain these voltages. These equations are not only more useful, they also tend to be simpler for

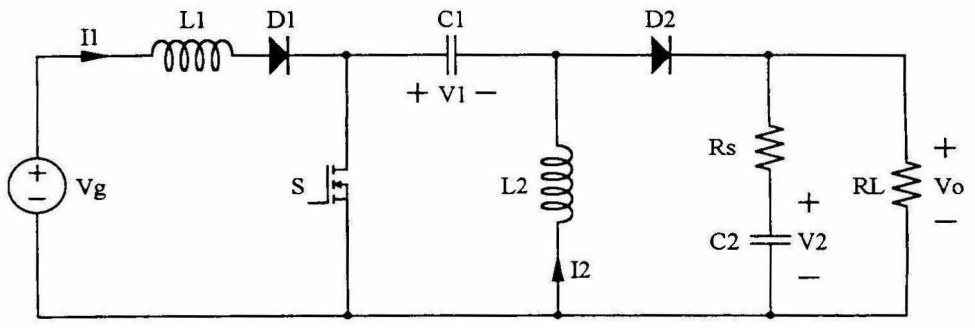

Figure 10.1: Bifred converter.

converters in DCM.

Having said all this, the steady state analysis can be initiated assuming V_g, V_o, V_1 and the processed power P are given. Since the analysis is rather simple and straightforward, only the results are stated here. Furthermore, a similar analysis of this converter for the more difficult case with an ac-input voltage has been carried out in Chapter 6.2.

The resulting inductor current waveforms are sketched in Fig. 10.2. The analysis reveals that the current I_2 can not become discontinuous before I_1, and I_1 can only become discontinuous if the following relation holds:

$$V_1 \geq V_g \tag{10.3.1}$$

Two more quantities need to be chosen by the designer. Firstly, the switching frequency T_s, and secondly, the conduction angle of L_2 or equivalently the relative length of the first three subintervals, denoted as D_c in Fig. 10.2. To ensure DCM in both inductors, D_c must obviously satisfy

$$D_c \leq 1 \tag{10.3.2}$$

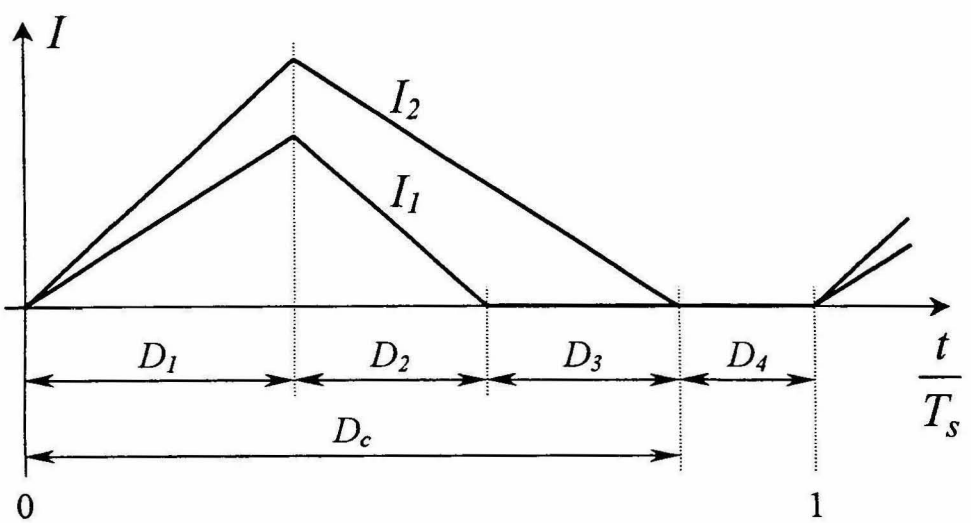

Figure 10.2: Typical inductor current waveforms of the Bifred with discontinuous conduction mode in both inductors.

The inductance values are given by

$$L_2 = D_c^2 \frac{T_s}{2P} \cdot \frac{V_1 V_o^2}{V_1 + V_o} \tag{10.3.3}$$

$$L_1 = L_2 \cdot \frac{V_g^2}{V_1 (V_1 + V_o - V_g)} \tag{10.3.4}$$

In addition, following relations apply:

$$D_1 = D_c \cdot \frac{V_2}{V_1 + V_o} \tag{10.3.5}$$

$$D_2 = D_1 \cdot \frac{V_g}{V_1 + V_o - V_g} \tag{10.3.6}$$

$$D_3 = D_1 \cdot \frac{(V_1 + V_o)(V_1 - V_g)}{V_o (V_1 + V_o - V_g)} \tag{10.3.7}$$

$$D_4 = 1 - D_1 - D_2 - D_3 \tag{10.3.8}$$

where D_1, D_2, D_3 and D_4 are the relative length of each subinterval as shown in Fig. 10.2. The capacitance values are not important for the determination of the steady state, hence, no formulas are given here.

The equivalent circuits for the four subintervals are depicted in Fig. 10.3. Note that in this example $l = 4$, $m = 2$, $n = 2$ and $k = 4$. The state vector **x** was chosen to be

$$x = \begin{bmatrix} I_1 \\ I_2 \\ V_1 \\ V_2 \end{bmatrix} \tag{10.3.9}$$

The matrices $\mathbf{A_i}$ and the vectors $\mathbf{b_i}$ can be determined using the four equivalent circuits. They are found to be as follows:

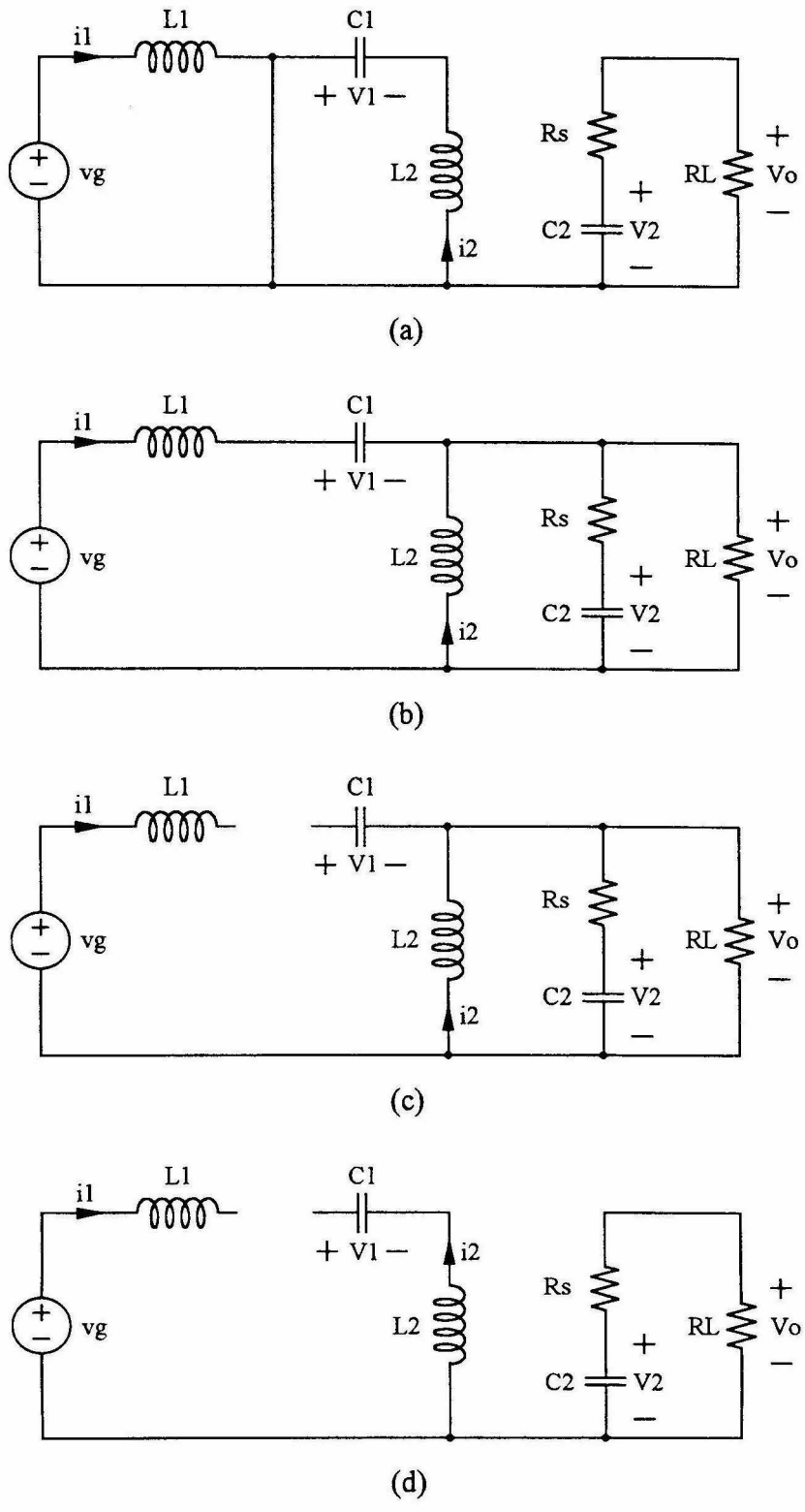

Figure 10.3: The equivalent circuits of the four subintervals during a switching cycle.

$$\mathbf{A_1} = \begin{bmatrix} 0 & 0 & 0 & 0 \\ 0 & 0 & \frac{1}{L_2} & 0 \\ 0 & \frac{-1}{C_2} & 0 & 0 \\ 0 & 0 & 0 & \frac{-1}{C_2(R_L + R_S)} \end{bmatrix} \quad \mathbf{b_1} = \begin{bmatrix} \frac{1}{L_1} \\ 0 \\ 0 \\ 0 \end{bmatrix} \tag{10.3.10}$$

$$\mathbf{A_2} = \begin{bmatrix} \frac{-R_P}{L_1} & \frac{-R_P}{L_1} & \frac{-1}{L_1} & \frac{1}{L_1}\left(\frac{R_P}{R_L} - 1\right) \\ \frac{-R_P}{L_2} & \frac{-R_P}{L_2} & 0 & \frac{1}{L_2}\left(\frac{R_P}{R_L} - 1\right) \\ \frac{1}{C_1} & 0 & 0 & 0 \\ \frac{R_P}{R_S C_2} & \frac{R_P}{R_S C_2} & 0 & \frac{-1}{C_2(R_L + R_S)} \end{bmatrix} \quad \mathbf{b_2} = \begin{bmatrix} \frac{1}{L_1} \\ 0 \\ 0 \\ 0 \end{bmatrix} \tag{10.3.11}$$

$$\mathbf{A_3} = \begin{bmatrix} 0 & 0 & 0 & 0 \\ 0 & \frac{-R_P}{L_2} & 0 & \frac{1}{L_2}\left(\frac{R_P}{R_L} - 1\right) \\ 0 & 0 & 0 & 0 \\ 0 & \frac{R_P}{R_S C_2} & 0 & \frac{-1}{C_2(R_L + R_S)} \end{bmatrix} \quad \mathbf{b_3} = \begin{bmatrix} 0 \\ 0 \\ 0 \\ 0 \end{bmatrix} \tag{10.3.12}$$

$$\mathbf{A_4} = \begin{bmatrix} 0 & 0 & 0 & 0 \\ 0 & 0 & 0 & 0 \\ 0 & 0 & 0 & 0 \\ 0 & 0 & 0 & \dfrac{-1}{C_2(R_L + R_S)} \end{bmatrix} \quad \mathbf{b_4} = \begin{bmatrix} 0 \\ 0 \\ 0 \\ 0 \end{bmatrix} \tag{10.3.13}$$

The output of the converter is V_o. This leads to the following output vectors.

$$\mathbf{c_1} = \begin{bmatrix} 0 & 0 & 0 & \dfrac{R_P}{R_S} \end{bmatrix} \tag{10.3.14}$$

$$\mathbf{c_2} = \begin{bmatrix} R_P & R_P & 0 & \dfrac{R_P}{R_S} \end{bmatrix} \tag{10.3.15}$$

$$\mathbf{c_3} = \begin{bmatrix} 0 & R_P & 0 & \dfrac{R_P}{R_S} \end{bmatrix} \tag{10.3.16}$$

$$\mathbf{c_4} = \begin{bmatrix} 0 & 0 & 0 & \dfrac{R_P}{R_S} \end{bmatrix} \tag{10.3.17}$$

where

$$R_P = R_L \,||\, R_S \approx R_S \tag{10.3.18}$$

Finally, the expressions for the discontinuous currents have to be found. The formulas must reflect the averaged current over the conduction time of the corresponding inductor and not over the whole switching cycle. It is noteworthy that the required formulas are much simpler than the expressions for the averaged current over one switching cycle. The averaged current over the conduction time of the corresponding

element is just half its peak value. The simplest way of expressing this mathematically is

$$I_1 = \frac{D_1 T_S}{2L_1} V_g \tag{10.3.19}$$

$$I_2 = \frac{D_1 T_S}{2L_2} V_1 \tag{10.3.20}$$

The algorithm summarized in Chapter 10.2 can now easily be applied.

10.4 Experimental Verification

An experimental circuit according to Fig. 10.1 was designed to compare the prediction with a measurement. The input and the output voltage of the converter and the component values were chosen according to Table 10.1. This circuit was operated with a switching frequency of 50kHz. First the measured transfer function was compared against the prediction using (10.2.23). The delay term was not taken into account. The result is shown in Fig. 10.4a over a frequency range from 10Hz to 25kHz (i.e., half of the switching frequency). The solid lines show the magnitude and the phase of the predicted transfer function. The measured values are represented as dashed lines. At higher frequencies the disagreement between the measured and predicted phase is quite significant. Therefore, in a second plot in Fig. 10.4b the delay term was included. (I.e., (10.2.27) was used to predict the transfer function.) The difference between measurement and prediction is much smaller in this case. A good agreement is observed over the whole frequency range. This is another indication that the theory of Chapter 9 is valid.

The small-signal analysis of the converter was repeated using the PWM switch model for converters in DCM [18]. The comparison of the prediction obtained by this

V_g	V_o	L_1	L_2	C_1	C_2	R_L	R_S
70V	45V	57µH	95µH	880µF	460µF	25Ω	65mΩ

Table 10.1: Specifications of the experimental circuit.

Modeling Method	Dc-Gain	Poles	Zeros
State-space Averaging	187.2	2.58 Hz 25.4 Hz 70.3 kHz	2.25 Hz 5.32 kHz 70.3 kHz (rhp)
PWM Switch Model	187.7	2.59 Hz 25.4 Hz 29.1 kHz 87.2 kHz	2.25 Hz 5.32 kHz 56.6 kHz 120 kHz (rhp)

Table 10.2: Salient features of the control-to-output transfer functions obtained with different modeling techniques (rhp → Right Half Plane).

method with the measured values is shown in Fig. 10.5a. The agreement close to half of the switching frequency tends to be somewhat better using state-space averaging together with the delay. Figure 10.5b compares the two modeling techniques. The only difference appears close to half of the switching frequency. The obtained poles and zeros for both cases together with the dc-gain are shown in Table 10.2.

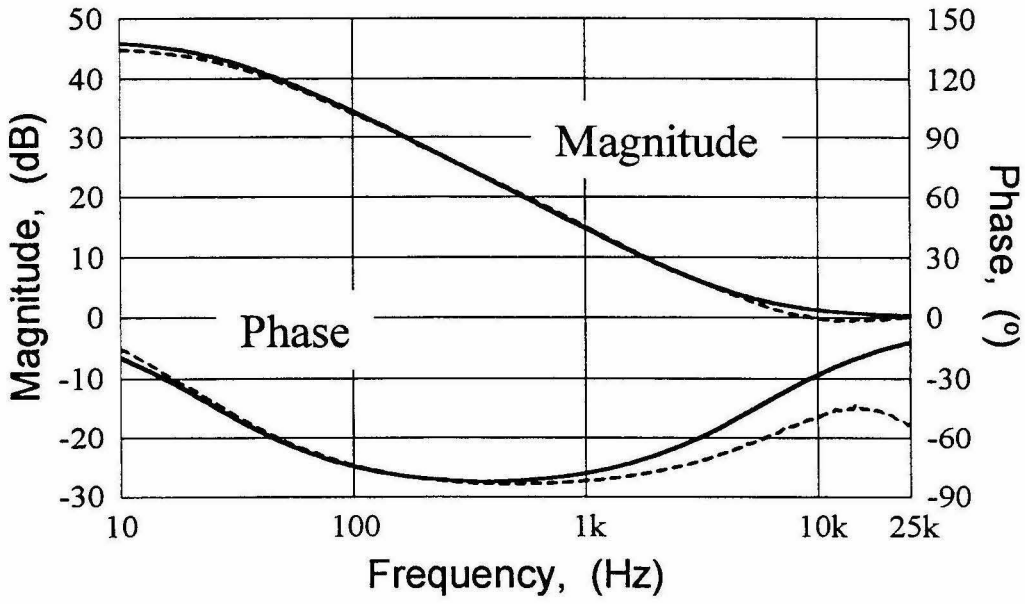

(a)

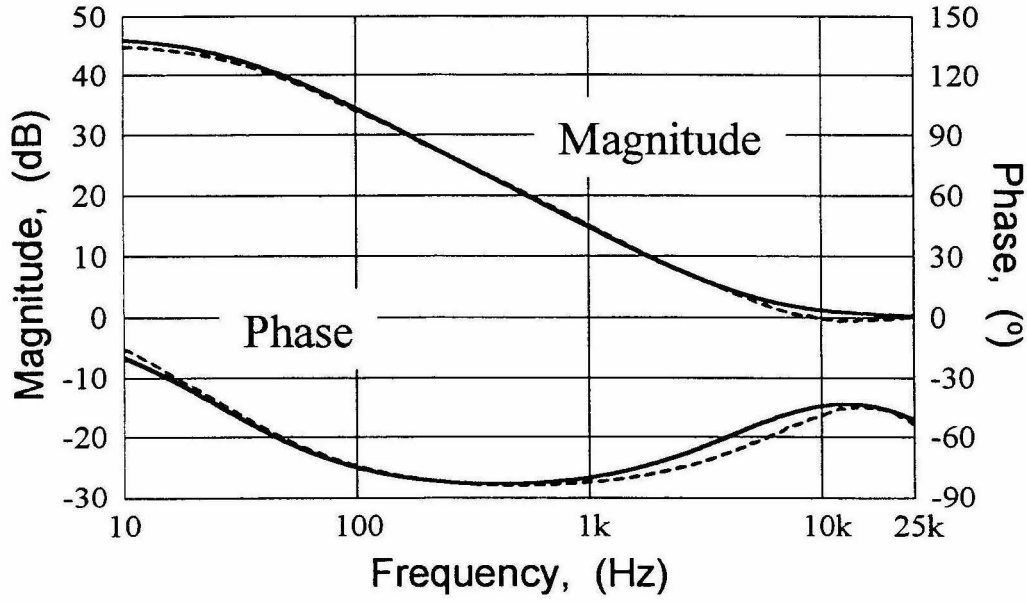

(b)

Figure 10.4: Control-to-output transfer function $A_c(s)$. Solid line: predicted; dashed line measured. (a) Without delay term and (b) including the delay term.

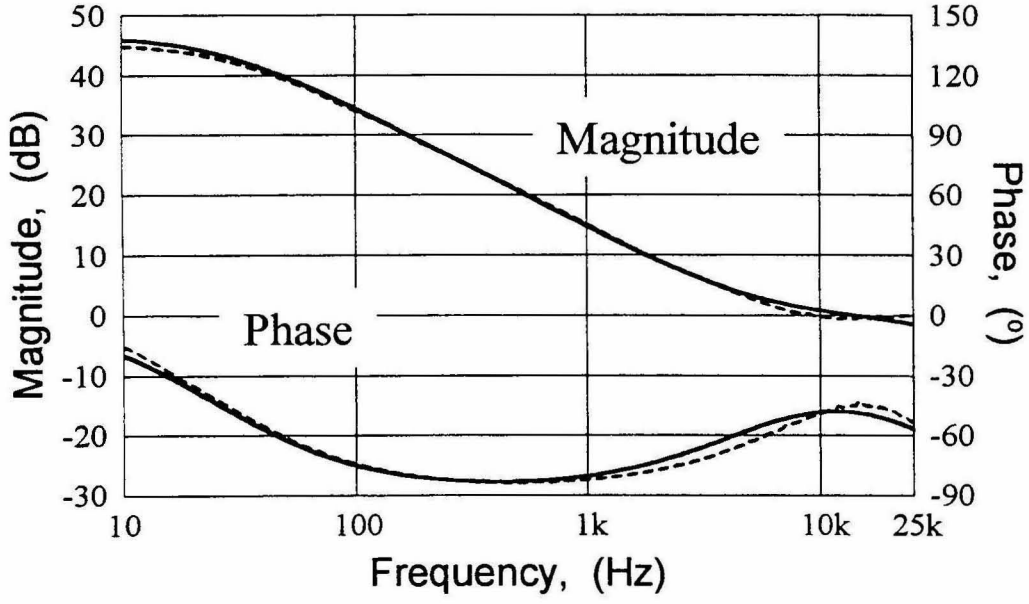

(a)

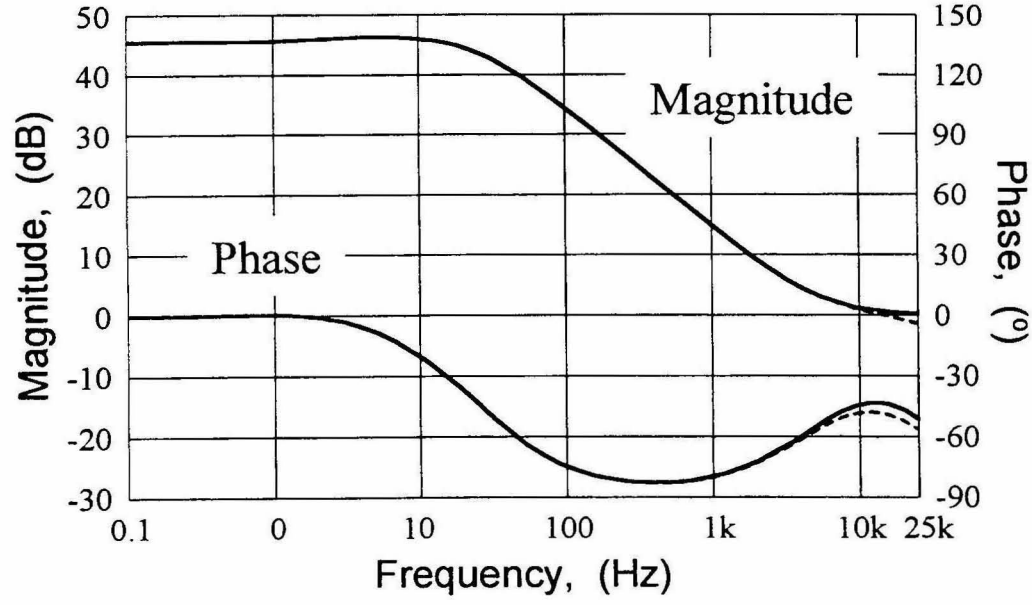

(b)

Figure 10.5: Control-to-output transfer function comparison with the PWM switch model. (a) Solid line: prediction using the PWM switch model; dashed line: measurement. (b) Solid line: prediction using state-space averaging; dashed line: prediction using the PWM switch model.

Chapter 11

Conclusion

In the second part of this thesis the small-signal analysis of the DCM is investigated from a different perspective. Reduced-order models do not accurately predict the transfer function when the frequency approaches half the switching frequency. It has been shown that this deficiency can be overcome by a simple additional term. This term is based on a fixed delay time which can easily be found from the steady state condition of the converter. The obtained results compare well with the measurements taken on an experimental circuit.

The derivation of the delay term is based on assumptions that rule out some of the basic converters such as the Buck converter. However, in those cases where it can be applied, it is very simple to determine. The result is at least as accurate as with conventional full-order models.

This result appears to be particularly instrumental in conjunction with the findings of Chapter 10. There, a standardized algorithm to perform the state-space averaging has been presented. This method does not increase its complexity as the number of discontinuous states increases. Using this method state-space averaging in DCM becomes a straightforward procedure. In these more complicated cases (multiple DCM) it is not always obvious how to use the conventional full order models.

The validity of the derived algorithm is supported by measurements on an experimental circuit.

Appendix A

General Properties of Three-Phase Systems

This appendix contains a listing of useful properties of three-phase systems. The list is by no means complete. Only those properties, which are used in the analysis carried out in this thesis, mainly in Chapter 4, are treated here.

A.1 The Ideal Three-Phase Source

A three-phase source is a system of voltage sources that can be represented using three individual ac voltage sources, which have one common terminal as shown in Fig. A.1. The common terminal is called the *neutral* whereas the unconnected terminals of the 3 voltage sources are called the *phases* or the *lines*. The neutral may or may not be accessible to a load. Thus, a three-phase source can have either three or four terminals. The two cases will be called the three-phase three-wire system and the three-phase four-wire system respectively.

In this thesis the ideal three-phase system is defined using symmetry properties of the three involved voltage sources. In particular, a three-phase system is considered to be ideal if it can be represented with three voltage sources satisfying the following three conditions:

1) The three voltage sources have sinusoidal waveforms with the same frequency.

2) The magnitudes of all three voltages are equal.

3) All three voltages have 120° mutual phase-shift with respect to each other.

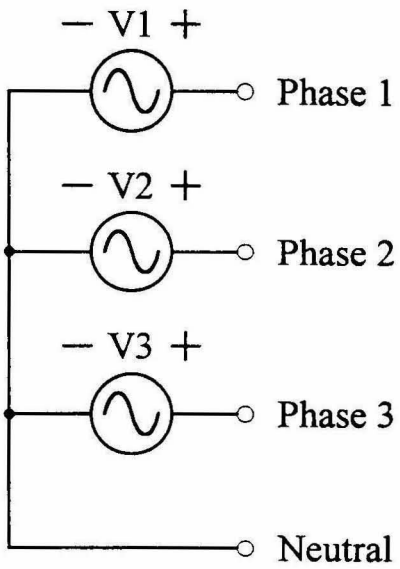

Figure A.1: Three-phase source.

Therefore, the voltages in the ideal three-phase system can be represented as

$$v_1(\theta) = V_L\sqrt{2}\sin(\theta) \tag{A.1.1}$$

$$v_2(\theta) = V_L\sqrt{2}\sin\left(\theta - \frac{2\pi}{3}\right) \tag{A.1.2}$$

$$v_3(\theta) = V_L\sqrt{2}\sin\left(\theta - \frac{4\pi}{3}\right) \tag{A.1.3}$$

Where V_L is the rms-value of the line-to-neutral voltages (i.e., of the three voltage sources in Fig. A.1). The voltage waveforms of an ideal three-phase system are shown in Fig. A.2. The time dependence of the voltages can be found by means of the following substitution:

$$\theta = \omega \cdot t \tag{A.1.4}$$

where ω is the angular frequency of the ac voltage.

Unless stated otherwise it is always assumed that the three-phase system is ideal. Using trigonometric identities it can be shown that for every θ the following equalities hold:

$$v_1(\theta)+v_2(\theta)+v_3(\theta)=0 \tag{A.1.5}$$

$$v_1^2(\theta)+v_2^2(\theta)+v_3^2(\theta)=3V_L^2 \tag{A.1.6}$$

The instantaneous power in a three-phase system is given by

$$p(\theta)=v_1(\theta)i_1(\theta)+v_2(\theta)i_2(\theta)+v_3(\theta)i_3(\theta) \tag{A.1.7}$$

If unity power factor is assumed, all the phase currents must be proportional to the corresponding phase voltage. This result was derived in Chapter 2.5. Therefore, the instantaneous power is proportional to the sum of the squares of the individual phase voltages, i.e.,

$$p(\theta)\propto v_1^2(\theta)+v_2^2(\theta)+v_3^2(\theta) \tag{A.1.8}$$

Using (A.1.6) it can be concluded that in the case of unity power factor, the instantaneous power in a system with an ideal three-phase source is constant. This is a

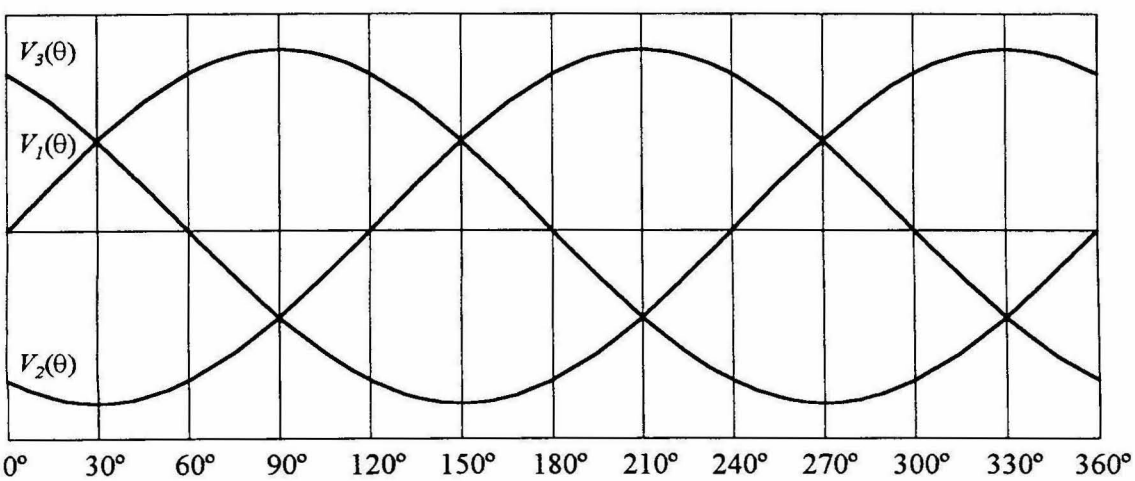

Figure A.2: Waveforms of an ideal three-phase source.

very useful property. Unlike in a single-phase power factor corrector, an energy storage capacitor is not necessarily required in the three-phase power factor corrector.

A.2 Symmetrical Waveform

In power factor correction circuits working in discontinuous conduction mode, one often encounters periodic current waveforms which exhibit the following symmetry properties:

1) The waveform is periodic with period length of 2π.
2) The waveform can be divided in two half waves with opposite sign but otherwise equivalent.
3) The interval 0 to 2π can be placed in such a way that the first half wave is symmetrical with respect to the vertical line at $\frac{1}{2}\pi$.

In mathematical terms this can be written as

$$f(\theta) = f(\theta + 2\pi) \tag{A.2.1}$$

$$f(\theta) = -f(\theta + \pi) \tag{A.2.2}$$

$$f(\theta) = f(\pi - \theta) \tag{A.2.3}$$

Consequently, if the first quarter of the waveform is known, the rest can easily be deduced. As a result, all the information about average value, rms-value and harmonic content are contained in only one quarter of the period length. This definition for the symmetrical waveform was also used in Chapter 2.7.

Given the properties represented by (A.2.1), (A.2.2) and (A.2.3), the rms-value of a periodic signal as defined in (2.3.1) can be found using

$$F_{rms} = \sqrt{\frac{2}{\pi}\int_0^{\pi/2} f^2(\theta)\,d\theta} \tag{A.2.4}$$

Under the same constraint, the coefficients of the Fourier representation defined in (2.2.2) through (2.2.4) are found to be

$$a_k = 0 \quad \text{for } k = 0,1,2,... \tag{A.2.5}$$

$$b_k = 0 \quad \text{for } k = 2,4,6,... \tag{A.2.6}$$

$$b_k = \frac{2\sqrt{2}}{\pi}\int_0^{\pi/2} f(\theta)\sin(k\theta)\,d\theta \quad \text{for k} = 1,3,5,... \tag{A.2.7}$$

It follows that there are only harmonics of odd order and only sine terms. One benefit of setting the upper integration limit to $\pi/2$ rather than to 2π is an improved accuracy in numerical calculations. Furthermore, this result will be very useful in the following section.

These results agree with the findings reported in Appendix A of [1] where the symmetrical waveform as defined here combine the definitions of the odd periodic extension and the alternating periodic extension.

A.3 The Symmetrical Three-Phase System

A symmetrical three-phase system is a three-phase system where all voltages and currents satisfy the following equations:

$$v_1(\theta) = v_2\left(\theta + \frac{2\pi}{3}\right) = v_3\left(\theta + \frac{4\pi}{3}\right) \tag{A.3.1}$$

$$i_1(\theta) = i_2\left(\theta + \frac{2\pi}{3}\right) = i_3\left(\theta + \frac{4\pi}{3}\right) \tag{A.3.2}$$

However, neither v_i nor i_i need to be sinusoidal.

Considering a three-phase three-wire system as shown in Fig. A.3, it can easily be seen that the sum of the three currents is zero, i.e.,

$$\sum_{i=1}^{3} i_i(\theta) = 0 \tag{A.3.3}$$

According to (2.2.5) the current i_i has a Fourier series representation of the form

$$i_1(\theta) = I_o + \sqrt{2}\sum_{k=1}^{\infty} I_k \sin(k\theta + \varphi_k) \tag{A.3.4}$$

where I_k is the rms-value of each individual harmonic component and φ_k is the corresponding phase angle. I_o is the dc-component which has to be zero to satisfy (A.3.3). Substituting (A.3.4) into (A.3.3) with the constraint (A.3.2) leads to

$$\sqrt{2}\sum_{k=1}^{\infty} I_k\left(\sin(k\theta + \varphi_k) + \sin\left(k\theta - \frac{2\pi k}{3} + \varphi_k\right) + \sin\left(k\theta - \frac{4\pi k}{3} + \varphi_k\right)\right) = 0 \tag{A.3.5}$$

To satisfy this equation for every θ each term inside the summation must be zero, i.e.,

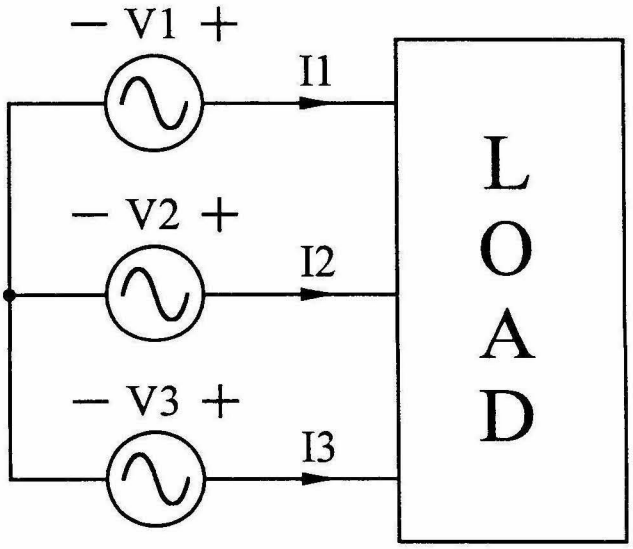

Figure A.3: Three-phase three-wire system.

$$I_k\left(\sin(k\theta+\varphi_k)+\sin\left(k\theta-\frac{2k\pi}{3}+\varphi_k\right)+\sin\left(k\theta-\frac{4k\pi}{3}+\varphi_k\right)\right)=0 \quad \text{for } k=1,2,3,... \tag{A.3.6}$$

Three different cases of k need to be distinguished, namely, $k=3n-2$, $k=3n-1$ and $k=3n$. If $k=3n-2$, then (A.3.6) becomes

$$\underbrace{I_k\left(\sin(k\theta+\varphi_k)+\sin\left(k\theta+\varphi_k-\frac{2\pi}{3}\right)+\sin\left(k\theta+\varphi_k-\frac{4\pi}{3}\right)\right)}_{=0}=0 \tag{A.3.7}$$

This is zero for an arbitrary I_k because the three sine waves have 120° mutual phase; therefore, their sum is zero, similarly as (A.1.5).

If $k=3n-1$, then (A.3.6) becomes

$$\underbrace{I_k\left(\sin(k\theta+\varphi_k)+\sin\left(k\theta+\varphi_k+\frac{2\pi}{3}\right)+\sin\left(k\theta+\varphi_k+\frac{4\pi}{3}\right)\right)}_{=0}=0 \tag{A.3.8}$$

Also this equation is satisfied for any value of I_k.

If $k=3n$, then (A.3.6) becomes

$$3I_k\sin(k\theta+\varphi_k)=0 \tag{A.3.9}$$

This third equation can only be zero for every θ if I_k is zero. The conclusion is that in a symmetrical three-phase three-wire system, no current harmonics of order 3n can exist. In mathematical terms this can be stated as

$$I_k=0 \quad \text{for } k=3n,\ n=1,2,3,... \tag{A.3.10}$$

A.4. Symmetrical Waveform in a Symmetrical Three-Phase System

Here, it is assumed that a function $f_1(\theta)$ satisfies the conditions (A.2.1), (A.2.2) and (A.2.3). It is also assumed that there are functions $f_2(\theta)$ and $f_3(\theta)$ such that they can

represent the voltages or the currents in a symmetrical three-phase system. (I.e., $f_1(\theta)$ through $f_3(\theta)$ satisfy conditions according to (A.3.1) or (A.3.2) respectively.) This leads to the following equation:

$$f_1(\theta) = f_1(\pi - \theta) = f_2\left(\theta + \frac{2\pi}{3}\right) = f_3\left(\theta + \frac{4\pi}{3}\right) \tag{A.4.1}$$

Simple substitutions using (A.2.1) through (A.2.3) lead to

$$f_2(\theta) = -f_1\left(\frac{\pi}{3} + \theta\right) \tag{A.4.2}$$

$$f_3(\theta) = f_1\left(\frac{\pi}{3} - \theta\right) \tag{A.4.3}$$

The significance of this result is that if $f_1(\theta)$, $f_2(\theta)$ and $f_3(\theta)$ are known over the interval $0 \le \theta \le 30°$, then $f_1(\theta)$ can easily be found over the range $0 \le \theta \le 90°$ using (A.4.2) and (A.4.3) (see Fig. A.4). Since both the symmetrical waveform and a symmetrical three-phase system is assumed, the functions $f_1(\theta)$, $f_2(\theta)$ and $f_3(\theta)$ are known over the whole interval $0 \le \theta \le 360°$.

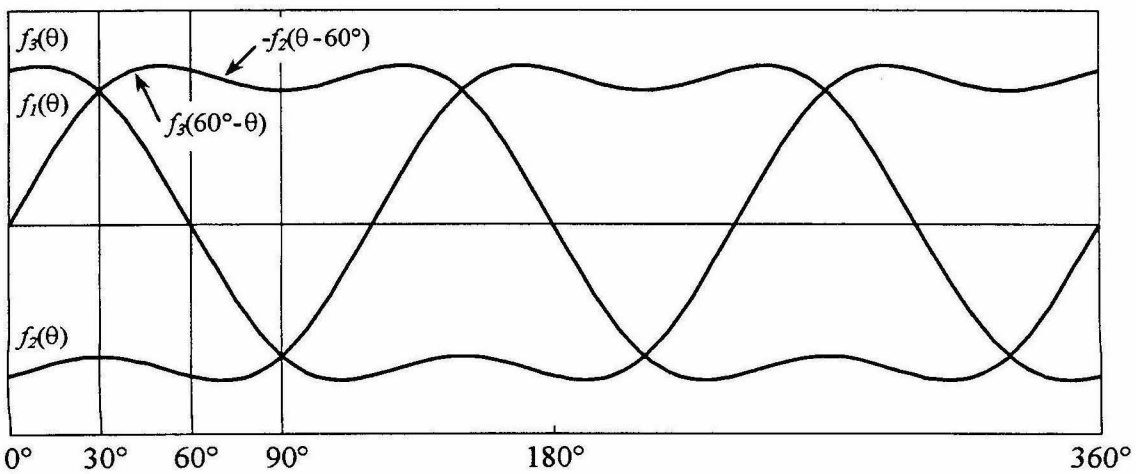

Figure A.4: Waveforms of a symmetrical three-phase system.

That means, all the information like the rms-value of $f_i(\theta)$ or the harmonic content is contained and can be found from this interval of 30° (i.e., from the interval $0 \le \theta \le \pi/6$). The equations (A.4.2) and (A.4.3) can be rearranged as

$$f_1(\theta) = -f_2\left(\theta - \frac{\pi}{3}\right) \tag{A.4.4}$$

$$f_1(\theta) = f_3\left(\frac{\pi}{3} - \theta\right) \tag{A.4.5}$$

Using (A.2.4) the rms-value for the symmetrical wave form is given by

$$F_{rms} = \sqrt{\frac{2}{\pi}\int_0^{\pi/2} f_1^2(\theta)\,d\theta} \tag{A.4.6}$$

Substitution of (A.4.4) and (A.4.5) into (A.4.6) leads to

$$F_{rms} = \sqrt{\frac{2}{\pi}\left(\int_0^{\pi/6} f_1^2(\theta)\,d\theta + \int_{\pi/6}^{\pi/3} f_3^2\left(\frac{\pi}{3} - \theta\right)d\theta + \int_{\pi/3}^{\pi/2} f_2^2\left(\theta - \frac{\pi}{3}\right)d\theta\right)} \tag{A.4.7}$$

Now the boundaries of the integrals can be adjusted such that they all run from 0 to $\pi/6$. This requires a substitution of θ in the 2nd and 3rd integral such that $\theta \to \theta + \pi/6$ and $\theta \to \theta + \pi/3$ respectively.

$$F_{rms} = \sqrt{\frac{2}{\pi}\left(\int_0^{\pi/6} f_1^2(\theta)\,d\theta + \int_0^{\pi/6} f_3^2\left(\frac{\pi}{6} - \theta\right)d\theta + \int_0^{\pi/6} f_2^2(\theta)\,d\theta\right)} \tag{A.4.8}$$

Notice that the following equality holds:

$$\int_0^{\pi/6} f_1\left(\frac{\pi}{6} - \theta\right)d\theta = \int_0^{\pi/6} f_1(\theta)\,d\theta \tag{A.4.9}$$

With this (A.4.8) can be rewritten as

$$F_{rms} = \sqrt{\frac{2}{\pi}\int_0^{\pi/6} f_1^2(\theta) + f_2^2(\theta) + f_3^2(\theta)\,d\theta} \tag{A.4.10}$$

According to (A.2.7) the rms-value of each individual harmonic is given by

$$b_k = \frac{2\sqrt{2}}{\pi}\int_0^{\pi/2} f_1(\theta)\sin(k\theta)\,d\theta \tag{A.4.11}$$

Once more, (A.4.4) and (A.4.5) can be used to find

$$b_k = \frac{2\sqrt{2}}{\pi}\left(\int_0^{\pi/6} f_1(\theta)\sin(k\theta)\,d\theta + \int_{\pi/6}^{\pi/3} f_3\left(\frac{\pi}{3}-\theta\right)\sin(k\theta)\,d\theta - \int_{\pi/3}^{\pi/2} f_2\left(\theta-\frac{\pi}{3}\right)\sin(k\theta)\,d\theta\right) \tag{A.4.12}$$

The same substitutions as in (A.4.8) lead to the following

$$b_k = \frac{2\sqrt{2}}{\pi}\int_0^{\pi/6} f_1(\theta)\sin(k\theta) + f_3\left(\frac{\pi}{6}-\theta\right)\sin\left(k\left(\theta+\frac{\pi}{6}\right)\right) - f_2(\theta)\sin\left(k\left(\theta+\frac{\pi}{3}\right)\right)d\theta \tag{A.4.13}$$

And after some more algebra

$$b_k = \frac{2\sqrt{2}}{\pi}\int_0^{\pi/6} f_1(\theta)\sin(k\theta) + f_2(\theta)\sin\left(k\theta-\frac{2\pi k}{3}\right) + f_3(\theta)\sin\left(k\theta-\frac{4\pi k}{3}\right)d\theta \tag{A.4.14}$$

The fundamental component b_1 is given by

$$b_1 = \frac{2\sqrt{2}}{\pi}\int_0^{\pi/6} f_1(\theta)\sin(\theta) + f_2(\theta)\sin\left(\theta-\frac{2\pi}{3}\right) + f_3(\theta)\sin\left(\theta-\frac{4\pi}{3}\right)d\theta \tag{A.4.15}$$

The question might be posed: why is it important to express all these quantities in terms of integrals running from 0 to 30°? Consider the waveforms in Fig. A.2 to be the input voltages of a converter. For the analysis of one switching cycle it can be important to know now what the polarity of each input voltage is during the switching cycle in

question. It must also be known which of the two voltages with the same polarity has the higher magnitude. Generally, this tends to apply to converters operating in discontinuous conduction mode (DCM). More importantly, it applies to the converter analyzed in Chapter 4.

Considering Fig. A.2 it can be concluded that the above described input voltage situation changes every 30°. The higher magnitude changes from one phase to the next one or one phase voltage changes its polarity. For an arbitrary converter the switching cycle must be analyzed for each of the 12 consecutive 30° intervals separately. If it can be concluded that the input currents satisfy simultaneously the symmetrical waveform condition and the symmetrical three-phase condition, then it is enough to analyze the operation of the converter for one single 30° interval. This applies to the converter analyzed in Chapter 4.

A.5 Power Considerations in a Symmetrical Three Phase System with an Ideal Three-Phase Voltage Source and the Symmetrical Current Waveform

In this section a symmetrical three-phase three-wire system is considered which is connected to an ideal three-phase voltage source. In addition the current waveform is assumed to satisfy the symmetrical waveform condition. In general, the instantaneous power is given in (A.1.7). This can be decomposed into three components, each of which represents the power delivered by each phase separately. These components are

$$\begin{aligned} p_1(\theta) &= v_1(\theta) i_1(\theta) \\ p_2(\theta) &= v_2(\theta) i_2(\theta) \\ p_3(\theta) &= v_3(\theta) i_3(\theta) \end{aligned} \tag{A.5.1}$$

The total instantaneous power of course is given by

$$p(\theta) = p_1(\theta) + p_2(\theta) + p_3(\theta) \tag{A.5.2}$$

According to (2.2.5) the current i_1 has a Fourier series representation of the form

$$i_1(\theta) = I_o + \sqrt{2}\sum_{k=1}^{\infty} I_k \sin(k\theta + \varphi_k) \tag{A.5.3}$$

Since the symmetrical waveform is assumed this reduces to

$$i_1(\theta) = \sqrt{2}\sum_{k=1}^{\infty} I_k \sin(k\theta) \tag{A.5.4}$$

where

$$I_k = 0 \quad \text{for} \quad k = 2,4,6,... \tag{A.5.5}$$

(According to (A.2.5) through (A.2.7).) Since a symmetrical three-phase three-wire system is considered the following also holds:

$$I_k = 0 \quad \text{for} \quad k = 3,6,9,... \tag{A.5.6}$$

Equation (A.5.4) and (A.1.1) can be substituted into the expression for $p_1(\theta)$ in (A.5.1).

$$p_1(\theta) = 2V_L \sum_{k=1}^{\infty} I_k \sin(k\theta)\sin(\theta) \tag{A.5.7}$$

Using a trigonometric identity this can be rewritten as

$$p_1(\theta) = V_L \sum_{k=1}^{\infty} I_k \cos((k-1)\theta) - \cos((k+1)\theta) \tag{A.5.8}$$

Thus, the k^{th} current harmonic contributes to the two power harmonics of order k-1 and k+1. The magnitude of both components is equal and the phase is 180° apart. From (A.5.5) and (A.5.6) it can be concluded that only the fundamental and harmonics of order

$$k = 6n \pm 1 \tag{A.5.9}$$

can exist. The possible numbers are shown in Fig. A.5. The arrows indicate which power harmonics each current component creates. Thus, $p_1(\theta)$ can contain a dc-part and

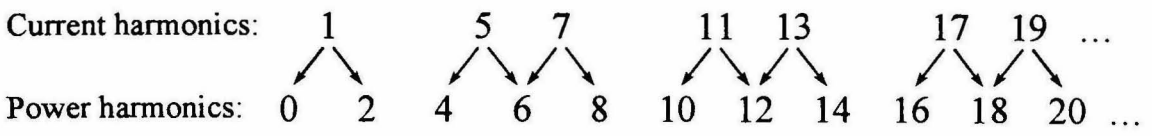

Figure A.5: Possible current and power harmonics in a symmetrical three-phase three-wire system with an ideal three-phase voltage source and symmetrical current waveform.

all even harmonics. Due to the assumed symmetry of the system the same relation must apply to $p_2(\theta)$ and $p_3(\theta)$. Since the voltages and the currents satisfy (A.3.1) and (A.3.2) respectively, the power in each phase must satisfy the same kind of equation. Therefore,

$$p_1(\theta) = p_2\left(\theta + \frac{2\pi}{3}\right) = p_3\left(\theta + \frac{4\pi}{3}\right) \tag{A.5.10}$$

In Appendix A.3 it has been shown that given (A.5.10) all harmonics that are not multiple of three add up to zero for every θ. Harmonics that are multiples of three do not mutually cancel if their magnitudes are non-zero in each individual phase. Consequently, the total instantaneous power $p(\theta)$ as given in (A.5.2) can only contain a constant part and harmonics of order six and multiples thereof. This is often referred to as the six times the line frequency ripple.

Inversely, if the total instantaneous power is constant, the power harmonics of order six and its multiples must be zero in each individual phase (i.e., in $p_1(\theta)$, $p_2(\theta)$ and $p_3(\theta)$ separately). In order for these harmonics to vanish, the contributions of the two neighboring current harmonics must mutually cancel (Fig. A.5). From (A.5.8) it can be concluded that this requires that these two harmonics must be equal. In mathematical terms this can be written as

$$I_{6n+1} = I_{6n-1} \tag{A.5.11}$$

If the instantaneous power is constant, the harmonics must appear in equal pairs with order numbers next to a multiple of six. A similar analysis has been carried out in [2]. A practical case where this relation holds is discussed in Chapter 4.4.

A.6 Summary

In this final section the results of this Appendix A are briefly summarized.

1) In an ideal three-phase source the following holds:
   - The sum of the phase voltages is zero.
   - The sum of the squares of the phase voltages is constant.

2) A symmetrical waveform as defined in Appendix A.2 has the following property:
   - The Fourier series expansion has no even harmonic components.

3) Currents in a symmetrical three-phase three-wire system satisfy the following:
   - The Fourier series expansion has no harmonic components of order $3n$.

4) If the currents in a symmetrical three-phase three-wire system possess the symmetrical waveform, then the following holds:
   - The Fourier series expansion contains only harmonic components of order $6n \pm 1$.
   - If all three currents are known over an interval of 30°, then all current waveforms are completely determined over the whole period. All the information about the currents (e.g., its *THD*, its rms-value, or the Fourier series expansion) is contained in a 30° interval.

5) The following can be said about a symmetrical three-phase three-wire system with an ideal three-phase source and with symmetrical current waveforms:
   - The instantaneous power has only harmonics of order $6n$.
   - If the instantaneous power is constant, the current harmonics appear in equal pairs, such that $I_{6n+1} = I_{6n-1}$.

Appendix B

Alternative Forms of Equations

The equations in Chapter 4 were stated in a way that appeared to be the simplest possible form. Using trigonometric identities and a number of substitutions, some of these equations can be stated alternatively in a form that increases the computation speed in numerical calculations tremendously. These equations are listed in this appendix.

B.1: Equation (4.1.63) or (4.6.7) respectively, i.e.,

$$\alpha_s(\theta) = \alpha_1{}^2(\theta) + \alpha_2{}^2(\theta) + \alpha_3{}^2(\theta) \tag{B.1}$$

is equivalent to

$$\alpha_s(\theta) = \frac{3}{2}M^2 \cdot \frac{M^2 + 2M\sin(2\theta)\sin\left(\theta - \frac{2\pi}{3}\right) + \sin^2(2\theta)}{\left(\left(M - \sqrt{3}\sin(\theta)\right)\left(M - \cos(\theta)\right)\right)^2} \tag{B.2}$$

B.2: Equation (4.1.68) or (4.6.8) respectively, i.e.,

$$\beta_k(\theta) = \alpha_1(\theta)\sin(k\theta) + \alpha_2(\theta)\sin\left(k\theta - \frac{2\pi k}{3}\right) + \alpha_3(\theta)\sin\left(k\theta - \frac{4\pi k}{3}\right) \tag{B.3}$$

is equivalent to

$$\beta_k(\theta)=\begin{cases}\dfrac{3}{2}M\dfrac{M\cos((k-1)\theta)+\sin(2\theta)\sin\left(k\theta-\dfrac{2\pi}{3}\right)}{\left(M-\sqrt{3}\sin(\theta)\right)\left(M-\cos(\theta)\right)} & \text{if } k=3n+1\\ \dfrac{-3}{2}M\dfrac{M\cos((k+1)\theta)-\sin(2\theta)\sin\left(k\theta+\dfrac{2\pi}{3}\right)}{\left(M-\sqrt{3}\sin(\theta)\right)\left(M-\cos(\theta)\right)} & \text{if } k=3n-1\\ 0 & \text{if } k=3n\end{cases} \qquad \text{(B.4)}$$

B.3: The integral in (4.2.3) or (4.6.9) respectively, i.e.,

$$A_1=\frac{\sqrt{3}M}{\pi}\int_0^{\pi/6}\alpha_d(\theta)\,d\theta \qquad \text{(B.5)}$$

can be analytically solved, such that A_1 can be expressed as

$$A_1=\frac{M^3}{\pi}\left(\frac{\tan^{-1}\left(\dfrac{\left(2-\sqrt{3}\right)\left(\sqrt{\left|3-M^2\right|}\right)}{M+3-2\sqrt{3}}\right)}{\sqrt{\left|3-M^2\right|}}+\frac{3\tan^{-1}\left(\dfrac{\left(2-\sqrt{3}\right)(M+1)}{\sqrt{M^2-1}}\right)}{\sqrt{M^2-1}}\right)-\frac{M^3}{3}-\frac{\sqrt{3}M}{2\pi} \qquad \text{(B.6)}$$

This expression has a zero divided by zero term at $M=\sqrt{3}$. The limit at this value of M is given by

$$A_1=\frac{1}{2\pi}\left(3\sqrt{3}-6-2\pi+9\sqrt{6}\tan^{-1}\left(\frac{\sqrt{3}-1}{\sqrt{2}}\right)\right) \quad \text{if} \quad M=\sqrt{3} \qquad \text{(B.7)}$$

B.4: Equation (4.2.5) or (4.6.10) respectively, i.e.,

$$A_2 = \sqrt{\frac{1}{\pi}\int_0^{\pi/6} \alpha_s(\theta)\, d\theta} \tag{B.8}$$

is equivalent to

$$A_2 = \sqrt{\frac{3M^2}{2\pi} \cdot \int_0^{\pi/6} \frac{M^2 + 2M\sin(2\theta)\sin\left(\theta - \frac{2\pi}{3}\right) + \sin^2(2\theta)}{\left(M - \sqrt{3}\sin(\theta)\right)\left(M - \cos(\theta)\right)^2}\, d\theta} \tag{B.9}$$

B.5: Equation (4.3.9) or (4.6.11) respectively, i.e.,

$$A_3 = \sqrt{\frac{3M^2}{\pi}\int_0^{\pi/6} \frac{{\alpha_d}^2(\theta)}{\alpha_s(\theta)}\, d\theta} \tag{B.10}$$

is equivalent to

$$A_3 = \sqrt{\frac{3}{2\pi} \cdot \int_0^{\pi/6} \frac{\left(M + \sin(2\theta)\sin\left(\theta - \frac{2\pi}{3}\right)\right)^2}{M^2 + 2M\sin(2\theta)\sin\left(\theta - \frac{2\pi}{3}\right) + \sin^2(2\theta)}\, d\theta} \tag{B.11}$$

B.6: Equation (4.4.4) or (4.6.12) respectively, i.e.,

$$A_4 = \sqrt{\frac{3}{\pi M^2}\int_0^{\pi/6} \frac{\alpha_s(\theta)}{{\alpha_d}^2(\theta)}\, d\theta} \tag{B.12}$$

is equivalent to

$$A_4 = \sqrt{1 + \frac{6}{\pi} \cdot \int_0^{\pi/6} \left(\frac{\sin(2\theta)\cos\left(\theta - \frac{2\pi}{3}\right)}{M + \sin(2\theta)\sin\left(\theta - \frac{2\pi}{3}\right)} \right)^2 d\theta} \tag{B.13}$$

B.7: Equation (4.2.8) or I_{krel} at constant D_1 in Table 4.1 respectively, i.e.,

$$I_{k_{rel}} = \frac{1}{\pi A_1} \int_0^{\pi/6} \beta_k(\theta)\, d\theta \tag{B.14}$$

is equivalent to

$$I_{k_{rel}} = \begin{cases} \dfrac{3M}{2\pi A_1} \cdot \displaystyle\int_0^{\pi/6} \dfrac{M\cos((k-1)\theta) + \sin(2\theta)\sin\left(k\theta - \dfrac{2\pi}{3}\right)}{\left(M - \sqrt{3}\sin(\theta)\right)\left(M - \cos(\theta)\right)} & \text{if } k = 6n+1 \\ \dfrac{-3M}{2\pi A_1} \cdot \displaystyle\int_0^{\pi/6} \dfrac{M\cos((k+1)\theta) - \sin(2\theta)\sin\left(k\theta + \dfrac{2\pi}{3}\right)}{\left(M - \sqrt{3}\sin(\theta)\right)\left(M - \cos(\theta)\right)} & \text{if } k = 6n-1 \\ 0 & \text{otherwise} \end{cases} \tag{B.15}$$

B.8: Equation (4. 3.15) or I_{krel} at optimal D_1 in Table 4.1 respectively, i.e.,

$$I_{k_{rel}} = \frac{\sqrt{3}M}{\pi {A_3}^2} \int_0^{\pi/6} \frac{\alpha_d(\theta)}{\alpha_s(\theta)} \beta_k(\theta)\, d\theta \tag{B.16}$$

is equivalent to

$$I_{k_{rel}} = \begin{cases} \dfrac{3}{2\pi A_3} \cdot \displaystyle\int_0^{\pi/6} \dfrac{\left(M\cos((k-1)\theta) + \sin(2\theta)\sin\left(k\theta - \dfrac{2\pi}{3}\right)\right)\left(M + \sin(2\theta)\sin\left(\theta - \dfrac{2\pi}{3}\right)\right)}{M^2 + 2M\sin(2\theta)\sin\left(\theta - \dfrac{2\pi}{3}\right) + \sin^2(2\theta)} & \text{if } k = 6n+1 \\ \dfrac{-3}{2\pi A_3} \cdot \displaystyle\int_0^{\pi/6} \dfrac{\left(M\cos((k+1)\theta) - \sin(2\theta)\sin\left(k\theta + \dfrac{2\pi}{3}\right)\right)\left(M + \sin(2\theta)\sin\left(\theta - \dfrac{2\pi}{3}\right)\right)}{M^2 + 2M\sin(2\theta)\sin\left(\theta - \dfrac{2\pi}{3}\right) + \sin^2(2\theta)} & \text{if } k = 6n-1 \\ 0 & \text{otherwise} \end{cases}$$

(B.17)

B.9: Equation (4.4.7) or I_{krel} in the constant I_d case in Table 4.1 respectively, i.e.,

$$I_{k_{rel}} = \frac{2\sqrt{3}}{\pi M} \int_0^{\pi/6} \frac{\beta_k(\theta)}{\alpha_d(\theta)} d\theta \tag{B.18}$$

is equivalent to

$$I_{k_{rel}} = \begin{cases} \dfrac{6}{\pi} \cdot \displaystyle\int_0^{\pi/6} \dfrac{M\cos((k-1)\theta) + \sin(2\theta)\sin\left(k\theta - \dfrac{2\pi}{3}\right)}{M + \sin(2\theta)\sin\left(\theta - \dfrac{2\pi}{3}\right)} d\theta & \text{if } k = 6n+1 \\ \dfrac{-6}{\pi} \cdot \displaystyle\int_0^{\pi/6} \dfrac{M\cos((k+1)\theta) - \sin(2\theta)\sin\left(k\theta + \dfrac{2\pi}{3}\right)}{M + \sin(2\theta)\sin\left(\theta - \dfrac{2\pi}{3}\right)} d\theta & \text{if } k = 6n-1 \\ 0 & \text{otherwise} \end{cases} \tag{B.19}$$

Appendix C

Dynamic Behavior of Currents in DCM

State-space averaging for switch mode converters was first introduced in [13]. In [22] the method was extended to converters operating in discontinuous conduction mode (DCM). The averaged system is always represented in the form

$$\dot{\mathbf{x}} = \mathbf{A}\mathbf{x} + \mathbf{B}V_g \tag{C.1}$$

where **A** is the averaged system matrix and **B** is the averaged input vector. The averaging is carried out using the matrices (or vectors, respectively) of each subinterval of one switching cycle weighted by the length of the corresponding subinterval. In a converter in continuous conduction mode (CCM), **A** and **B** are given by

$$\mathbf{A} = \mathbf{A}_1 D_1 + \mathbf{A}_2 D_2 \tag{C.2}$$

$$\mathbf{B} = \mathbf{B}_1 D_1 + \mathbf{A}_2 D_2 \tag{C.3}$$

The state vector **x** contains all the currents and voltages of the reactive elements and $\dot{\mathbf{x}}$ contains their time derivatives. In order to find the small-signal behavior of a converter, the system represented in (C.1) is perturbed around its point of operation. This leads to a small-signal description of the form

$$\dot{\mathbf{x}} = \mathbf{A}\hat{\mathbf{x}} + \mathbf{B}\hat{v}_g + \mathbf{F}\hat{d}_1 . \tag{C.4}$$

In [22] it has been pointed out that if a state operates in DCM, its corresponding time derivative in $\dot{\mathbf{x}}$ must be set to zero. Consequently, in Chapter 10.1 of this thesis the whole vector $\dot{\mathbf{x}}_\mathbf{d}$ must be set to zero (see (10.1.35) and (10.1.38)). This point can cause

some confusion because at first sight it seems to imply that the discontinuous states are not time varying or that they are approximated by constants.

Of course, these states have a dynamic behavior similar to the ones in CCM. The di/dt of currents in DCM is often even larger than the one of the same converter in CCM. The purpose of this appendix is to show that this fact is not neglected by state-space averaging. It will be shown that if a state operates in DCM, the corresponding element in $\dot{\mathbf{x}}$ must be set to zero.

Fig. C.1a shows a typical waveform in continuous conduction mode. The waveform does not represent a steady state situation since the current value at the end of the switching cycle is different from the one at the beginning. The equation for the current during the first subinterval is given by

$$i(t) = \frac{V_1}{L} t \tag{C.5}$$

where L is the inductance value of the component that carries the current i, and V_1 is a certain voltage in that converter. It can be a composed of different states plus the input voltage. Similarly, during the second subinterval the current can be described by

$$i(t) = \frac{V_2}{L} t \tag{C.6}$$

where V_2 is another combination of states and maybe the input voltage. The current difference between the beginning and the end of the switching cycle can now be determined by using the geometry of the triangles in Fig. C.1a. For convenience the length of one switching cycle is here denoted by ΔT.

$$\Delta I = \frac{(V_1 D_1 + V_2 D_2)\Delta T}{L} \tag{C.7}$$

This can be rearranged as follows:

$$\frac{\Delta I}{\Delta T} = \frac{V_1 D_1 + V_2 D_2}{L} \tag{C.8}$$

If the switching frequency is sufficiently high (i.e., if ΔT is sufficiently short), $\Delta I/\Delta T$ is approximately the same as di/dt. Thus,

$$\frac{di}{dt} \approx \frac{V_1 D_1 + V_2 D_2}{L} \tag{C.9}$$

A much more detailed derivation is given in [22]. State-space averaging is just an organized way to arrive at equations like (C.9) for all states simultaneously.

Figure C.1b shows the waveforms if this current of the same converter enters the discontinuous conduction mode. The current slopes still depend on the same V_1 and V_2 as before. The values may have changed but it is the same combination of the same states. In this case there is no ΔI that can be calculated as before. Using the geometry the triangles in Fig. C.1b, an equation equivalent to (C.8), must read as follows:

$$0 = \frac{V_1 D_1 + V_2 D_2}{L} \tag{C.10}$$

It must be pointed out that the right-hand side of (C.8), (C.9) and (C.10) are the same. Like in the CCM case, also in the DCM case, applying state-space averaging provides the-right-hand side of (C.10). In this case, the left-hand side is not the time derivative of a current. From Fig. C.1b it is clear that it is always zero if the converter operates in DCM even during transients. It must also be zero if a small-signal perturbation is applied. Consequently, the corresponding component in $\dot{\mathbf{x}}$ must be set to zero; anything else is wrong. The equations of the form like (C.10) obtained in DCM are not used to determine the di/dt or dv/dt, or any of the states, they serve to determine D_2.

In CCM the current and voltages are described by differential equations like (C.9). In contrast, in DCM they are described by algebraic equations. Therefore, the derivatives of these currents or voltages are of no consequence to the solution of the network, no matter what they are. Figure C.2 shows an example of a changing current in DCM and its average value. The expression for the average current is found using the geometry of the triangles in Fig. C.1b. For this example it is

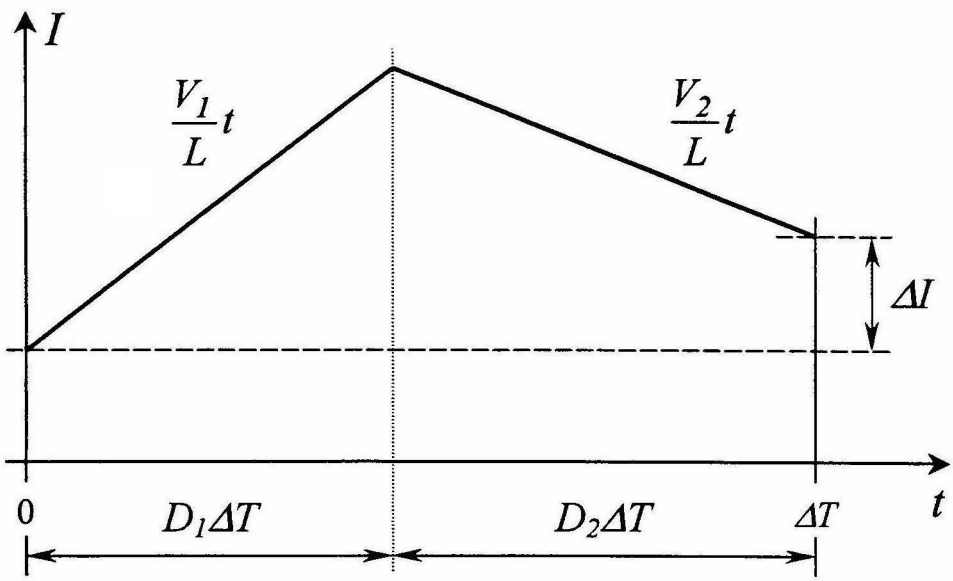

(a)

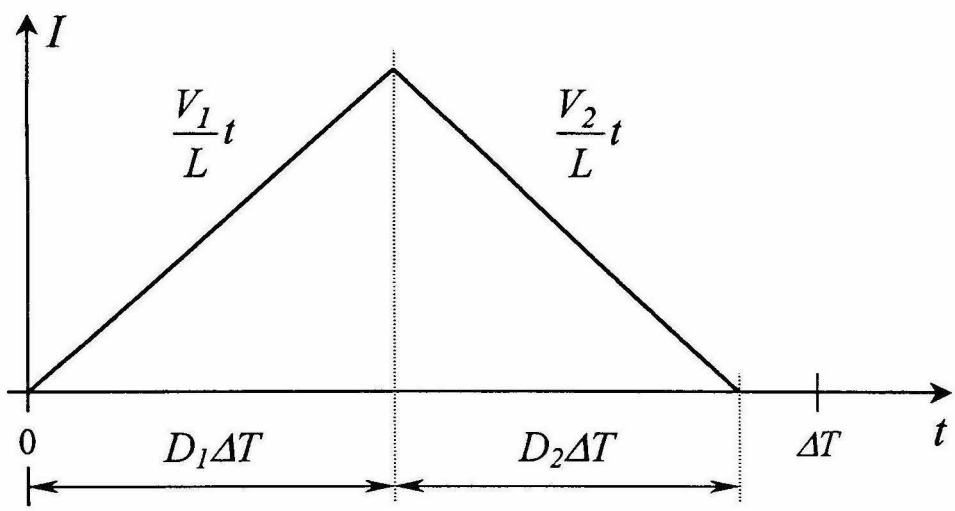

(b)

Figure C.1: Typical current waveforms: (a) in continuous conduction mode and (b) in discontinuous conduction mode.

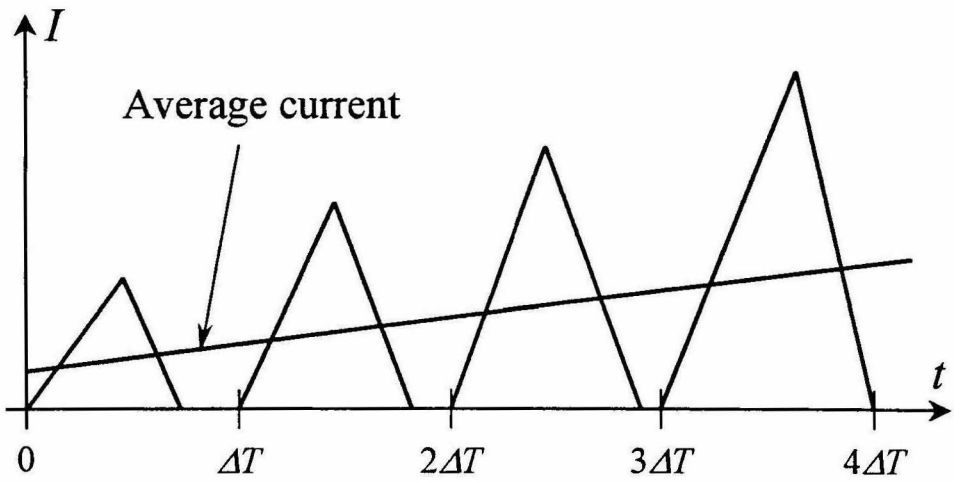

Figure C.2: Changing current in discontinuous conduction mode.

$$\bar{I} = \frac{V_1 D_1 (D_1 + D_2) \Delta T}{2L} \tag{C.11}$$

This expression does not contain any derivatives. At least one of V_1, D_1, or D_2 must change as time progresses. If incremental changes are required, as in the small-signal analysis, partial derivatives can be used. In this case that leads to

$$\Delta i = \frac{\partial I}{\partial V_1} \Delta v_1 + \frac{\partial I}{\partial D_1} \Delta d_1 + \frac{\partial I}{\partial D_2} \Delta d_2 \tag{C.12}$$

Similar equations are used in the state-space averaging method in [22]. The same principle was applied in (10.1.42) of Chapter 10.1 in this thesis.

References

[1] James F. Lazar, "Analysis of Single Phase Ac/Dc Rectifier Circuits," Ph.D. thesis, California Institute of Technology, Pasadena, CA, March 1997.

[2] Esam H. Ismail and Robert W. Erickson, "Application Of One-Cycle Control To Three-Phase High Quality Resonant Rectifier," IEEE Power Electronics Specialists Conference, 1995 Record, pp. 1183-1190.

[3] A. Prasad, P. Ziogas and S. Manias, "An Active Power Factor Correction Technique For Three-Phase Diode Rectifiers," IEEE Power Electronics Specialist Conference, 1989 Record, pp. 58-66.

[4] L. Malesani, L. Rossetto, G. Spiazzi, P. Tenti, I. Toigo and F. Dal Lago, "Single-Switch Three-Phase Ac/Dc Converter With High Power Factor and Wide Regulation Capability," IEEE International Telecommunications Energy Conference, 1992 Record, pp. 279-285.

[5] J. Pomilio and G. Spiazzi, "Low-Loss Single-Switch Three-Phase Ac-Dc Converter Feeding Inductive Load," IEEE Power Electronics Specialist Conference, 1995 Record, pp. 1279-1280E.

[6] E. Ismail and R. Erickson, "A Single Transistor Three Phase Resonant Switch For High Quality Rectification," IEEE Power Electronics Specialist Conference, 1992 Record, pp. 1341-1351.

[7] E. Ismail and R. Erickson, "A New Class Of Low Cost Three-Phase High Quality Rectifiers With Zero-Voltage Switching," IEEE Applied Power Electronics Conference, 1993 Record, pp.182-189.

[8] Dorin O. Neacsu, Ziwen Yao and Venkatachari Rajagopalan, "Optimal PWM Control for Single-Switch Three-Phase AC-DC Boost Converter," IEEE Power Electronics Specialist Conference, 1996 Record, pp. 727-732.

[9] J. Kolar, H. Ertl and F. Zach, "Space Vector-Based Analytical Analysis Of The Input Current Distortion Of A Three-Phase Discontinuous-Mode Boost Rectifier System," IEEE Transactions on Power Electronics, Vol. 10. No. 6. November 1995, pp. 733-145.

[10] Q. Huang and F. Lee, "Harmonic Reduction In A Single-Switch, Three-Phase Boost Rectifier With High Order Harmonic Injected PWM," IEEE Power Electronics Specialist Conference, 1996 Record, pp. 1266-1271.

[11] D. Simonetti, J. Sebastian and J. Uceda, "Single-Switch Three-Phase Power Factor Preregulator Under Variable Switching Frequency And Discontinuous Input Current," IEEE Power Electronics Specialist Conference, 1993 Record, pp. 657-662.

[12] G. W. Wester and R. D. Middlebrook, "Low-Frequency Characterization of Switched Dc-to-Dc Converters," IEEE Power Processing and Electronics Specialists Conference, 1772 Record, pp. 9-20.

[13] R. D. Middlebrook and Slobodan Cuk, "A General Unified Approach to Modelling Switching-Converter Power Stages," IEEE Power Electronics Specialist Conference, 1976 Record, pp.18-34.

[14] L. D. Stevanovic and Slobodan Cuk, "Capacitive Idling Converters with Decoupled Input and Load Regulation Loops," IEEE Power Electronics Specialist Conference, 1993 Record, pp. 681-686.

[15] R. M. Madigan, R. Erickson and E. Ismail, "Integrated High Quality Rectifiers Regulators," IEEE Power Electronics Specialists Conference, 1992 Record, pp. 1043-1051.

[16] K. Liu and Y. Lin, "Current Waveform Distortion in Power Factor Correction Circuits Employing Discontinuous Mode Boost Converter," IEEE Power Electronics Specialists Conference, 1989 Record, pp. 825-829.

[17] Vatche Vorperian, "Simplified Analysis of PWM Converters Using the Model of the PWM Switch, Part I: Continuous Conduction Mode," IEEE Transactions on Aerospace and Electronic Systems, Vol. 26. No. 2. March 1990.

[18] Vatche Vorperian, "Simplified Analysis of PWM Converters Using Model of PWM Switch, Part II: Discontinuous Conduction Mode," IEEE Transactions on Aerospace and Electronic Systems, Vol. 26, No. 3, May 1990, pp. 497-505.

[19] Dragan Maksimovic and Slobodan Cuk, "A Unified Analysis of PWM Converters in Discontinuous Modes," International Power Conversion and Intelligent Motion Conference, Munich, Germany, 1989 Record.

[20] Jian Sun, Daniel M. Mitchell, Matthew F. Greuel, Philip T. Krein and Richard M. Bass, "Modeling of PWM Converters in Discontinuous Conduction Mode – A Reexamination," IEEE Power Electronics Specialists Conference, 1998 Record, pp. 615-622.

[21] Robert W. Erickson, *Fundamentals in Power Electronics*, Chapman Hill, 1997.

[22] R. D. Middlebrook and Slobodan Cuk, "A General Unified Approach to Modeling Switching Dc-to-Dc Converters in Discontinuous Conduction

Mode," IEEE Power Electronics Specialists Conference, 1977 Record, pp. 36-57.

[23] Jian Sun and Horst Grotstollen, "Averaged Modelling of Switching Power Converters: Reformulation and Theoretical Bases," IEEE Power Electronics Specialists Conference, 1992 Record, pp. 1166-1172.

[24] Richard Tymerski and Vatche Vorperian, "Generation, Classification and Analysis of Switched-Mode Dc-to-Dc Converters by the Use of Converter Cells," IEEE International Telecommunications Energy Conference, 1986 Record, pp. 181-195.

[25] Gene F. Franklin, J. David Powell and Abbas Emami-Naeini, *Feedback Control of Dynamic Systems*, Addison Wesley, 1991.

[26] R. D. Middlebrook, "Predicting Modulator Phase Lag in PWM Converter Feedback Loops," Proceedings of Powercon 8, 1981 Record, pp. H4.1-H4.6.

[27] IEC 1000-3-2, Electromagnetic compatibility (EMC), Part 3: Limits – Section 2: Limits for harmonic current emissions (equipment input current $\leq$ 16A par phase), First edition 1995-03.

[28] Richard Redl andre S. Kislovski and Brian P. Erisman, "Input-Current-Clamping: An Inexpensive Novel Control Technique To Achieve Compliance with Harmonic Regulations," IEEE Applied Power Electronics Conference and Exhibiton, 1996 Record, pp. 145-151.